2013

An Investigation of the weldability of high hardness armour steels

Lenka Kuzmikova
University of Wollongong

An Investigation of the Weldability of High Hardness Armour Steels

A thesis submitted in fulfilment of
the requirements for the award of the degree
Doctor of Philosophy

by

Lenka Kuzmikova, B.Sc.

Faculty of Engineering

University of Wollongong

DECLARATION

I hereby declare that this submission is my own work and that, to the best of my knowledge and belief, it contains neither material previously published or written by another person nor material which has been accepted for the award of any other degree or diploma of a university or other institution, except where explicitly specified and referenced.

Lenka Kuzmikova, B.Sc.
October 2012

ACKNOWLEDGEMENTS

I would like to thank Professor John Norrish and Associate Professor Huijun Li for their kind guidance, support and encouragement during the whole course of this research study.

I am grateful to Defence Materials Technology Centre (DMTC) for providing the scholarship enabling me to undertake and finally complete this research work.

I also would like to thank Dr Frank Barbaro for his advice and sharing his insight during weld hydrogen measurements.

I thank University technical officers for machining the samples for the numerous experiments, assisting during some experimental work and willingly lending the hand to overcome the technical difficulties.

Special thanks to Nathan Larkin for his great help with all the welding trials.

And last but not least I would like to thank my partner Michael for his patience and support.

ABSTRACT

The main objective of this PhD research was to develop safe highly optimised welding procedures for high hardness armour (HHA) steel welded with austenitic stainless steel consumable. This involved optimisation of currently used flux-cored arc welding (FCAW) process, adjustment of the procedure for fully automated welding in combination with metal-cored consumable and finally assessment of feasibility of the advanced laser-gas metal arc welding (laser-GMAW) hybrid welding using solid consumable for potential future replacement of the current process. The aim was to significantly improve economics of welding fabrication while ensuring weldment with desired properties.

The alloy design of the HHA has been altered prior to commencement of this research adopting novel low manganese approach. To develop welding procedures with optimised parameters a deep understanding of parent material properties was crucial. Hence, the initial effort focused on detailed property and weldability characterisation of the modified HHA steel. This included comprehensive metallography investigation, hardness testing and also development of continuous cooling transformation diagrams directly applicable to welding.

The optimisation of preheat temperature was required as the industry recently adopted austenitic stainless steel consumable that replaced the conventional ferritic filler and because AS 1554 does not differentiate between austenitic and ferritic fillers the level of preheat employed in industry practice remained as per procedure developed for ferritic filler. Further, AS 1554 does not provide any guidelines for determination safe interpass temperature range which has a significant effect on productivity particularly for robot controlled welding thus upper interpass temperature threshold was also determined experimentally.

The main concern when welding high strength Q&T steels is hydrogen assisted cold cracking (HACC) and heat affected zone (HAZ) softening. Preheating is carried out to eliminate the risk of HACC therefore the process of determination of lower preheat temperature threshold considered all three factors contributing to this phenomenon.

The level of diffusible and residual hydrogen present in the HAZ and weld metal were measured employing collection of hydrogen over mercury and inner gas melt extraction methods for all three consumable types (flux-cored, metal-cored and solid). Magnitude of residual stresses resulting from different levels of preheat were evaluated by measuring the angular distortion. Susceptibility of HAZ microstructure formed under variety preheat conditions was assessed using hardness testing and colour etching technique to determine volume fraction of various microstructural constituents. The degree of HAZ softening resulting from different levels of interpass temperature was evaluated utilising colour etching and hardness testing.

Feasibility of laser-GMAW hybrid welding was investigated employing 3.5 kW diode laser coupled with GMAW torch in combination with solid austenitic stainless steel consumable. The procedure for typical joint of a land platform was developed significantly reducing the number of welding passes compared to weldments produced using conventional GMAW. The joint properties were assessed using the same techniques as employed for weldments produced with metal-cored arc welding (MCAW) and FCAW.

The objectives of this work have been achieved resulting in optimised welding procedures for HHA steel. Additionally, from the entire family of high strength Q&T steels HHA possesses a highest carbon content, carbon equivalent, hardenability and thus it is the most difficult to weld hence the findings of this research work can be applied to all high strength Q&T steels. Further, the proposed approach based on the difference in transformation temperature of WM and HAZ can be used as an effective tool for future assessment of hydrogen control in steel welding.

Findings of this research regarding optimised preheat and interpass temperatures for welding of high strength Q&T steels are being reviewed by DSTO and Australian Standard Committee to be incorporated into standard AS/NZS 1554.4 - Structural steel welding - Welding of high strength quenched and tempered steels and also relevant defence standard.

LIST OF CONTENTS

LIST OF FIGURES

LIST OF TABLES

1 LITERATURE REVIEW

This literature review was undertaken to provide an overview of the current armour materials, various aspects of their metallurgy and their weldability. An introduction to design specifications and manufacturing processes for steel armour is provided, as well as their metallurgy, alloying and microstructural characterisation. The focus of this research is the welding of steel armour; hence, relevant research findings related to this topic are summarised in the following literature review.

1.1 ARMOUR

This section introduces the roles and challenges of armour in modern combat vehicles, as well as describing steel armour for ballistic protection, its history and development and the specifications used for armour design.

1.1.1 Roles and challenges

Armour has three main roles in order to defeat the penetrator and ensure protection and integrity of the combat vehicle and its occupants. These three roles are often described as: the absorption of the penetrator's energy and/or transfer of energy to the supporting structure; rebounding or changing of direction of the penetrators away from the vehicle; and deformation of the penetrator.

A key issue for armour is its weight. Increasing the thickness of armour will increase the protection level, as well as increase the weight of the combat vehicle. Increased weight drastically reduces the fighting ability of the vehicle through a number of aspects, including speed and acceleration; fuel efficiency and thus the range attainable; the number of troops/goods transported; and the types of defensive or offensive weaponry carried. Thus, it is evident that the challenge is to produce armour with good weight efficiency, ensuring adequate ballistic protection capabilities, for the particular type of combat vehicle and its intended role in battle.

Armoured vehicles possess a degree of protection from their structural arrangement, as even light-armoured vehicles require substantial hull structure for the power plant, suspension and load carrying [1]. Light vehicles are manufactured using relatively thin armour plate. Therefore, the threat protection level generally encompasses small and medium arms infantry projectiles and blast. The optimal armour system requires a combination of hard layers, that oppose penetration as well as blunting the penetrators and tough layers, which have the ability to absorb the energy of the penetrators.

1.1.2 Steel armour

Armour materials are chosen as a function of their intended application, ballistic performance, weight and price [2]. For ballistic protection against small-arms and other intermediate threats, steel is a very competitive armour material [3, 4]. Indeed, with the development of modern armour technologies, steel armour accounts for a significant amount of the total armour protection package [5]. This is due to favourable mechanical properties, ease of manufacture and relatively low cost, in comparison with other modern armour materials such as composites. From a mechanical properties perspective, steels possess high hardness, strength, toughness and good ductility. From a manufacturing viewpoint, they have good formability and are easily joined.

1.1.2.1 History and development

During World War II cast steel was predominantly used in the U.S.A. for tank structures, providing reductions in cost and increased production capability, although welding technology was already developed for rolled steel plates. In the past, U.S. manufacturers used cast steel for hulls and turrets particularly for the M60 tank. Because of the need to employ more complex vehicle designs and reduce the cost of the fabrication, rolled homogeneous armour (RHA) steel has replaced cast steel, as indicated by its use in the Ml Abrams tank [6].

Two main groups of armour steel are used in the manufacturing combat vehicles. The first is high hardness armour (HHA), to MIL-A-46100D specification that possesses

very high hardness levels in order to provide protection against projectile penetration. The second type is class 1 rolled homogeneous armour (RHA), to MIL-A-12560H, that possesses lower hardness levels than HHA, but gives improved toughness and ductility in order to avoid material failure by brittle fracture, as well as providing better weldability. These two specifications have been used since World War II without any significant change. The MIL-A-12560H specification was modified in 2002 by introducing the improved rolled homogeneous armour (IRHA), developed by U.S. Army Research Laboratory, as a class 4 - wrought armour plate. This new class is divided into two sub-classes:

- Class 4A: Tempered at 425°C to achieve hardness levels of HRc 47-48
- Class 4B: Tempered at 985°C to achieve hardness levels of HRc 39-41 [4, 6]

Before the development of improved rolled homogeneous armour (IRHA), manufacturers of combat vehicles in U.S. used two different armour alloys: manganese-molybdenum-boron (Mn-Mo-B) alloy, which was employed for thicknesses 1.5 inches and less and the nickel-chromium-molybdenum (Ni-Cr- Mo) alloy for thicker plates [6].

1.1.2.2 Specifications

No universal standard for the design of armour steels exists. Rather, each country has particular armour specifications that are adhered to, when used to manufacture armour for combat vehicles. A comparison in the classes of armour steels for the USA, UK and Australian specifications, as well as steels produced by the current Australian manufacture Bisalloy Steels, is presented in Table 1-1.

Military-based and performance-based specifications are the two main specifications used in armour steel manufacture. However, recent research [7, 8] presented the possibility of the development of an alternative type of specification, which relates the microstructure of the armour steel and its effects on mechanical properties, and ballistic performance.

Table 1-1 A comparison of the classes of armour steels for the US, UK and Australia, as well as Bisalloy Steels [4].

Armor Class According to DEF(AUST) 8030	Hardness Equivalences (HB)			
	DEF(AUST) 8030[1]	U.S. Military Specification Approx. Nominal Equivalent Grade	DEF STAN 95-24 Approx. Nominal Equivalent Grade	**BISALLOY STEELS GRADES**
Class 1	Not Explicitly Specified	No Equivalent	No Equivalent	**Bisplate 80A (235-293)**
Class 2	2A: 260-310 2B: 280-330	MIL-A-12560H Class 2 <31.8 mm (277-321)	Class 1 (262-311)	**Bisplate High Impact Armor (HIA) Class 2 (277-321)**
Class 3	340-390	MIL-A-12560H Class 1 <12.7 mm (341-388) 12.7 to <19.1 mm (331-375) 19.1 to <31.8 mm (321-375) 31.8 to <50.5 mm (293-331)	Class 2 <9 mm (341 min) 9 to <15 mm (311 min) 15 to <35 mm (285 min) 35 to <50 mm (262 min)	**Bisplate High Impact Armor (HIA) Class 1 (290-390)**
Class 4	370-430	MIL-A-12560H Class 4B (381 max)	No Equivalent	**Bisplate High Toughness Armor (HTA) (370-430)**
Class 5	420-480	MIL-A-12560H Class 4A (442 min)	Class 3A 5 to <50 mm (420-480)	**Bisplate Ultra High Toughness Armor (UHTA) (420-480)**
Class 6	470-535	MIL-A-46100D	Class 3 <15 mm (470-540) 15 to <35 mm (470-535)	**Bisplate High Hardness Armor (HHA) (477-534)**
Class 7	530-605	No Equivalent	Class 4 <15 mm (530-605) 15 to <50 mm (495-605)	No Equivalent
Class 8	560-655	No Equivalent	Class 5 (560-655)	No Equivalent

[1]Each hardness range in DEF(AUST)8030 applies for all thicknesses from 3 to 35 mm, unless otherwise specified.

Military specifications control the mechanical and chemical integrity of the armoured structure. The US uses two specifications for armour steel alloys, MIL-A-12560H [9] rolled homogeneous armours (RHA) possessing hardnesses from 241 to 388 brinell (HBN) and MIL-A-46100D [10] high hardness (HH) with hardnesses from 477-534 HBN. For armour to be accepted into service in the US, steels must meet these

specifications. These specifications originated in World War II and have not changed significantly.

Performance-based armour specifications require the performance of the armour to be met by the manufacturers. Australia (AUST DEF 8030 [11]) and the UK(UK DEF STAN 95-24 [12]) use performance-based armour specifications, which enable the alloy manufacturers the freedom and flexibility in the design of armour meeting particular performance constraints, this also aids in reducing cost.

Joint research by Australia and the US [4], has attempted to add to the data relating armour hardness and toughness to ballistic performance, in order to develop a unified armour steel specification that controls armour steel properties over a range of steel hardness. However, this type of specification has not yet been put into practice.

1.2 STEEL ARMOUR METALLURGY

This section describes some manufacturing aspects and provides details of the low manganese approach for the production of quenched and tempered (Q&T) steel plates. The addition and effects of micro-alloying elements on the parent and weld heat affected zones (HAZ) are examined, as well as some of the microstructural characteristics and considerations of Q&T armour steels.

1.2.1 Manufacturing aspects

High hardness and good strength to weight ratio are important requirements for Q&T steels for military applications. The superior properties [13] are ensured with carefully designed chemical composition and heat treatment processes.

The manufacturing process of Q&T steel plates involves vacuum degassing and calcium treatment of the green feed stock. These steels are designed to give optimal ballistic performance whilst at the same time maintaining good fabrication properties and very good weldability. After hot rolling, all classes of steel armour are quenched and tempered in a modern Drever roller to achieve the desired levels of hardness and

toughness for each class. This heat treatment consists of two phases: rapid water-quenching from the austenite field resulting in the formation of brittle microstructure consisting of untempered martensite and subsequent tempering that improves the plate's toughness while lowering the level of hardness. The tempering temperature is based on desired balance between hardness and toughness required for particular application. This two-step heat treatment results in a microstructure associated with superior combination of hardness, strength, ductility, toughness and weldability.

The required hardenablity of the steel is achieved by alloying with elements which retard the diffusion controlled transformation from austenite to ferrite-pearlite. Alloying elements can be divided into two groups:

- austenite stabilisers: C, Mn, Ni, Cu
- ferrite stabilisers: Mo, Si, Cr, Ti, V, Nb

Ferrite stabilisers achieve high hardenability with relatively small additions compared to austenite stabilisers. Conversely the competition process of carbides of ferrite stabiliser elements forming depletes the austenite of both C and alloy additions resulting in lower hardenability.

1.2.2 The Low manganese approach for the production of quench and tempered steel plate

Before the low manganese approach was introduced, the levels of manganese in Q&T steel plate produced by the BlueScope Steel varied between 0.8 to 1.5 wt% [14]. Mn combines with S and results in formation of MnS inclusions, which tend to concentrate in the through thickness centreline region and are detrimental to properties of steel. During hot rolling, these MnS inclusions tend to elongate and form 'stringers'. The elongated MnS inclusions can act as crack initiators and result in inhomogeneity in the steel. The degree of inclusion elongation depends on various factors, such as rolling parameters, relative properties of inclusions and the surrounding metal and importantly on the size of the inclusion [15]. To minimize the negative effect of the presence of sulphide inclusions, the high Mn approach in the manufacture of steels requires very low levels of sulphur, in order to suppress the

formation of large volumes of MnS inclusions. To achieve very low sulphur levels, quite expensive techniques have to be introduced, together with sulphide shape control. Lower levels of Mn allow higher sulphur content without extensive formation of MnS.

The low Mn approach (0.20 to 0.50 wt% Mn) has been developed mainly to reduce centreline segregation and improve the through thickness mechanical properties, by lowering the volume of manganese sulphide (MnS) inclusions present in the material [14] as shown in Figure 1-1. During casting, S segregates in the centerline region and results in formation of relatively large MnS inclusions in this area [15]. However, it has been reported that decreasing Mn below certain levels, can lead to hot shortness due to formation of iron sulphides (FeS), instead of the MnS, caused by the lack of Mn to compete with Fe for S [15]. Lowering the Mn content to 0.3wt% resulted in quite consistent distribution of relatively small globular MnS inclusions, however it has been observed that some large MnS inclusions were present in the centre of steel slabs [15].

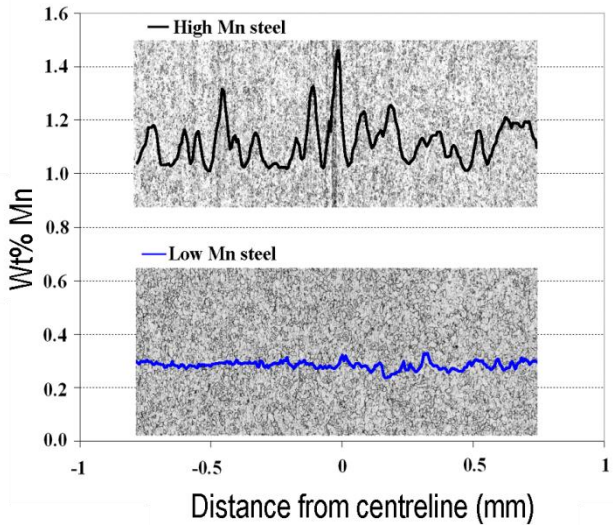

Figure 1-1 X-ray line scan across centreline region of high and low Mn hot rolled strip sample [14].

Another benefit of the low manganese approach is that MnS inclusions are formed from the melt at a lower temperature range and this results in smaller size of inclusions. Ti is also a sulphide forming element. Alloying steel with amounts as low

as 0.020 to 0.035 wt% Ti, was found to be beneficial for the steels toughness, as it favours the formation of complex sulphides such as (Fe,Ti)S_2 and (Mn,Ti,Fe)S, which are less prone to elongation during hot rolling [14].

Mn is added to steel to promote solid solution strengthening, facilitate grain refinement during hot rolling through lowering the $\gamma \rightarrow \alpha$ transformation temperature [15] and as can be seen in Figure 1-2, with a lower carbon equivalence (CE), it significantly increases steel strength and hardenability. Alloying elements (Ni, Cr, and Mo) are added to steel to provide a high level of through-thickness hardenability [6]. By lowering the Mn content, steel looses its original features and therefore Mn should be partially substituted with some other alloying element/combination of elements, to ensure the required levels of hardenability and strengthening, without negative influence on the other properties. It has been suggested that if the Mn content is lowered, it could be replaced to some extent with Cr [14] plus addition of some other microalloying elements such as V, Ti, Nb and B, to achieve optimal properties of the alloy. The main advantage of Cr is that it does not increase the CE value as much as Mn and thus would have favourable effect on weldability [14]. However, it was reported that more investigation is needed to approve its suitability for this use.

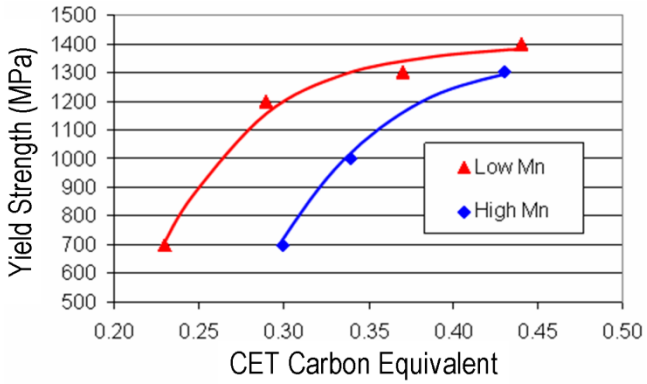

Figure 1-2 Increase in yield strength of low manganese Q&T wear and structural grades compared to conventional high manganese Q&T grades for a given CET value [14].

1.2.2.1 Microalloying elements

In general, the most common microalloying elements are Ti, V, Zr, Nb, B. These elements have strong affinity to C, O and N and their compounds with C and N have very good solubility in solid solution and through retardation of the γ→α phase transformation they considerably increase the hardenability of the steel [16]. The lower the enthalpy of formation of the compound, the more stable the precipitates are [16]. Figure 1-3 shows the enthalpies of formation of typical oxides, nitrides, sulphides, and carbides of microalloying elements.

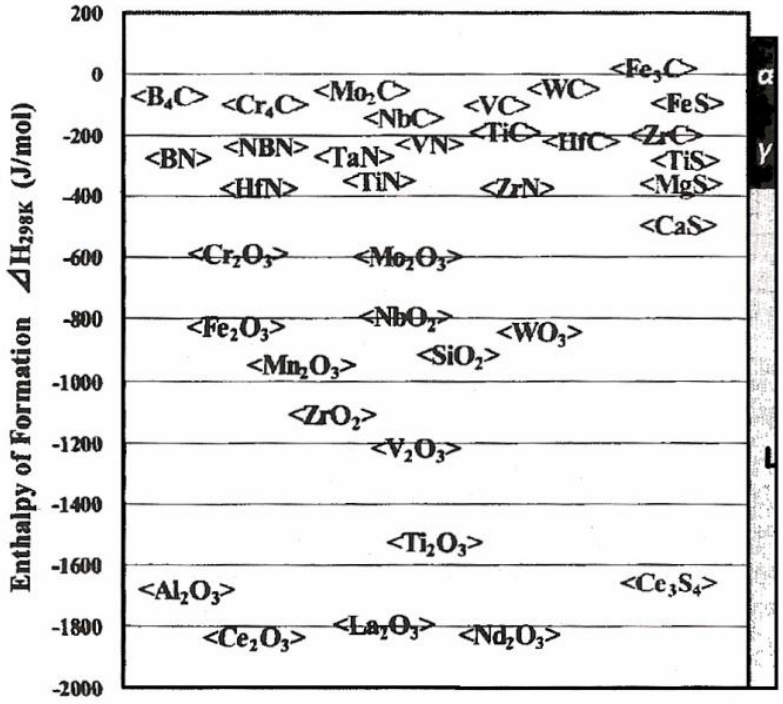

Figure 1-3 Enthalpies of formation of typical oxides, nitrides, sulphides, and carbides of microalloying elements (the right bar shows the steel phases from which the compounds generally precipitate [16].

The temperature range within which precipitates form is very a important parameter for thermo-mechanical control processing (TMCP). It is possible to enlarge the metallurgically useful temperature range to some extent by microalloying steel with a combination of microalloying elements (for example, with both Ti and Nb). However, under certain conditions complex Ti-Nb carbo-nitrides are formed and can reduce beneficial influence of each single element [16].

Microalloying elements are strong carbo-nitride formers and the face-centered (FCC) austenite lattice allows fast diffusion of interstitial C and N, so the microalloy carbo-nitride precipitation takes place immediately after the steel cools down beyond their soluble ranges. A low content of microalloying elements slows down the precipitation growth. As a result the precipitates are fine and dispersed in the steel matrix and can induce a range of thermo-mechanical effects in austenite, such as, retardation of grain growth, retardation of recrystalization, retardation of phase transformation [16].

1.2.2.2 Effect of microalloying elements on HAZ

When steel is subjected to the welding process, the original microstructure surrounding the weld pool undergoes major changes. This area (the heat affected zone, HAZ) experiences a very quick and steep local thermal cycle, unlike those encountered during the production process. This thermal cycle does not allow nitrides or carbides of microalloying elements to maintain their original form. The final microstructure of the HAZ is in some way affected by the chemical composition and size distribution of precipitates in the parent metal. During the welding thermal cycle, changes are observed in the HAZ that are connected to the complex precipitates. These include dissolution, re-precipitation and coarsening and as a result, austenite grain growth [16].

At the high temperatures reached during austenitising, the precipitates are dissolved and elements such as Ti, Nb, C and N reform a TiN-rich precipitates. This is due to the compound's stability at high temperatures. During the welding process, after the HAZ experiences peak temperature, it cools down at a particular rate. Further precipitation takes place here, usually on the surface of the existing particles. This causes particle coarsening. Particle dimensions are strongly influenced by the heat input. The higher the heat input the coarser particles that precipitate [16]. Figure 1-4 shows the HAZ microstructure and dissolution positioning of micro-alloying compounds.

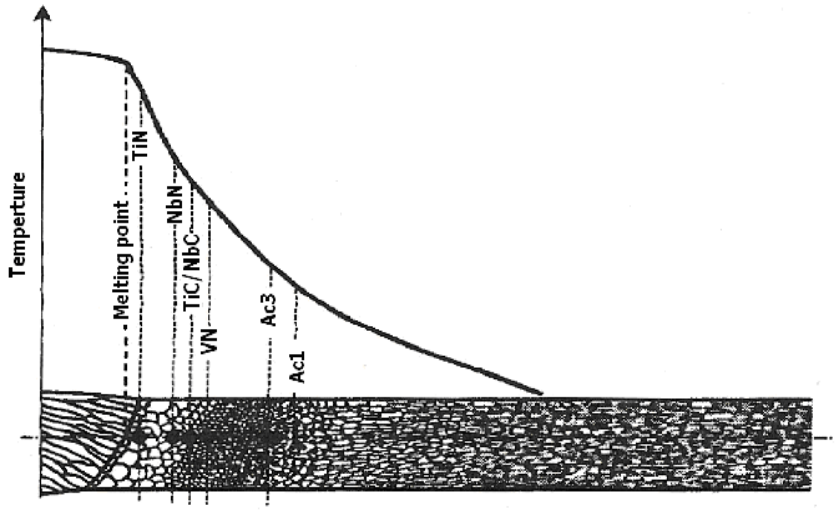

Figure 1-4 HAZ microstructure and dissolution position of micro-alloying nitrides and carbides [16].

If the carbo-nitrides of the alloying elements stay un-dissolved during the weld thermal cycle, they play an important role in suppressing the austenite grain growth in the HAZ. But these elements once dissolved in solid solution have a significant detrimental effect to the HAZ toughness [16]. NbN precipitates have quite a favourable effect to the base metal properties. But when the temperature during the weld thermal cycle is high enough to dissolve these particles, both Nb and N in solid solution have deleterious influence on the HAZ toughness [16].

Research [15] has revealed that when steel is microalloyed with Ti and Nb, the complex Ti-Nb carbosulphides ($(TiNb)_2CS$) are formed on surface of larger more stable MnS particles, by a solid-state precipitation reaction on cooling after hot rolling. These complex particles are in addition to the (Ti,Nb)CN particles that are traditionally used for grain refinement and precipitation strengthening of thermo-mechanically processed steels [15].

Vanadium

Vanadium easily combines with P and N and forms complex V-P and V-N compounds, which precipitate upon cooling. This reduction in free P and N can lower the segregation of these elements on the grain boundaries and is beneficial for the

mechanical properties of the steel. The equilibrium solubility product of V_4C_3 in austenite and kinetics of precipitation during cooling from the austenite field, define the quantity of V in solid solution [17].

Titanium

Previous research [18] has identified the favourable influence of TiN precipitates on the properties of low heat input weld heat affected zones in the case of C-Mn structural steels. The significant benefit of micro-alloying steels with Ti, is the reduced peak hardness of the HAZ, due to a decrease in the prior austenite grain size by the grain boundary pinning action of TiN particles (Figure 1-5). The consequence of the smaller austenite grain size is lower hardenability in comparison with Ti free steels. Another beneficial feature of Ti bearing steels is the narrower coarse grain region adjacent to the fusion boundary. It was observed that increasing the Ti/N ratio lowered the austenite grain size and gave an increase in transformation start temperature. However, Ti should be added in levels high enough to form an adequate amount of TiN precipitates. Insufficient levels of Ti can cause the formation of very small TiN particles, which are less thermally stable and in the higher range of temperatures (1350-1400°C) tend to dissolve. This results in diminishing the grain boundary pinning effect and consequently lowers the control of austenite grain size [18].

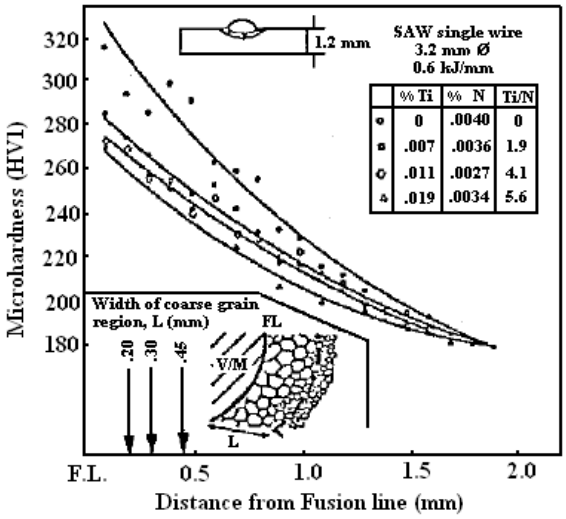

Figure 1-5 Effect of micro Ti additions on microhardness from the fusion line in bead on plate welds. Effect on the width of the coarse grain zone is also shown [18].

1.2.3 Microstructural characteristics

It is well established, that martensite in the tempered condition is the most desirable microstructure for steel armour plates. Armour plate material in this condition, gives superior performance against projectile penetration, while microstructures consisting of bainite and martensite, or fully bainitic structures are less susceptible to hydrogen assisted cold cracking (HACC). For materials used in armour applications, the requirements of high hardness and resistance to HACC cannot be met simultaneously [13]. Therefore, a compromise has to be made to achieve satisfactory results for both these requirements. It has been reported [6] that materials with a microstructure consisting of bainite are relatively brittle with low impact energies and these materials are likely to crack or shatter under ballistic loading.

1.2.3.1 Continuous Cooling Transformation (CCT)

Continuous-cooling-transformation (CCT) diagrams indicate the typical transformation behaviour of an austenitised steel subjected to various cooling rates. CCT diagrams are a useful tool to determine the volume percentage of the microstructures present as a function of cooling rate, as well as the start and finish temperatures of phase transformation. CCT diagrams can be determined by

metallography, thermal arrest, dilatometry methods or optically utilising a confocal microscope. Dilatometry is the technique most often used when constructing CCT diagrams. It is based on the detection and interpretation of structural and expansion coefficient changes on transformation of austenite to diffusion or diffusionless products. The change in length with temperature for a given material can be expressed by equation:

$$L_1 = L_2\left(1 + \int_{T_1}^{T_2} \alpha . dT\right) \tag{1.1}$$

where L_1 and L_2 are lengths at temperatures T_1 and T_2 and α is the coefficient of linear expansion.

This measurement of the length change is used to determine the onset and completion of microstructural transformation. The temperature when the transformations take place can be identified by defining the temperature at which temperature vs. dilatation curve starts to diverge from linearity [19]. Continuous cooling of steel is used in the majority of metallurgical processes, in order to obtain the desired microstructure. The γ→α transformation reaction on cooling is described using CCT diagrams, which have practical advantages when compared with other methods such as time temperature transformation (TTT) diagrams [20].

CCT diagrams are also very useful in the area of welding. After more methodical and in depth studies of transformation kinetics and mechanical properties of weld metal, a large number of CCT diagrams which are directly applicable to weld metals have also been constructed. These CCT diagrams assist in a better understanding of the microstructural changes. These changes take place on cooling after welding and the effects of various parameters such as chemical composition, oxygen content (hence size distribution and population of inclusions), welding parameters, have significant effect on factors such as cooling rate and prior austenite grain size and the γ→α transformation of weld metals [20].

When designing safe welding procedures the information about the transformation temperature range of WM and HAZ are important from hydrogen management view

point. If a ferritic consumable is used the relative time between transformation of the WM and HAZ determines the direction of hydrogen diffusion: the solubility of hydrogen in the molten pool and the high temperature austenitic phase is high but it is much lower in the lower temperature ferritic or martensitic microstructure. If the WM transforms before the austenitised area of HAZ zone during cooling of the weld zone any hydrogen in the weld will evolve into the HAZ of the parent material.

1.2.3.2 Martensite

To achieve a martensitic transformation, rapid cooling is needed, this must be fast enough to suppress the higher temperature, diffusion-controlled ferrite and pearlite reactions, as well as formation of other intermediate phases such as bainite [21]. Martensite transformation begins when the martensite start temperature, $T_{Ms,}$ is reached. The temperature range where martensitic transformation starts is quite wide (from as high as 500°C to well below room temperature), and is strongly influenced by the amount of alloying elements which stabilise the γ-phase and the cooling rate. When T_{Ms} is reached, martensite starts to form. Transformation continues during further cooling until the martensite finish temperature, T_{Mf}, is reached. At this stage, austenite should be transformed to martensite, but often a small fraction of the austenite remains untransformed, even when temperature is very low. Some alloying elements, when added in high enough amounts, moves T_{Mf} well below room temperature and results in large volume fraction of retained austenite if the steel is not further cooled to reach T_{Mf} [21]. Retained austenite has a role to play in the ballistic performance of armour steels and will be examined in a further section.

Classical thermodynamic factors affect the austenite decomposition temperature, while ΔT_m is influenced by the ability of martensite nucleation and growth within the austenite matrix. The parameters that affect the ΔT_m incorporate external shear stresses and any other product that can have effect on the resistance of base γ-lattice to mechanical shear during the martensite transformation (such as hardening mechanism, point defects, dislocations, and precipitates) [21].

Influence of alloying elements on martensitic transformation

Alloying elements can be divided into two groups with regard to the formation of martensite. The first group contains alloying elements that affect the equilibrium austenite decomposition temperature (T_0), and second are those that affect the necessary undercooling below T_0, i.e., $\Delta T_m = T_0 - T_{Ms}$ [22]. During studies on the influence of alloying elements on martensitic formation, it was also found that Al, Ti, V, Nb and Co efficiently increased the T_{Ms}, and Si, Cu, Cr, Ni, Mn, and C decreased the T_{Ms} temperature.

It has been reported by Suzuki *et al.* [23] that nitrogen has an extremely adverse effect on martensite-containing microstructures, but its detrimental effect is not so significant in fine ferrite-pearlite microstructures.

Prediction of martensite start temperature (T_{Ms})

Various empirical equations for calculation of Ms transformation temperature have been developed over the years. The most extensively used formula providing predictions with good accuracy was developed in 1965 by Andrews [24]. Note: T_{Ms} is expressed in °C.

$$T_{Ms} = 539 - 423C - 30.4Mn - 17.7Ni - 12.1Cr - 7.5Mo \quad (1.2)$$

1.2.3.3 Bainite

It has been reported [17] that if upper bainite occurs in the martensitic microstructure, it improves the toughness without negatively effecting the steel's strength. At the strength levels of the fully martensitic structure, up to 12% increase in fracture toughness and 18% increase in impact toughness were obtained. This phenomenon was not observed when lower bainite was present in martensitic microstructure.

There are a number of characteristic features of both upper and lower bainite. Characteristic features of lower bainitic structure are well defined plates of ferrite

within which carbides oriented at a characteristic angle to the long axes of the plates can be seen [17]. Conversely, characteristic feature of the upper bainitic structure are laths of ferrite in between which cementite occurs. In the case of mixed martensite-upper bainite structures, bainite can be seen as brighter areas in comparison to the darker martensite [17].

1.3 WELDING OF ARMOUR MATERIALS

This section discusses the different welding techniques commonly utilised for joining steel armour and outlines the potential benefits of introducing the laser hybrid welding process. Important mechanical properties of the welds and the effect of welding parameters are described. This section also reviews the different types of welding consumables available for GMAW and their applications. In addition principles of developing safe welding procedures and the benefits of using austenitic stainless steel consumables are explained.

1.3.1 Introduction

Fusion welding procedures are employed in the majority of armour fabrications [25]. Welding produces heat affected zones (HAZ) between the parent and weld metal, which includes sub-zones of various hardnesses (rehardened, softened/tempered) (Figure 1-6). Based on clause 5.1.3 in MIL-STAN-1185 (AT), on any ballistic surfaces 5/8 inch (15.9 mm) from toe of the weld, at any location of weldment, the Brinnel hardness shall not be lower than that permitted by MIL-A-46100. This limit of hardness is 477 HB (equivalent to 509 HV) [25].

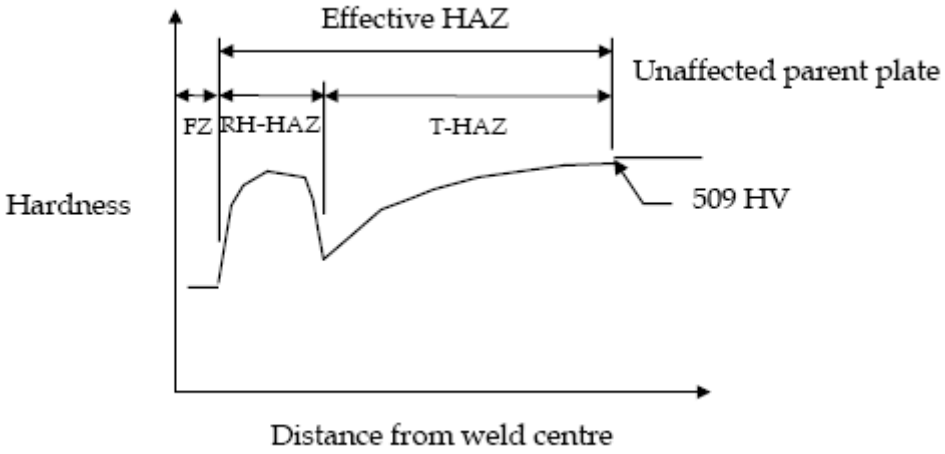

Figure 1-6 Schematic diagram of typical weldment hardness profile. FZ – fusion zone, RH-HAZ – rehardened HAZ, T-HAZ – tempered HAZ [25].

When Q&T steels are to be welded, special precautions have to be made, because the HAZ of these steels are susceptible to hydrogen-assisted cold cracking (HACC), as well as HAZ softening (tempering). Both of which can affect the ballistic performance of the armour material. The extent to which the HAZ softens depends on factors such as chemical composition, weld thermal cycle (welding method), kinetics of the phase transformation [26]. Whether HACC will occur depends on various factors such as hardness, which is influenced by the steels microstructure, type and magnitude of residual stresses and importantly level of diffusible hydrogen which enters the weld pool [25].

As shown in Figure 1-7 [25], the typical structure of welds in Bisalloy HHA plate consists of three different sub zones, namely, fusion zone (FZ), rehardened zone of the HAZ (RH-HAZ) and tempered (softened) zone of the HAZ (T-HAZ). During welding, the temperature experienced by the RH-HAZ reaches the austenitisation region and material is subsequently cooled down rapidly by heat transfer to the surrounding plate. The T-HAZ experiences a temperature sufficient only to temper this region [25].

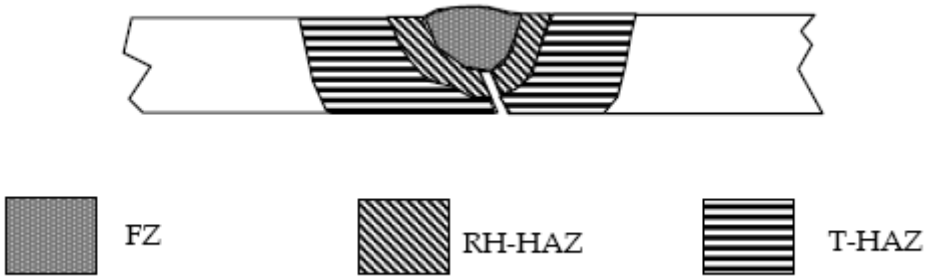

Figure 1-7 Schematic diagram of section from Y-groove test weldment showing the three different HAZs sub zones [25].

Although HAZ softening has an adverse effect on ballistic performance of high strength Q&T joints welded utilising common arc welded processes, mechanical testing (tensile and bend tests) reveal that it does not have a significant effect on joint tensile strength because of overall plastic restraint on the total joint [27].

To minimise the risk of HACC during and after welding and produce crack free joints with an acceptable degree of softening, optimal welding conditions must be determined. A number of cracking tests are used when developing safe welding procedures [25]. Hydrogen assisted cracking tests can be divided into two basic groups. These are described by Yurioka [13] as external restraint tests and self-restraint tests, both of which are incorporated in a number of specific tests as follows:

Types of external restraint tests:

- Constant load rupture (CLR) test
- Tensile restraint cracking (TRC) test
- Rigid restraint cracking (RRC) test (Figure 1-8)
- Implant test and Modified implant test with modified helical notch
- Augmented strain cracking test
- Corner joint weld cracking (CJC) test

Types of self-restraint tests:

- Control thermal severity (CTS) test
- y-groove restraint test (also called Tekken test)
- Single bevel test
- Lehigh restraint test
- Slot weld test (also called Lehigh slot weld test)
- Restraint circular groove weld test
- H-slit restraint test
- Instrumented restraint cracking (IRC) test

The use of these tests in relation to HHA steels was discussed by Williams et al. [14]. As mentioned in section 1.2.2 alloy design of HHA steel utilises low Mn approach that improves the weldability of the steel through lowering the volume of manganese sulphide (MnS) inclusions and also lower resultant carbon equivalent content compared to high Mn variant. Figure 1-8 indicates the improved weld cracking performance of low Mn Q&T steel compared to high Mn variant in RRC test. From the graph it is obvious that in case of low Mn steel crack free welds can be produced employing much lower heat input compared to high Mn version.

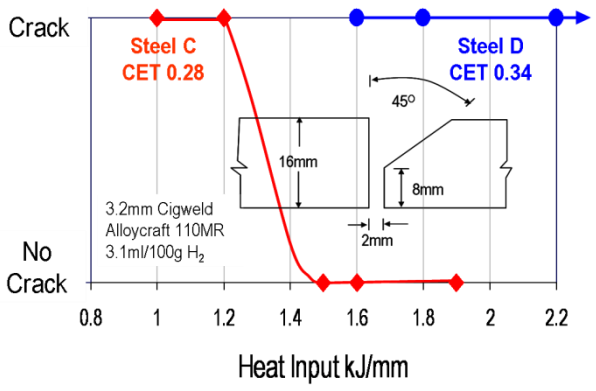

Figure 1-8 Rigid Restraint Cracking (RRC) test. Cracking incidence vs. heat input for low Mn Q&T Steel C vs. high Mn Q&T Steel D [14].

1.3.2 Important mechanical properties of welds

There are a number of mechanical properties which are considered important for weldments. The microstructure and mechanical properties in the HAZ of steel with a specific chemical composition and heat treatment are a function of the thermal history experienced by given point. Welding procedures should be designed to ensure that these properties are close to those possessed by the parent material, in order to guarantee similarity in both structural integrity and ballistic performance.

1.3.2.1 Hardness

Controlling the hardness levels of the HAZ, is an important aspect when assessing the risk of HACC and stress corrosion cracking in steels [18]. Usually, the higher volume fraction of hard martensitic structures present in the HAZ and weld metal itself, the higher susceptibility to HACC. When developing safe welding procedures, the maximum hardness obtained in the HAZ is often a key measure in the welding procedures designed to avoid HACC. There is also correlation between hardness and toughness of the weldment [18], therefore it is necessary to choose appropriate welding parameters, as well as suitable chemical composition of the parent and filler metal, to achieve the most beneficial compromise between these two properties for a given application.

1.3.2.2 Toughness

The toughness of the HAZ of the micro-alloyed steel is often reduced by local brittle zones (LBZ). The microstructure of the LBZ consists of lath martensite-austenite (MA) islands in the large prior austenite grains; this is considered to be the main cause of the decreased toughness. Hard and brittle MA constituents are mainly formed in the coarse-grained region of HAZ, which is the reason that this region has the lowest toughness. The HAZ toughness can be improved by controlling the quantity of LBZ, controlling the amount of MA constituents, by careful design of micro-alloy additions [16] and also by controlling the welding heat input as indicated in Figure 1-9.

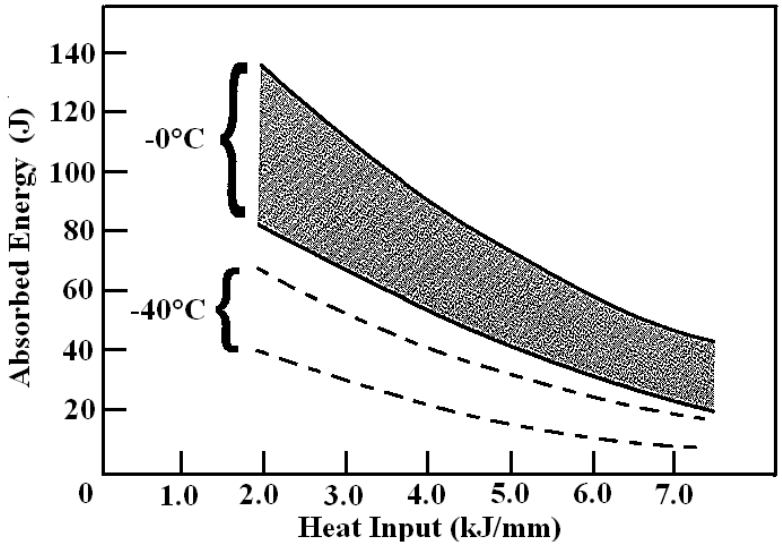

Figure 1-9 Effect of heat input on HAZ toughness of an AS 3597 700 Q&T steel [27].

1.3.2.3 Strength

The tensile strength of the HAZ varies depending on the thermal profile experienced by the different HAZ subzones, consumable, joint configuration and dimensions, and the carbon and carbon equivalent contents of the steel.

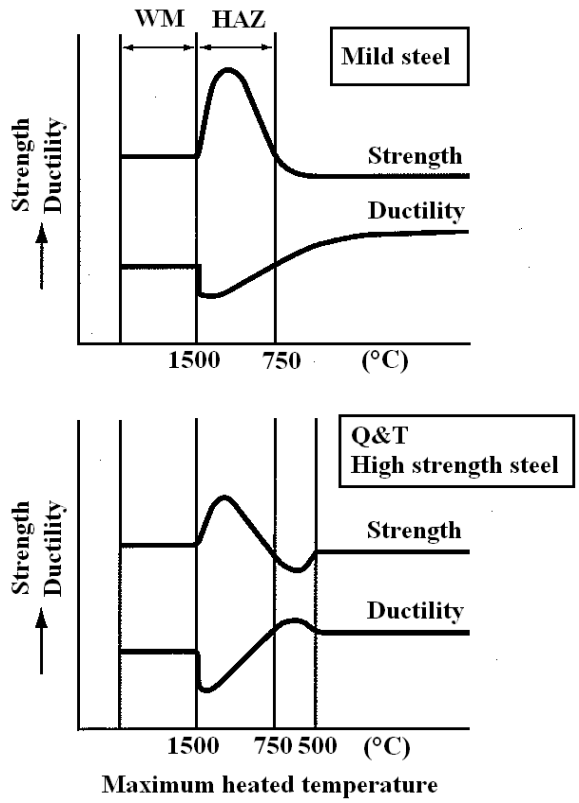

Figure 1-10 Different strength and ductility profiles of mild steel and Q&T steel weldments [27].

From the Figure 1-10 it is obvious that in case of Q&T steels, the maximum strength and hardness are observed in the area near the fusion line (coarse-grained (CG) HAZ) and minimum values are measured in the over-tempered (OT) HAZ region. In contrast ductility reaches its minimum in GC HAZ, and then increases with maximum values obtained in OT HAZ before it slightly drops to the value of unaffected parent metal [27].

1.3.3 Welding techniques

A number of welding techniques are used when welding armour components. Q&T armour steels are readily weldable using conventional arc welding processes. Although, additional care must be taken to avoid both HACC and softening in the HAZ. Trade-offs do exist and different welding techniques offer advantages in different areas. Several techniques and some of their advantages are described in the following section.

1.3.3.1 Manual Metal Arc Welding (MMAW) vs. Flux cored arc welding (FCAW)

In the past, British Aerospace Engineering (BAE) Systems used large diameter manual metallic arc (MMA) consumables for the principal structural welding in manufacturing of armoured fighting vehicles. Nowadays, semi-automatic welding procedures are reportedly used, in order to improve quality, productivity and aesthetics of the welded components. It is reported that the preferred method at BAE Systems when welding armour plate is flux cored arc welding (FCAW) with austenitic stainless steel (ASS) 20Cr 9Ni 3Mo consumable. For down-hand welding of conventional armoured vehicles, semi-automatic self-shielded FCAW and for positional welding semi-automatic shielded (composition of shielding gas: Ar + 20% CO_2) FCAW is employed. For detail work, final attachment to the structure and on-site work, small diameter MMA consumables are still utilised mainly because of their positional welding capability [28].

1.3.3.2 GMAW

In last 20 years the GMAW process utilising flux-cored consumable (or FCAW process) has been preferred method used by major defence contractors for welding fabrication of armour structures. It provides superior productivity compared to MMAW. The wire is continuously fed into the weld pool preventing frequent starts and stops (the areas with increased risk of HACC) as in case of MMAW. The shielding atmosphere ensures low weld hydrogen content. More recently the need to increase productivity has necessitated the move to automation and this has led to an increased use of metal-cored and solid wires.

Welding wires for GMAW

The main objective when selecting the welding consumable is to achieve stable process, optimum integrity of the weld and high productivity at low cost. Three types of wire: solid, metal-cored and flux-cored are available for GMAW process. To select the optimum type of wire for a given application many aspects have to be considered. Leading determinants of the cost effectiveness of a consumable are deposition rate

(the amount of weld metal deposited per hour) and deposition efficiency (how much of the welding consumable actually becomes part of the weld deposit).

Solid wire

Solid wire was the first wire used for GMAW. The biggest advantage over cored wires is total absence of slag which eliminates the need for inter-pass cleaning. Fluxes also have the major potential to pick-up hydrogen from surrounding atmosphere if seamed consumables are stored inappropriately and to introduce this hydrogen into the weld pool.

Flux-cored wire

Flux cored wires offer better fusion, penetration, higher deposition rates, smoother arc transfer and lower spatter levels than solid GMAW wires. Flux-cored wires are capable of all positional welding without a need to switch to short arc transfer or pulsed mode. Selection of an all positional flux-cored electrode for out of position applications significantly reduces the set up time and cost of welding fixtures. The disadvantage of flux-cored wires is that in case of multi-pass welding the slag needs to be removed from the bead surface before deposition of subsequent passes which has an adverse influence on both productivity and cost [29].

Gas shielded FCAW is particularly appropriate for welding high strength Q&T armour steels due to generally low levels of hydrogen associated with this process [27].

Metal-cored wire

Metal–cored wire has the same structure as the flux-cored wire and welding characteristics similar to solid wire. The main advantages of metal-cored wire are the absence of slag (although sometimes small silicon islands from the deoxidized products can form on the bead's surface), higher duty cycles, faster travel speeds, low fume formation and very good cost effectiveness. To be able to fully utilise their performance, these wires are most suitable for automated processes. The composition of core consists mainly of alloying elements plus very low levels of arc stabilising constituents such as sodium and potassium compounds with the balance being iron

powder. The alloy design of the core can be adjusted to the specific needs for different applications. Besides the core, arc stabilisers can also be applied to the wire surface enhancing stability of the arc, and very low levels of spatter can be achieved compared to solid wires.

Cored wires consist of external metallic sheath, seam or seamless, which conducts electrical current and inner core of which composition varies between flux and metal cored wires. This complex characteristic results in higher current density and thus higher deposition rates at equivalent current levels normally achieved with solid wires [29].

1.3.3.3 Pulsed spray metal transfer (GMAW-P)

GMAW-P is a modified spray transfer process, which continuously detaches and drives drops of molten metal across the welding arc in a controlled manner. The main advantage of pulsed transfer is that spatter free spray transfer may be achieved at currents below the spray transition current. When used with solid wires this process introduces very low levels of hydrogen into the weld pool, due to the use of flux free consumables and shielding gas [25, 30].

The benefits of GMAW-P, compared with GMAW process are described by Alkemade [25, 30] as follows:

- Lower hydrogen weld deposit (<5 mL H2/100 g)
- Better weld fusion
- Lower formation of slag and weld spatter
- Faster travel speeds
- Higher deposition rates and efficiency
- Lower distortion
- Possibility to weld in all positions
- Lower fume emissions

1.3.3.4 Hybrid laser-GMAW welding

Laser welding alone is not the most suitable option for welding of armour alloys. It is a high productivity low heat input process which produces a narrow HAZ and steep spatial and temporal gradients which may result in brittle microstructures, and this does not favour ballistic performance. The laser radiation produces welds with a high ratio between welding depth and seam width, caused by the high power density of the laser beam. This produces a cavity in the workpiece, which remains open due to the vapour pressure of the evaporating material. The laser beam penetrates the workpiece through this cavity, the condensing vapour flows around the cavity, solidifies and forms a slim weld seam and consequently results in poor gap bridging capability [31, 32]. Due to this phenomenon, laser beam welding requires high precision edge preparation and set-up.

The relatively high heat input of the GMAW process results from the significantly lower energy density of the arc with a larger focused spot on the material surface. This results in reduced cooling rates, a wide HAZ often with improved ductility (it should be noted that for improved ballistic performance of welded components, the HAZ should be kept as narrow as possible). Another disadvantage of high heat input process is that it can cause undesirable distortion and/or buckling particularly when welding thin plate [31, 32]. Welding of thicker plates almost always requires multiple passes as the character of the GMAW procedure prevents deep penetration, since the penetration depth is a function of the heat conduction [33]. Welding of thicker sections with one pass would be possible by employing low welding speeds, resulting in even higher heat input and unacceptably wide and soft HAZ and increased risk of buckling and distortion.

The hybrid laser-GMAW welding technique, combining laser welding with GMAW, has the potential to achieve even faster welding speeds than laser welding itself thereby improving productivity (Figure 1-11 and Figure 1-12). The filler material of the GMAW process can be selected to produce improved HAZ properties [31]. The hybrid laser-GMAW process derives its benefits from the synergic effect of the laser beam and the arc. To achieve this synergy, the spacing between laser beam and arc, as

well as the angle of attack must be carefully selected (Figures 9 and 10). According to Gao et al. [34] the ideal separation distance when welding 7 mm thick mild steel plate was found to be 2 mm. When the distance is too big (especially in combination with faster welding speeds), full penetration is not achieved. Conversely, when laser beam and arc are set too close to each other (especially when slower welding speed is employed), it results in unacceptable welding defects at the reverse side of the weld called ‘blow-through’ [33].

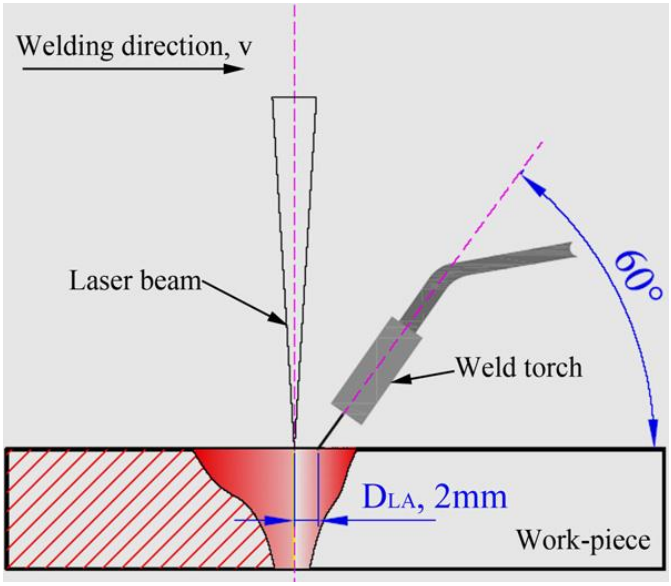

Figure 1-11 Ideal spacing of laser beam and arc to achieve synergy of both processes when welding 7mm thick mild steel plate [34].

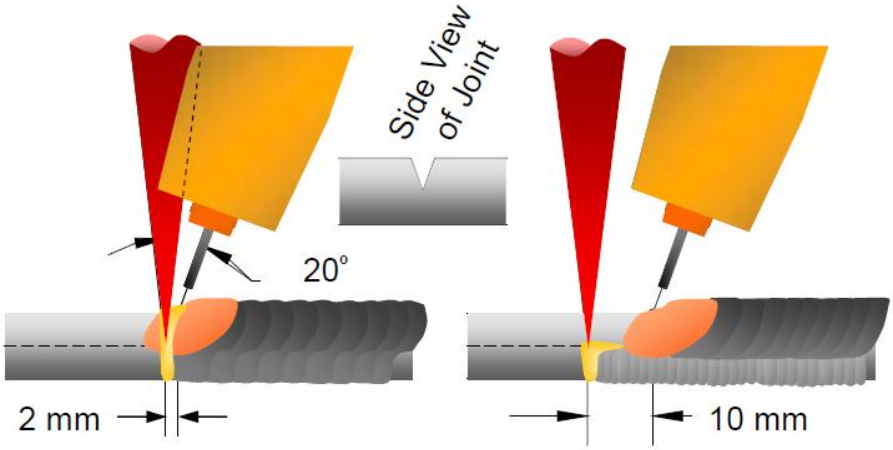

Figure 1-12 How close spacing may cause laser the beam to interact with the GMAW puddle, while increased spacing permits laser to directly irradiate the bottom of the joint [33].

Weld seam geometries

A schematic comparison of weld seam geometries is shown for three welding techniques, laser, hybrid laser-GMAW and gas metal arc (GMA) welding in Figure 1-13. Gao et al. [34] described the characteristics of hybrid laser-GMAW welds as a 'wine-cup' shape which consisted of wider (arc) zone above the narrow (laser) zone, as shown in Figure 1-14. These two zones differed from each other in terms of alloying element distribution, microstructure, hardness and the width of the HAZ. The microstructure of the arc zone consisted of coarse columnar dendrites and fine acicular dendrites between the columnar dendrites. The microstructure of the laser zone consisted of fine equiaxed dendrites in the weld centre and columnar dendrites around the equiaxed dendrites. The observed dissimilarities were attributed to the difference of temperature gradient, solidification and the effects of arc pressure on the molten pool between the laser zone and the arc zone. The 'wine cup' shape of hybrid laser-GMAW weld is a result of synergism between laser and arc processes.

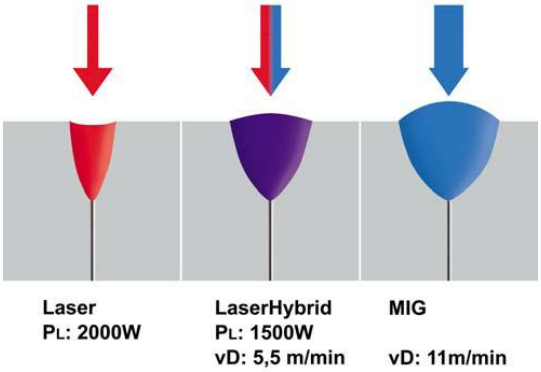

Figure 1-13 Comparison between the seam geometry of laser, GMA and hybrid laser-GMAW weld seams with the same penetration depth and the same welding speed [32].

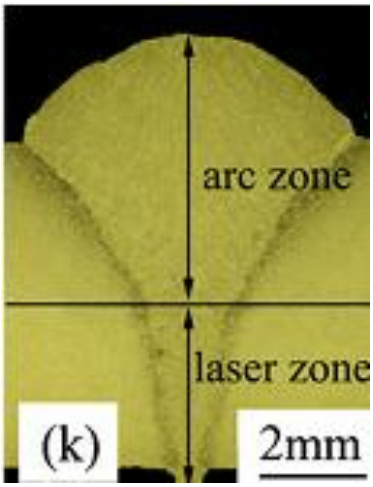

Figure 1-14 Typical shape of hybrid laser-GMAW weld [34].

Advantages of hybrid laser-GMAW welding

During hybrid laser-GMAW welding the metal vapour is obtained not only from workpiece but to a greater extent from welding wire. This can assist the input of laser radiation into the surface and also prevent process dropout [35]. Conversely, metal vapours combine with the shielding gas and form the plasma plume above the laser keyhole that can reduce laser efficiency. Depending on the required properties of the weld, the contribution of laser welding and GMAW power input can be modified, so the overall process may be determined to a greater or smaller degree by either the laser or the arc [32, 35].

The advantages of the laser arc hybrid process compared to single GMAW and laser welding [33, 34, 36, 37] are described below as well as being shown schematically in Figure 13:

- deeper welding penetration and narrow seams - less thermal input, greater scope for improving weld appearance
- higher welding speeds - shorter fabrication times and lower costs - higher productivity
- higher weld seam ductility, joint strength and scope for influencing the structure by means of the filler metal
- greater gap bridgeability
- higher process stability
- less distortions
- welding of thick sections
- reduced consumption of filler material
- capability of handling highly reflective materials

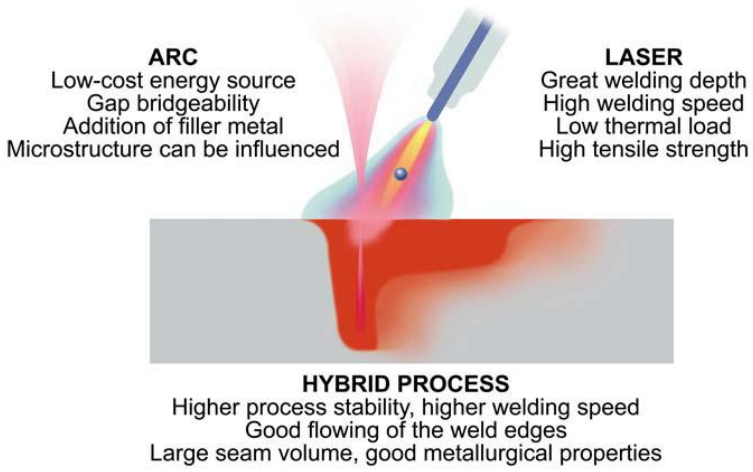

Figure 1-15 Schematic representation: Advantages of LaserHybrid welding [32].

Figure 1-16 shows the microhardness as well the width of the HAZ for hybrid laser-GMAW, as well as single arc and laser welding techniques. During the hybrid laser-GMAW process a smaller weld pool is formed in comparison with the GMAW

technique. This results in smaller heat input and consequently a narrower HAZ. Staufer [32] reported the possibility of reducing the peak hardness of laser welded area (especially in case of larger distance between laser beam and arc), by tempering it as a result of subsequent pass of GMAW and this could favour the ballistic performance of the whole structure.

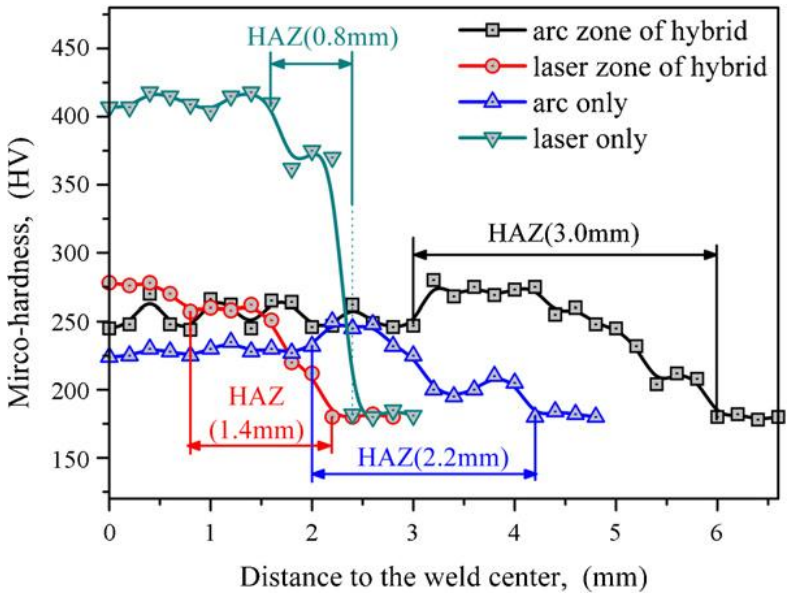

Figure 1-16 Microhardness values and the width of HAZ of hybrid laser-GMAW process compare to GMAW and laser welding processes [34].

Influence of shielding gas composition

When welding thicker sections where deep penetration is required, precautions have to be taken also when selecting the shielding gas composition. This is because the interaction of gas/metal vapour (plasma plume) formed above the keyhole with laser beam, can lead to unstable transfer of the GMAW droplet, which in turn results in spatter formation. The plasma plume can also shield the laser beam (especially for higher laser power and when Ar is used. However, GMAW commonly utilises gas mixtures containing very high Ar content) even to the extent that the laser keyhole is completely closed. The laser welding process is disrupted until the vapour clears away, so that a new keyhole can be formed. To avoid this, the use of He mixtures is recommended, because higher ionisation potential of He reduces plasma formation

[36]. Good quality hybrid laser-GMAW welds can be produced utilising various shielding gas composition ranges [38, 39]. It has been reported that I-butt and T-butt C-Mn steel joints with optimum quality were produced utilising mixture containing 40 – 50% of He and 2 – 5% of CO_2 in Ar [38]. However, Tani et al. [40] claim that shielding gas mixtures containing 30 - 40% He are the most beneficial for both the laser and the GMAW component and additions of above 40% He produce unstable welding arc.

1.3.4 Selection of welding consumable

When selecting optimum consumables for welding high strength Q&T steels guidance may be sought in relevant welding standards and technical publications (for example AS/NZS 1554.4: Structural steel welding - Welding of high strength quenched and tempered steels [41], WTIA Technical Note No. 15 - Welding & fabrication of quenched and tempered steel [27]) and these are often referred to by the manufacturer of the steel.

The main factors to be taken into account are the required strength and toughness as well as restraint conditions. High strength welds often have poor toughness. Assuming that welds are positioned in lower stress areas, the most favourable compromise between these two properties is usually obtained by selecting a consumable with lowest acceptable strength given by the specification. Over-matching should be avoided in order to produce crack free joints with improved toughness and ductility [42].

In previous research [43] it was shown that beside austenitic stainless steel (ASS) consumables, Q&T steel can be readily welded with high nickel steel (HNS) and low hydrogen ferritic steel (LHFS) consumables, with very low levels of hydrogen in weld metal deposits. However, pre-heating the parent metal to 100°C prior to welding is often employed to ensure that sufficient amounts of hydrogen will diffuse out of the weld and HAZ. The base metal used in this investigation was Q&T steel, closely conforming to AISI 4340 specification. It was also reported that when LHFS electrodes were employed, the weld joints showed favourable transverse tensile

properties and the HAZ exhibited lower softening in comparison with welds fabricated with ASS and HNS consumables. Conversely, use of HNS electrodes was shown to give better impact properties, compared to ASS and LHFS weldments, although the HAZ was observed to exhibit greater softening caused by different weld thermal cycle.

LHFS consumables with no hygroscopic compounds have recently been developed. The benefit of these consumables is their lower price compared to both ASS and HNS fillers. Whilst this reduces one potential hydrogen source the possibility of contamination from other sources remains. The common practice is to select filler material that produces slightly under-matching strength compared with the base metal fusion zone . It is argued that this will reduce the level of weld restraint and should result in a reduced risk of hydrogen-induced cold cracking (HACC) [25].

Magudeeswaran et al. [44] investigated three welding consumables for shielded metal arc welding (SMAW) of Q&T steel, namely austenitic stainless steel (ASS), high nickel steel (HNS) and low hydrogen ferritic steel (LHFS). The weld metal (WM) region of the ASS joint consisted of a skeletal delta ferrite in a plain austenitic matrix, the LHFS joint showed an acicular ferrite morphology and the HNS joint exhibited a plain austenitic matrix with a scattered delta ferrite matrix. Acicular ferrite was claimed to be desirable, as the WM was observed to have a high hardness and yield strength. Conversely, welds containing higher levels of delta ferrite showed lower toughness and ductility. The micrographs of fine-grained HAZ (FGHAZ) regions showed a softened region of untempered martensite, whereas coarse-grained HAZ (CGHAZ) regions contained tempered martensite in all of the joints. In both cases (FGHAZ and CGHAZ) LHFS gave finer structure than ASS and HNS. CGHAZ of the joint fabricated with LHFS consumable showed the least degree of softening compare to joints fabricated with ASS and HNS fillers.

1.3.4.1 Austenitic stainless steel (ASS) consumables

When welding high hardenability steels, the use of austenitic stainless steel (ASS) consumables can offer great advantages. The solubility of hydrogen in austenite is

much higher and diffusivity lower than that of ferrite, hence allowing higher hydrogen levels without cracking taking place [25, 45]. If a ferritic filler is used the relative time between transformation of the filler and heat affected zone on cooling from weld peak temperature determines the direction of hydrogen diffusion: the solubility of hydrogen in the molten pool and the high temperature austenitic phase is high but it is much lower in the lower temperature ferritic or martensitic microstructure. If the filler material transforms before the austenitised area of the heat affected zone during cooling of the weld zone any hydrogen in the weld will be 'pushed' into the heat affected zone of the parent material. One obvious way to prevent this effect is to use austenitic filler which is itself insensitive to hydrogen and thus able to accommodate the higher amount of hydrogen. This mechanism is illustrated in Figure 1-17.

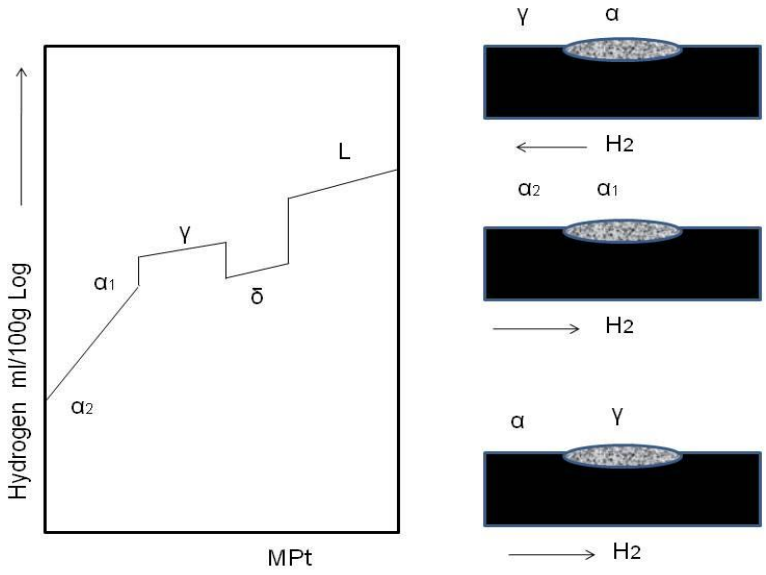

Figure 1-17 Suggested hydrogen diffusion mechanism.

Influence of nickel and chromium on weld metal microstructutre

ASS consumables are highly alloyed with nickel and chromium. Both, nickel and chromium have a significant influence on the microstructural control of weld metal. Nickel additions result in improved weld metal toughness by two means: firstly, it reduces the amount of (δ) ferrite (phase more brittle and thus more susceptible to

HACC than austenite) as well as stabilising the austenitic phase against the formation of martensite and secondly, nickel additions improve the toughness of the fully austenitic microstructure. Chromium greatly retards the rate of phase transformation to aid the formation of fully austenitic structure. It is well known that as opposed to nickel, chromium additions stabilise ferrite and also promote formation of δ ferrite which reduces the weld metal toughness and ductility [46].

When welding steels with carbon content up to 0.2% C, pre-heating prior to welding is a common practice in order to avoid formation of crack sensitive alloyed martensite at the fusion boundary. In the case of steels with carbon levels up to 0.4% C, the minimum pre-heat temperature required in order to avoid crack formation at the fusion boundary as well as hydrogen cracking, is reported to be 150°C [45]. Figure 1-18 gives a guidance to pre-heat temperatures when using austenitic metal-arc electrodes [45].

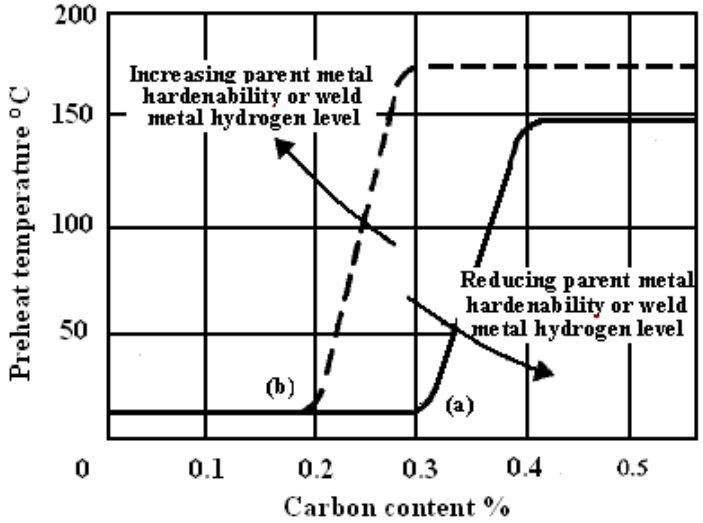

Figure 1-18 Guidance to pre-heat temperatures when using austenitic metal-arc electrodes at about 0.8 - 1.6 kJ/mm: a – low restraint (material thickness < 30 mm), b - high restraint (material thickness >30 mm) [45].

ASS consumables have higher coefficients of thermal expansion which make them prone to solidification cracking as shown in Figure 1-19 and/or can introduce high levels of strain into the material, as a result of shrinkage on cooling. It can be argued

that this could increase susceptibility to hydrogen cracking. It is also important to select the type of the ASS consumable carefully, ensuring its ability to accommodate sufficient levels of dilution from parent metal without formation of high volume fractions of martensite in the weld metal (localized martensitic band along the fusion line caused by diffusion of of alloying elements from the HAZ which increase the hardenability of the weld metal). This effect can be lowered by employing a high heat input and techniques that ensure low levels of dilution of weld metal [45]. Post weld heat-treatment (PWHT) is not recommended for ASS welds, because of the great difference of thermal expansion between parent and weld metal [45].

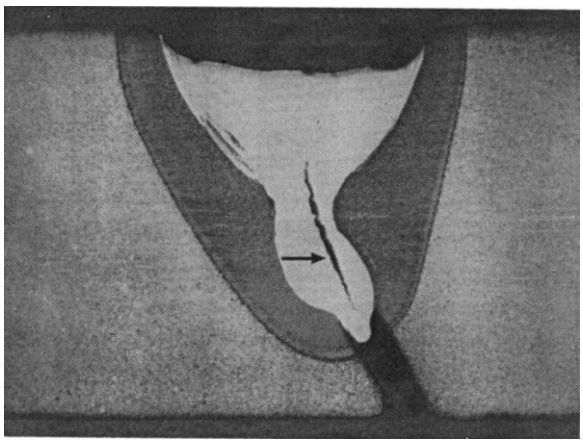

Figure 1-19 Solidification crack in high strength Q&T steel joint welded with ASS consumable [27].

1.4 HYDROGEN CRACKING

This section offers detailed information about hydrogen assisted cold cracking (HACC). Despite years of extensive research, it remains a commonly experienced welding defect when welding steels. All four factors contributing to HACC namely hydrogen, residual stresses, microstructure and temperature are examined. The concepts of avoidance of HACC are reviewed.

1.4.1 Introduction

To ensure good ballistic protection some armour applications require heat treatment of high strength steels to achieve high hardness levels. Conversely, it is well known that

steels in high hardness condition are more prone to cold cracking. The microstructure of armour steels usually contains a high volume percentage of martensite. The high hardness of martensitic structures as well as stresses generated by welding (thermal shrinkage on cooling and expansion that accompanies the austenite to martensite transformation), increase the susceptibility of the microstructure to cracking. If sufficient levels of hydrogen is present in the HAZ and weld metal itself, the material will often fail by the mechanism commonly known as HACC. HACC is not confined to welding, but can occur in steels during manufacture, fabrication and in service.

Generally, the susceptibility of steel to HACC increases with increasing hydrogen content, the propensity of hydrogen being trapped in hydrogen traps and the steel's yield strength [47].

Hydrogen cracking can occur in the HAZ of the parent metal or in the weld metal itself. In the case of weld metal, cracking can occur at lower hardness levels [45]. The welding process produces a hardened HAZ, which in turn becomes prone to hydrogen cracking. The microstructure, stress state and stress distribution resulting from the welding process largely dictate whether cracking will occur in WM or HAZ. When employing ferritic consumables, the martensite transformation temperature range of base metal and weld metal also influences the increased susceptibility of either PM or WM cracking. Olson and Liu described this phenomenon as follows [48].

$$\Delta Ms = Ms_{WM} - Ms_{HAZ} \tag{1.3}$$

where: ΔMs [°C] is a difference between WM and HAZ martensite start transformation temperatures, Ms_{WM} and Ms_{HAZ} are martensite start temperature of WM and HAZ respectively.

- If ΔMs > 0 (parent metal possesses higher strength than weld metal), the martensite transformation in weld metal takes place at higher temperature than in the parent metal, promoting the evolution of hydrogen from supersaturated WM's bct lattice into the HAZ (still having austenitic lattice) due to much

higher solubility of hydrogen in fcc lattice. This results in accumulation of hydrogen in HAZ, thus increased risk of HAZ cracking.

- If ΔMs < 0 (the weld metal strength is overmatching the parent metal), hydrogen will accumulate in WM's microstructure, increasing the susceptibility to WM cracking.

Formulae developed by Self et al. [49] provide a tool which enables the calculation of the Ms temperature (expressed in°C) of both the HAZ and WM over a wide range of alloying designs:

$$Ms_{HAZ} = 521 - 350C - 14.3Cr - 17.5Ni - 28.9Mn - 37.6Si - 29.5Mo - 1.19Cr.Ni - 21.3(Cr + Mo).C \quad (1.4)$$

$$Ms_{WM} = 521 - 350C - 13.6Cr - 16.6Ni - 25.1Mn - 30.1Si - 20.4Mo - 40Al - 1.07Cr.Ni + 21.9(Cr + 0.73Mo).C \quad (1.5)$$

It would be desirable to develop improved formulae for calculation of weld metal Ms temperature that would consider the effect of oxygen level since the WM contains substantial amount of oxide inclusions that have a significant effect on austenite decomposition kinetics [50].

The cracking in the HAZ typically occurs at the weld toe, weld root or under-bead area, as shown in Figure 1-20. In the case of fillet welds, cracks are generated alongside the weld. Cracks oriented perpendicularly to the weld can be often found in the butt welds [45]. If cracking occurs in the weld metal, it can be either parallel or transverse to the weld direction. The orientation of the transverse cracks can be perpendicular or characteristically at a 45° angle to the weld surface (chevron cracks) [45]. Hydrogen cracks can follow the intergranular or transgranular path, however a mixture of these two types can often occur [45]. It should be noted that before evaluation of the microstructure an incubation period is needed, because cracks often form some time after completion of the welding.

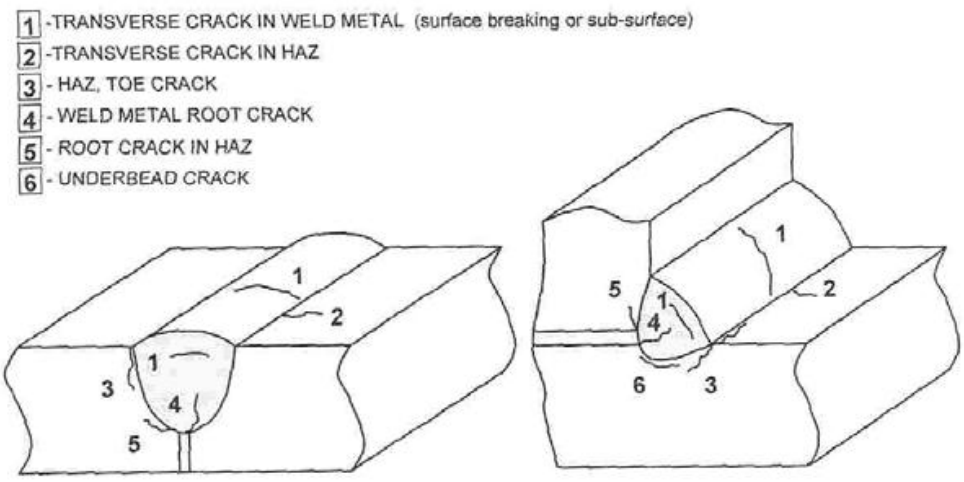

Figure 1-20 Hydrogen assisted cracks: a) butt weld, b) fillet weld [51].

Yurioka and Suzuki [13] reported that hydrogen cracking can occur by two means:

- During welding (or some time after the weld is completed). Hydrogen enters into the HAZ and weld metal during welding.

- During service (often called stress corrosion cracking (SSC) of hydrogen embrittlement). Hydrogen enters into the welded area during service of the welded component, from moisture, hydrogen sulphide gas or other hydrogeneous environments.

1.4.2 HACC during welding

Despite extensive research over many decades, in an effort to prevent HACC, it is still the most common cracking problem experienced during welding fabrication of steel structures, particularly those employing high-strength steels.

For HACC to occur during welding, four basic conditions have to be met simultaneously [45, 52].

- Presence of diffusible hydrogen to a sufficient degree
- Tensile triaxial stress acting on weld (residual and/or applied)

- Presence of a susceptible microstructure
- Critical temperature is reached (below about 200°C - so that H atoms are both diffusible and trappable)

This situation is illustrated in Figure 1-21.

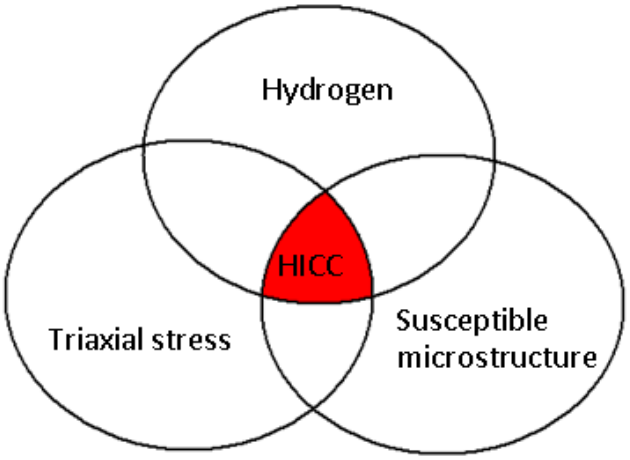

Figure 1-21 Basic factors responsible for HACC. If any of these factors is not present, cracking will not occur.

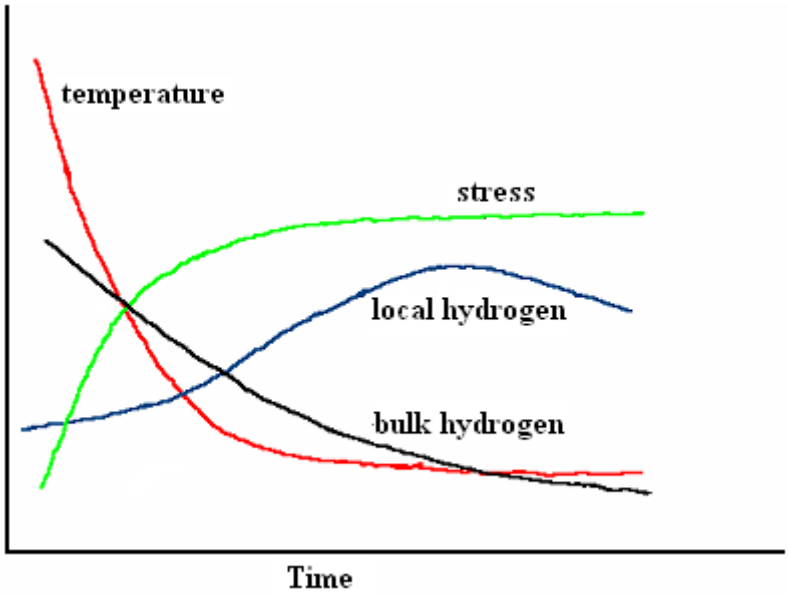

Figure 1-22 Changes in temperature, stress, local and bulk hydrogen levels as a function of time after completion of welding [53].

HACC is typically initiated when temperature of weld drops below 200°C but cracks are often formed and propagated some time (several hours or days) after completion of welding. This makes it very difficult to detect HACC under manufacturing process conditions where productivity is important. Therefore safe welding procedures using parameters that do not allow generation of cracks have to be developed.

Cracking in the weld metal and HAZ of armour steels is a result of many factors. Some of these include: fabrication and repair welding, degree of restraint; levels of preheat, heat input and inter-pass temperature; thermodynamic conditions in the plate; and welding position, weld geometry, set-up and shielding gas used. Thus, setting the right parameters for the avoidance or cracking can be a very complicated procedure [25].

1.4.3 Hydrogen in welding

During arc welding some level of hydrogen is always absorbed into the molten weld pool. Hydrogen initially introduced into the weld pool quickly diffuses through lattice following concentration and thermal gradients. The heterogeneous as-cast microstructure of the weld metal contains high level of defects. During diffusion through the lattice hydrogen is attracted to these extraordinary sites also called hydrogen sinks or traps. Depending on the binding energy of the trap hydrogen is slowly released into the surrounding microstructure or becomes totally immobile. The total hydrogen content of the weldment comprises: hydrogen able to move through lattice, referred to as diffusible hydrogen and immobile or trapped hydrogen, referred to as residual.

Diffusible hydrogen is the main factor contributing to HICC therefore to qualify and quantify it’s amount is of major importance when designing the welding procedure specifications/qualifications.

The most widely used methods for measuring the levels of diffusible hydrogen in weldments are [44]:

- Mercury method

- Glycerine replacement method
- Silicone oil replacement method
- Gas chromatography method

All of these methods were developed to measure the diffusible hydrogen content of ferritic weld metal deposited using arc welding processes with filler material. They involve collection of diffusible hydrogen evolved from welded samples. These methods are primarily used to classify welding consumables and processes based on their tendency to introduce hydrogen into the weld pool and thus the tendency to cause HACC. The mercury method also called IIW method is according to Australian welding standard AS/NZS 3752:2006 considered to be the primary method for determination of diffusible hydrogen content in the weldment.

1.4.3.1 Absorption of hydrogen during welding

The prime welding process related factors affecting the amount of hydrogen initially absorbed are type of welding process, consumable and partial monoatomic hydrogen gas pressure resulting from dissociation of moisture and hydrogenous compounds in the arc column [54]. The dissolution reaction of the water molecule during welding is given by the following equation:

$$H_2O\ (g) \rightarrow 2H + O \tag{1.6}$$

The equilibrium concentration of hydrogen absorbed into molten metal is mostly determined from Sievert's law. The dissolution reaction of diatomic hydrogen is represented by equation [55]:

$$^1/_2\, H_2 = H \tag{1.7}$$

The change of a free energy required for dissolution reaction is given by equation [56]:

$$\Delta G^0 = -RTlnK \tag{1.8}$$

where: ΔG^0 [10^3.N.m.mol^{-1}] is the standard free energy for reaction, R is gas constant, T is temperature, K is equilibrium constant.

Engelhard et al. [56] published the value of change of a free energy required for dissolution reaction for two high strength alloys and pure austenitic iron as follows:

AISI4130: $\Delta G^0 = 5573.7 - 8.3320T$ [4.184.N.m.mol^{-1} H_2]
AISI4130: $\Delta G^0 = 7708.9 - 10.784T$ [4.184.N.m.mol^{-1} H_2]
Pure iron: $\Delta G^0 = 10816 - 14.89T$ [4.184.N.m.mol^{-1} H_2]

Then, according Sievert's law the equilibrium concentration of hydrogen in molten steel at constant temperature is a function of square root of the partial pressure of diatomic hydrogen above the molten weld pool [55]:

$$H = K(P_{H2})^{1/2} = \exp\left(-\frac{\Delta G^0}{RT}\right)(P_{H2})^{1/2} \quad (1.9)$$

where: H [mg.kg^{-1} or ppm] is the dissolved hydrogen concentration in equilibrium with the diatomic gas, ΔG^0 is the standard free energy for reaction, K is equilibrium constant for reaction, P_{H2} is partial gas pressure of H_2, R is universal gas constant and T is temperature of molten metal.

From Sievert's law it is evident that higher temperature and higher partial gas pressure result in higher hydrogen level absorbed into molten weld pool. However, the maximum temperature achieved in weld pool is limited by evaporative cooling effect of iron vapour, which limits the amount of hydrogen that can access the molten pool by two means: it lowers the maximum temperature of the weld pool and the evaporation stream opposes the hydrogen absorption direction. In contrast; according to a study conducted by Howden [57], the amount of monoatomic hydrogen absorbed by weld pool is significantly higher around the cooler outer edge whereas the absorption level of diatomic form is almost identical across the weld pool. It was also found that amount of hydrogen absorbed by the molten weld pool decreases with

increasing oxygen content. Nb has strong deoxidation properties therefore according to this theory has the potential to increase the amount of initially absorbed hydrogen. As the temperature decreases the Nb oxides provide sites for hydrogen to reside. Conversely, by increasing alloying content of Chromium, Molybdenum and Tungsten hydrogen content can be reduced. The large quantity of initially absorbed hydrogen diffuses out of the specimen within seconds after molten pool solidifies [55, 56].

As mentioned earlier, when welding Q&T high strength steels, the Coarse Grained HAZ is the most susceptible to hydrogen cracking. Whether or not a sufficient amount of hydrogen is available to diffuse into the HAZ to initiate cracking is largely influenced by the amount of hydrogen absorbed into the molten weld pool, the cooling rate and the solubility of the hydrogen in the WM.

Factors influencing the amount of hydrogen initially introduced into the molten weld pool are:

- level of hydrogen in:
    - parent metal (oil, grease, dirt, rust, paint, degreasing fluids, hydrogen remaining from the casting process – particularly in the interior of heavy sections),
    - consumables (electrode coatings, fluxes, oil, grease, dirt, rust),
    - arc atmosphere (shielding gas composition, moisture content and flow rate),
- heat input,
- hydrogen fugacity during welding,
- contact-tip to workpiece distance (CTWD)

1.4.3.2 Solubility of hydrogen

The hydrogen solubility decreases with decreasing temperature and this results in weld metal oversaturation with hydrogen. Some hydrogen is lost to the surrounding atmosphere, some diffuses into the HAZ. Figure 1-23 shows the solubility of hydrogen in weld metal as a function of temperature. The quantity of hydrogen that diffuses out of the weldment depends primarily on the initially absorbed amount,

thermal profile experienced during welding and the alloying composition of the WM and the PM but also on the partial hydrogen pressure in the atmosphere adjacent to the cooling weld bead and the weld geometry.

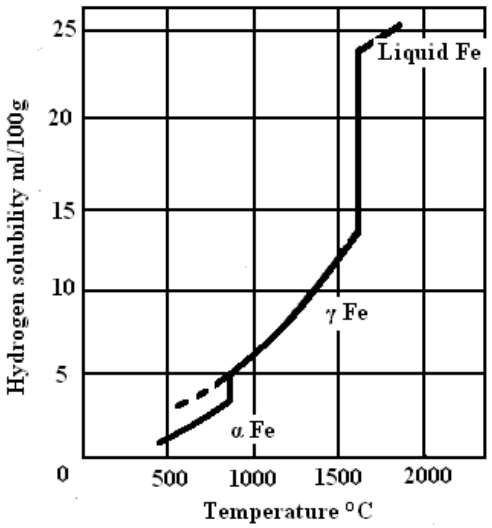

Figure 1-23 Solubility of hydrogen in weld metal and HAZ decreases with decreasing temperature [45].

The solubility of hydrogen in liquid iron and low alloy steels is approximately 30ppm by weight but less than 1ppm in the solidified ferritic/martensitic microstructure [58, 59]. The solubility of hydrogen in alloyed steels across the whole temperature range is lower than solubility in pure iron. High strength alloys have generally less impurities (possible hydrogen traps) than mild steel and require less hydrogen, approximately 1ppm, to cause hydrogen embtittlement. No hydrogen embrittlement occurs in mild steel, if hydrogen is present in quantities less than about 1.7 ppm [56].

In solid solution hydrogen atoms occupy interstitial sites of the metal's lattice. The interstitial site size of fcc lattice is 1.04Å (angstrom) and the bcc lattice is 0.38Å. The radius of hydrogen atom is approximately 0.46Å. It is therefore evident that bcc lattice can accommodate much lower levels of hydrogen with much higher energy required to enlarge interstitial sites. Thermal shrinkage on cooling introduces stresses into both WM and HAZ. Inhomogenities in the metal's lattice (e.g. inclusions, defects, discontinuities) act like stress concentrators resulting in enlargement of interstitial sites (lattice dilation) in these areas [59]. This is the reason why hydrogen (especially

considerable in case of bcc lattice) is attracted to areas with high triaxial stresses. The significantly longer dwell time of hydrogen in enlarged interstitial sites compared to the normal lattice results in much higher equilibrium hydrogen concentration in the area of stress concentration. When a critical concentration is reached (the harder the microstructure, the lower critical level of hydrogen is needed to form the crack) a small crack is formed and stress is relieved. The crack tip acts as a stress concentrator which again attracts diffusible hydrogen and the crack propagates through discontinuous jumps until it reaches the surface (fracture of the material) or conditions no longer promote hydrogen accumulation. Austenitic steels are distinguished by lower susceptibility to HACC and lower crack growth rates compared to ferritic steels. There is extensive debate over the exact mechanism by which accumulated hydrogen causes cracking [59, 60].

Engelhard et al. [56] summarised the most common proposed theories explaining the mechanism of hydrogen cracking:

- Apparent fracture stress is lowered as a consequence of evolution of gaseous hydrogen at internal inhomogenities developing the additional pressure
- Lattice cohesive strength is lowered by interaction of dissolved hydrogen
- Hydrogen either limits the mobility of dislocations or introduces localized accumulations embrittling the lattice
- Fracture stress is lowered and the surface energy required to initiate crack decreases as a result of hydrogen adsorption
- Formation of hydrogen rich areas having altered mechanical properties than matrix

1.4.3.3 Hydrogen diffusion in metals

The driving force for migration of hydrogen through lattice is the gradient in chemical potential which is a consequence of a gradient in the lattice hydrogen concentration. The lattice diffusivity increases with increasing temperature as shown in Figure 1-24 and can be expressed by Arrhenius equation [56]:

$$D = D_0 exp^{-Q/RT} \quad (1.10)$$

where: D [10^{-4}.m^2.s^{-1}] is lattice diffusivity, D_0 is pre-exponential factor, Q is activation energy for diffusion, R is gas constant, T is temperature.

Engelhard et al. [56] studied the diffusivity of two high strength steel grades namely AISI 4130 and AISI 4340 and determined both pre-exponential factor D_0 and activation energy for diffusion Q for these steels. The parameters determined for the above mentioned steel grades are presented in Table 1-2.

Table 1-2 Values of pre-exponential factor D_0 and activation energy for diffusion Q of steel grades AISI 4130 and AISI 4340.

Steel Grade	D_0 [cm^2/s]	Q [kJ/mol]
AISI 4130	0.551	92.05
AISI 4340	0.794	96.03

The less closely packed bcc and bct lattice compared to fcc lattice allow greater mobility of interstitial hydrogen atoms even at room temperature. Diffusivity of hydrogen in iron and low-alloy steels and in austenitic steels at room temperature was measured to be approximately 10^{-6} cm^2s^{-1} and 10^{-12} cm^2s^{-1} respectively. The distance travelled by a hydrogen atom during given time exposure is a function of the atom's diffusivity and can be generally expressed by the equation [59]:

$$x \sim 2(Dt)^{1/2} \quad (1.11)$$

where: x [$m.10^{-2}$] is distance travelled by hydrogen atom, D is diffusivity of hydrogen atom and t is the time exposure.

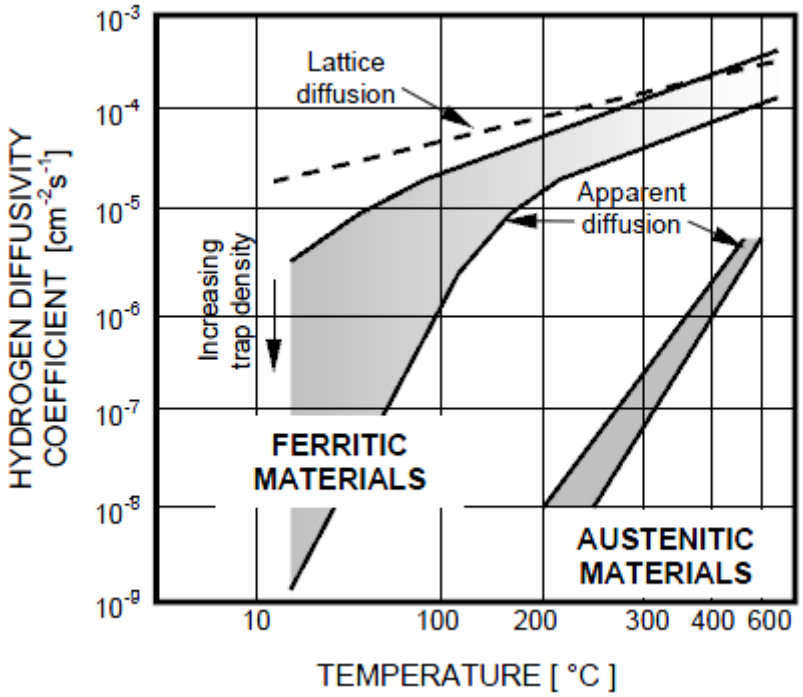

Figure 1-24 Variation of overall diffusivity coefficient, D, with temperature for ferritic and austenitic materials [45].

To illustrate the significant difference of hydrogen diffusivity in ferrite and austenite, the time required for a hydrogen atom to travel the distance of 1mm to the area of stress concentration at room temperature would be approximately 42 minutes and more than 79 years in bcc and fcc structures respectively [59]. A higher amount of dislocations contributes to the lower diffusion rates in austenitic fcc lattice [53].

In theory grain boundaries represent the faster diffusion tracks for hydrogen atoms, however no significant difference in diffusion rates has been found between fine and coarse-grained steels [53].

Hydrogen diffusion is also influenced by the microstructure of the martensitic HAZ formed on cooling. It was concluded that lath martensite separated with retained film like austenite has the most beneficial effect on the HAZ toughening and its ability to resist HACC. The thin film of austenite distributed around the martensite lath represents an efficient barrier for hydrogen diffusion and also traps the hydrogen in immobile form which does not contribute to HACC [61]. On the contrary, Maroef et al. [62] claim that on cooling, residual austenite becomes oversaturated with hydrogen

that can later be slowly released into its surrounding thus increase the susceptibility to HACC. In addition the residual stresses resulting from the welding process have the ability to pull hydrogen out of residual austenite.

Various hydrogen diffusion coefficients in steel and steel welds have been proposed in literature. Work published by Boellinghaus et al. [53] offers a very comprehensive review on hydrogen diffusion coefficients in both ferritic-martensitic and austenitic steels. The block diagram presented in Figure 1-25 summarises the major factors influencing hydrogen diffusivity.

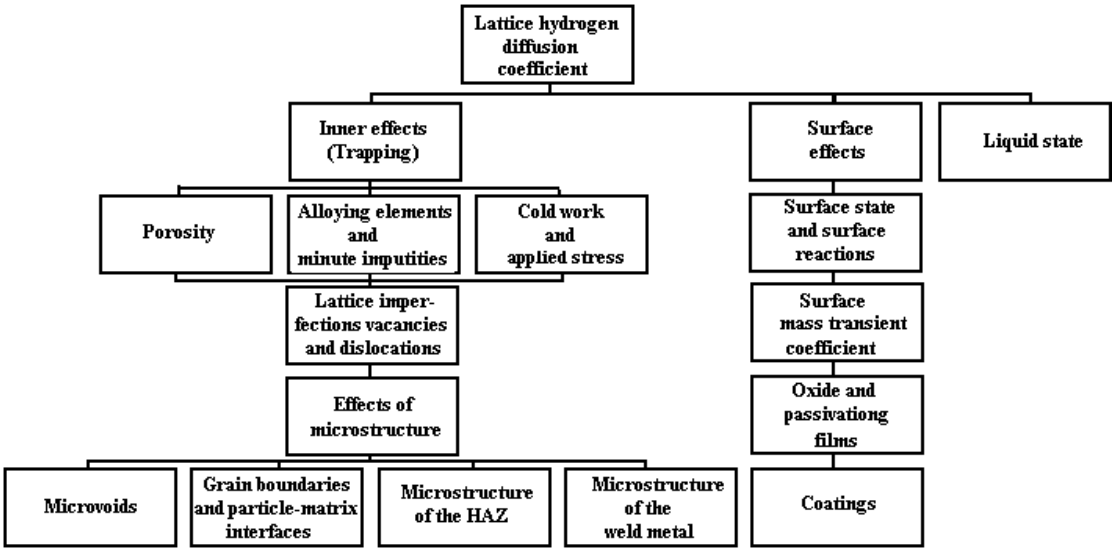

Figure 1-25 Summary of the major factors which influence the hydrogen diffusivity in low carbon mild steels [53].

1.4.3.4 The effect of flux type on diffusible hydrogen content

The type of flux used in MMAW consumables and flux cored wires is one of major factors influencing the level of hydrogen in weld metal and also it's diffusivity.

The use of the GMAW in combination with solid wire is generally coupled with very low hydrogen levels followed by the use of moisture resistant basic electrodes. Submerged arc welding (SAW) and FCAW processes usually introduce somewhat higher levels of hydrogen into the molten weld pool. Similarly in MMAW acidic and

rutile flux coated electrodes, especially those with cellulosic flux formulations produce deposits with very high hydrogen levels [54].

Work by Odengard et al. [63] examined the effect of rutile and basic fluxes on the diffusivity of hydrogen in weldments. The results showed that the diffusivity is higher by a factor of 10 in basic-flux than in rutile-flux weld deposits. The use of rutile flux resulted in higher volume of non-metallic inclusions and oxygen levels in the lattice which in turn retard the hydrogen diffusion rate. The evolution rate of hydrogen is also slowed by the presence of micro-voids at the manganese sulphides – steel lattice interface.

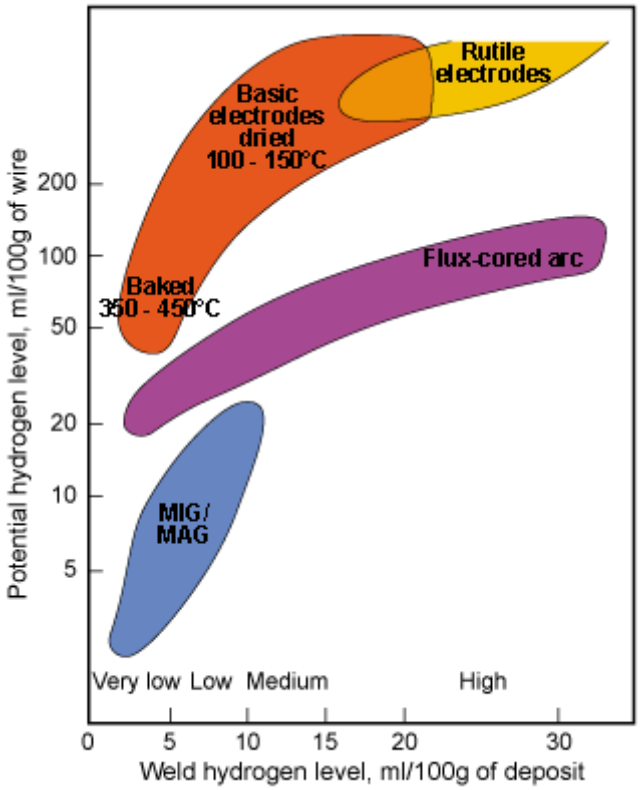

Figure 1-26 General relationships between potential hydrogen and weld metal hydrogen levels for arc welding processes [63].

1.4.3.5 Hydrogen trapping

HACC is also closely related to hydrogen diffusion and trapping which are influenced by microstructural factors. Mobility energy (E_m) is the energy required for a hydrogen atom to travel through the lattice. Alloyed steels contain fewer sites available for

hydrogen diffusion compared to pure iron. This results in hydrogen being trapped at structural defects and in turn results in less hydrogen available for diffusion. The partitioning of the total hydrogen content between trap sites and lattice sites is represented by equilibrium fractional hydrogen occupation at the trap site φ_{eq} as presented in Figure 1-28. A schematic diagram illustrates the concept of trap theory in Figure 1-27. Trap binding energy (E_b) is important factor to be considered to be able to predict the amount of hydrogen available for diffusion. The higher binding energy traps are able to arrest and maintain the hydrogen at higher temperature compared to those with lower binding energy.

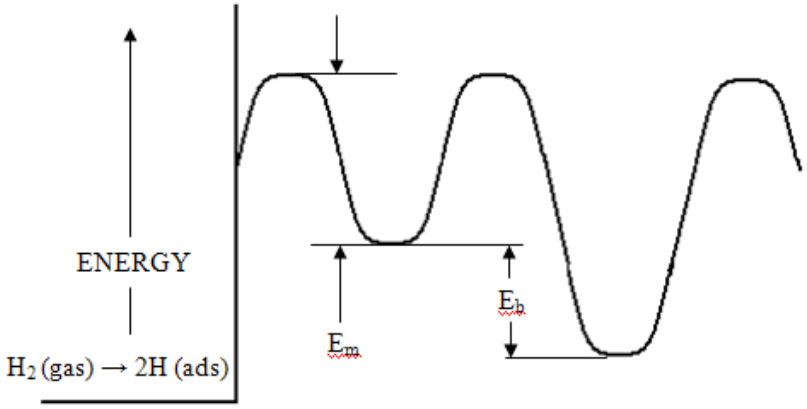

Figure 1-27 Schematic view of energy relations in hydrogen – iron equilibrium with trapping [56].

Hydrogen traps are generally divided into two groups based on their binding energies. Although these limiting values slightly vary across the literature:

- Weak (reversible) traps are characterised by the binding energies lower than 30 kJ/mol (interstitial lattice sites, elastic stress fields, dislocations, substitutional atoms, grain boundaries, vacancy, ferrite/carbide and ferrite/cementite interfaces, tempered martensite, etc.).
- Strong (irreversible) traps are characterised by binding energy levels higher than 60 kJ/mol (microvoids, Fe_2O_3, Fe_3O_4, MnS, Al_2O_3, SiO_2, TiC, Ce_2O_3, etc.).

In multipass welding the presence of strong traps is especially beneficial as the heat introduced by multiple passes releases only minor part of hydrogen contained in these

traps. On cooling the released hydrogen is readily recaptured back into strong traps before it can diffuse to potential crack initiation sites. Weak traps easily and repeatedly release a considerable amount of hydrogen even at lower temperatures. This hydrogen can accumulate at stress concentrators and increase risk of HACC.

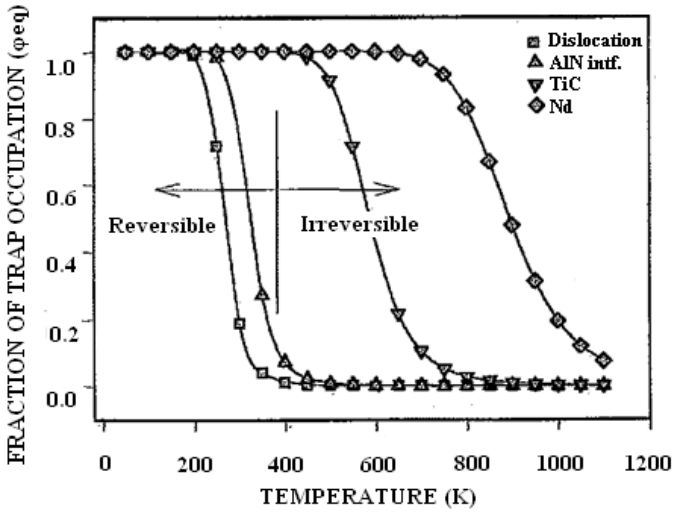

Figure 1-28 Equilibrium fractional occupation of hydrogen at trap sites, φeq. Calculations were done for atmospheric P_{H2} = 0.0545 Pa [62].

To be able to predict the behaviour of hydrogen trap, it is useful to know the trap activation energy for hydrogen release, which can be calculated utilising equation [64]:

$$\frac{\partial \ln(\frac{\phi}{T^2 c})}{\partial(\frac{1}{Tc})} = -\frac{E_{aT}}{R} \tag{1.12}$$

where: ϕ is heating rate, Tc is the peak temperature, E_{aT} is the trap activation energy for desorption and R is the gas constant.

1.4.4 Influence of stress level on HACC

Stress is almost unavoidable in welded joints due to the contraction stresses and restraint. The level of stress may increase due to the joint design and section thickness. Joint design and welding sequence may be modified to decrease stress but

it must be assumed that in more complex fabrications sufficient stress is available to contribute to HACC.

Residual stresses are fixed displacement stresses that remain in the weldment after removing all external forces. It is well known that high tensile residual stresses in areas close to the weld increase the susceptibility to HACC and do not favour the toughness and fatigue performance of the welded structure. Further, if present to a sufficient degree of magnitude they can result in distortion of welded component especially when welding thin sections.

During welding, the steel is subjected to rapid heating resulting in compressive yielding around the molten weld pool as the steel expands. Subsequent cooling causes thermal shrinkage which in turn gives rise to tensile residual stresses, particularly in longitudinal direction. Changes of temperature and the resulting stresses that occur during welding are schematically shown in Figure 1-29. Furthermore on cooling steel undergoes solid state transformations which impose additional strains in the material. Volume changes that accompany phase transformations, together with thermal shrinkage determine the type (compressive or tensile) and magnitude of the final residual stresses. These stresses generally concentrate at the toe and root of the weld joint, as well as at notches created by inclusions and other defects. The stress level depends on many aspects such as welding parameters (heat input, number of weld passes, welding sequence, preheat and inter-pass temperature), design parameters (joint geometry, weld size, fit-up, external restraint), material parameters (martensite start and finish temperature the yield strengths of the weld and base metal) [45].

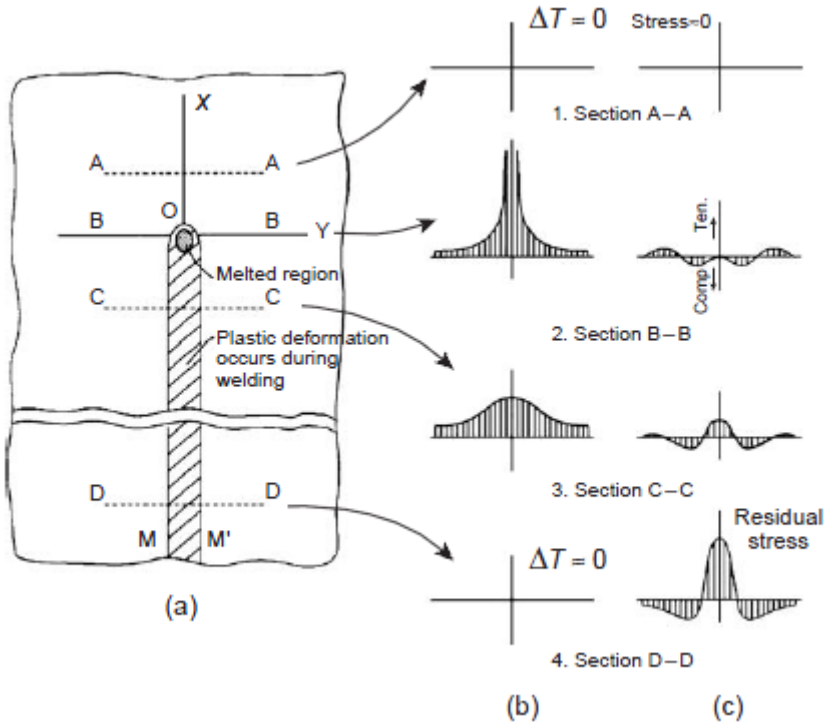

Figure 1-29 Schematic presentation of changes of temperature and thermal stresses during bead-on-plate welding [65].

The type and distribution of longitudinal residual stresses tend to be invariant and magnitude often approaches the yield stress of the parent metal. Whereas transverse residual stresses vary with different welding processes [66]. Figure 1-30 shows transverse residual stress in a high strength Q&T steel joint welded with austenitic stainless steel consumable as a function of distance from weld centre line for a number of welding processes. The use of ASS consumable generates high levels of residual stresses due to high coefficient of thermal expansion of austenite. Matsuda et al. proposed a theory that the displacive lattice dilatation that accompanies martensitic transformation in the HAZ could aid compensation of the tensile residual stresses generated by thermal shrinkage of austenitic weld metal [67]. These tensile stresses promote the formation of specific crystallography related variants of the martensite plates which counteract build up of tensile residual stresses. This beneficial phenomenon is more distinctive when the transformation occurs at low temperatures thus preventing additional thermal contraction during further cooling to ambient temperature.

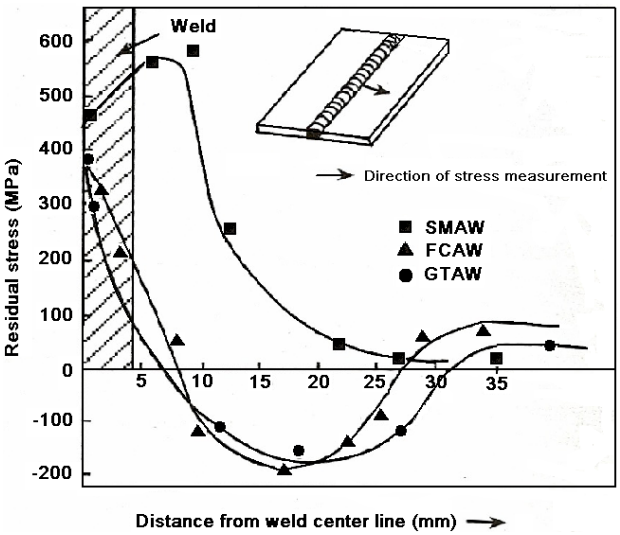

Figure 1-30 Effect of welding process on residual stress distribution in high strength Q&T steel joint welded with austenitic stainless steel consumable [68].

To ensure the best possible performance of welded components, it is important to know the influence of these residual stresses on service performance. Residual stresses generated by welding are strongly influenced by martensite start and finish temperatures [21]. The type of residual stress has an influence on the ballistic performance and fatigue life of the welded component [21, 68]. When welding steel structures tensile residual stresses enhance the effect of applied tensile stress. Conversely, compressive residual stresses are algebraically added to the applied tensile stresses. The consequence is a lower overall magnitude of stress in the weld. This improves the fatigue life of the welded material, through inhibition of crack initiation [21].

1.4.4.1 Influence of weld residual stress on ballistic performance

As investigation of HSLA steel in the quenched and tempered condition [68] has shown that tensile residual stresses present in the coarse-grained HAZ region resulted in better ballistic performance, in comparison with HAZ regions containing compressive residual stresses. It was observed that tensile stresses oppose the projectile attack direction, hence aiding the ballistic performance. Compressive residual stresses were found to be detrimental in resisting projectile penetration. This was due to the orientation of the projectiles trajectory and the compressive stress

being the same. Furthermore, it was reported that for superior ballistic performance, the width of the compressive residual stress region, to that of the projectile diameter ratio, should be as small as possible [68]. A schematic of the type of residual stress and its effect on stresses due to ballistic penetration is shown in Figure 1-31.

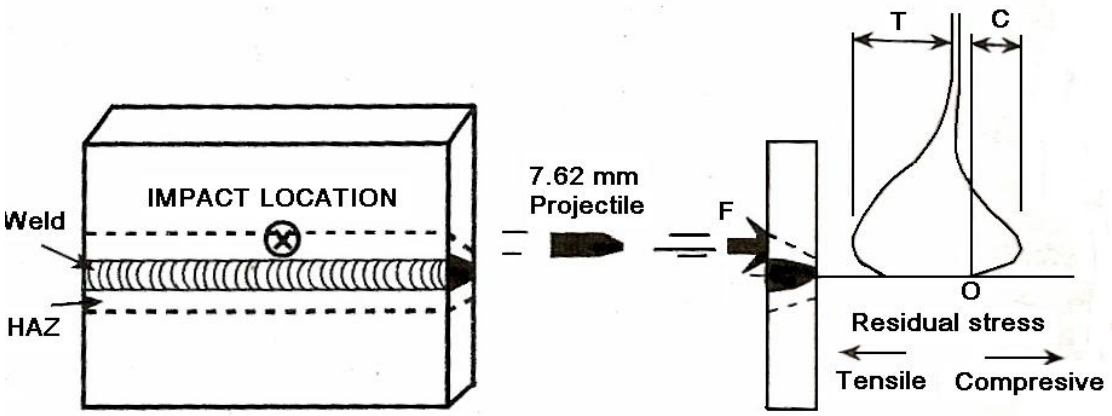

Figure 1-31 A schematic diagram of the type of residual stress affecting the effective ballistic stress (EBS), where F is ballistic stress, T is tensile residual stress, C is compressive residual stress. In case of tensile stress: EBS = F – T. In case of compressive stress EBS = F + C [68].

In order to minimise the adverse effect of residual stress, a number of procedures have been developed (e.g., preheat and interpass temperature control, post weld heat treatment (PWHT), shot peening, applying a controlled temperature field parallel to the weld, trailing heat sink with or without rollers) to decrease their magnitude. Modification of the welding process itself or considering alternative weld pass sequences is a different approach to achieve the desired type and level of residual stress. It is an accepted fact that low heat input procedures and small size of the weld pool reduce residual stress [21]. Furthermore, when the transformation takes place at lower temperatures, the residual stresses present at ambient temperature are reduced.

1.4.4.2 Measurements of residual stresses

Residual stresses may be determined analytically or experimentally. The analytical methods are based on utilising of finite element models that enable the computation of magnitude and distribution of residual stresses based on input information such as

material and mechanical properties of the steel, geometry of the weldment, welding heat input and loading conditions. However, these models are very complex and essential material data and how they change during a weld thermal cycle are often unavailable. The experimental methods can be divided into non-destructive (ultrasonic measurements, X-ray and neutron diffraction methods) and destructive (hole drilling, ring-core technique) methods. During destructive testing, the sample after completion of welding is cut and the residual stresses are quantified based on deformation resulting from cutting. Non-destructive experimental methods involve measurement of various physical phenomena in the residual stress field [69, 70].

1.4.5 Temperature

In the case of ferritic steels HACC occurs at relatively low temperatures, where the diffusibility of hydrogen is greatly reduced. Hydrogen embrittlement is also influenced by strain rate, with highest susceptibility at slow strain rates. During the latter stages of cooling when cooling rates are reduced, the strain rate is slow, thus the risk of cracking is high during this period. The risk of HACC can be significantly reduced by maintaining adequately high temperature after completion of welding. This allows a sufficient amount of hydrogen to diffuse out of the weld and HAZ. Commonly, techniques such as pre-heating the steel prior to welding, interpass temperature control and post weld heat treatment (PWHT) are used. The notch tensile strength of steel containing hydrogen is shown Figure 1-32. It is observed that a minimum occurs at approximately room temperature.

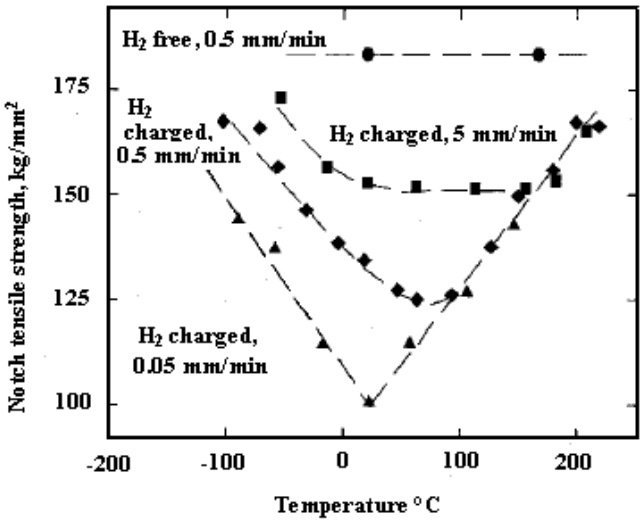

Figure 1-32 Notch tensile strength of steel containing hydrogen as a function of temperature [45].

1.4.6 Microstructure of weld metal and HAZ

The alloy design of armour grades of steel is carefully chosen to give very good hardenability (even when slow cooling rates are employed) in order to provide good ballistic performance. However, when these steels are subjected to welding it results in formation of very hard structures within the HAZ. As previously discussed steels with high hardenablity posses increased tendency to HACC, and this represents a significant factor affecting the overall integrity of a ballistic structure by introducing cracks that in case of ballistic attack raise the risk of failure with a catastrophic outcome.

The nature of the microstructure formed on the cooling is influenced by the hardenability of the steel, cooling time through the transformation region ($t_{8/5}$) and prior austenite grain size. Cooling time through the transformation range ($t_{8/5}$), depends mainly on the preheat temperature, heat introduced during welding [45], and also on base metal thickness and joint geometry. Yurioka [71] claims that the maximum HAZ hardness of structural steel is directly influenced by cooling time through the transformation region ($t_{8/5}$). The $t_{8/5}$ of the weldment is inversely related to the welding cooling rate and is determined by the welding parameters, especially the welding heat input. Welding employing low heat input reduces $t_{8/5}$ and if $t_{8/5}$ is less

than the critical cooling time to produce martensite (t_M) it gives rise to formation of hard structures in the HAZ. Steels possessing high hardenability are characterised by high value of t_M. Figure 1-33 shows the increase of HAZ hardness for medium and low carbon steel vs. $t_{8/5}$ cooling time. The hardness of medium carbon steel increases significantly with decreasing $t_{8/5}$, while in case of low carbon steel the increase is less significant. The microstructure of medium carbon steels with higher hardenability will consist of full martensite even when slower cooling rates are employed.

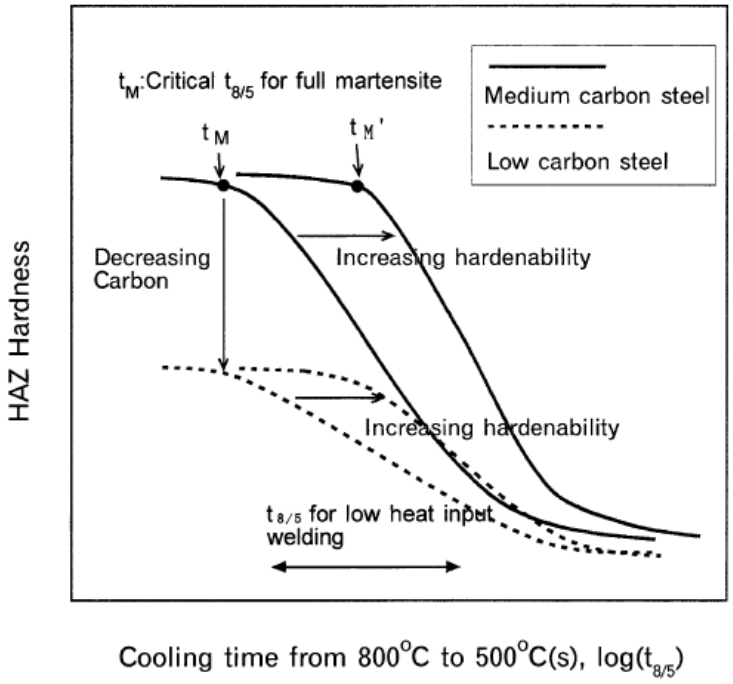

Figure 1-33 Effect of steel composition on the relation between HAZ hardness and $t_{8/5}$ [71].

The hardenability of the steel is given mainly by its chemical composition as shown in Figure 1-34. Various alloying elements affect the hardenability to different extents. This is well described by the carbon equivalent (CE) formulae, which are a useful tool in prediction the hardness of the structures formed on cooling.

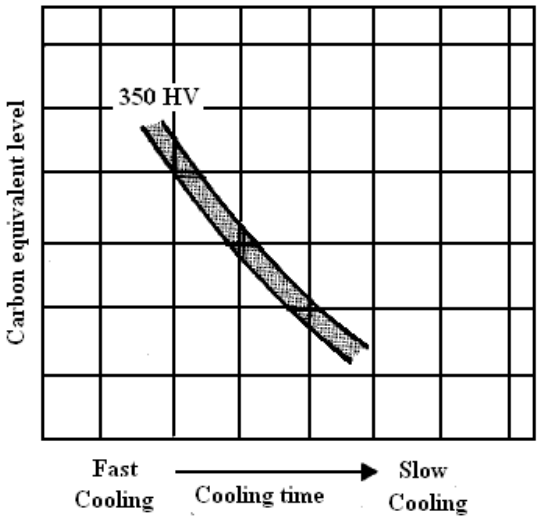

Figure 1-34 Relationship between chemical composition (CE value), cooling rate and microstructural hardness level. Diagram applies for carbon-manganese steels [45].

The two formulae most commonly used for CE calculation are shown in equation (1.13 and (1.14):

$$CE_{IIW} = C + \frac{Mn}{6} + \frac{Cr + Mo + V}{5} + \frac{Ni + Cu}{15} \qquad (1.13)$$

$$Pcm = C + \frac{Si}{30} + \frac{Mn}{20} + \frac{Cu}{20} + \frac{Ni}{60} + \frac{Cr}{20} + \frac{Mo}{15} + \frac{V}{10} + 5B \qquad (1.14)$$

The later takes into account the additional microalloying element boron which significantly increases hardenability of the steels (for this purpose it is also utilised in HHA alloy design in relatively high concentration) as it can be seen gives rise to a significant increase in CE [45]. In Figure 1-35 Pcm with the diffusible hydrogen content are utilised to specify the conditions under which HACC is likely to occur in high strength steel weldments. However, Pcm not recommended to be used for steels containing carbon level in excess of 0.15 wt%.

Many more different carbon equivalents for various types of steel have been proposed over the years. The most widely used formulas as summarised by Yurioka [13] in his extensive publication on HACC. They are as follows (CE_{IIW} and P_{cm} were excluded from this list as they are presented above):

$$CE_{WES} = C + \frac{Si}{24} + \frac{Mn}{6} + \frac{Ni}{40} + \frac{Cr}{5} + \frac{Mo}{4} + \frac{V}{14} \quad (1.15)$$

$$CE_{Wintarton} = C + \frac{Mn}{6} + \frac{Cu}{40} + \frac{Ni}{20} + \frac{Cr}{10} + \frac{Mo}{50} + \frac{V}{10} \quad (1.16)$$

$$CE_{Stout} = C + \frac{Mn}{6} + \frac{Cu}{40} + \frac{Ni}{20} + \frac{Cr + Mo}{10} \quad (1.17)$$

$$CE_{Cottrell} = C + \frac{Mn}{6} + \frac{Cr}{5} + \frac{Mo}{5} + \frac{V}{3} + \frac{Nb}{4C} + \frac{0.0001}{S} \quad (1.18)$$

$$CE_{DoV} = C + \frac{Si}{24} + \frac{Mn}{10} + \frac{Ni + Cu}{40} + \frac{Cr}{5} + \frac{Mo}{4} + \frac{V}{14} \quad (1.19)$$

$$P_n = C + \frac{Si}{20} + \frac{Mn}{10} + \frac{4P}{3} + \frac{Cu}{20} + \frac{Cr}{30} + \frac{Mo}{20} \quad (1.20)$$

$$CE_{HSLA} = C + \frac{Mn}{16} - \frac{Ni}{50} + \frac{Cr}{23} + \frac{Mo}{7} + \frac{Nb}{5} + \frac{V}{9} \quad (1.21)$$

$$CE_{PLS} = C + \frac{Si}{25} + \frac{Mn}{16} + \frac{Cu}{16} + \frac{Ni}{60} + \frac{Cr}{20} + \frac{Mo}{40} + \frac{V}{15} \quad (1.22)$$

$$CEN = C + A(C)\left(\frac{Si}{24} + \frac{Mn}{6} + \frac{Cu}{15} + \frac{Ni}{20} + \frac{Cr + Mo + Nb + V}{5} + 5B\right) \quad (1.23)$$

where $A(C) = 0.75 + 0.25\tanh[20(C - 0.12)]$

However, the use of carbon equivalent formulas is restricted to situations involving similar heat input, plate thickness and joint geometry as they do not take into account the cooling rate which is crucial factor influencing microstructural evolution in the weldment.

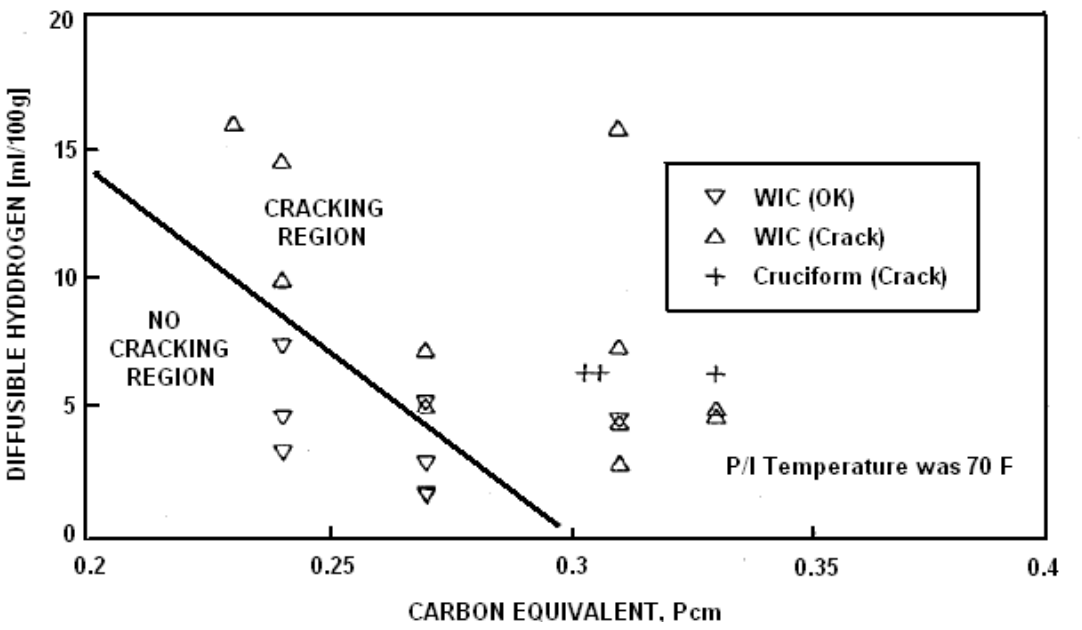

Figure 1-35 Incidence of hydrogen cracking as a function of diffusible hydrogen content and Pcm [50].

Peak HAZ hardness is an indicator widely used to predict the susceptibility to HACC. In the case of Q&T high strength steels the coarse grain heat affected zone (CGHAZ), is the most susceptible to hydrogen cracking. It is adjacent to weld metal (WM), therefore it experiences the highest peak temperature (this gives rise to the formation of a very hard microstructure with large grain size). Subsequent rapid cooling from the peak temperature results in formation of hard structures with low ductility [45]. The CGHAZ usually possesses the highest hardness and highest diffusible hydrogen concentrations out of all HAZ subzones. It is commonly accepted that when developing safe welding procedures, the parameters should be selected so that the hardness of the HAZ does not exceed 350 HV [72] for structural steels and 450HV [41] for high strength Q&T steels. These values are considered to be the maximum acceptable values for avoiding hydrogen cracking. Although when the level of the weld metal hydrogen is controlled the material is not likely to crack even when the hardness levels are higher than above mentioned values.

A number of regression formulae for calculation of the maximum hardness have been developed over the years. An expression developed by Yurioka et al. [73] is widely used for steels with $C \leq 0.3$ wt% :

$$HVmax = 442C + 99CEIII + 206 + (402C - 90CEIII + 80).\arctan(x) \quad (1.24)$$

where:

$$x = \frac{logt_{8/5} - 2.30CEI - 1.35CEIII + 0.882}{1.15CEI - 0.673CEIII - 0.601}$$

$$CEI = C + \frac{Si}{24} + \frac{Mn}{6} + \frac{Cu}{15} + \frac{Ni}{12} + \frac{Cr}{8} + \frac{Mo}{4} + \Delta H$$

$$CEII = C + \frac{Si}{24} + \frac{Mn}{5} + \frac{Cu}{10} + \frac{Ni}{18} + \frac{Cr}{5} + \frac{Mo}{2.5} + \frac{V}{5} + \frac{Ni}{3}$$

$$CEIII = C + \frac{Mn}{3.6} + \frac{Cu}{20} + \frac{Ni}{9} + \frac{Cr}{5} + \frac{Mo}{4}$$

$\Delta H = 1.5(0.02\text{-}N)$ when $B \leq 2ppm$

In the case of multipass fillet welding the increased risk of HACC is in the area of the weld toe as the HAZ of the first pass might not be fully tempered by the heat introduced by subsequent passes. This HAZ are can exhibit increased hardness levels and diffusible hydrogen content, thus increased susceptibility to HACC.

1.4.7 Avoidance of hydrogen cracking

The interaction of the three factors causing HACC and the magnitude of each is still not fully understood. This is the reason why the use of HACC prediction models is restrained and accuracy is limited. To be able to reliably predict whether hydrogen cracking will occur under given conditions it would be necessary to develop improved predictive methods which would consider all of factors contributing to HACC.

When developing safe welding procedures two approaches can be adopted to minimise the risk of HACC:

- Minimise amount of hydrogen entering weld pool (the use of low hydrogen welding processes, shielding atmosphere, selection of low-hydrogen consumable or consumable itself insensitive to hydrogen etc.)
- Allowing sufficient amount of hydrogen to diffuse out of the weldment (by preheating, interpass temperature control, postweld heat treatment, isothermal temperature control)

Often a combination of both measures provides the best practical solution.

Preheating steel prior to welding in combination with interpass temperature control is common practice to reduce the risk of HACC in weldments by removing moisture from plate's surface and decreasing the cooling rate. The later in turn produces a softer microstructure, allows more time for hydrogen to diffuse out of the weldment and also results in lower residual stresses, thus it effectively eliminates all three factors contributing to HACC.

Determination of minimum preheat temperature

The calculation of minimum preheat temperature for welding Q&T steel recommended by various standards and the WTIA guidelines [27] use the following index P_w [%] that considers three factors contributing to HACC, hardenability of the steel, diffusible hydrogen content and restraint:

$$P_w = P_{cm} + \frac{H_D}{60} + \frac{R_F}{4000} \tag{1.25}$$

where: H_D is weld metal diffusible hydrogen content [ml/100g], R_F is restraint intensity factor (usually less than 40 x plate thickness).

From this the minimum preheat temperature [°C] can be calculated using the formula:

$$Minimum\ preheat = 1440P_W - 392 \tag{1.26}$$

In case of Q&T armour steels the manufacturers often do not recommend postweld heat treatment and restrict preheat temperatures to below 150ºC this results in limitation of the use of temperature control method and exclusion of the use of isothermal transformation method. In these cases the use of austenitic stainless steel and high nickel consumables offer an alternative solution. But whilst this may be expected to expand the process parameter field its use is often restricted by adherence to procedures previously developed for ferritic consumables implementing preheating. Additional research to confirm the safety of welding procedures has to be carried out before preheating can be excluded from the welding practice.

In addition, temperature control methods for avoidance of HICC significantly increase the fabrication costs in terms of both time and energy. The desire in welding community is to eliminate time consuming and costly practices. Lowering hydrogen content entering weld pool is effective way to reduce risk of HICC. Welding procedures resulting in introducing 2-5 ml/100g of WM have been considered safe for welding of high strength steels [56, 62].

1.5 SUMMARY OF LITERATURE REVIEW

In this literature review an introduction into steel armour was given, in addition to developments of steel armour and design specifications. Information on steel armour metallurgy was provided, describing manufacturing processes, alloying and microstructural characterisation. The focus of this literature review was welding of steel armour. An overview of traditional and also advanced welding techniques and welding consumables applicable for joining armour steels was presented. The main risk when welding quenched and tempered (Q&T) steels in high hardness condition is hydrogen assisted cold cracking (HACC), hence all factors contributing to this phenomenon and also methods of avoidance of HACC were reviewed. The most effective measure to lower the risk of HACC is the use of low hydrogen process and consumable in combination with preheating [27, 41, 45, 74].

High hardness quenched and tempered steels are mostly used in mining industry applications where the weld metal and heat affected zone (HAZ) are required to possess principally different properties (impact abrasion resistance, slighting and gouging abrasion resistance) compared to joints for defence applications (ballistic and blast protection). Due to this fact austenititc stainless steel consumable is not suitable for some wear resistance applications. Consequently, available manufacturers' recommendations and procedure specifications are related only to welding high hardness Q&T steels employing ferritic consumables.

The primary objective of this research work was to optimise welding procedures (identify lower preheat and upper interpass temperature threshold) for high hardness

armour steels when welded with austenitic consumables. It is suggested that the procedures originally developed for ferritic consumables and currently used for joining high hardness armour (HHA) are unduly conservative when welding these materials with austenitic stainless steel consumables. There are numerous standards, specifications and other literature available on determination of minimum safe level of preheat for welding ferritic steels with ferritic consumables [27, 41, 74-76] but little guidance on safe practice when austenitic stainless steel consumables are used. It is well accepted that the use of austenitic stainless steel consumable effectively lowers the risk of HACC therefore the level of preheat can be reduced [45, 72, 76]. However the information about the determination of minimum safe preheat temperature is lacking in welding standards and was not found published elsewhere in public domain. Therefore, comprehensive investigation into the effects of preheat temperature on HACC (microstructure, hydrogen level and distribution and also residual stresses) was carried out. Additionally, information about determination of maximum interpass temperature that would result in acceptable degree of HAZ softening in the chosen steel was not available for this reason the effect of interpass temperature on HAZ microstructure was also carefully examined.

Another project objective was to investigate advanced welding procedures that would deliver improved quality and productivity for this application. Due to the advantages of hybrid laser-GMAW process this method was selected as an appropriate subject for the present study. To the best knowledge of the author this method has not been used before for welding of high hardness Q&T steels with austenitic stainless steel consumable. In this work feasibility of hybrid laser-GMAW for this application was assessed based on number of welding trials.

In summary the overall aim of the work was to establish viable, improved productivity and safe procedures for welding high strength quench and tempered steels.

2 EXPERIMENTAL METHODS, EQUIPMENT AND MATERIALS

2.1 OBJECTIVES

The main objective of this PhD research is the development of safe highly optimised welding procedures for Q&T steels. Specifically for high hardness armour (HHA) steel produced by Bisalloy Steels Ltd in Australia. The main concern when welding Q&T steels is the risk of HACC in weldments. In order to minimise the risk of HACC, a low hydrogen welding process combined with the use of austenitic stainless steel (ASS) consumable and preheating the plate prior to welding are currently employed by fabricators. The ASS consumable was chosen for increased resistance to HACC. As explained in the literature review this added resistance arises from the fact that austenitic weld metal possesses much higher solubility and much lower diffusion rate of hydrogen compared to the ferritic fillers. Preheating is however often carried out to eliminate the risk of HACC in weldments based on the use of Australian Standard 1554 which does not differentiate between austenitic and ferritic fillers. Preheat is normally employed to remove moisture from the plate surface, decrease the cooling rate after welding (allowing longer time for hydrogen to diffuse out of the weldment), create a less susceptible microstructure as well as reducing residual stresses. Conversely, preheating represents an additional step in the welding process; it significantly reduces productivity and increases fabrication costs. Further to reduce the risk of HACC and HAZ softening interpass temperature is maintained at the preheat temperature. From productivity view point it is beneficial to employ highest interpass temperature that does not produce extensively wide soft HAZ areas that may deteriorate the ballistic protection. Current preheat and interpass temperature ranges used in industry are between 80°C and 120°C. This temperature range was determined to be safe for the previously used ferritic filler and is currently used because of lack of data available on joints welded with ASS consumable. To develop welding procedures with optimised parameters a deep understanding of parent HHA material properties and also continuous cooling behaviour is crucial. To confirm safety of the proposed welding procedures with reduced (ideally removed) preheat and increased interpass temperatures the information about the effect of various levels of these two temperatures on the HAZ microstructure and hardness is essential. Reducing preheat

also requires information about the level of hydrogen and residual stresses present in the weldments under various preheat conditions. The productivity and cost-effectiveness and quality of welding of armour structures could be further improved by employing innovative welding techniques. This option was explored by investigating the feasibility of advanced hybrid laser-GMAW for joining HHA plate.

The summary of strategy steps to develop safe highly optimised solutions for welding of HHA were as follows:

1. Develop in-depth understanding of the **metallurgy and mechanical properties of the** current HHA steel grade;
2. Investigate the **continuous cooling transformation behavior** of a current HHA steel grade;
3. Define acceptable **lower preheat and upper interpass temperature thresholds** for selected welding processes, heat inputs and consumables applied to the welding of HHA steel. This involves:
    a) Investigation of the effect of various selected **preheat** and **interpass temperatures** on **microstructure** and **hardness** of the samples welded employing GMAW in combination with flux-cored and metal-cored austenitic stainless steel consumables.
    b) Determination of the **hydrogen levels** present in the weldment under different **preheat** conditions, for various types of austenitic stainless steel consumable (flux-cored, metal-cored and solid) and compare these with hydrogen levels introduced into the weldment with previously used ferritic filler.
    c) Assessment of the resultant **weld residual stresses** formed under various **preheat** conditions, for various types austenitic stainless steel wire (flux-cored, metal-cores and solid).
4. Explore the feasibility of **hybrid laser-GMAW** process in combination with solid austenitic stainless steel consumable for welding of armour platforms.

2.2 MATERIAL

The HHA steel subjected to investigation complies with Australian specification DEF AUST 8030 [11] and belongs to a family of Q&T steels for armour applications. The chemical composition (max) and typical mechanical properties of the investigated armour steel is listed in Table 2-1 and Table 2-2 respectively. The steel plates for experimental investigation were obtained in two batches approximately 18 months apart. A representative sample out of each batch was tested for chemical composition analysed by the atomic emission spectroscopy method. The certificates of analysis can be found in the Appendix 1. The alloy design of this steel utilises the novel low manganese approach (described in detail in section 1.2.2) in order to reduce centreline segregation of MnS inclusions and thus improve mechanical properties and weldability. The steel is microalloyed with Nb, Ti, V, and B in order to increase hardenability and enhance the HAZ properties.

This HHA steel is manufactured by BluscopeSteel utilising the BOS (Basic oxygen seelmaking) process. The manufacturing process involves vacuum degassing and calcium treatment. Plates are hot rolled to desired thicknesses and supplied in as rolled "green feed" condition to Bisalloy Steel Group Ltd to undergo heat treatment. Green feed plates are quenched and tempered in a modern Drever roller at to achieve desired levels of hardness and toughness. This heat treatment consists of two phases: rapid water-quenching from austenite field which results in the formation of brittle microstructure consisting of untempered martensite and subsequent low temperature tempering which improves the plate's toughness while lowering the level of hardness. This two step heat treatment results in microstructure associated with superior combination of hardness, strength, ductility, toughness and weldability properties. HHA steel has strength to weight ratio of more than three times that of mild steel.

Table 2-1 Chemical composition of 8.5mm HHA steel in wt % max [74].

Element	C	Mn	Si	Ni	Cr	Mo	S	P
Wt% max	0.32	0.4	0.35	0.35	1.15	0.3	0.005	0.02

Element	Cu	Al	Nb	Ti	V	B	CE_{IIW}	P_{cm}
Wt% max	0.2	0.06	0.005	0.03	0.05	0.002	0.72	0.46

Table 2-2 Typical mechanical properties of 8.5mm HHA steel [74].

Property	**Typical value**
0.2 % Proof Strength	1400 MPa
Ultimate Tensile Strength	1640 MPa
% Elongation (50 mm G.L).	14%
Charpy V-notch @ -20°C (Trans./Long.)	8J/10 J
Hardness	500 HB

The microstructure of the 8.5 mm thick HHA plate in the green feed as well as Q&T condition is shown in Figure 2-1. The microstructure of the plate in Q&T condition consists of tempered martensite with an average hardness of 519 HV 200 g. The morphology of martensite is a function of carbon content. In the case of low carbon steels martensite is present in lath form [77]. The maximum carbon content of HHA steel is 0.32 wt% thus formed martensite exhibits mainly lath morphology with small amount of plate form also being present. The visible bands are a result of segregation of alloying elements during the casting and hot rolling process. Because of the higher concentration of alloying elements present in the bands these areas are typically characteristic by slightly higher hardness values compared to surrounding matrix. This phenomenon is especially pronounced in the centreline region. Hardness of the plate was measured utilising a Vickers micro hardness tester Leco M-400-H1. The load of 200 grams was applied for 10 seconds. The through thickness hardness profile of 8.5mm thick HHA steel is presented in Figure 2-2. The slightly higher hardness measured in the plate's centre is due to centreline segregation.

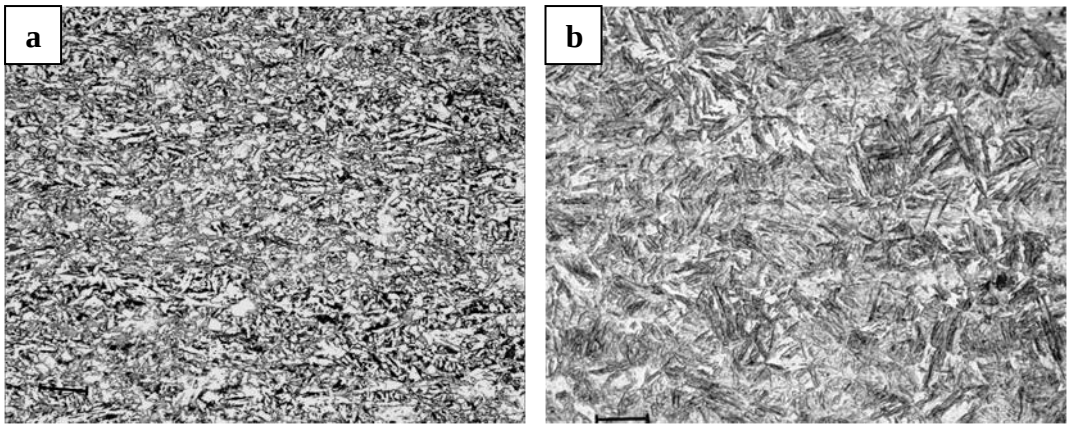

Figure 2-1 Representative microstructure of investigated 8.5mm HHA steel: a – in green feed (as-rolled) condition, b – in Q&T condition. Note the micron bar represents 20 μm.

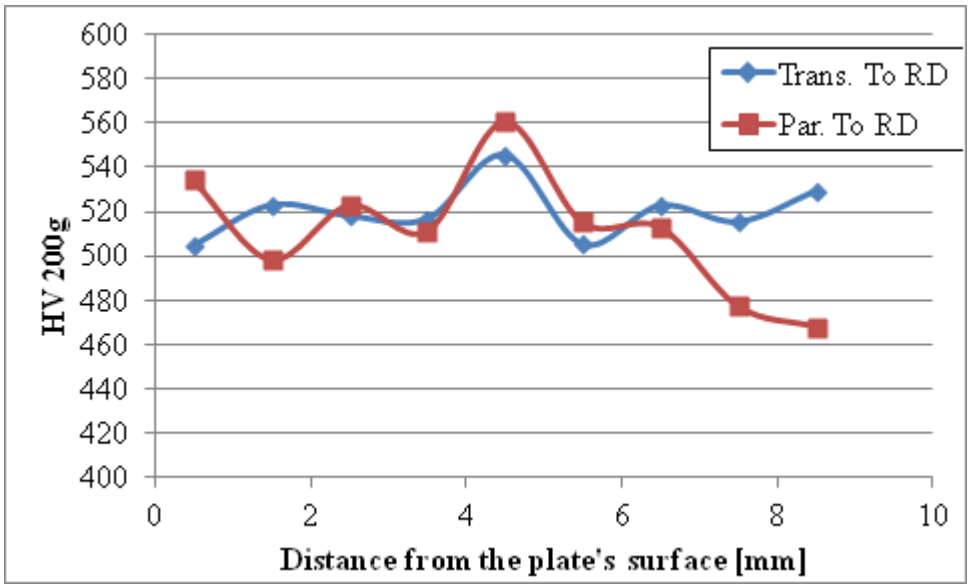

Figure 2-2 Vickers micro (200 g load) hardness profile of 8.5 mm HHA plate in Q&T condition measured in through thickness orientation transverse (Trans.) and parallel (Par.) to the rolling direction (RD).

2.3 CONTINUOUS COOLING TRANSFORMATION BEHAVIOUR OF HHA STEEL

The alloy design of the HHA steel plate has been altered, thus before commencing welding trials an in depth investigation into transformation behaviour and resultant microstructures had to be carried out.

The objective was to construct CCT diagrams directly applicable to welding to provide information about the transformation behaviour and microstructure formed when the steel is subjected to various cooling rates. Actual cooling rates for real welds were measure (see later in this section). The dilatometry technique was selected to generate data necessary to construct CCT diagrams. These diagrams help to assess the risk of HACC during welding based on the microstructure formed in the HAZ during welding. It has been shown that the risk of HACC cracking is linearly related to the $\gamma \rightarrow \alpha$ transformation temperature, as well as to the martensite finish (M_f) temperature during transformation, both of which may be predicted from experimental cooling curves (dilatometry) [78].

The aim was to simulate the microstructural evolution of CGHAZ as in case of welding Q&T steels in high hardness condition this sub-zone is most susceptible to HACC. During welding CGHAZ is typically exposed to peak temperatures between 1200°C to 1450°C [19]. Therefore the austenisation temperature for CGHAZ simulation testing was selected to be 1350°C.

In the present work a preliminary CCT diagram of the HHA steel was determined using dilatometry. Different heat treatment cycles, involving systematic variations of cooling rate were used to test the response of the steel in terms of the microstructure and hardness produced on cooling. HHA $\gamma \rightarrow \alpha$ transformation start and transformation finish (Ts and Tf) temperatures at various cooling rates were determined, the resulting microstructures were examined and hardness was measured for all generated dilatometry samples.

2.3.1 Dilatometry

The dilatometry samples were 10 mm long hollow cylinders with a 5 mm diameter and 0.75 mm wall thickness and were machined from 8.5mm HHA plate. A schematic drawing of the sample geometry is shown in Figure 2-3. Experiments were carried out in the vacuum chamber of a computer aided Theta II thermo-mechanical simulator shown in Figure 2-4.

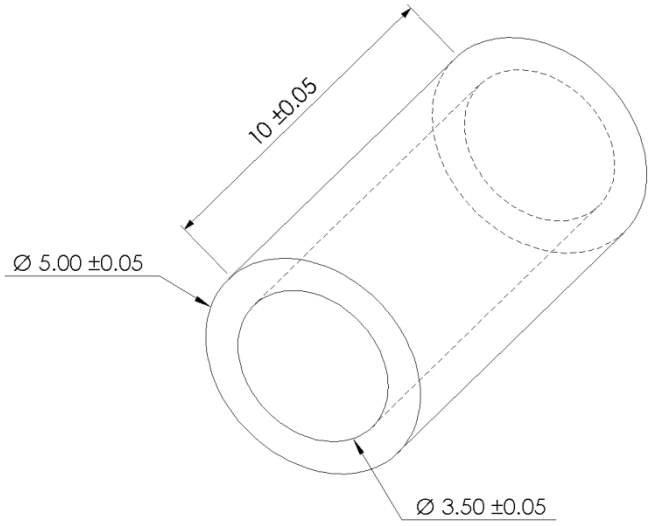

Figure 2-3 Schematic diagram of the hollow cylindrical dilatometer specimen. Dimensions are in mm.

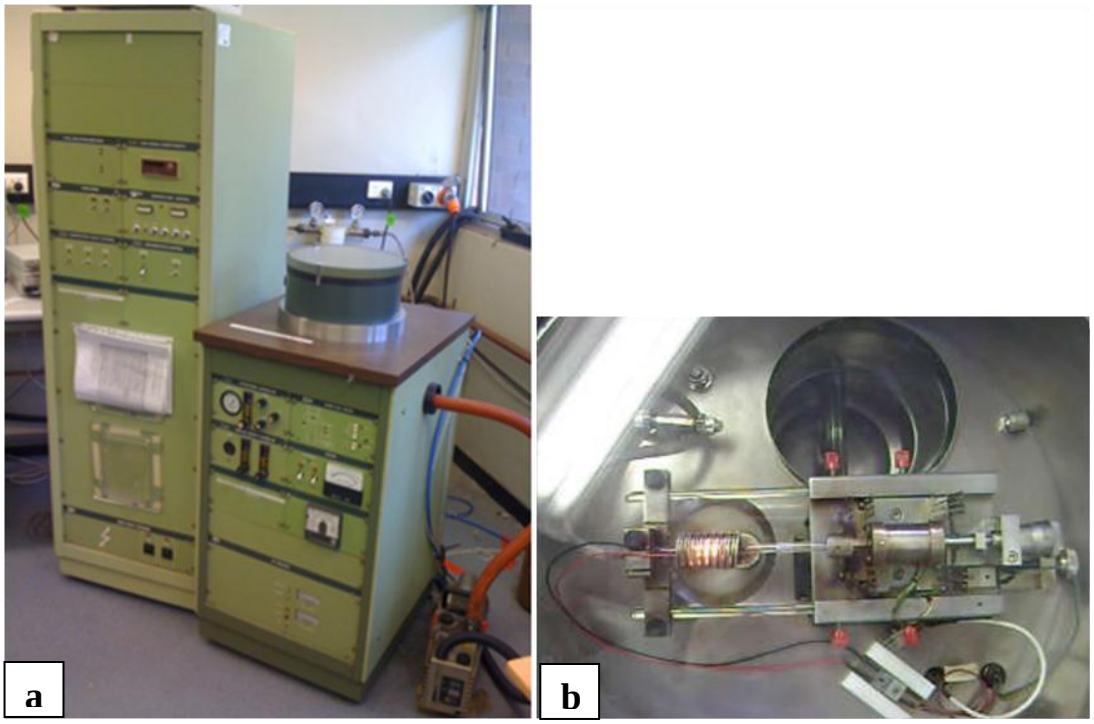

Figure 2-4 Photograph of Theta II high speed dilatometer machine, b - detail of Theta II sample chamber with test in progress.

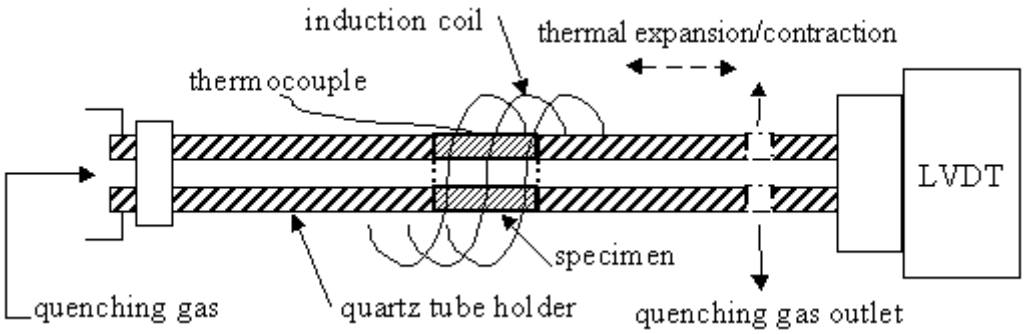

Figure 2-5 Schematic diagram of the dilatometer sample chamber configuration.

An S-type thermocouple was spot-welded in the middle of the sample to the exterior surface to ensure good temperature monitoring and control. The Theta II high speed dilatometer measures the dilatation of samples in the direction of long axis. Samples were placed in between the fixed support tube and quartz pushrod. The pushrod was lightly spring loaded in order to hold the samples in position. A high vacuum of about 10^{-4} Torr was generated in the dilatometer sample chamber in order to protect the surface of the samples from oxidation. After a stable vacuum was achieved, samples were heated at rate of 50°C/s to the austenitisation temperature of 1350ºC, held for 2 seconds (shorter holding time simulating real welding conditions more accurately could not be achieved due to the equipment limitations) and then cooled to 100ºC using various constant cooling rates, namely 1°C/s, 5°C/s, 10°C/s, 20°C/s, 30°C/s, 50°C/s, 70°C/s, 100°C/s, and 200ºC/s. The thermal cycles experienced by the dilatometry samples are schematically shown in Figure 2-6. Heating was realized with an induction coil encompassing the sample. Various cooling rates were achieved by passing compressed air (to achieve slower cooling rates) or He (to achieve fast cooling rates) at different flow rates through the centre of the samples. During the thermal cycle the dilation of the samples was determined by the linear displacement of the quartz tube caused by the expansion/contraction of the sample and interpreted by the linear variable differential transducer (LVTD). Before each test the LVTD was manually adjusted to compensate sample length variations. A schematic diagram of the dilatometry apparatus is shown in Figure 2-5.

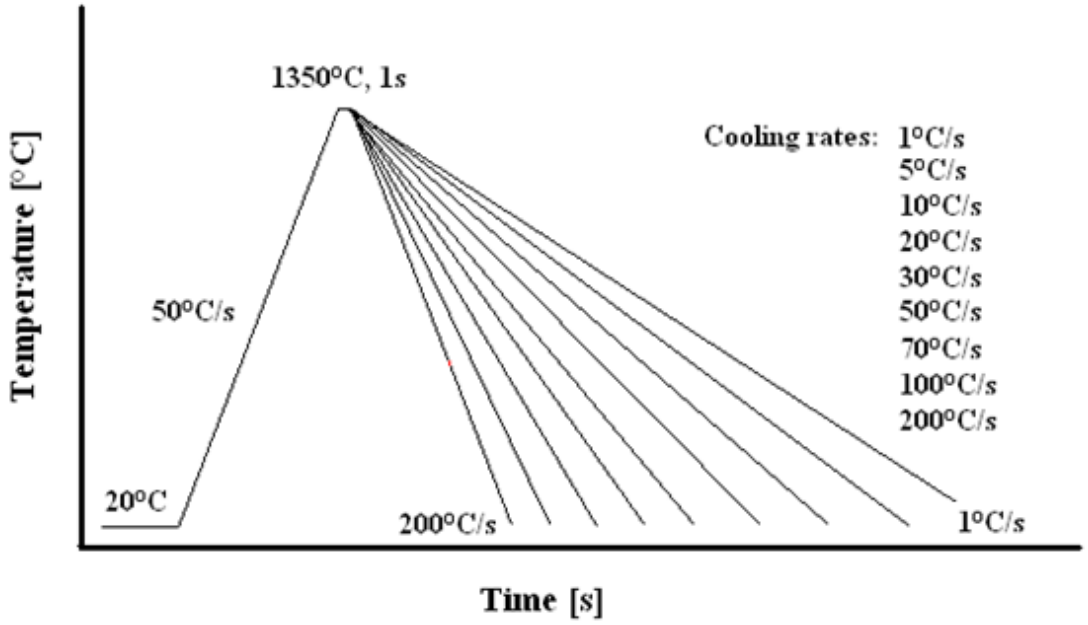

Figure 2-6 Schematic diagram of the heat treatment cycles of dilatometry samples.

2.3.1.1 Determination of Ts and Tf temperatures

During the thermal cycle the sample dilatation resulting from thermal expansion/contraction was recorded. For all cooling rates the dilation curves were established by plotting dilatation versus temperature. Dilation curves show the expansion that occurred due to phase transformation. Phase transformation is represented as a variation in line slope due to a change of coefficient of expansion. Extractions of transformation start and finish temperatures from the dilatation curves were carried out using the analysis program OriginPro 8. The linear part of the dilation cooling curve was identified then the tangent parallel to the linear part of the curve was drawn beyond the point when the dilation curves start to arc below and above the start and finish of the transformation regime respectively. The transformation start and finish temperatures were determined where the dilatation curves started to deviate from the linearity. The reported values of transformation start and finish temperatures are the mean values of three measurements. The process of determination of transformation start and finish temperatures is schematically illustrated in Figure 2-7.

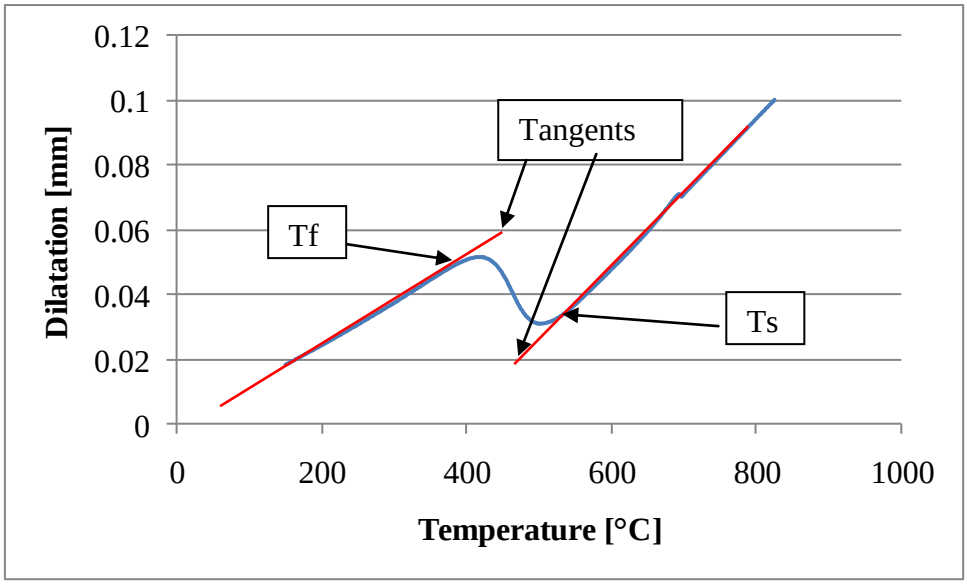

Figure 2-7 Schematic illustration of the method used to determine the transformation start and finish temperatures.

2.3.1.2 Microscopy and hardness testing

All test samples were cold mounted in epoxy resin and prepared according to standard metallographic procedures for metallographic examination using optical microscopy and Vickers microhardness measurements (utilising Leco M-400-H1 microhardness testing equipment). The load used during hardness testing was 200 g. The hardness was measured parallel to the long sample axis in the middle of the polished surface. The reported hardness values are the mean average of ten measurements.

2.4 WELDING TRIALS

In every industry there is a demand to increase the quality and productivity but at the same time lower the cost. The direction of this work was largely predetermined by the industry requirements; testing was carried out to deliver highly optimised solutions without compromising the quality of the weldments.

The practical objectives of this work are to optimise welding procedures and to significantly increase productivity and this would not be possible without employing innovative approaches that could include the use of welding automation or even

implementing completely new processes. Industry currently uses the semi-automatic GMAW process in combination with ASS flux-cored consumables. The full automation of these procedures requires the use of a metal-cored consumable enabling high process speeds to be used with robotic welding. Productivity and also cost effectiveness could be further enhanced by reducing the number of weld passes necessary to produce joints with the required geometry and properties. Novel hybrid laser-GMAW process in combination with solid austenitic stainless steel wire would appear to be an ideal candidate with the capability to deliver the required solution. For any of these approaches to be adopted it is important to fully understand their implications on the properties of the weldment.

Experimental welding trials were carried out at University of Wollongong and are divided into two separate segments based on the work objectives:

1. To optimise process parameters of presently used GMAW process. The aim was to define the lower preheat and upper interpass temperature threshold for currently used flux-cored wire and also for metal-cored wire intended to be used with fully automated robotic welding.
2. To investigate the feasibility of hybrid laser-GMAW process for welding HHA plate.

The experimental work carried out to optimise GMAW procedure is described in the following section. The hybrid laser-GMAW trials are described in the section 2.5.

2.4.1 GMAW welding trials

Due to its very high hardenablity HHA steel is extremely susceptible to HACC. Preheating the steel prior to welding minimises the risk of HACC. by removing moisture from the plate surface, decreasing the cooling rate after welding (allowing longer time for hydrogen to diffuse out of the weldment, which is especially prolonged in the case of ferritic consumables), and reducing residual stresses imposed on the weldment as a result of thermal shrinkage on cooling as well as creating a less susceptible microstructure. Another effective measure to reduce the risk of HACC is employing austenitic stainless steel consumable. When this type of consumable is used the minimum required preheat temperature prescribed by relevant standards can

by greatly reduced [76]. The industry partner had replaced ferritic consumable with austenitic stainless steel filler however due to the lack of evidence that this was a satisfactory arrangement to produce HACC free welds level of preheat remained unchanged (80°C-120°C).

Further, in order to minimise the risk of HACC, the minimum interpass temperature is usually identical to be the same as the minimum preheat temperature. From a productivity view point, it is beneficial to employ the lowest preheat and highest interpass temperature possible, whilst producing a weldment with optimised material properties. Moreover, it is essential to determine the lower preheat and upper interpass temperature thresholds for a given heat input, that prevent formation of both hydrogen cracks and excessively wide softened areas of HAZ, with loss of both strength and hardness [79].

The following section describes the research undertaken to establish a systematic approach to the development of optimum, cost effective procedures for welding HHA steel with austenitic filler. This involved in depth study of the effect of a number of preheating and interpass temperatures on cooling rate, HAZ microstructure evolution and consequently mechanical properties of single and multi-pass welds.

The multipass corner joint configuration shown in Figure 2-8 was selected for the present investigation. The currently used procedure utilises 5 passes deposited with flux-cored wire. The configuration was intended to be used in the future with robotic welding and was expected to employ a metal-cored wire. The revised joint geometry involves a 2mm plate overlap what reduces the volume of the groove to be filled with weld metal, thus 4 passes are sufficient to produce a joint with desired geometry. This joint configuration was selected because it involves a significant number of weld passes amplifying the effect of interpass temperature, the findings of this investigation can also be applied to the cases of welding HHA employing less weld passes with similar heat inputs. The effect of preheat temperature was studied by deposition of a single pass onto the fillet weld configuration (simulating 1st pass of the 4 and 5 pass joints) and the findings of this investigation can be applied to all single and multipass HHA joints welded with ASS consumable involving similar heat inputs.

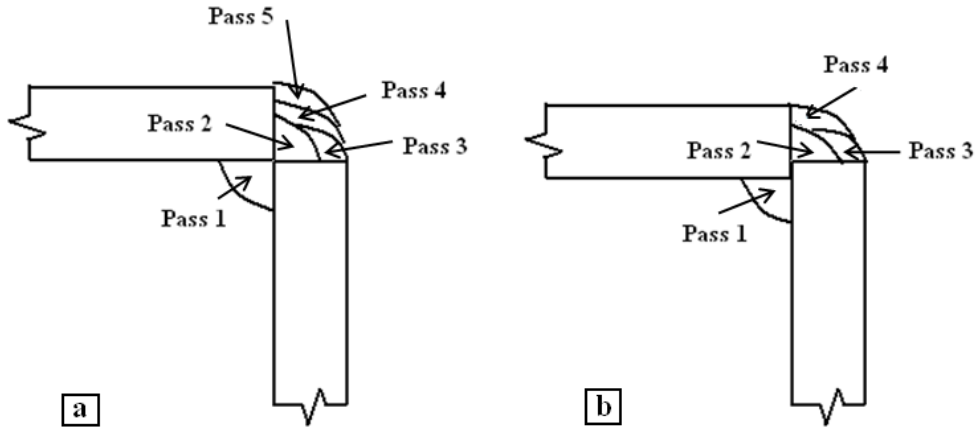

Figure 2-8 Schematic drawing of the corner joint geometry and location of the weld beads: a – 5 pass joint configuration used for welding with flux-cored wire, b – 4 pass joint configuration utilised for welding with metal-cored wire.

2.4.1.1 GMAW welding equipment

Welding power source

All GMAW trials were carried out employing a robot-controlled process. The welding equipment consisted of fully digital and microprocessor-controlled GMA power source; Fronius TransPuls Synergic 5000 CMT and a wire feeder as shown in Figure 2-9.

Welding table

A high precision welding table with set of clamps and accessories shown in Figure 2-9 was used to position and secure the samples at the exact locations defined in the robot programmes to ensure excellent repeatability and accuracy of the produced welds.

Figure 2-9 Photograph showing the set-up in the welding cell: Fronius welding power source and wire feed (back), welding robot (right), high precision work table with set of clamps (left).

Robot carrying welding torch

Welding applications are ideal candidates for automation because they are repetitive, require high-quality and consistent results. Robots are also extremely helpful when access to a part is limited or difficult to reach. Implementing robots into manufacturing process brings many advantages like enhanced repeatability, increased output, reduced costs and improved safety. The 6-axis industrial robot ABB ARB 4400 – 60 shown in Figure 2-10 was used for all GMAW trials. For each set of experimental trials a robot programme in the generic programming language was written defining the number of weld passes, exact weld path location, travel and wire feed speed, torch angle, stickout. A touch-sensing function was introduced to compensate for the geometrical variations of the steel plates to be welded in order to achieve excellent repeatability of the weld seam positioning for all the weldments. During operation (for example for a fillet weld) the robot moves the welding torch in the horizontal direction towards one end of the vertical steel plate. The welding power source is in active state sending a very low current to the filler wire. When the tip of welding wire touches the plate the electrical circuit closes and the location of the welding torch at that point is identified as an x coordinate of the start of the weld

seam. The same process is repeated at the other end to acquire the x coordinate of the end of the weld seam. Y coordinates of the start and end of the weld seam are obtained in the same manner touch-sensing the horizontal base plate. If the weldment requires multiple passes, the position of the start and end of the subsequent passes are offset from the coordinates of the first pass. The example of the robot program used in the welding trials investigating optimal of the interpass temperature for a five pass corner joint configuration utilising a flux-cored consumable is shown in Appendix 2.

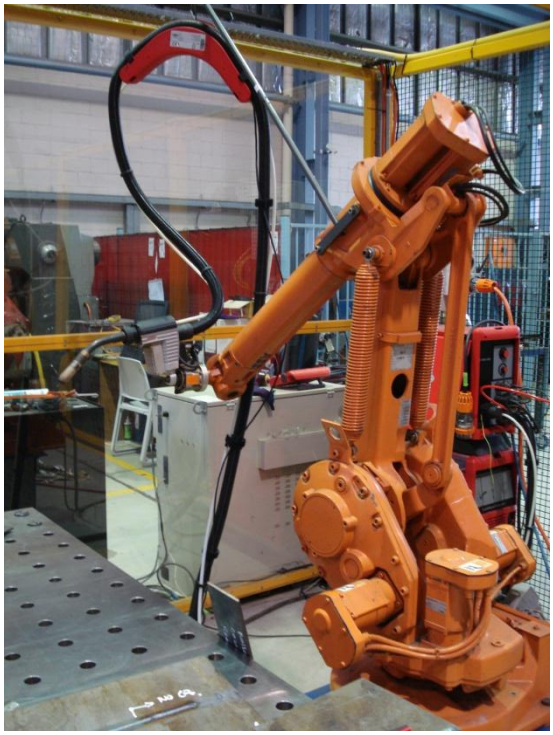

Figure 2-10 ABB ARB 4400 – 60 – 6 axis industrial robot carrying weld gun used for GMAW trials.

2.4.1.2 Consumables

GMAW trials were performed using two types of austenitic stainless steel wire, flux-cored and metal-cored. The diameter of both wires was 1.2 mm. The austenitic consumable was selected because it offers obvious benefits over ferritic consumable (refer to section 1.3.4.1) used in the past. Typical all weld metal chemical composition and mechanical properties of these two consumables types are presented in Table 2-4 and Table 2-5 respectively.

Table 2-3 Consumable name and classification of flux-cored and metal-cored austenitic stainless steel wire used in the investigation.

Type of ASS wire	**Consumable name**	**Classification**
Flux-cored	TETRA S 20.9.3	AWS A5.22 E308 MoT1
Metal-cored	VEGA 20.9.3-G	AWS A5.9 EC308Mo

Table 2-4 Typical all weld metal chemical composition of consumables used in the investigation.

Type of ASS wire	**Chemical elements in [wt%]**							
	C	Mn	Si	Cr	Ni	Mo	S max	P max
Flux-cored	0.05	1.5	0.8	20.5	9.7	2.9	0.005	0.02
Metal-cored	0.05	1.5	0.8	20.5	9.7	3.2	0.008	0.02

Table 2-5 Typical mechanical properties of weld metal deposited with flux-cored and metal-cored of austenitic stainless steel wire.

Type of ASS wire	**Mechanical property**				
	YS [N/mm^2]	UTS [N/mm^2]	Elong. [%]	Red. of area [%]	Charpy impact @ 20°C [J]
Flux-cored	530	710	30	50	50
Metal-cored	600	780	35	50	60

The flux-cored consumable TETRA S 20.9.3 is a versatile, gas shielded, seamed wire designated for welding in downhand position. The rutile flux system provides a smooth arc transfer characteristic, excellent bead appearance with self releasing slag. Argoshield 52 consisting of 25% CO_2 in argon was used as a shielding gas in combination with this flux-cored wire.

The metal-cored consumable VEGA 20.9.3-G is a versatile gas shielded, seamless wire capable of out of position welding. VEGA 20.9.3-G has enhanced productivity and wetting action when compared to an equivalent solid wire. This wire is especially suitable for automation as it does not produce slag on the surface of the bead.

Stainshield consisting of 1.5% O_2 in argon was used as a shielding gas in combination with this metal-cored wire.

In general, robot welding employing a correctly calibrated robot is well known for its excellent precision. To ensure high accuracy and repeatability of the produced weldment the accuracy and consistency of travel speed (robot speed) and wire feed speed were tested before commencing welding trials.

Determination of the robot motion speed (welding speed) accuracy.

A series of experiments to determine the accuracy of travel speed were carried out. The robot was programmed to travel along the 1000 mm gauge length at various speeds. The travel time was measured and travel speed accuracy evaluated.

As seen from the values in Table 2-6 the robot speed is extremely consistent. Discrepancies in single measurements were attributed to random error introduced by human factor related to the precision of timing.

Table 2-6 Parameters measured during calibration testing of the robot travel speed.

Set speed [mm/min]	Calc. time /1000mm [s]	Exp. time/1000mm [s]			Ave. time /1000mm [s]	Exp. speed [mm]	% Error [%]
		1	2	3			
500	120	120.16	120.18	120.22	120.19	499.01	-0.2
600	100	100.25	100.13	100.09	100.16	599.04	-0.16
2,000	30	30.09	30.14	30.08	30.1	1993.16	-0.34
10,000	6	6.06	6.04	6.07	6.06	9901.19	-0.99

Calc. = calculated, Exp. = experimental, Ave. = average

Determination of WFS accuracy

The accuracy of the WFS was measured by a WFS sensor. The WFS sensor consisting of two rollers connected to DC motor was initially calibrated. The welding wire was attached to the head of the robot. The robot was programmed to draw the wire through the wire feed speed sensor at various speeds. The output voltage is directly proportional to the supplied speed. A calibration curve of the sensor is presented in

Figure 2-11. The wire feed speed sensor was attached to the weld gun and the system was set to feed the wire through WFS sensor at various speeds. The voltage generated by various wire feed speeds was substituted in the equation and the experimental WFS was calculated. Measured values presented in Table 2-7 show that Fronius wire feed speed unit possesses excellent accuracy.

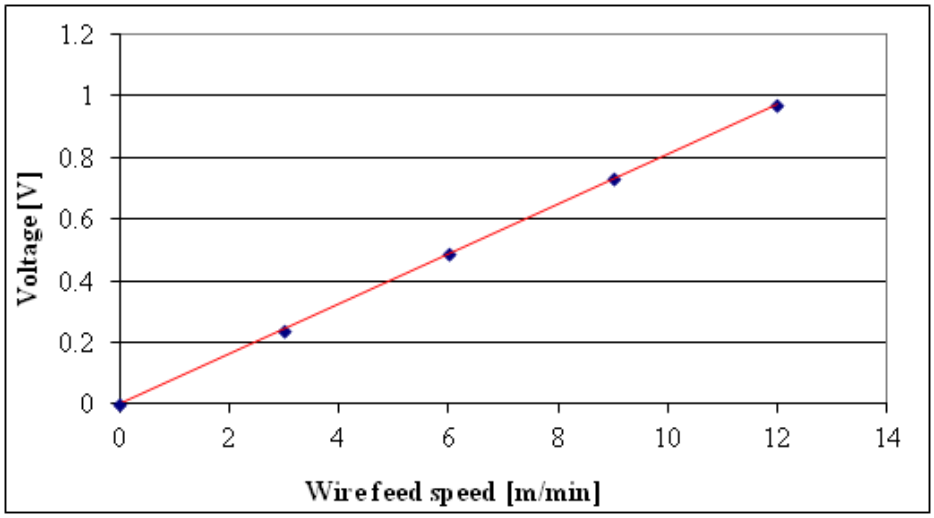

Figure 2-11 Calibration curve of the WFS sensor.

Table 2-7 Parameters measured during testing of the accuracy of the wire feed speed

Set WFS [m/min]	Average voltage [V]	Experimental WFS [m/min]	% Error [%]
0	0	0	0
3	0.24	3	0
6	0.48	5.9	-1.7
9	0.74	9.1	1.1
12	0.98	12.1	0.8

2.4.1.3 Optimisation of preheat temperature

A single pass fillet weld configuration was selected to determine the lower preheat temperature threshold. This arrangement simulates the first pass of the multipass corner joint (displayed in Figure 2-8) (the first pass is the most susceptible to HACC as the HAZ is not tempered by the subsequent passes and the cooling rate is likely to be higher compared with the capping pass). As mentioned in section 2.4 the preheat temperature was optimised for procedures utilising both flux-cored and metal-cored wire.

Two water jet cut HHA steel plates of dimensions 300 x 100 x 8.5 mm were tacked at the opposite side to the future weld bead. The assembly was then preheated to various temperatures (ambient (20°C), 40°C, 60°C and 80°C) utilising the electric resistance heating blanket shown in Figure 2-12. The manufacturing plant likely to utilise these procedures is located in area where ambient temperature during winter can drop down to 7°C. For this reason the final preheat temperature was selected to be 7°C. Undercooling of the test piece assembly was achieved using "dry ice" (solid CO_2). It should be noted that current industry practice requires pre-heating between 80°C to 120°C. To achieve precise temperature control during preheating and to record the weld thermal profiles, two K-type thermocouples were spot-welded to the middle of the plate surface, approximately 10 mm from the edge. The location of the thermocouples is shown in Figure 2-13. The plates were allowed to soak for about 1minute after the required preheat temperature was measured on the surface to achieve homogenous temperature throughout the whole thickness. A contact thermometer was used as a secondary temperature measuring system. Plates were then moved onto the welding table to deposit the single pass weld. Tacked plates and single pass deposit are shown in Figure 2-13. The welding parameters are presented in Table 2-8.

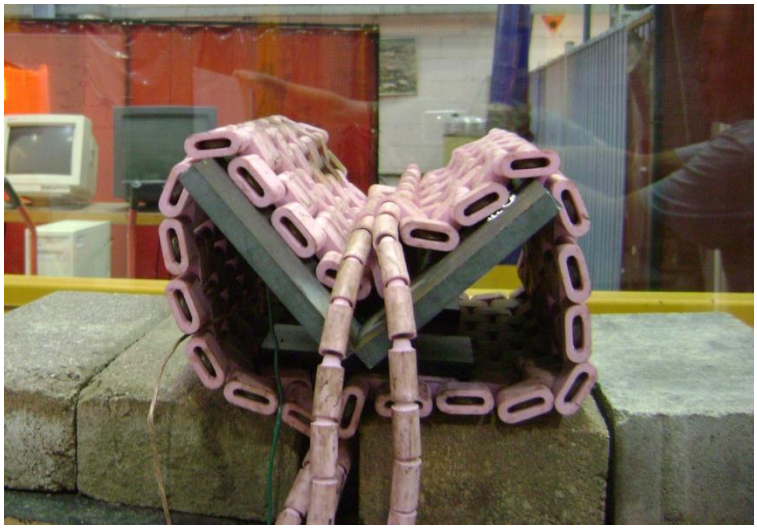

Figure 2-12 Electric resistance heating blanket used to preheat the plates.

Table 2-8 Welding parameters of the single pass filet welds.

Consumable	Current [A]	Potential [V]	TS [mm/min]	WFS [m/min]	HI [kJ/mm]	Shielding gas
Flux-cored	212	27	400	9.5	0.86	Argoshield 52
Metal-cored	275	23.6	450	8.5	0.87	Stainshield

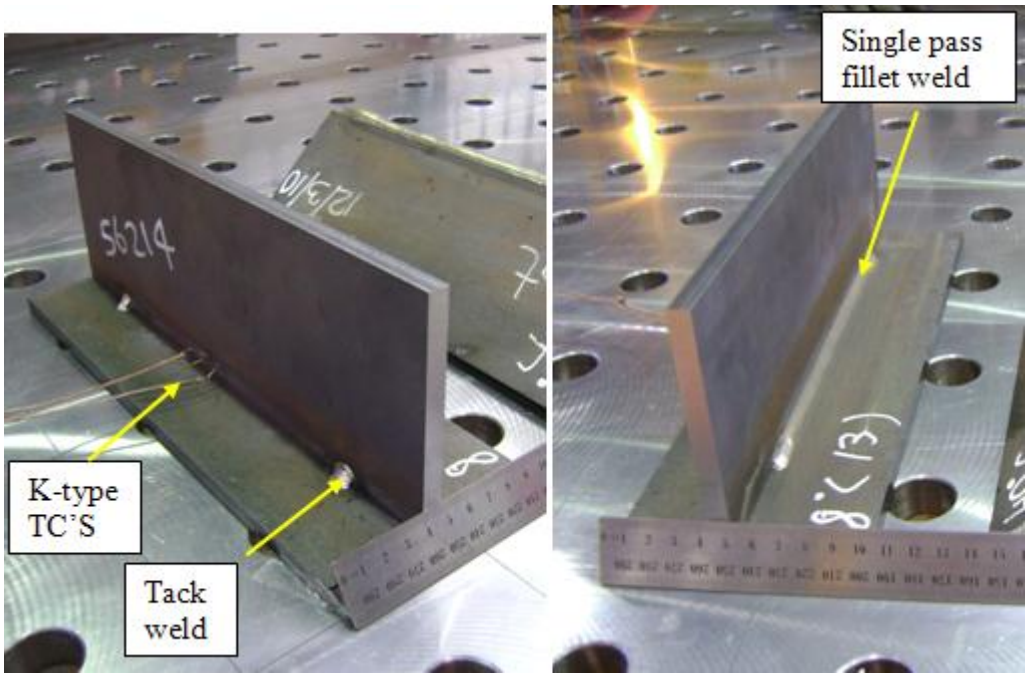

Figure 2-13 Single pass fillet joint configuration utilised to determine the lower preheat temperature threshold.

2.4.2 Metallography and hardness testing

Samples for metallographic examination and hardness testing were sectioned from the middle of weldments. A band saw was used to roughly extract the required section from the welded plates and Acutom 50 cutting machine was utilised to precisely cut the sample to final dimensions. Samples were then cold mounted in epoxy resin and prepared according to standard metallographic procedures. Vickers microhardness measurements were carried out utilising a Leco M-400-H1 microhardness testing facility employing a 200 g load. The orientation of hardness measurements is shown schematically in Figure 2-14. The indentations were located 0.5 mm apart to provide information about the hardness variations across the HAZ.

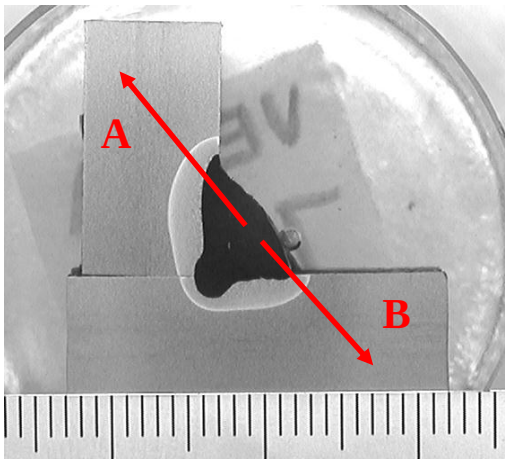

Figure 2-14 Orientation of the hardness testing measurements for 1 pass fillet welds deposited employing GMAW process in combination with flux-cored and metal-cored consumable.

2.4.2.1 Optimisation of interpass temperature

To optimise the interpass temperature 5 pass and 4 pass joint configurations as shown in Figure 2-8 were selected for flux-cored and metal-cored wire respectively. The area of concern is the cap region as the deposition of multiple passes can result in formation of extensively wide softened zone especially when high interpass temperatures are employed. An interpass temperature of 120°C is currently used in the industry. Whilst this is safe from a HACC view point, it takes quite some time for

weldment to cool down to this temperature particularly before deposition of the final weld deposit as the previous passes introduce a substantial amount of heat into the workpiece. This results in prolonged stand-off times that do not favour productivity. The aim of this work was to identify the upper temperature threshold that does not compromise the HAZ properties.

The welding sequence employed in this investigation simulated the routine used commonly in industry. Two water jet cut HHA steel plates of dimensions 300 x 100 x 8.5 mm were positioned to achieve the required joint geometry and tacked at either end of the inside corner. The inner pass was then deposited employing ambient (20°C) preheat. To simulate the procedure used by industry, before deposition of the cap passes, samples were allowed to cool down to ambient temperature. Interpass temperatures of 120°C, 160°C, 200°C and 250°C were maintained in between the deposition of the remaining cap passes. To study any higher interpass temperature would not have a practical benefit (especially for longer weld sections) as the weld initially cools very rapidly and only during the later stages of the cooling is the cooling rate significantly reduced. To achieve precise interpass temperature control and to record the cooling rate, two K-type thermocouples were spot-welded to the middle of the plate surface, approximately 10 mm from the edge. A contact thermometer was again used as a secondary temperature measuring system. The welding parameters are presented in Table 2-9.

Table 2-9 Welding parameters used to produce multipass corner welds.

Consumable	Pass	Current [A]	Potential [V]	TS [mm/min]	WFS [m/min]	Shielding gas
Flux-cored	1	220	26	400	9.5	Argoshield 52 25% CO_2 in Ar at 16 l/min
	2	220	31.5	500	11	
	3	205	30	500	9.5	
	4	205	30	550	9.5	
	5	205	30	550	9.5	
Metal-cored	1	275	24	450	8.5	Stainshield 1.5% O_2 in Ar at 20 l/min
	2	275	24	500	8.5	
	3	275	24	550	8.5	
	4	275	24	550	8.5	

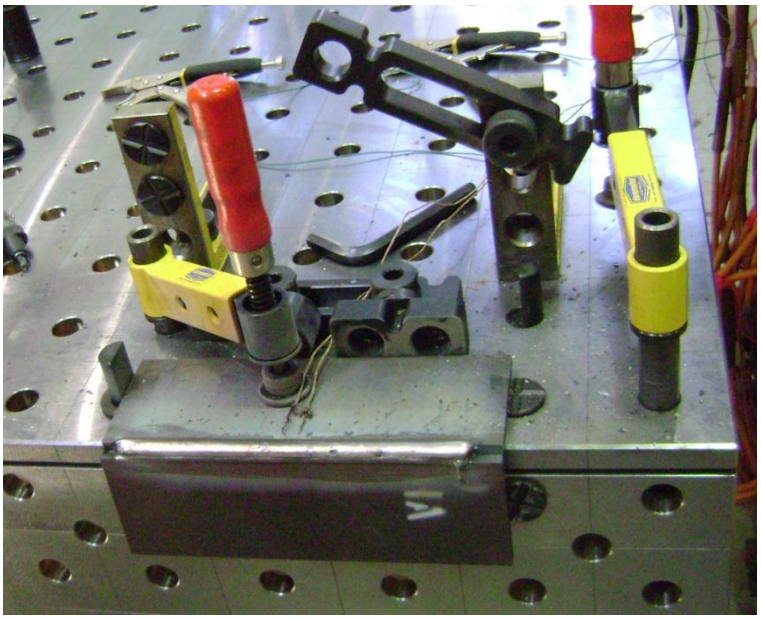

Figure 2-15 Four pass corner joint produced employing metal-cored consumable.

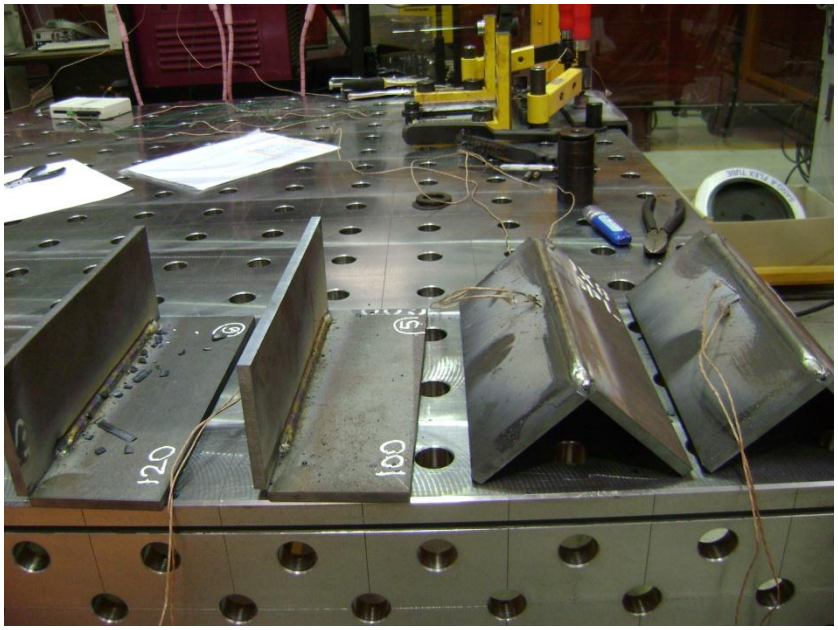

Figure 2-16 Five pass corner joints produced employing flux-cored consumable.

Determination of weld bead offsets for cap area of 5 pass corner joint utilising a flux-cored consumable

In order to achieve the required geometry for the 5 pass weld the off-sets for single passes in cap area were calculated and the final corrections were determined experimentally.

The first (inner) and second (first cap) pass were deposited with the welding wire directed at the root of the weld. Then bead on plate welds were deposited utilising the parameters for the third, fourth and fifth pass. The bead profiles of the cap passes were scanned employing a laser profiler and their cross-section areas were calculated. Based on this information and the information about the cross-section area of the cap groove which needed to be filled the off-sets for single passes were determined and are presented in the second column in Table 2-10. To confirm the correctness of the calculated offsets welding trials were carried out. It was observed that the transition in between single beads was not smooth and the third pass was slightly overhanging over the edge of the plate. To correct these geometrical discrepancies the off-set coordinates were slightly adjusted to values presented in the third column of Table 2-10.

Table 2-10 The offset positions of the weld beads for 5 pass welding procedure utilising flux-cored. Note: the weld root coordinates are [0; 0]

Pass	Calculated offsets	Corrected offsets
1	[0; 0]	[0; 0]
2	[0; 0]	[0; 0]
3	[4; 2]	[4; 2.5]
4	[2; 4.5]	[3; 4.5]
5	[0; 6]	[1.5; 6]

2.4.3 Metallography and hardness testing

Samples for metallographic examination and hardness testing were prepared in the same manner as for the 1 pass fillet welds described in section 2.4.1.3. The orientation of hardness measurements is schematically shown in Figure 2-17. The indentations were also located 0.5 mm apart to provide information about the hardness variations across the HAZ.

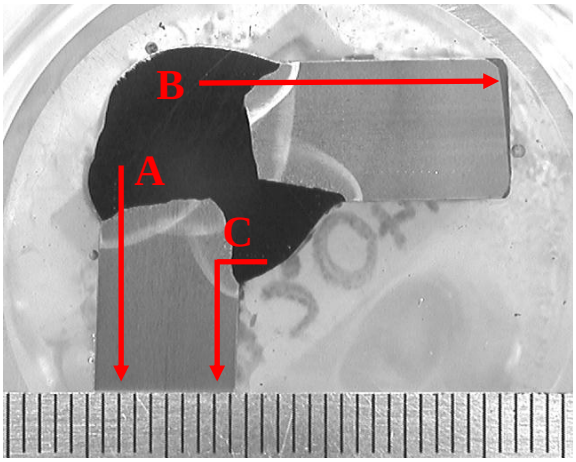

Figure 2-17 Orientation of the hardness testing measurements for 5 and 4 pass corner welds deposited employing GMAW process in combination with flux-cored and metal-cored consumable.

To be able to quantify the effect of the proposed procedure with optimised preheat and interpass temperature reference samples were produced utilising both flux and metal-cored consumables employing preheat temperature of 80°C and interpass temperature of 120°C as currently used in the industry.

2.4.3.1 Measuring the thermal history of the coarse-grain HAZ

The resultant microstructure and hence mechanical properties of the HAZ are a function of the chemical composition of the steel, peak temperature and cooling cycle experienced during welding. The coarse-grain subzone of the parent HHA steel is the most susceptible to HACC thus it is important to know the thermal history experienced by this area. Preheat temperature is the critical variable influencing the susceptibility to HAZ cracking. Part of this project focuses on identifying the lower preheat temperature threshold therefore the aim was to record thermal cycles experienced by the coarse-grain region as a function of different preheat conditions. In order to acquire reliable thermal history of coarse-grain HAZ of HHA welded employing preheat levels of 7°C, ambient (23°C) and 80°C, a method involving embedding thermocouples into the HHA plate prior to welding was adopted.

The bead on plate technique was selected for this investigation due to relative ease of embedding thermocouples. To achieve cooling rate as close as possible to the cooling rate during actual 1 pass fillet joint trials, the weld beads were deposited onto the top plate of previously welded corner joint consisting of two identical HHA plates.

To ensure that the acquired thermal history is that of coarse-grain HAZ thermocouples had to be precisely positioned in the location of future coarse-grain region. The weld metal penetrates into the parent plate to varying depths therefore a series of four thermocouples were strategically embedded into each HHA plate in such a manner that one of them would be located in the future coarse-grain region. Thermocouples were placed 1 mm under the surface and 10 mm and 1 mm apart in the direction parallel and transverse to the welding direction respectively as shown in Figure 2-18. Weld runs were deposited employing robot controlled welding in combination with flux-cored consumable; 7°C, ambient (23°C) and 80°C preheat and welding parameters presented in Table 2-8. Temperature and time data were acquired through thermocouples connected to data acquisition card and computer. To validate the acquired data a contact thermometer was applied as a secondary temperature measurement method. The set-up used during these trials is displayed in Figure 2-19.

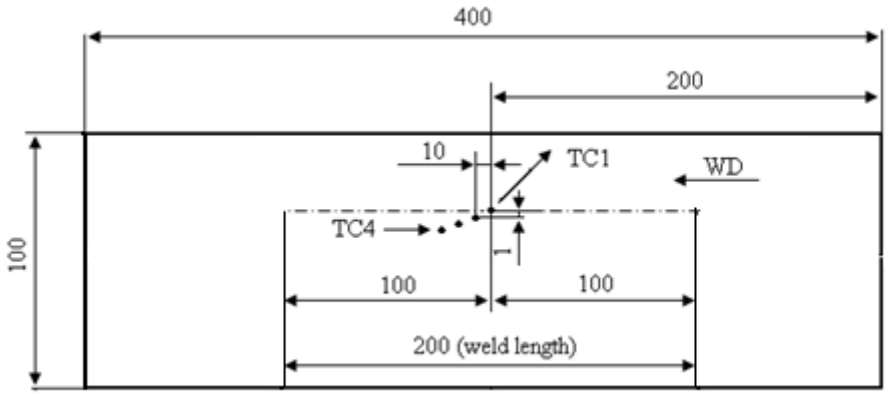

Figure 2-18 Schematic drawing showing dimensions of the HHA plate and location of four embedded thermocouples (TC1 – TC4) used to acquire thermal history of coarse-grain HAZ.

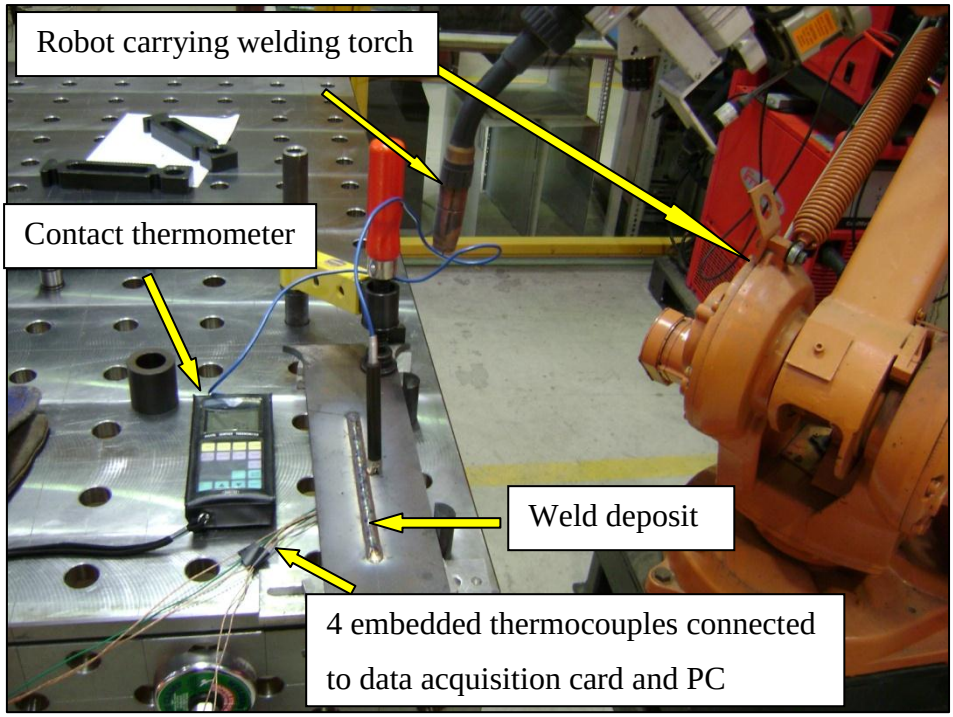

Figure 2-19 Test set-up used to record weld thermal cycles.

2.5 FEASIBILITY OF HYBRID LASER-GMAW PROCESS FOR JOINING HHA STEEL

The Hybrid laser-GMAW process utilises the synergy between a laser beam and welding arc and has the potential to offer a more productive solution for welding HHA steel. It couples the benefits and largely overcomes the disadvantages of the two individual processes [80]. The Hybrid laser-GMAW process is claimed to achieve much faster welding speeds compared to GMAW alone. This results in lower heat input and consequently a narrower HAZ. The HAZ hardness of laser welded area (in laser welding alone possesses high hardness and has increased susceptibility to HACC) but is tempered by the GMAW heat input [32]. The properties of the HAZ produced by current FCAW process could theoretically be further improved due to the reduction of weld passes and this would also lead to significant time and cost savings.

The main benefits resulting from successfully implementing this process would be:

1. Reduction in the amount of filler material required to produce an equivalent joint using conventional GMAW.

2. Reduction of the number of weld passes required leading to improvement in productivity.
3. Potential for improvement of joint hardness and minimisation of the HAZ.

To achieve the beneficial synergy between laser and arc to produce joints with the desired geometry and properties, optimal process parameters such as laser to wire distance, travel speed and wire feed speed have to be experimentally determined. The target of this work is to investigate the feasibility of the hybrid laser-GMAW process to produce joints with the geometry shown in Figure 2-20.

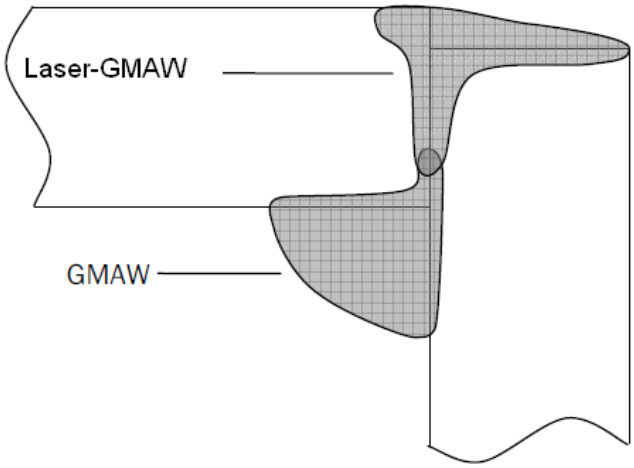

Figure 2-20 Ideal geometry of the hybrid Laser-GMAW joint.

2.5.1 Welding equipment

This experimental work was completed using the robot controlled GMAW process to produce the inner pass and a hybrid laser-GMAW test bed to deposit the outside cap pass. The Hybrid laser-GMAW test bed utilises a 3 kW diode laser power source, a GMAW power source and wire feeder, and a lathe bed capable of motion with 2 degrees of freedom. The lathe provides a precise positioning system and controlled movement of work piece during welding. The test bed is shown in Figure 2-21.

The laser beam is delivered through an optical fibre into a 50mm collimator and a 200 mm final focus lens. A significant practical advantage of utilising a diode laser in

combination with an optic fibre is the ability to easily position and move the laser source making it ideal candidate for industrial use and automation.

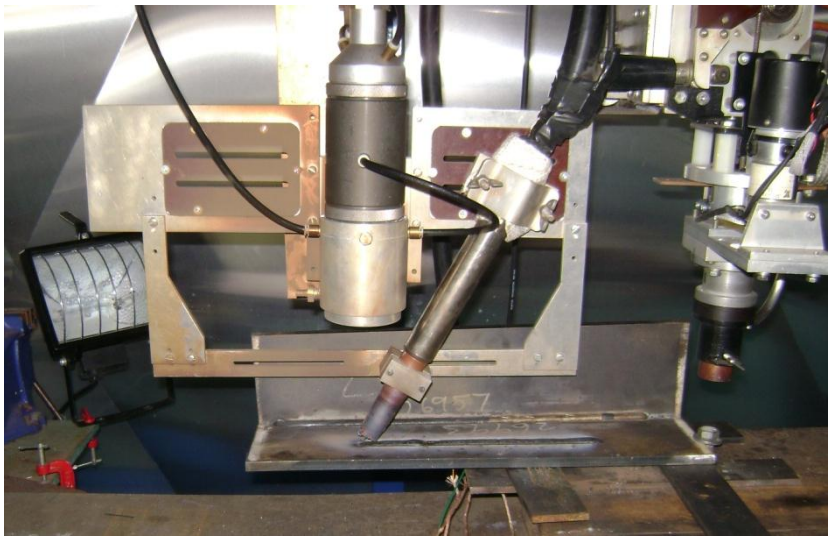

Figure 2-21 Hybrid laser-GMAW set-up.

2.5.2 Welding consumable

The hybrid laser-GMAW process utilised a solid wire consumable; SANDVIK 18.8 Mn complying with AWS A5.9 ER(307) – high Mn standard. Due to the total absence of flux the solid wire achieves the highest efficiency and avoids potential laser attenuation problems associated with the high fume rates of flux cored wires. The joint configuration requires deep penetration and the use of the cored wire could also result in entrapment of the slag in the weld root. The SANDVIK 18.8 Mn is a gas shielded wire designed for welding in downhand position. In this work it was used in combination with BOC Stainshield shielding gas consisting of 1.5% O_2 in argon.

Table 2-11 Typical all weld metal chemical composition of solid austenitic stainless steel consumable SANDVIK 18.8 Mn.

Consumable	**Chemical elements in [wt%]**						
	C	Mn	Si	Cr	Ni	S max	P max
SANDVIK 18.8 Mn	0.07	6	0.8	18	8	0.009	0.01

Table 2-12 Typical mechanical properties of weld metal deposited with solid austenitic stainless steel wire SANDVIK 18.8 Mn.

Consumable	**Mechanical property**				
	YS [N/mm^2]	UTS [N/mm^2]	Elong. [%]	Red. of area [%]	Charpy impact @ 20°C [J]
SANDVIK 18.8 Mn	462	648	41	61	130

2.5.3 Methodology of investigation of feasibility of hybrid laser-GMAW for welding HHA

Weld test sections were prepared by tacking 300 x 100 x 8.5 HHA test plates, with the specified geometry parameters, on the inside corner. It is to be noted that test plates were sectioned using water jet cutting and no edge preparation was done prior to welding. The inner pass was deposited first followed by the outer cap pass.

Initial testing was conducted to understand the capability and limits of the testing infrastructure. The following work focused on optimisation of the process and joint geometry parameters to obtain full penetration and good fusion in the welded joint. The welding parameters common to all trials are presented in Table 2-13.

Table 2-13 Hybrid laser-GMAW parameters common to all welding trials.

Welding parameter	**Value**
Laser power	3 kW
Hybrid Laser-GMAW filler material	ø1.2 mm solid austenitic stainless steel wire
Hybrid Laser-GMAW shielding gas	1.5% O_2 in Ar at 20 l/min
Hybrid Laser-GMAW voltage	30 V
Laser focal point	2 mm under plate surface
GMAW filler material	ø1.2 mm solid austenitic stainless steel wire
GMAW shielding gas	1.5% O_2 in Ar at 20 l/min
GMAW voltage	26.3 V
GMAW wire feed speed	9.5 m/min

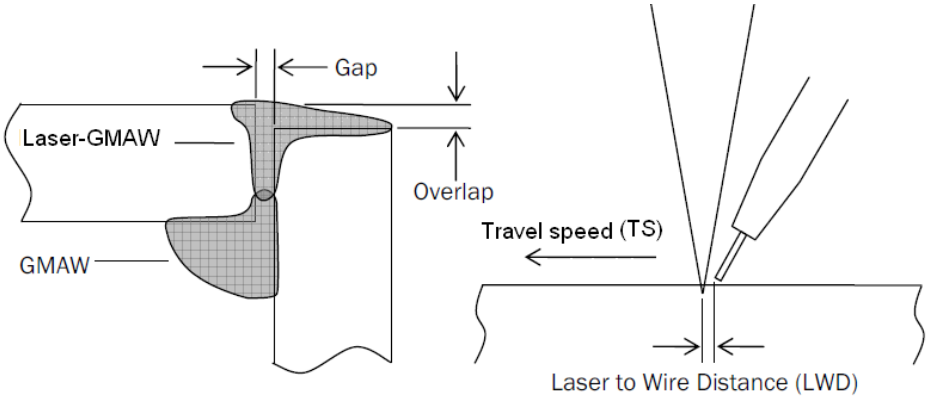

Figure 2-22 Diagram of experimental parameters subjected to optimisation.

2.5.4 Metallography and hardness testing

Samples for metallographic examination and hardness testing were prepared in the same manner as for the single pass fillet welds described in section 2.4.1.3. The orientation of hardness measurements is schematically shown in Figure 2-23. The indentations were also located 0.5 mm apart to provide information about the hardness variations across the HAZ.

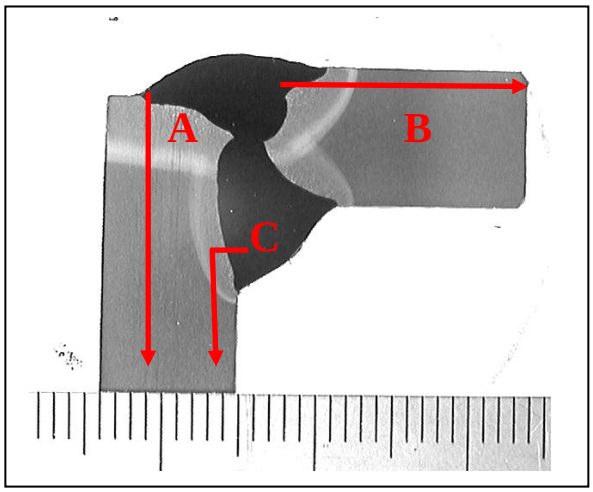

Figure 2-23 Orientation of the hardness testing measurements for 2 pass corner welds deposited employing hybrid laser-GMAW process in combination with solid consumable.

2.6 HYDROGEN TESTING

The objective of the hydrogen testing was to investigate the difference in hydrogen distribution when ferritic and austenitic consumables were used, the effect of preheat (PH) and type of GMAW wire (flux-cored, metal-cored and solid) on weld hydrogen levels.

2.6.1 Deposition of weld beads onto test piece assembly

Samples were wire-cut from HHA plate. The dimensions of run-on, run-off pieces were 15 x 45 x 9 mm and centre piece 15 x 30 x 9 mm. Prior to welding samples were ground and degreased to remove the surface corrosion and scale resulting from shot blasting.

Robot controlled GMAW was utilised to deposit single weld beads onto the test piece assembly clamped in the copper jig. The design of the welding jig is shown in Figure 2-24. Samples were not degassed prior to welding (as required in the relevant standard) in order to simulate the real welding conditions in industry. Preheating was carried out utilising an electric resistance heating blanket and undercooling of the test piece assembly to 7°C was achieved using dry ice (solid CO_2). After deposition of the weld beads, samples were quenched in stirred iced water and transferred in to the bath of liquid nitrogen. Samples were observed for uniform heat-tinting on the reverse side of the test piece assembly and the total length and centre piece to weld crater distance were measured. The run-on and run-off pieces were broken off and the centre piece was thoroughly cleaned with a steel wire brush. The intervals spent outside the liquid nitrogen did not exceed 15 s.

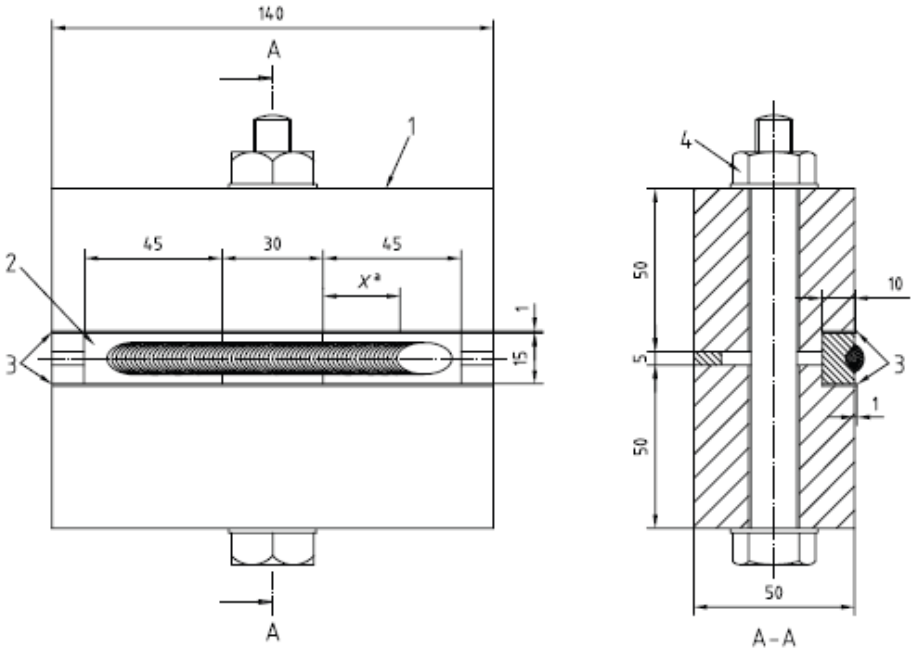

Figure 2-24 Welding fixture and test piece assembly for weld deposits made with heat inputs less than 2 kJ/mm used in this investigation. 1 – copper block; 2 – test piece assembly; 3 – copper foil, 4 – M12 bolt. Note: the dimensions are in mm.

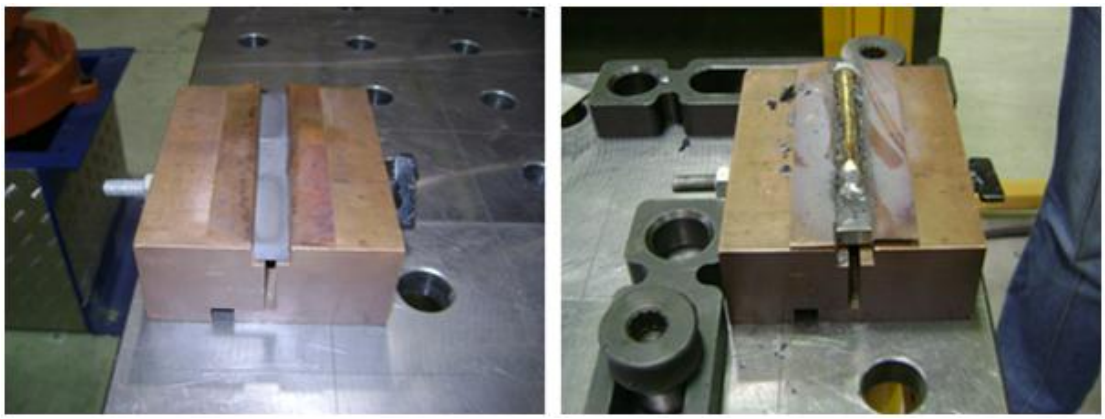

Figure 2-25 a – welding fixture with test piece assembly before the deposition of the single weld pass; b – welding fixture with test piece assembly immediately after deposition of test run with flux-cored consumable.

Recording of welding data

All welding data were recorded on the welding procedure sheets. Parameters that were kept constant for all trials are presented in Table 2-14. As the testing was carried out during the time period of three months and the weather conditions were changing, the

relative humidity was measured before every welding trial using a wet and dry thermometer.

Table 2-14 Welding parameters common to all welding trials.

Welding parameter	**Value**
Travel speed	400 mm/min
Wire feed speed	9.5 m/min
Stick out	16 mm
Voltage	26.3 V
Polarity	DC+
Wire diameter	1.2 mm

2.6.2 Diffusible hydrogen testing

Various test methods for determination of diffusible hydrogen content were reviewed. The 'Reference test method' - collection of hydrogen over mercury was selected to measure the diffusible hydrogen content present in the weldments. The gas collection apparatus is shown in Figure 2-26. Testing was performed according to the AS/NZS 3752:2006 standard with few minor modifications. Every test was repeated three times for consistency. The first series of experiments was carried out two times in order to test the welding as well as hydrogen measurement apparatus and develop the skill needed to perform the experiments and secondly to gain the confidence in repeatability of the testing.

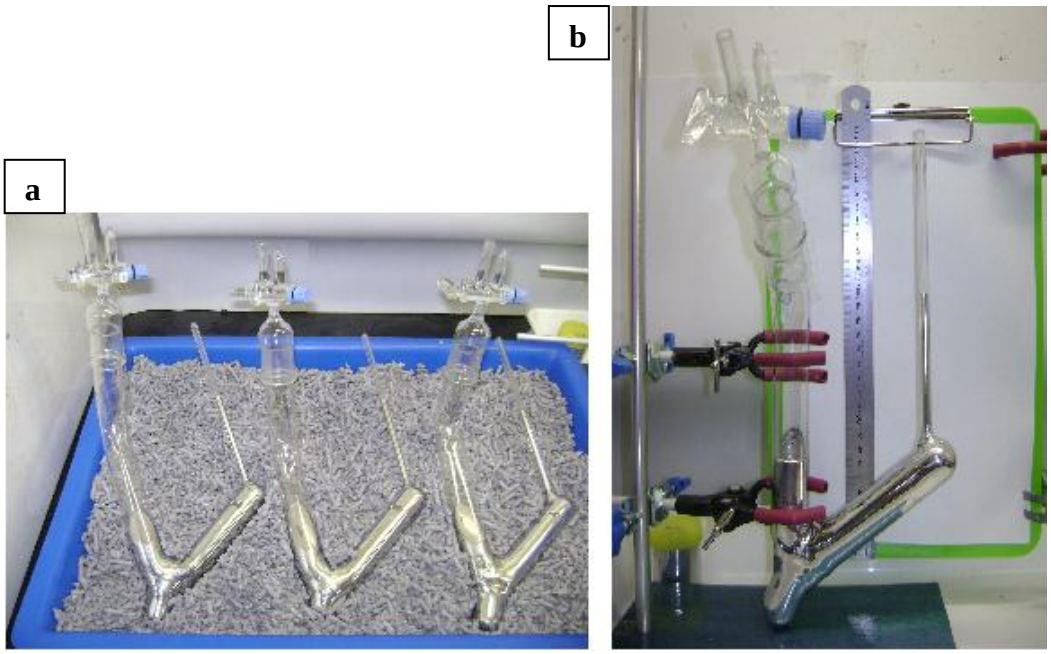

Figure 2-26 a – Centre test pieces submerged in mercury in evacuated Y-tube. Three tests welded under the same conditions running at the same time; b – Erected Y-tube during measuring the volume of evolved hydrogen (hydrogen can be seen in the capillary tube).

Before transferring the test samples from liquid nitrogen into the y-tube containing mercury and evacuating the inner space, samples were placed into an acetone bath, allowed to rise to room temperature and dried with a jet of air. Samples were left undisturbed in the y-tube for 7 days at room temperature (around 20°C) to allow the majority of diffusible hydrogen to evolve and collect in capillary tube. The readings of atmospheric temperature and pressure were taken every day prior to measuring the volume of hydrogen. The volume of the evolved hydrogen was corrected to standard temperature and barometric pressure measured and calculated by the equation:

$$V = \frac{273(P - H)(\pi r^2 C)}{760(273 + T)100} \tag{2.1}$$

where: V – volume of collected hydrogen at STP in millilitres; P – barometric pressure in mm of Hg; H – is the differential head of mercury between the two limbs of the y-tube in mm; C – length of the gas column above the mercury in mm; r – inner

radius of capillary tube in mm; T – ambient temperature at the time of hydrogen measurements in °C.

The weight of the centre test pieces was determined before the deposition of the weld bead (m_1) and also after completion of diffusible hydrogen testing (m_2) to nearest 10mg.The volume of diffusible hydrogen H_D in ml at STP per 100 g of WM was calculated from the equation:

$$H_D = V\frac{100}{(m_2 - m_1)} \tag{2.2}$$

2.6.3 Residual hydrogen testing

Various test methods for determination of residual hydrogen content were reviewed. The inert gas melt extraction method was selected because it is fast, it has shown very good reliability, and it is used by the DMTC project partner BluescopeSteel and is thus relatively easily accessible. Testing was carried out according to the AS/NZS 1050 standard. The total hydrogen testing facility is shown in Figure 2-27.

After completion of diffusible hydrogen testing, three slices transverse to the longitudinal axis of each centre piece were sectioned utilising a precision cutting machine. The weld metal was separated from the rest of the sample using a grinding wheel. In between grinding steps, samples were cooled in water to prevent heating of the sample due to the friction and possible loss of residual hydrogen. The resultant samples of WM of approximately 1g were washed in acetone, dried and subjected to residual hydrogen testing utilising an Eltra ONH-2000.

Figure 2-27 Eltra ONH-2000 - Inert gas melt extraction test facility at BluescopeSteel.

During the test samples were heated to melting temperature to release all residual (in case of ASS WM residual hydrogen = diffusible hydrogen in austenite fcc lattice + hydrogen trapped in strong traps) hydrogen, which was transported by carrier gas to the analyser to determine its quantity in ppm. The volume of residual hydrogen in ppm was converted to ml/100 g of WM considering "normal" atmospheric pressure of 101325 Pa and temperature of 20°C.

Conversion of ppm to ml of hydrogen per 100g of WM

$$m = 1ppm\ of\ H = 0.1mg\ of\ H\ in\ 100g\ of\ WM \tag{2.3}$$

$$V[ml\ of H\ per\ 100g\ of\ WM] = {}^{m}/_{\rho} \tag{2.4}$$

where: V = volume of the gas, m = weight of the gas, ρ = density of the gas.

Density of hydrogen was calculated from the Equation of state of ideal gas:

$$pV = NkT \tag{2.5}$$

where: p = atmospheric pressure, N = number of particles in the gas, k = Boltzmann constant = 1.38×10^{-23} N.m.K^{-1} and T = temperature.

The formula for calculation of the number of particles:

$$N = nN_A = {}^{m}/_{M_m N_A} \tag{2.6}$$

where: n = amount of substance, N_A = Avogadro constant = 6.03×10^{23} mol^{-1}, M_m = molar mass.

Then,

$$pV = {}^{m}/_{M_m R_m T} \tag{2.7}$$

where: R_m = molar gas constant = 8.316 N.m.K^{-1}mol^{-1}.

Then, the density of hydrogen can be calculated:

$$\rho = {}^{m}/_{V} \rightarrow \rho = {}^{pM_m}/_{R_m T} \tag{2.8}$$

2.6.4 Experimental theory

<u>The level of diffusible hydrogen in weld HAZ welded with ferritic and ASS consumable</u>

The aim of this series of tests was to demonstrate that the measured amount of diffusible hydrogen in the case of ferritic filler is much higher than when an ASS filler is used indicating that hydrogen is safely “locked” in ASS WM and thus cannot diffuse into the susceptible HAZ.

Samples were produced using austenitic flux-cored wire TETRA S 20.9.3 (AWS A5.22 E308 MoT1) and ferritic flux-cored wire VERTICOR 3XP (AWS A5.20 E71T-1). VERTICOR 3XP was selected because it possesses the same rutile flux type as TETRA S and type of flux used in cored wires is one of major factors influencing the level of hydrogen in WM and also its diffusivity. To be able to compare the difference in hydrogen level introduced into the weld pool with ferritic and ASS consumables, samples were quenched immediately after extinction of the welding arc to retain the maximum amount of hydrogen in the structure. The WM residual hydrogen was measured to demonstrate that ASS wire also introduces certain level of hydrogen into the weld pool but this becomes effectively trapped in WM fcc lattice and strong traps, whereas in case of ferritic filler the WM hydrogen level is very low, confirming that majority of the introduced hydrogen diffused through bcc / bct lattice out of the weldment / into the HAZ.

To prove that the total hydrogen measured during diffusible hydrogen testing originates from the HAZ, a series of ASS weld beads were deposited onto ASS PM (ASS 304) and samples were also subjected to both diffusible and residual hydrogen testing.

<u>The level of diffusible hydrogen in weld HAZ of the samples welded with flux-cored ASS consumable under different PH conditions</u>

The aim of this series of testing was to investigate the effect of PH temperature on level of diffusible hydrogen in the HAZ.

Samples were produced using austenitic flux-cored wire TETRA S 20.9.3 (AWS A5.22 E308 MoT1). The first trials were deposited at an ambient PH (20°C). For the second series, the test pieces assembly together in the welding fixture were preheated to 80°C. An initial temperature of 7°C was also selected to test extremes of temperature under winter conditions. After extinction of the welding arc, samples were removed from the welding fixture, placed onto the positioning table and allowed to cool down to 150°C prior quenching to allow some hydrogen to diffuse out of the weldment. A contact thermometer (as shown in Figure 2-28) was utilised to monitor the temperature of the cooling weldmnets.

Figure 2-28 Contact thermometer used to monitor the temperature of the cooling welds. Note: photograph was taken during test trial. During actual valid trials the sample was removed form the welding fixture immediately after extinction of welding arc.

The level of diffusible hydrogen in weld HAZ welded with 3 different types of ASS consumable, namely flux-cored, metal-cored and solid.

The aim of this series of testing was to study the effect of different types of ASS consumable on the weld hydrogen content.

Samples were produced using three types of austenitic stainless steel wire: flux-cored wire TETRA S 20.9.3 (AWS A5.22 E308 MoT1), metal-cored wire VEGA 20.9.3-G (AWS A5.9 EC308Mo) and solid wire SANDVIK 18.8 Mn (AWS A5.9 ER(307)). Samples were allowed to cool down to 150° prior quenching.

2.7 EVALUATION OF RESIDUAL STRESSES

Residual stresses are one of the factors contributing to HACC as the diffusible hydrogen is attracted to the locations of tensile triaxial stresses. These stresses are fixed displacement stresses that remain in the weldment after removing all external forces. The investigation described in following section utilises assumption that the distortion of the corner joint configuration is related to the level of residual stresses which exceed the yield strength of the material resulting form welding. The objective

of the conducted testing was to assess the effect of the level of preheat on the magnitude of resultant residual stresses. Due to the weld geometry (corner joint), relatively short length of the plates to be welded (300 mm with 250 mm long weld deposit) and relatively high thickness (9 mm) of the HHA plates the angular distortion was considered to be the main mode of distortion resulting from welding. Angular distortion is a result of transverse thermal contraction stresses leading to rotation of one plate of the corner joint with respect to the second one [81].

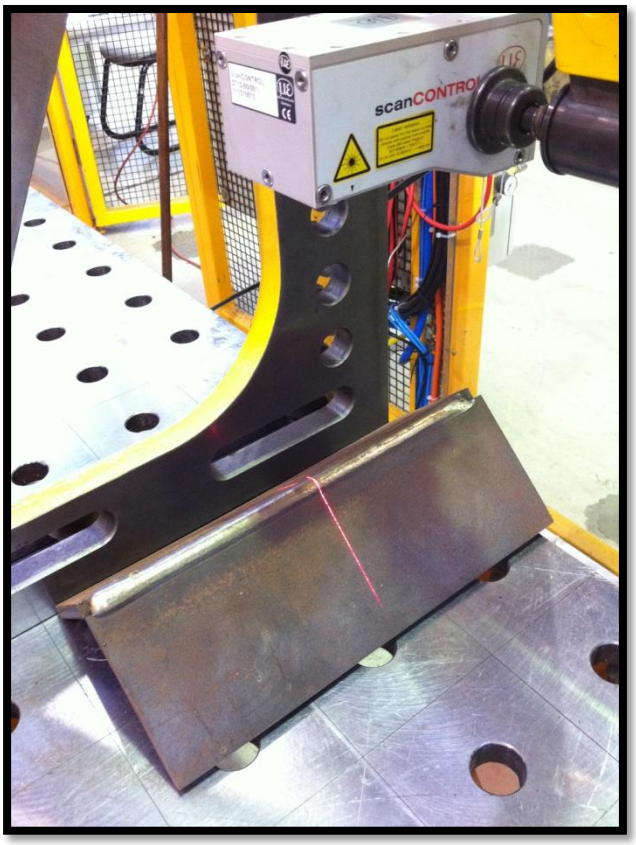

Figure 2-29 Laser profile sensor scanning the surface profile of the weldment.

For this testing a 5-pass corner joint configuration was selected as shown in Figure 2-8 – a. The weldments were produced simulating the 1st pass of the welding procedure provided by industry partner described in Table 2-9 employing flux-cored austenitic stainless steel consumable and preheats of 80°C and 21°C (ambient). To ensure good accuracy and repeatability welding trials employing both levels of preheat were performed three times. The required 90° corner weld geometry (refer to Figure 2-8 – a) was achieved using number of angles and fixtures. HHA plates were

tightly secured by a series of clamps to prevent any movement of the plates on cooling after welding. The clamps were released after the weldments reached ambient temperature and the weld geometry was scanned using laser profile sensor shown in Figure 2-29. The first step involved deposition of tack welds onto both ends of the inner corner of the HHA plates employing ambient preheat. The acquired surface profiles represented reference joint geometry. The second step involved deposition of the single weld pass onto the HHA plates preheated to 80°C and 21°C (ambient temperature). The surface profiles obtained were compared with the reference and the angular distortion was calculated using Microsoft Excel. The laser profiles consisted of 239 single points with defined by the coordinates in space. The trendline was added to the portion of points measured from the straight section of the weldment corresponding to HHA plates. The angle of the HHA plates was calculated from the equations of the lines representing the orientation of the two plates creating the corner joint.

3 RESULTS

3.1 CONTINUOUS COOLING TRANSFORMATION BEHAVIOUR OF HHA STEEL

Continuous cooling transformation (CCT) diagrams are a source of useful information about the transformation behaviour of particular austenitised steel subjected to various cooling rates. The transformation temperature range, resultant microstructure and hardness of steel can be directly determined from these diagrams. By selecting a suitable austenitisation temperature during the experiments these diagrams can become directly applicable to real welding conditions providing much needed knowledge to develop safe welding procedures. CCT information can be of great help when designing appropriate heat input, preheat temperature and postweld heat treatment to promote formation of microstructures with desired hardness within the weld HAZ. As mentioned before the alloy design of HHA steel was recently modified and CCT diagram has not been previously constructed for steel with this chemistry thus research carried out to construct CCT diagrams will expand the knowledge envelope about current HHA steel.

A series of thermal cycle simulations have been carried out with particular focus on the effect of cooling rate on microstructure and resultant hardness of HHA steel. The peak temperature of 1350°C was chosen to simulate the coarse-grain HAZ as in real welding conditions this zone is particularly susceptible to HACC. Collected data were analysed with respect to the close relation between imposed cooling rate and resultant type of microstructure.

The CCT diagram presented in Figure 3-2 was constructed based on the information acquired during heat treatment cycles in the dilatometer. The transformation start (Ts = Ar_3) and finish (Tf = Ar_1) temperatures and also transformation start temperature of second phase (Ts_2 in this investigation = Ms) for each cooling rate were determined and the hardness of the produced samples was measured and are graphically shown in CCT diagram and numerically in Table 3-1. Transformation start and finish temperatures decrease and hardness increases with increasing cooling rate as a result of formation of low temperature products. A common experimental error of ±25°C

should be allowed for when determining the transformation temperatures employing the dilatometry method [82]. The dilatation curve acquired for 1°C/s cooling rate is presented in Figure 3-1. The dilation curves for all nine cooling rates are shown in Appendix 3. Dilation curves at 5°C/s, 10°C/s and 20°C/s cooling rate show more complex features through transformation region as a result of formation of microstructure consisting of mixture of bainite and martensite products. The actual value of the dilation during transformation on cooling does not represent any phenomena since the expansion is relative to the dimensions of the sample that inherently varies. Transformation start and finish temperatures were determined by specifying the points where experimental curve deviate from linearity.

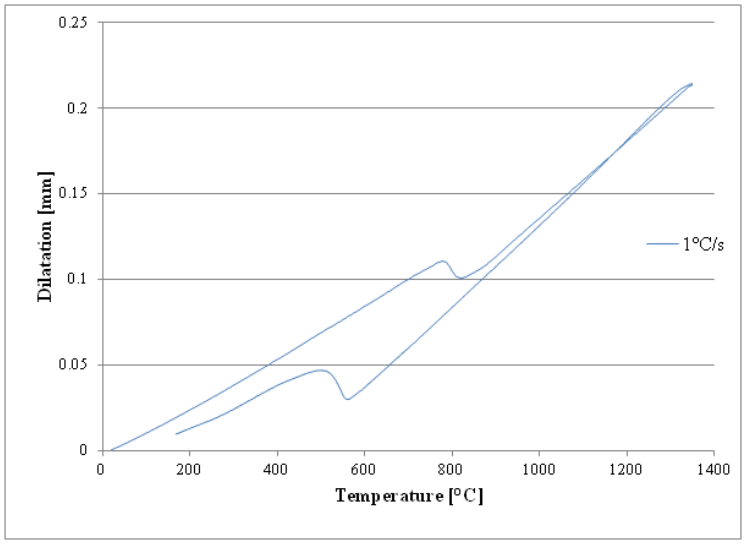

Figure 3-1 Dilatation curve of the sample subjected to heat treatment trial simulating 1°C/s cooling rate.

Applying the slowest cooling rate of 1°C/s produced a microstructure consisting of single phase - bainite with average hardness of 272 HV. This product started to form at temperature of 582°C and transformation finished when temperature of the sample dropped to 392°C/s. With increasing cooling rate to 5°C/s it was found that small amount of martensite already started to form at temperature of 328°C. This was represented by slight slope change on the dilation curve and small portion of martensite (approximately 5%) was also observed during microstructural investigation. The cooling rates from 5°C/s to 20°C/s produced microstructures containing mixture of bainite and martensite. The average hardness increased from

365 HV to 451 HV and 541 HV with increasing cooling rate from 5°C/s to 10°C/s and 20°C/s respectively. This together with data extracted from dilatation curves suggests that volume fraction martensite to bainite increased with increasing the cooling rate in this range. Martensite start temperature in the area of bainite and martensite on the CCT diagram initially increased from 328°C to 350°C with increasing cooling rate from 5°C/s to 10°C/s then slightly dropped to 344°C at 20°C/s cooling rate. The dilation curve corresponding to 30°C/s cooling rate suggests that transformation started at 404°C and finished at 221°C and did not exhibit any signs of the second transformation suggesting formation of only one phase – martensite. Also microstructure formed at this cooling rate appeared to be fully martensitic. However very small portion of bainite could still form at this cooling rate as dilatometry technique is not sensitive enough to detect formation of minute fractions of transformation products. Additional difficulty to recognise the negligible amounts of bainite arises from overlapping transformations regions of bainite and martensite. It is also very difficult to differentiate bainite from martensite using optical microscopy. A further increase in cooling rate produced single phase – martensite and both transformation start and finish temperatures formed a plateau.

Under real welding conditions depending on heat input and preheat temperature the HAZ typically experiences cooling rates in transformation region corresponding to the range of 20°C/s to 50°C/s presented on the CCT diagram. These cooling rates resulted in formation of low temperature transformation products consisting of mixture of hard phases including lower bainite and lath martensite with bainite rapidly diminishing from the structure with increasing cooling rate above 20°C/s.

3.1.1 Transformation temperature range and critical cooling rates

The transformation temperature range initially widens from 190°C at 1°C/s cooling rate to approximately 240°C at 5°C/s - 20°C/s cooling rates then drops back to around 180°C at 30°C/s with only minor changes with further increasing cooling rate. In the tested range of cooling rates HHA steel undergoes a $\gamma \rightarrow \alpha$ transformation at relatively low temperatures associated with formation of constituents promoting high hardness. The transformation start temperature initially slightly decreased with increasing

cooling rate from 1°C/s to 5°C/s from 582°C to 565°C following by more abrupt decrease with increasing cooling rate to 30°C/s to 403°C and then formed plateau with further increasing cooling rate to 200°C/s.

The plot of transformation start temperature for different cooling rates exhibits a plateau for each single constituent. The transformation start temperature initially decreases with increasing cooling rate reflecting the formation of multiple products then it flattens out. With further increase of cooling rate the critical cooling rate for formation of a new product occurs and is associated with a change of hardness. The critical cooling rate for bainite formation could not be determined as even slower cooling rates (that would have no practical use) would have to be employed. As it can be seen from the CCT diagram shown Figure 3-2 the investigated HHA steel has extremely high hardenability as the martensite was found to form even at relatively slow cooling rates such as 5°C/s. Based on the data from dilation curve and microstructural observation the critical cooling rate for martensite formation is most like to be at cooling rate slightly slower than 5°C/s. The martensite start temperature initially increases with increasing cooling rate and then plateaus out when the field of formation of the single martensitic phase is entered. This is due to carbon partitioning: during formation of high temperature products; untransformed austenite becomes oversaturated with carbon suppressing the martensite start temperature to lower range. The critical cooling rate for formation of 100% martensite is likely to occur around 30°C/s.

The Ms temperature is a crucial parameter characterising martensitic transformation in steels. For reference, the Ms temperature was calculated to be 372°C using the formula developed by Self et al. [49]. Calculated Ms_{HAZ} temperature of the HAZ in real welding condition is slightly lower than Ms temperature determined experimentally and presented in the CCT diagram. The calculated value reflects the non-uniform cooling during real welding conditions affecting the kinetics of the phase transformation.

$$Ms_{HAZ}\,[°C] = 521 - 350C - 14.3Cr - 17.5Ni - 28.9Mn - 37.6Si - 29.5Mo - 1.19Cr.Ni - 21.3(Cr + Mo).C \quad (3.1)$$

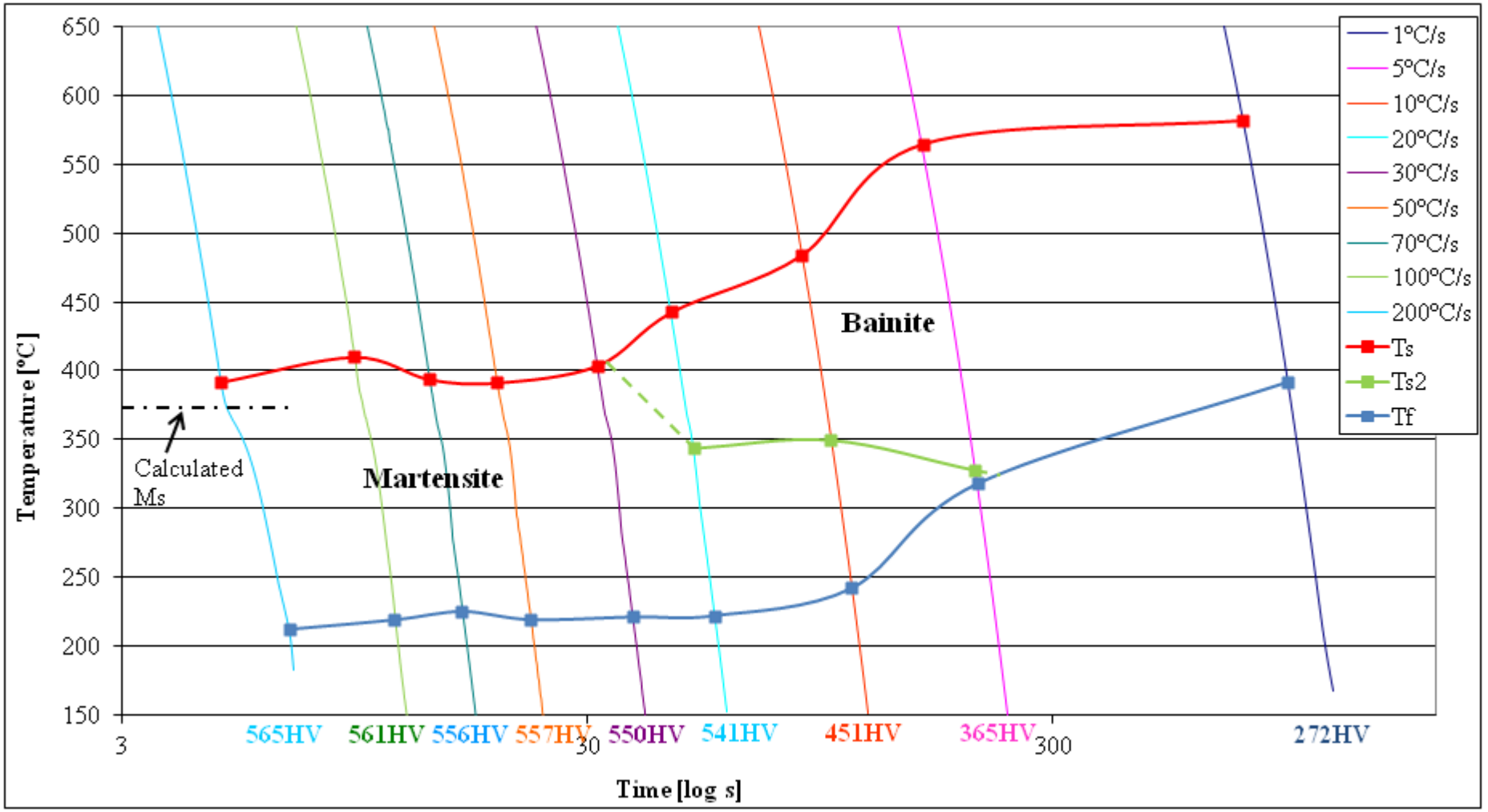

Figure 3-2 CCT diagram of the HHA steel showing transformation start (Ts = Ar3) and finish (Tf = Ar1) temperatures and also transformation start temperature of second phase (Ts2 in this investigation = Ms) as a function of cooling rate. Resultant hardness for each cooling rate is also displayed.

Table 3-1 CCT diagram data acquired from dilatation curves for HHA steel: cooling rate, cooling time $\Delta t_{600/200}$, Ar_3, Ar_1, calculated Ms and measured hardness.

Cooling rate [°C/s]	**Cooling time $\Delta t_{600/200}$ [s]**	**Ar_3 [°C]**	**Ts_2 [°C]**	**Ar_1 [°C]**	**HV 200g**
1	403.5	582		392	272
5	80.1	565	328	318	365
10	40.1	484	350	242	451
20	20.1	442	344	222	541
30	13.4	404		221	550
50	8	391		219	557
70	5.7	394		225	556
100	4.1	410		219	561
200	2.3	392		212	565
		Ms = 372°C			

3.1.2 Microstructural characterisation

Figure 3-4 displays the microstructures of dilatometry samples of HHA steel formed at all the cooling rates employed. The microstructure formed at slowest cooling rate of 1°C/s consisted mainly of upper granular bainite (ferritic bainite) with occasional randomly distributed grains of polygonal ferrite. Cooling rate of 5°C/s produced ferritic laths of upper bainite in lower bainite matrix with randomly distributed grains of quasi polygonal ferrite. Also martensite was observed in the structure formed at this cooling rate. Moving to faster cooling rate of 10°C/s proeutectoid ferrite was no longer present in the microstructure and ferritic laths of upper bainite diminished in favour of the formation of lower bainite and martensite. Very rare features of upper bainite (bainitic feathers) were still observed at a cooling rate of 20°C/s the formation of which was strongly suppressed in favour of a lower bainite - lath martensite mixture with increasing cooling rate. It is evident that increasing the cooling rate assisted formation of harder structures and microstructural features became finer. A fully martensitic structure was obtained at cooling rates faster that 30°C/s as seen in Figure 3-4 f, g, h and i. Due to the carbon content of 0.3 wt% martensite with primarily lath morphology was formed. Lath martensite contains negligible amount of residual austenite compared to higher carbon

plate and butterfly morphology thus it is expected that the martensite transformation was almost completed resulting in only marginal amount of residual austenite. Large grains similar to those found in the coarse-grained heat affected zone (CGHAZ) in real welding conditions were observed in the microstructure formed under all cooling rates.

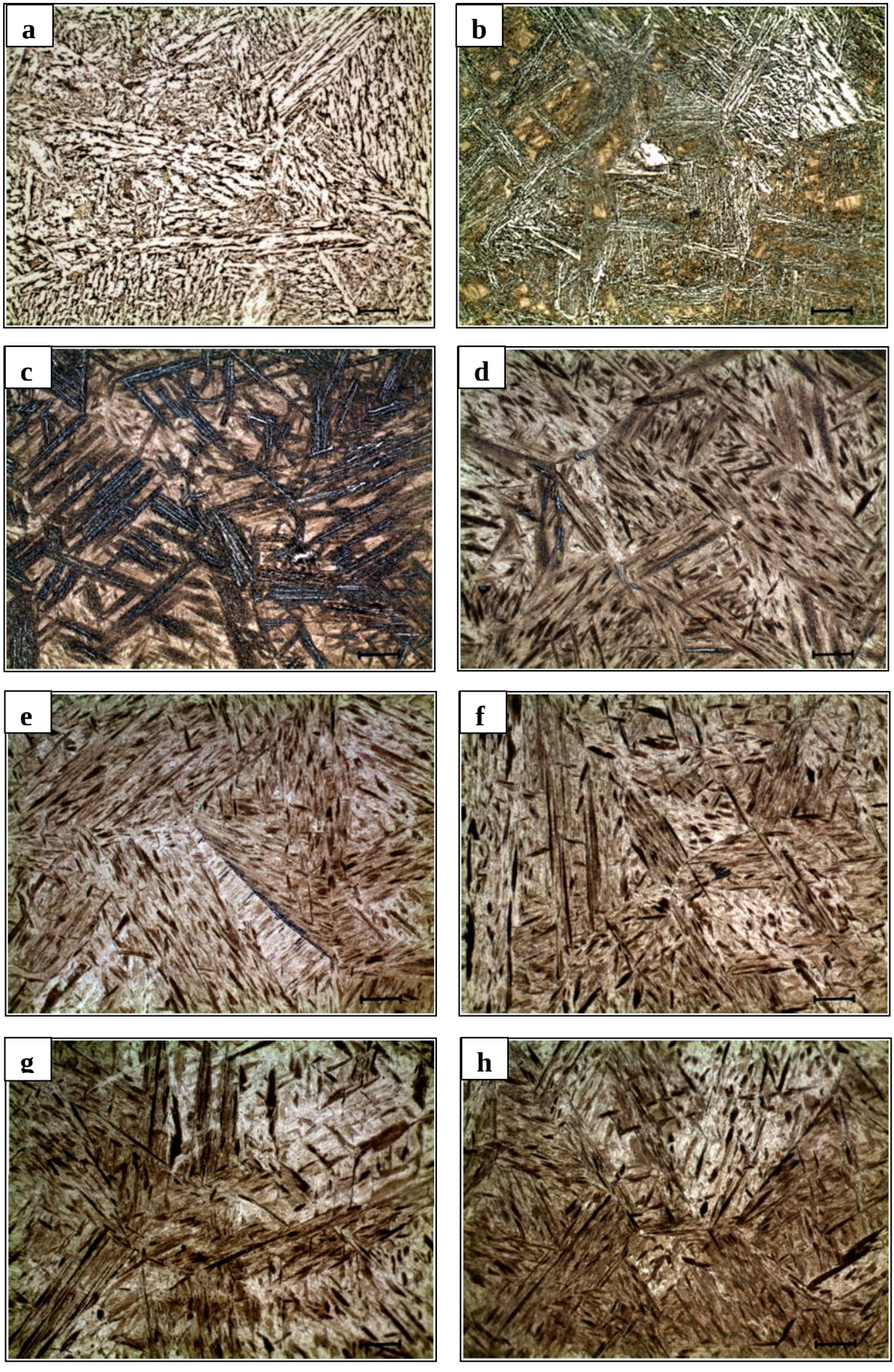
a
b
c
d
e
f
g
h

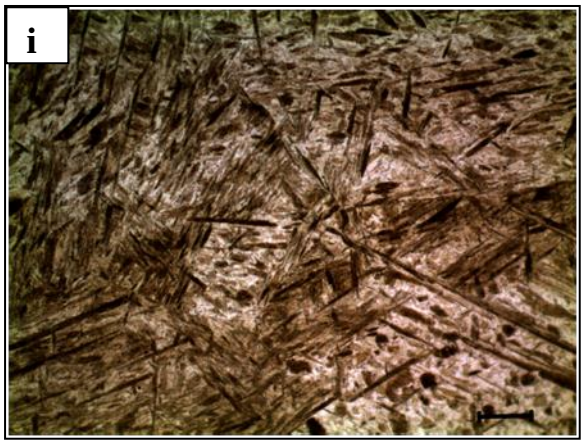

Figure 3-4 Typical microstructures of HHA dilatometer samples formed under different cooling rates: a – 1°C/s, b – 5°C/s, c – 10°C/s, d – 20°C/s, e – 30°C/s, f – 50°C/s, g – 70°C/s, h – 100°C/s and i – 200°C/s. Samples were austenitised at 1350°C for 2 seconds before cooling. Micron bar represents 20 μm.

3.1.3 Hardness of dilatometry samples

Figure 3-5 shows the relationship between the hardness of the dilatometry samples and cooling rate. Initially the hardness rapidly increased from 272 HV to 550 HV with increasing cooling rate from 1°C/s to 30°C/s. This was due to the formation of softer microstructures (ferritic bainite formed at cooling rates of 1°C/s and 5°C/s) being replaced by the development of hard phases (lower bainite + lath martensite formed at cooling rates of 10°C/s and 30°C/s) as a consequence of increased cooling rate. Further increase in cooling rate resulted in a hardness plateau with only very slight hardness increase of 15 HV with increases in the cooling rate from 30°C/s to 200°C/s. The fastest cooling rate of 200°C/s produced a fully martensitic microstructure possessing a hardness of 565 HV. Correspondence between hardness and transformation temperature was also observed. The transformation temperature was found to decrease, while hardness increased with increasing cooling rate from 1°C/s to 30°C/s. With further increasing cooling rate both characteristics formed a plateau

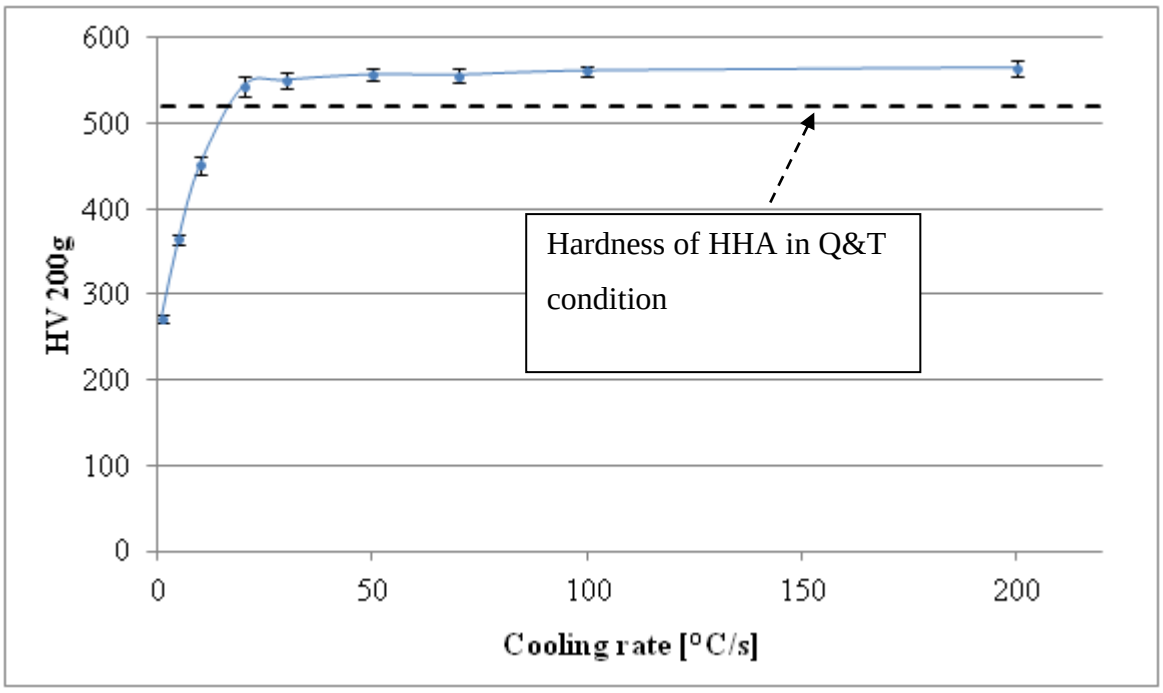

Figure 3-5 Hardness of dilatometry samples as a function of imposed cooling rate. Broken line represents average measured hardness HV of HHA steel in Q&T condition.

3.2 GMAW WELDING TRIALS

The following section details the results of investigations that have been undertaken to understand and quantify the effects of varying pre-heating and interpass temperatures during the welding of both fillet joints and multi-pass corner joints of high hardness armour steel by the conventional gas metal arc welding process employing flux-cored and metal-cored austenitic stainless steel consumable. Fundamental testing and analysis including weld thermal history, hardness and metallurgical assessments have been undertaken.

3.2.1 Weld thermal history

The microstructure formed in the HAZ and consequently mechanical properties are a function of the thermal cycle experienced during welding. Hence it is important to measure the thermal history in the crucial zones of the weldment. One of the objectives of this research project was to investigate the effect of lowering preheat temperature on susceptibility of HHA steel to HACC. The area of particular interest was coarse-grain HAZ therefore the aim was to acquire thermal cycle experienced by this region.

Figure 3-6 displays the measured thermal cycles experienced by the coarse-grained HAZ of the bead on plate welds deposited employing flux-cored consumable and preheat levels of 7°C, Ambient (21°C) and 80°C. It is well established fact that the coarse-grain HAZ typically experiences temperatures of 1200°C - 1450°C [19]. The measured peak temperature during the three trials was in the range of 1349°C to 1411°C confirming that the acquired thermal history was that of the coarse-grain HAZ. The most important part of the thermal history is the cooling leg which influences the resultant microstructure, diffusible hydrogen level and also the residual stresses formed as a consequence of welding process.

The cooling time from 800°C to 500°C (t8/5) is usually selected to define the critical cooling cycle of a weldment. The susceptibility to HACC for various heat inputs and preheat conditions is often assessed based on this parameter. This temperature range corresponds to the $\gamma \rightarrow \alpha$ transformation region on cooling from welding peak temperature for most C-Mn steels. For a given heat input t8/5 increases with increasing preheat temperature. If it is not practical to measure the t8/5 experimentally there are a number of formula available to determine this cooling time through calculation [83, 84]. The accuracy of the prediction models varies depending on variables accounted for in the method and also correctness of the welding efficiency factors considered for different welding techniques. However the continuous cooling transformation investigations of the HHA steel revealed that transformation of the HHA steel examined here occurs in the temperature interval of 600°C to 200°C. Therefore a cooling time t6/2 more accurately represents cooling conditions crucial for evolution of microstructure. The hydrogen diffusion is the most active at high temperatures but continues to take place at lower temperatures at slower rate. HACC typically occurs when temperature of the weldment drops below 200°C; therefore overall cooling time from the peak temperature to 100°C (tp/1) most precisely describes the conditions for hydrogen diffusion.

Cooling time (t8/5), (t6/2), average cooling rate through 800°C to 500°C temperature range and overall cooling time to 100°C (tp/1) were determined from the acquired cooling curves. The values of these parameters are presented in Table 3-2.

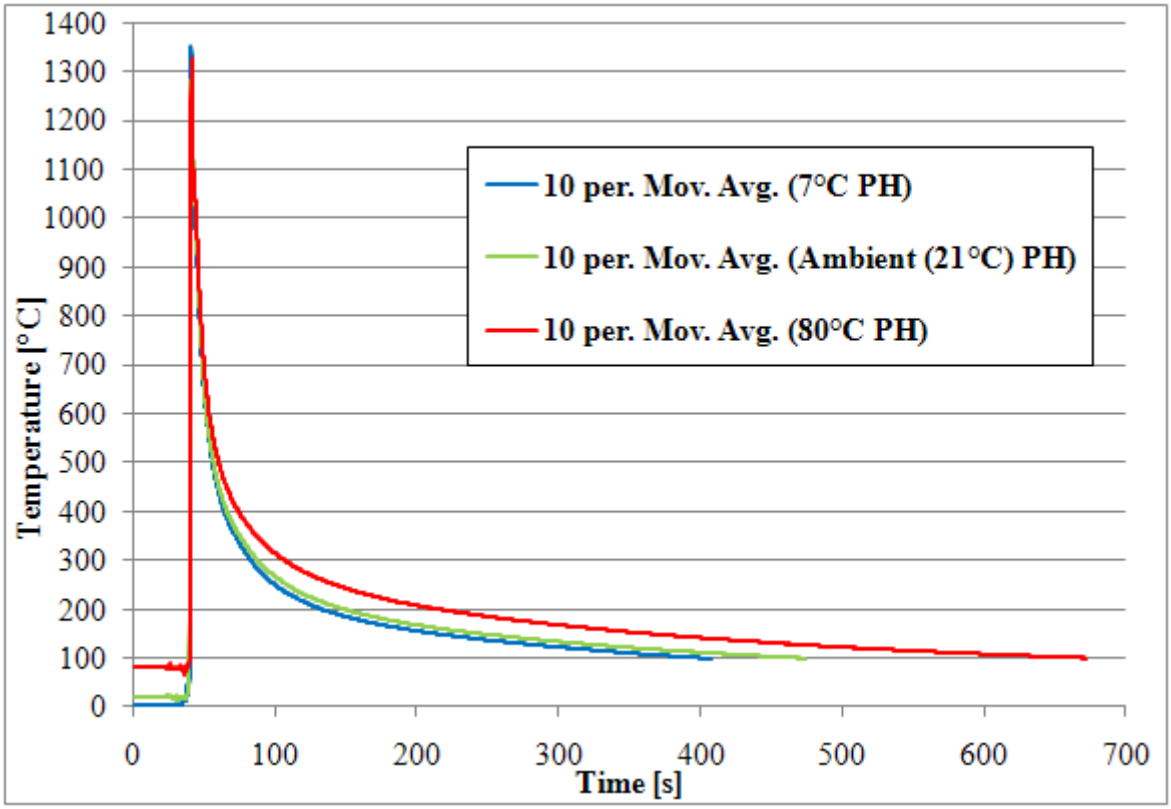

Figure 3-6 Weld thermal history of coarse-grain HAZ of HHA steel measured during deposition of bead on plate welds employing 7°C, Ambient (21°C) and 80°C.

Note: Abbreviation "10 per. Mov. Avg" in the legend means that data sets have been smoothed by a moving average of ten. This was necessary to achieve smooth profile because portion of the temperature data was acquired while welding was in progress what interfered with the data acquisition equipment causing relatively large scatter. The data acquisition rate was 100 Hz. These conditions apply to all thermal history measurements.

Table 3-2 Cooling cycle characteristics (cooling time t8/5, t6/2 average cooling rate through 800°C - 500°C, and tp/1) measured for coarse-grain HAZ of HHA weldments preheated to 7°C, Ambient (21°C) and 80°C.

Preheat temperature [°C]	**t8/5 [s]**	**Average cooling rate (800°C - 500°C) [°C/s]**	**t6/2 [s]**	**tp/1 [s]**
7	9	32	81	353
23 (ambient)	9.7	31	97	410
80	12.6	24	159	608

From data presented in Figure 3-6 and Table 3-2 it is obvious that increasing preheat temperature results in longer cooling times and slower cooling rates through the whole course of cooling. The value of conventional parameter describing the cooling conditions t8/5 increased from 9.3 s to 12.6 s with increasing the preheat temperature from 7°C to 80°C. Also average cooling rate in the temperature range of 800°C - 500°C decreased from 32 °C/s to 31 °C/s and 24 °C/s moving from 7°C to ambient (21°C) and 80°C preheat temperature respectively. The cooling time through the transformation region of HHA steel t6/2 doubled with increasing the level of preheat from 7°C to 80°C. The overall cooling time from peak temperature to 100 °C tp/1 increased by 72% with increasing the level of preheat from 7°C to 80°C. For the range of preheat levels investigated it was found that cooling times t8/5, t6/2 and tp/1 increased linearly with increasing preheat temperature as it can be seen from Figure 3-7.

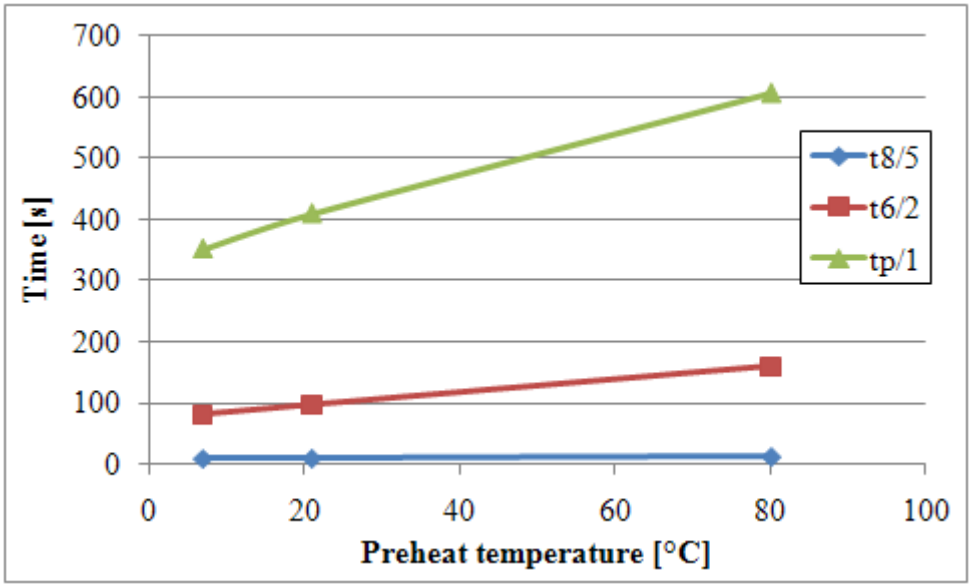

Figure 3-7 Cooling times t8/5, t6/2 and tp/2 as a function of preheat temperature.

3.2.2 Optimisation of preheat temperature

To study the effects of lowering preheat temperature on the microstructure and resultant hardness of the HHA weldments, a single weld pass was deposited in a fillet joint configuration employing preheats from 80°C to Ambient (22°C) in 20°C decrements. Due to the possibility of lower ambient temperatures experienced at the manufacturing plant during winter periods the weldments were also produced simulating ambient temperature of around

7°C. To ensure consistency and repeatability of the results, all trials involving preheat temperatures lower than the industry standard were repeated two times for both flux-cored and metal-cored ASS consumable. Samples subjected to microstructural investigation and hardness testing were sectioned from the middle of the 300mm long welded plates where stable welding conditions were obtained.

The macrographs of the cross-sections of the weldments deposited with flux-cored and metal-cored consumable employing welding parameters described in Table 2-8 are presented in Figure 3-8 and Figure 3-9 respectively. From the macrographs a gradual slight decrease in HAZ width with lowering preheat temperature may be observed.

The metal-cored consumable produced joints with significantly deeper penetration compared to flux-cored consumable. This is due to different composition of the core of the two wires, the metal-cored lacking the flux and containing higher powdered metal to additives and arc stabilisers ratio, requires higher energy density to melt the consumable resulting in deeper penetration. In addition the shielding gas used for the metal cored wire is known to produce a 'wine glass' type penetration. The metal-cored consumable also has improved deposition efficiency compared to flux-cored filler. For welding trials utilising the metal-cored consumable, travel speed was increased and wire feed speed decreased to match the bead geometry and to achieve identical heat input conditions for joints produced with both consumables.

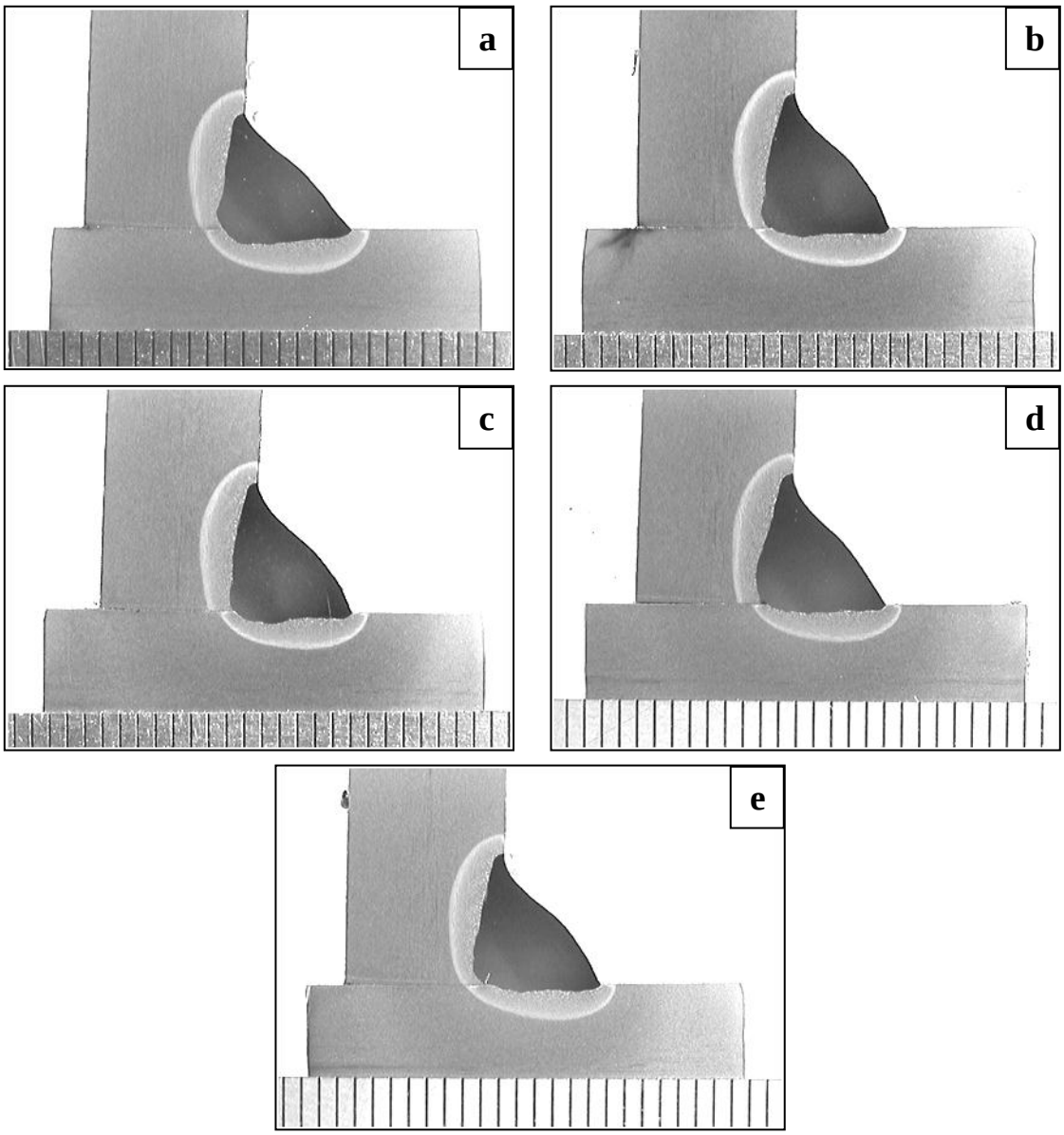

Figure 3-8 Macrophotographs of the 1 pass fillet welds deposited with flux-cored consumable under various preheat conditions; a - 80°C PH, b – 60°C PH, c - 40°C PH, d - Ambient (22°C) PH, e - 7°C PH. Note: scale is in millimetres.

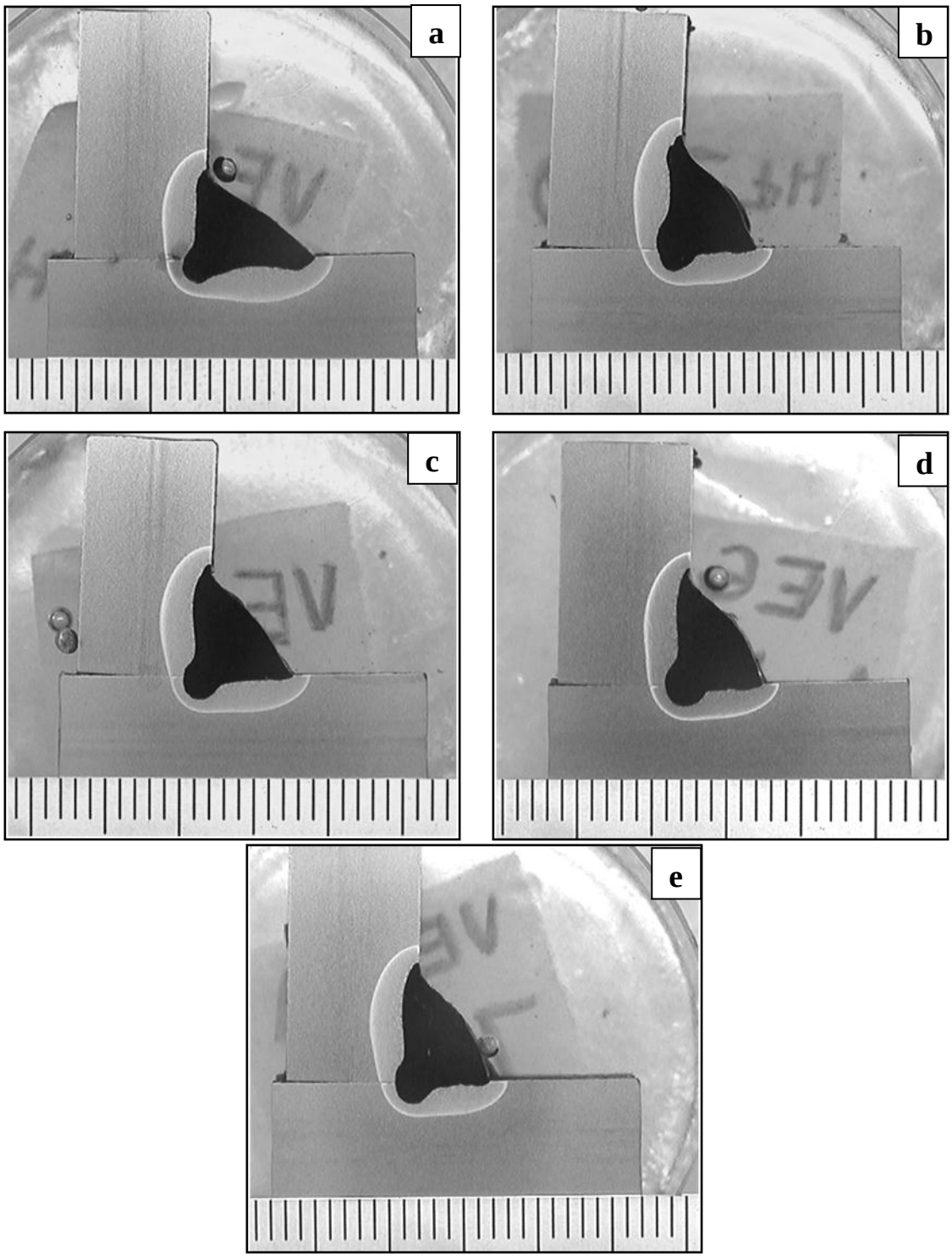

Figure 3-9 Macrophotographs of the 1 pass fillet welds deposited with metal-cored consumable under various preheat conditions; a - 80°C PH, b – 60°C PH, c - 40°C PH, d - Ambient (22°C) PH, e - 7°C PH. Note: scale is in millimetres.

3.2.2.1 Weld thermal history

During welding trials weld thermal history was recorded for all preheat temperatures and for both selected consumables.

Figure 3-10 and Figure 3-11 show the weld thermal history of the single pass fillet welds deposited with flux-cored and metal-cored consumable respectively. As expected and evident from the graphs the cooling rate decreased and cooling time increased with increasing preheat temperature. It is to be noted that the subject of the present study was not to record thermal history directly in the weld metal or HAZ. That is also evident from the location of the thermocouples (refer to Figure 2-13). Temperature was recorded to ensure high precision of the preheating plates to target temperature and thermal history of the welds was acquired to provide comparative information about the effects of various levels of preheat on overall cooling rate and cooling times of the welded joints.

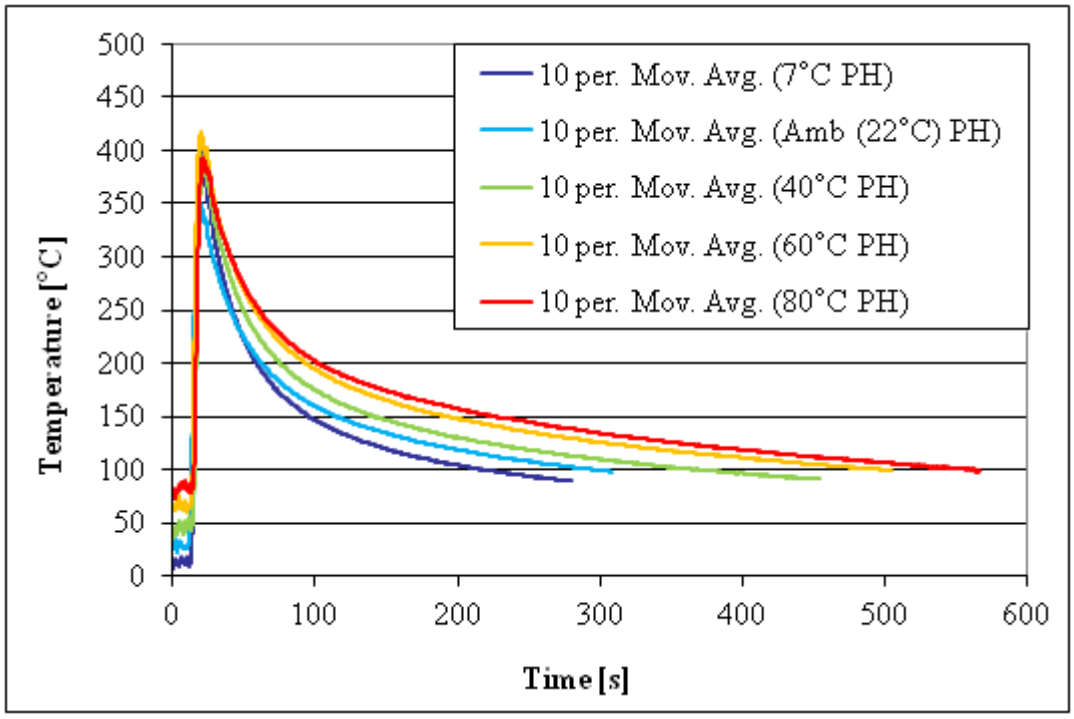

Figure 3-10 Thermal history of the 1 pass filet weldments welded with flux-cored consumable.

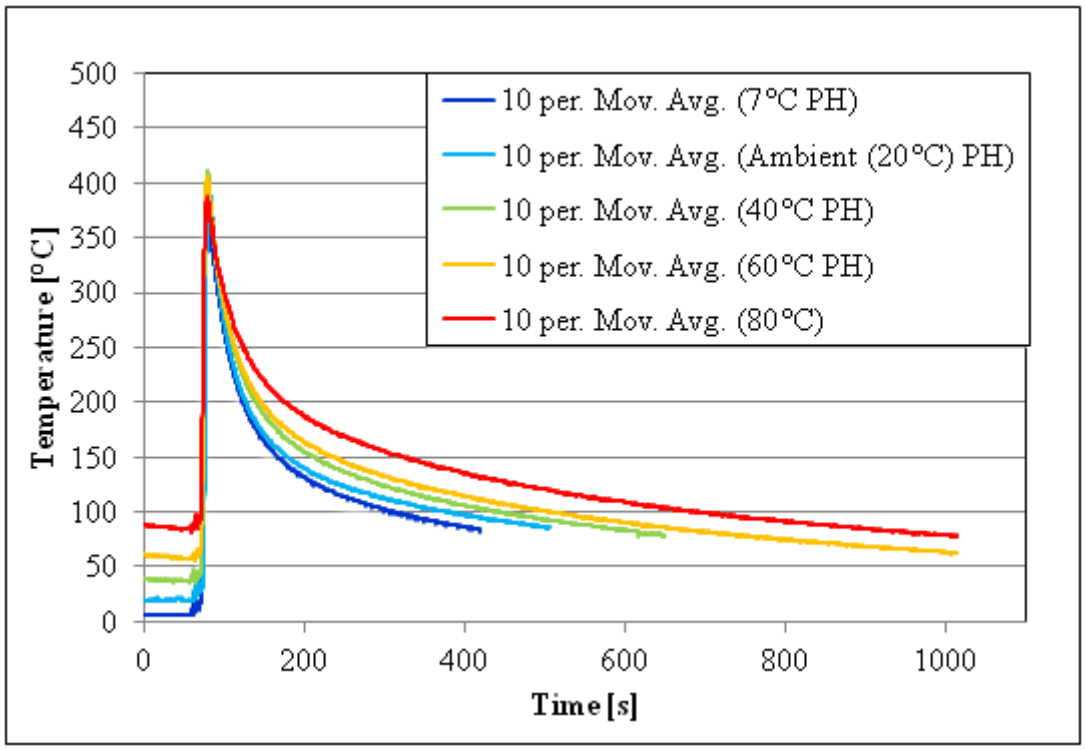

Figure 3-11 Thermal history of the 1 pass filet weldments welded with metal-cored consumable.

The cooling time from the peak temperature to 100°C determined from acquired data for all preheat temperatures and both consumables is presented in Table 3-3 and Table 3-4. This cooling time provides important information not only from a productivity view point but also about time available for diffusion of hydrogen during cooling. Variation in cooling time is obvious, increasing from approximately 198 s to 538 s for minimum and maximum pre-heats in the case of flux-cored consumable and from 242 s to 609 s in case of the metal-cored consumable. It was found that the cooling time from peak temperature to 100°C for the plate welded with ambient preheat was half the time taken for cooling at a preheat of 80°C for both tested consumables. Reducing pre-heat from 80°C to ambient (no pre-heat) resulted in reduction in cooling time of approximately 4.5 minutes (for the flux-cored consumable) and 5 minutes (metal-cored consumable). Further time would be saved by removing the need to carry out the step of preheating.

Table 3-3 Cooling times of the 1 pass filet weld welded with flux-cored consumable.

Preheat temperature [˚C]	7	Ambient (22)	40	60	80
Cooling time (t_p to $t_{100˚C}$) [sec]	198	276	350	480	538

Table 3-4 Cooling times of the 1 pass filet weld welded with metal-cored consumable.

Preheat temperature [˚C]	7	Ambient (22)	40	60	80
Cooling time (t_p to $t_{100˚C}$) [sec]	242	309	372	438	609

3.2.2.2 Weld hardness profiles

Hardness measurement traverses of fillet weldments were undertaken in two directions as shown in Figure 2-14. Figure 3-12 - Figure 3-15 shows the weld hardness profiles measured in both orientations for all employed preheat conditions. All zones of the weldment are shown: weld metal (WM), fusion line (FL), heat affected zone (HAZ), over-tempered region (OT) and parent metal (PM). Some scatter is observed in the data, in particular in the HAZ (due to the size and often inhomogenity within HAZ subzones), which is inherent in micro-hardness indentations. Also hardness values measured in the weld metal area show large discrepancies due to the nature of the as cast weld metal microstructure containing a large number of inhomogenities including solute segregation, banding, inclusions. It is to be noted that hardness variations across the weld metal was not the subject of present investigation as the weld metal microstructure is not susceptible to HACC. However, the overall hardness trend can be easily observed. Hardness measured in both orientations displayed similar trends and values for both tested consumables.

To be able to more precisely describe the variation in hardness across the welded joint, the weldment was divided into two separate sections:

1. Inner HAZ (consisting of coarse-grained (CG), fine grained (FG) and inter-critical (IC) subzones) - the area that is during welding reheated to austenite region, thus undergoes dramatic microstructural changes.
2. OT region - the area of the weldment that experiences temperature sufficient only to temper the original microstructure. This area is located between IC (visible on the etched weldment) region and PM (the OT - PM boundary was selected to be where the structure achieved hardness of 500 HV)

HAZ hardness

The fundamental trend in the hardness for both consumables and both orientations was gradual increase in hardness across the entire weldment, with respect to decreasing preheat temperature. This is due to the formation of harder microstructures as a result of increased cooling rate. From the graphs it can be observed the HAZ hardness scatter with differences in hardness of approximately 50 HV and 65 HV measured in orientation A and approximately 20 HV and 40 HV measured in orientation B for flux-cored and metal-cored consumable respectively. The HAZ width was found to decrease by maximum 0.5 mm with decreasing the preheat temperature from 80°C to 7°C.

OT region hardness

With decreasing preheat from 80°C to 7°C less scatter was found within the over-tempered zones with gradual increase in hardness of 60 HV and 50 HV measured in A orientation and 65 HV and 30 HV measured in orientation B for flux-cored and metal-cored consumable respectively. The width of the over-tempered region noticeably decreased with decreasing cooling rate from 80°C to 7°C by 2 mm measured in orientation A for both investigated consumables and 3.5 mm and 3 mm measured in orientation B for flux-cored and metal-cored consumable respectively.

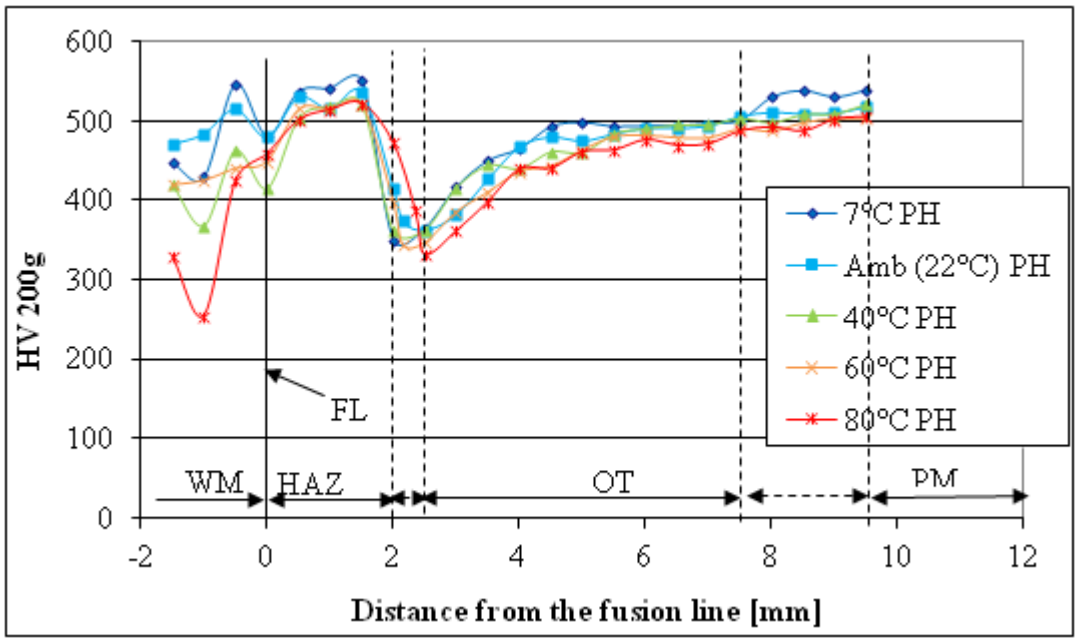

Figure 3-12 Weld hardness profiles measured in A orientation of the 1 pass filet joints welded with flux-cored consumable employing preheat temperatures of 7°C, Ambient (22°C), 40°C, 60°C and 80°C. Note: Each hardness value represents the average value of the three measurements. Standard deviations for WM, HAZ and OT regions were in the range of ±23 to ±56, ±5 to ±29 and ±2 to ±21 respectively.

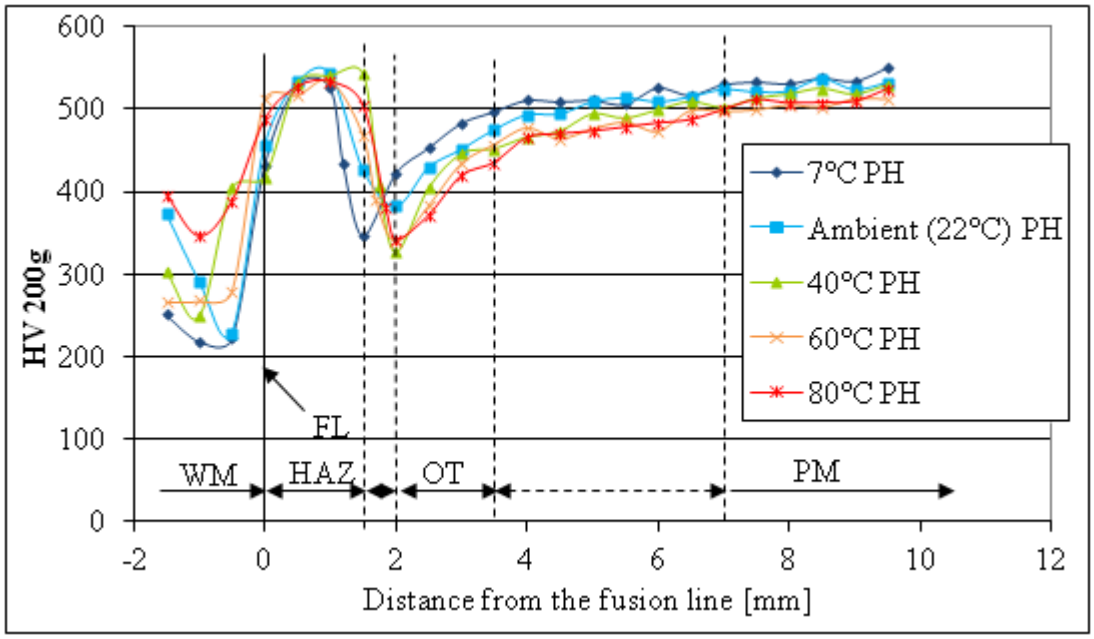

Figure 3-13 Weld hardness profiles measured in B orientation of the 1 pass filet joints welded with flux-cored consumable employing preheat temperatures of 7°C, Ambient (22°C), 40°C, 60°C and 80°C. Note: Each hardness value represents average the value of the three

measurements. Standard deviations for WM, HAZ, OT and PM regions were in the range of ±31 to ±42, ±5 to ±17, ±2 to ±27 and ±2 to ±13 respectively.

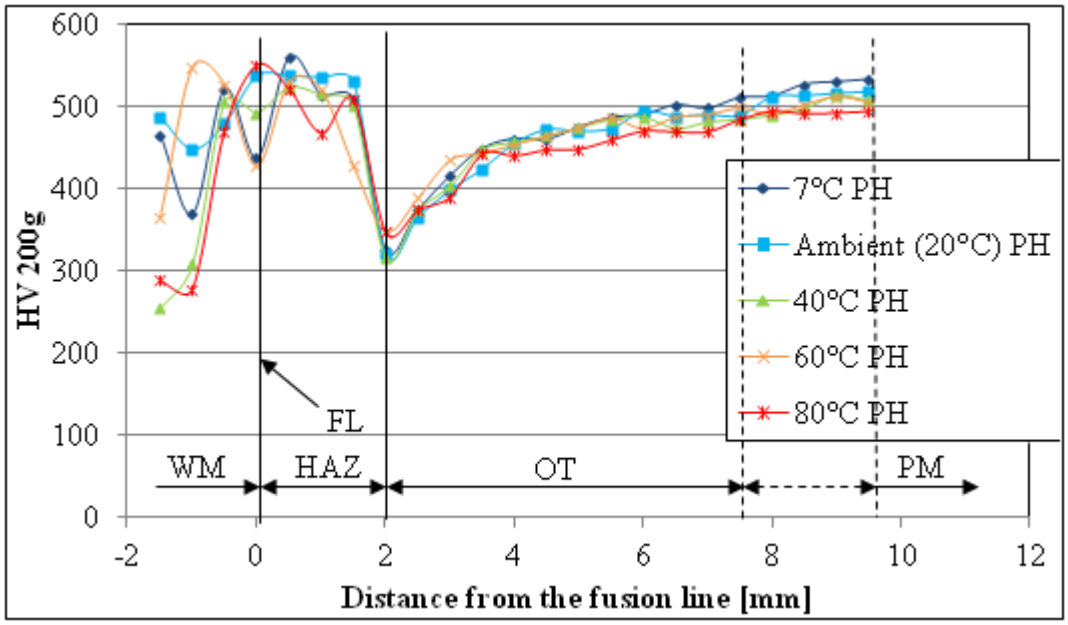

Figure 3-14 Weld hardness profiles measured in A orientation of the 1 pass filet joints welded with metal-cored consumable employing preheat temperatures of 7°C, Ambient (22°C), 40°C, 60°C and 80°C. Note: Each hardness value represents the average value of the three measurements. Standard deviations for WM, HAZ and OT regions were in the range of ±18 to ±81, ±6 to ±23 and ±5 to ±26 respectively.

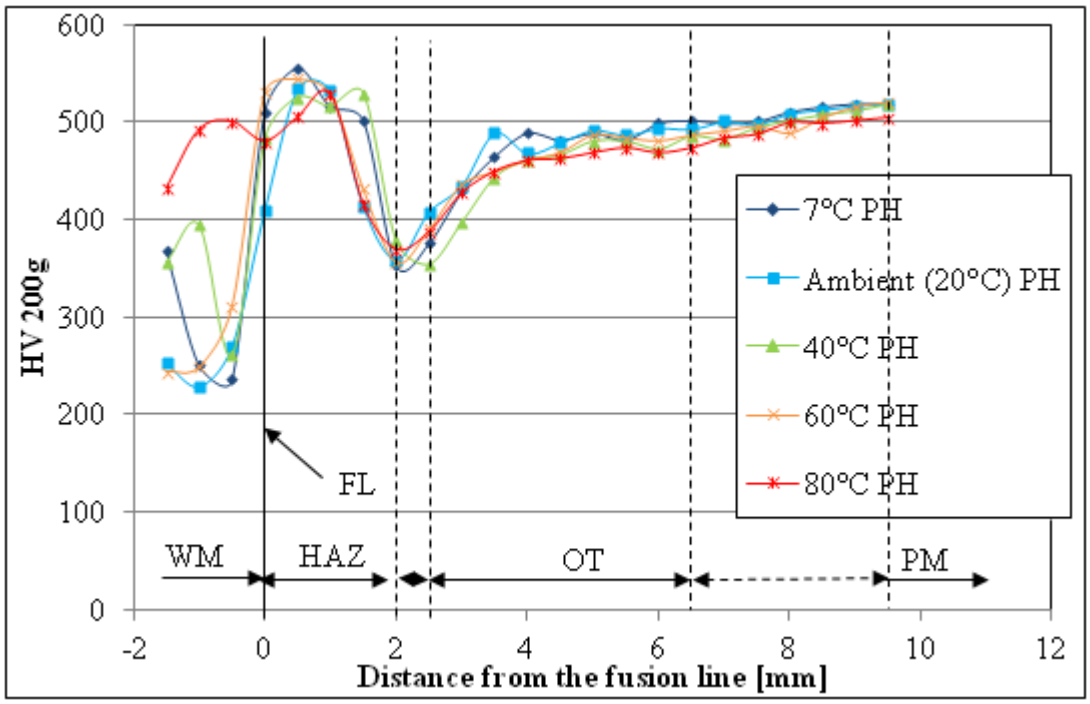

Figure 3-15 Weld hardness profiles measured in B orientation of the 1 pass filet joints welded with metal-cored consumable employing preheat temperatures of 7°C, Ambient (22°C), 40°C, 60°C and 80°C. Note: Each hardness value represents the average value of the three measurements. Standard deviations for WM, HAZ and OT regions were in the range of ±34 to ±87, ±3 to ±31 and ±2 to ±15 respectively.

Table 3-5 presents the hardness values measured in coarse-grained HAZ sub-zone of the weldments produced by flux-cored and metal-cored consumable as a function of preheat temperature. The coarse-grained sub-zone is the most susceptible to HACC out of all HAZ areas, thus the information about the hardness obtained in the region is a good indication about the level of risk of cracking. From the measured values the trend in hardness of the coarse-grained region can be observed. The hardness measured in both locations and for both consumables increases with decreasing preheat temperature. The values measured in A location of the weldment welded with flux-cored consumable employing 60°C preheat and A and B location of the weldment welded with metal-cored consumable employing 40°C preheat are not consistent with the hardness trend. This could be due to nature of the microhardness testing (very small indentations providing the information about very small area) and the inhomogeneous microstructure including constituents possessing various hardness values compared to the matrix such as inclusions, grain boundaries, and different phases.

Table 3-5 Vicker's microhardness values measured in the coarse-grained HAZ sub-zone of the 1 pass fillet welds deposited with flux-cored and metal-cored consumable employing different levels of preheat measured in two locations A & B (refer to Figure 2-14). Note: presented hardness is average value of three measurements acquired from the same area of 3 different weldments welded under the same conditions.

	Flux-cored		**Metal-cored**	
Preheat temperature [°C]	**A [HV 200g]**	**B [HV 200g]**	**A [HV 200g]**	**B [HV 200g]**
80*	501	527	520	505
60	515	516	529	544
40	503	531	523	525
22 (ambient)	530	533	536	534
7	537	529	559	556

*current industry practice

3.2.2.3 Metallographic analysis

After hardness testing the samples were subjected to metallographic observation to investigate the effect of selected levels of preheat on HAZ microstructure. To ensure good comparativeness of the acquired micrographs presented in following section, photos for all the single pass fillet weld samples were taken in the same area shown in Figure 3-16.

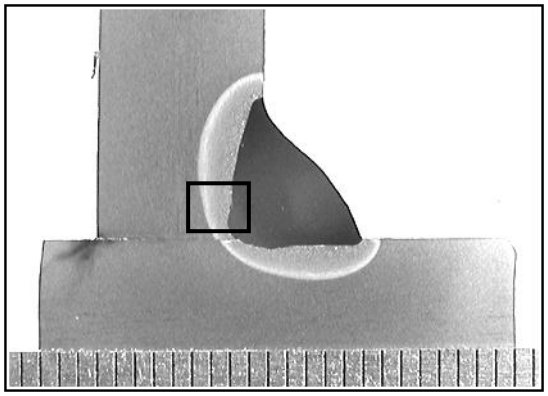

Figure 3-16 Macrograph of 1 pass fillet weld showing the area subjected to microstructural investigation.

Low magnification micrographs of each experiment are shown in Figure 3-17 and Figure 3-18 for flux-cored and metal-cored consumables respectively. The micrographs capture weld metal, coarse-grained HAZ, fine-grained HAZ, inter-critical HAZ, over-tempered zone and parent metal. It can be seen that with a decrease in pre-heat temperature, the width of the HAZ also decreased in size as is consistent with the hardness data presented in the previous section. This decrease is attributed to faster cooling rates with decreasing pre-heat temperatures.

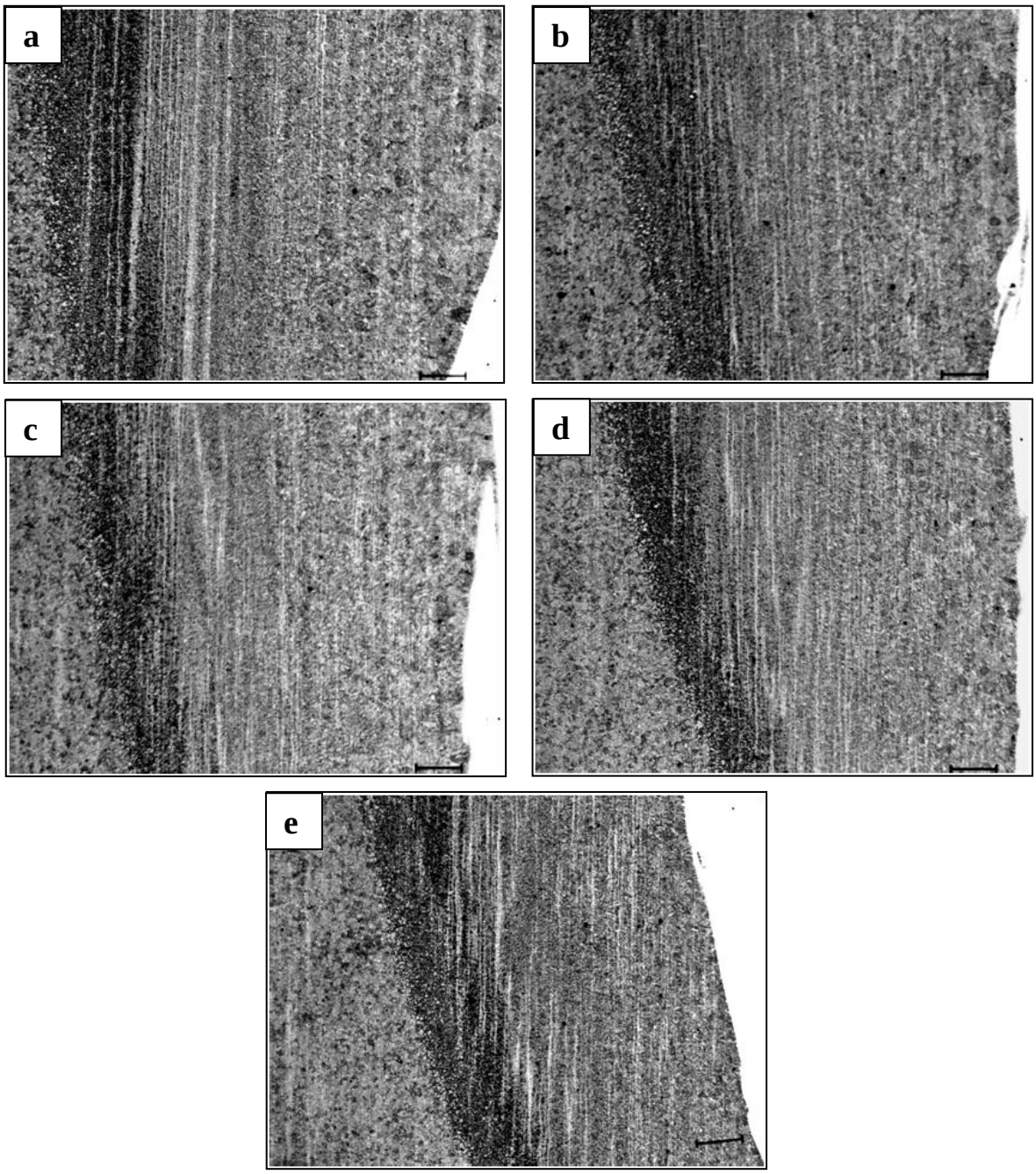

Figure 3-17 Microphotographs depicting different HAZ subzones (from right: weld metal, coarse-grained region, fine-grained region, inter-critical region, over-tempered region) of the 1 pass fillet welds deposited with flux-cored consumable under various preheat conditions; a - 80°C, b – 60°C, c - 40°C, d - Ambient (22°C), e - 7°C. Note: micron bar represents 200 micrometers.

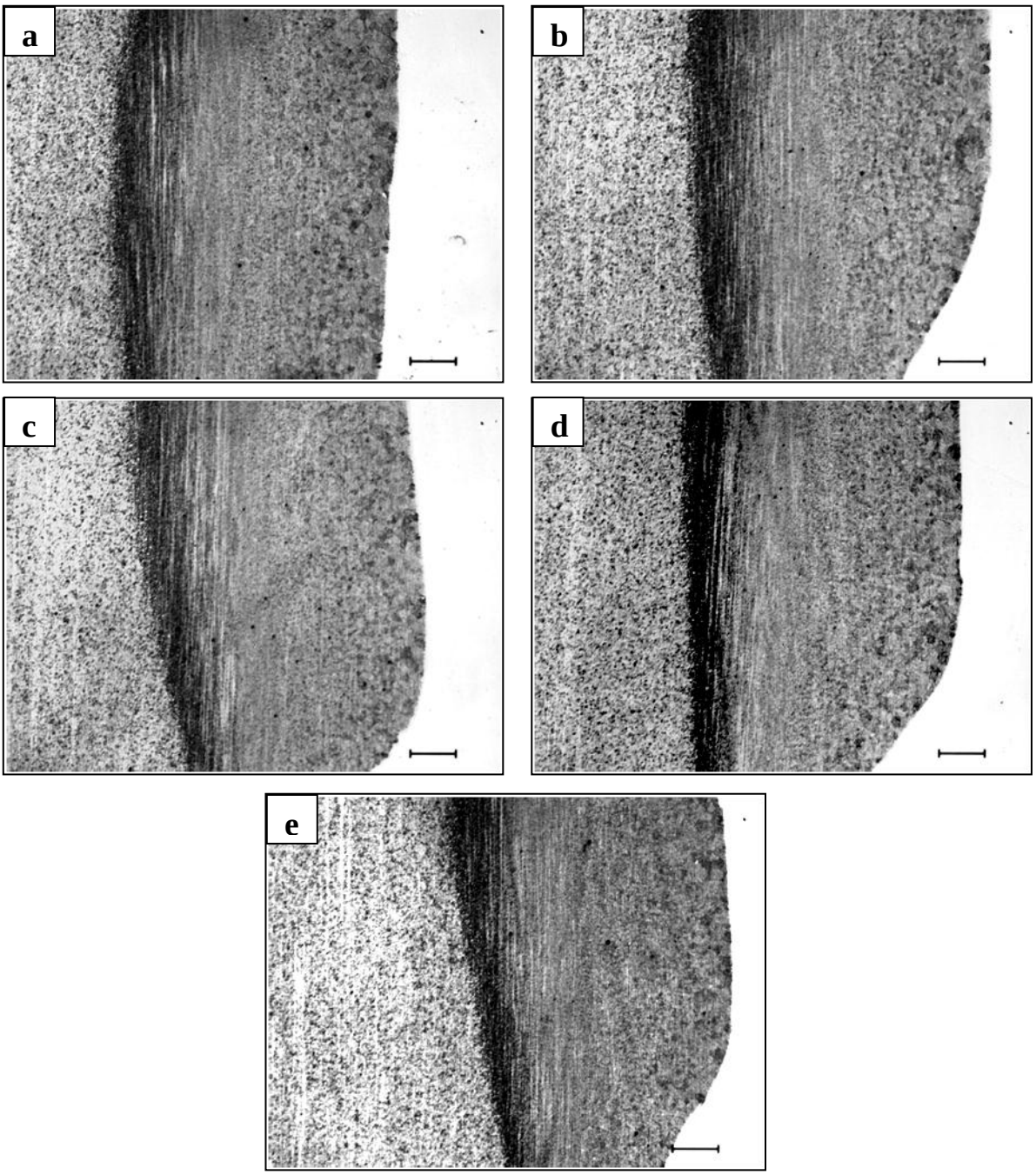

Figure 3-18 Microphotographs depicting different HAZ subzones (from right: weld metal, coarse-grained region, fine-grained region, inter-critical region, over-tempered region) of the 1 pass fillet welds deposited with metal-cored consumable under various preheat conditions; a - 80°C, b – 60°C, c - 40°C, d - Ambient (22°C) , e - 7°C. Note: micron bar represents 380 micrometers.

The widths of the HAZs were measured utilising the image analysis program Video Pro 32 and results for both W_1 and W_2 orientations (refer to Figure 3-19) are presented in Table 3-6 and Table 3-7 for flux-cored and metal-cored consumable respectively. Both W_1 and W_2 orientations represent the location where the HAZ possessed the greatest width. The widths for the two orientations are not identical due to welding torch angle, whereby slightly more heat is introduced into material in W_1 orientation. Widths were observed to decrease slightly with decreasing pre-heat temperature. For example, by reducing pre-heat from 80°C to 7°C, a reduction in HAZ (including OT region) width was approximately 11% and 14% in W_1 orientation and 22% and 19% W_2 orientation for flux-cored and metal-cored consumable respectively.

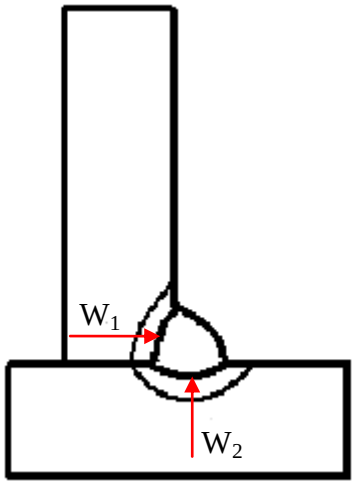

Figure 3-19 Orientation of the width measurements for 1 pass fillet welds.

Table 3-6 A slight decrease of HAZ width with decrease of preheat temperature measured in two orientations. Presented results were obtained for the welds produced employing flux-cored consumable.

Preheat temperature [°C]	**W_1 [mm]**	**W_2 [mm]**
80*	2.08	1.87
60	2.00	1.81
40	1.96	1.72
22 (ambient)	1.89	1.68
7	1.85	1.46

*current industry practice

Table 3-7 A slight decrease of HAZ width with decrease of preheat temperature measured in two orientations. Presented results were obtained for the welds produced employing metal-cored consumable.

Preheat temperature [°C]	**W_1 [mm]**	**W_2 [mm]**
80*	2.57	2.37
60	2.48	2.01
40	2.39	2.04
22 (ambient)	2.38	1.94
7	2.22	1.93

*current industry practice

Figure 3-20 and Figure 3-21 display the microstructure of the coarse-grained HAZ subzone of the single pass fillet weld deposited with flux-cored and metal-cored consumable respectively employing preheat temperatures of 80°C, 60°C, 40°C 22°C (ambient) and 7°C.

The coarse-grained subzone experiences the highest temperatures causing extensive grain growth (loss of toughness). Because HHA possesses very high hardenability, the resultant microstructure consists of mixture of hard brittle phases. The coarse-grained region is adjacent to the fusion line, thus if the weld metal upon cooling becomes oversaturated with the hydrogen introduced into the weld pool hydrogen diffusion can be promoted into coarse-grained region. Due to these facts the coarse-grained area is the most susceptible to HACC out of all HAZ subzones. In this section micrographs of the coarse-grained HAZ subzones are shown as the objective of this investigation was to identify the lower preheat temperature threshold that is safe from HACC view point. Micrographs of all HAZ subzones are shown in Figure 4-7 and Figure 4-8 where the current industry practice and potential candidates for its replacement are compared in detail.

The microstructure of the coarse-grained region of the weldments deposited with both consumables followed the same trend; of formation of harder constituents with decreasing the preheat temperature. Samples preheated to 80°C (current industry practice) consisted of a mixture of upper and lower bainite and lath martensite. Ferrite was also present in the form of ferritic laths of upper bainite. Ferrite appears on the photomicrographs as white phase, bainitic laths are dark brown and martensite shows light brown colour. With decreasing the

preheat temperature to 40°C, the ferritic lath diminished and when ambient preheat temperature was employed they were no longer present in the structure of the coarse-grained region. Lowering the preheat temperature favoured the formation of higher volume fraction of harder phases and the microstructural features became finer. The samples welded with preheat lower than 40°C contained predominantly lower bainite and lath martensite in the microstructure of their coarse-grained region with increasing amounts of martensite at the expense of bainite at lower preheat temperatures.

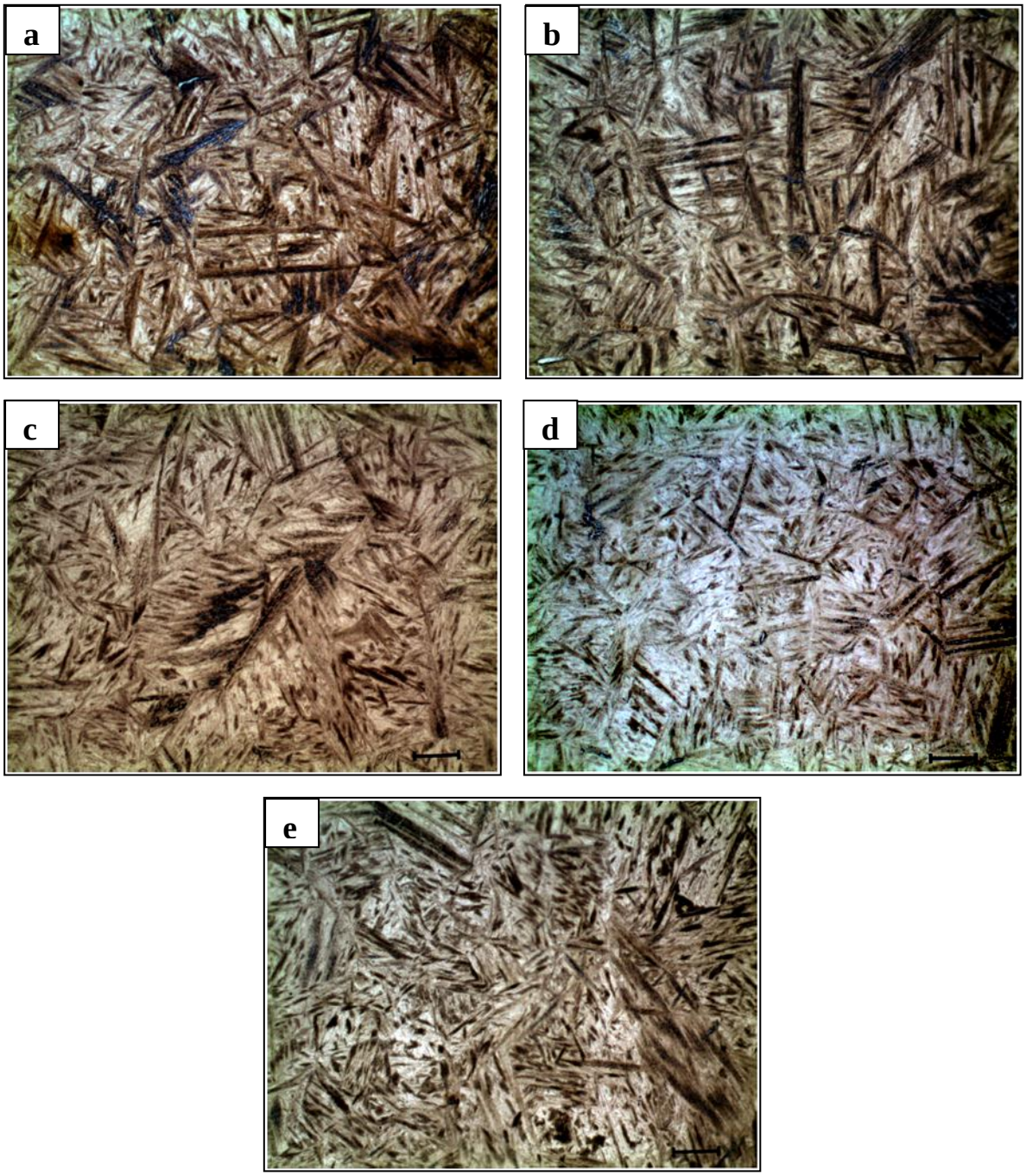

Figure 3-20 Microstructure of the coarse-grained HAZ subzone of the single pass fillet welds deposited with flux-cored consumable under various preheat conditions; a - 80°C, b – 60°C, c - 40°C, d - Ambient (22°C) , e - 7°C. Note: micron bar represents 20 micrometres.

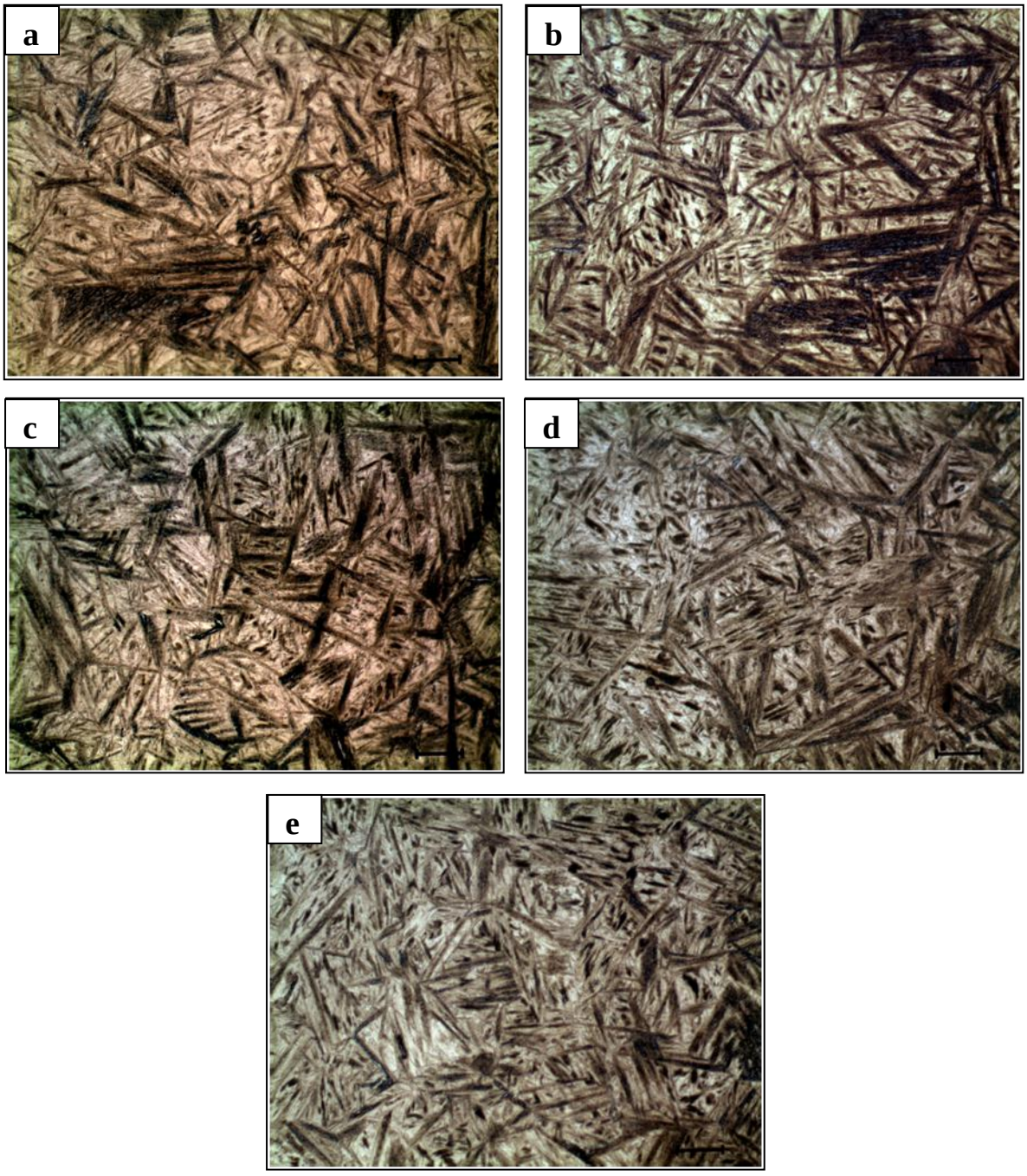

Figure 3-21 Microstructure of the coarse-grained HAZ subzone of the 1 pass fillet welds deposited with metal-cored consumable under various preheat conditions; a - 80°C, b – 60°C, c - 40°C, d - Ambient (22°C), e - 7°C. Note: micron bar represents 20 micrometers.

3.2.3 Optimisation of interpass temperature

In the fabrication of HHA structures, especially to join the thicker plates welding procedures employing multiple passes are often required. The interpass temperature has to be maintained within a certain range in order to avoid both HACC and HAZ softening. Current industry

practice utilises an identical temperature range of 80°C - 120°C for preheating and also interpass temperature. Unlike preheating, to minimise the waiting periods necessary for the weldment to cool down after deposition of previous pass it is beneficial to employ the highest interpass temperature possible. To study the effect of increasing the interpass temperature on microstructure and resultant hardness of HHA plates multiple pass corner joints were produced employing 20°C (ambient) preheat and interpass temperatures of 120°C, 160°C, 200°C and 250°C. The interpass temperature of 250°C does not have a practical use particularly for longer welds as the temperature initially decreases very rapidly and prolonged cooling times are experienced in temperature range below 250°C. This temperature was investigated as the worst case scenario to expand the temperature window when depositing short welds. The welding procedure for the flux-cored consumable utilised five weld passes. Due to the modified weld geometry employing a 2 mm plate overlap only four passes were required to produce joint with metal-cored consumable. To ensure consistency and repeatability of the results, all trials involving interpass temperatures higher than the industry standard were repeated two times for both flux-cored and metal-cored austenitic stainless steel consumables. Samples subjected to microstructural investigation and hardness testing were sectioned from the middle of the 300 mm long welded plates where stable welding conditions were obtained.

The macrographs of the cross-sections of the weldments deposited with flux-cored and metal-cored consumables employing welding parameters described in Table 2-9 are presented in Figure 3-22 and Figure 3-23 respectively. It is clear from the macrographs that there is a slight increase in HAZ area with increasing interpass temperature. It can also be noticed that the coarse-grained region of the 2nd pass (1st cap pass) of the joint welded with metal-cored consumable and interpass temperature of 250°C was reheated to inter-critical region by subsequent passes.

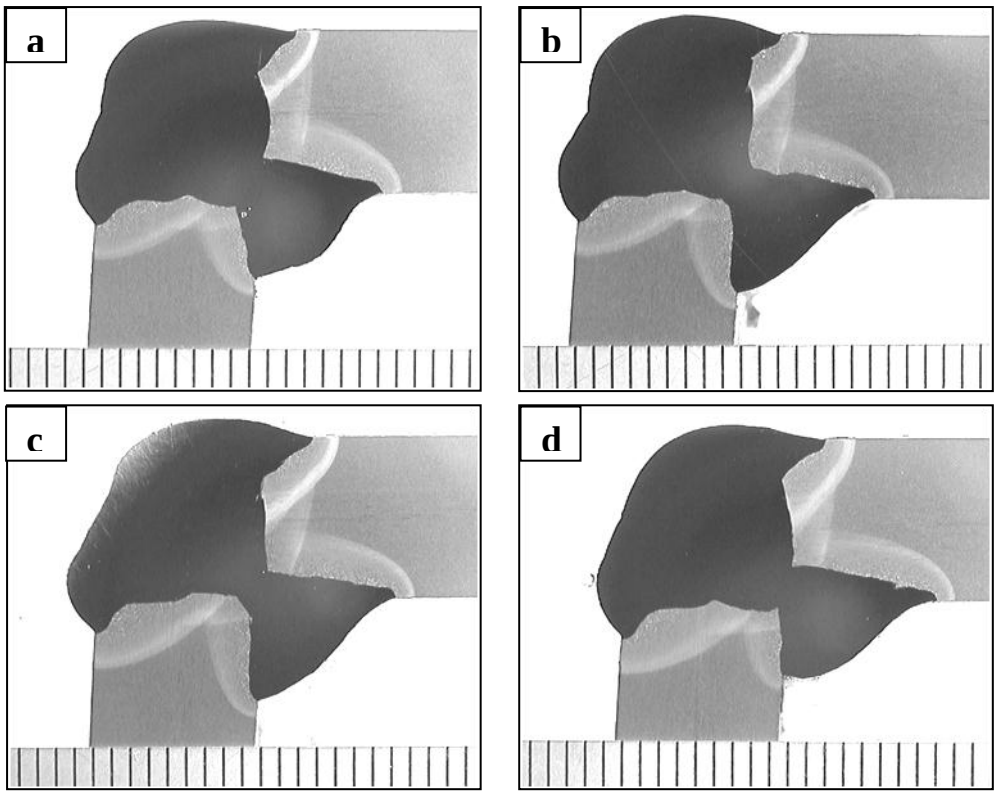

Figure 3-22 Macrophotographs of the 5 pass corner welds deposited with flux-cored consumable employing ambient preheat and various interpass temperature conditions; a - 120°C, b – 160°C, c - 200°C, d - 250°C. Note: scale is in millimetres.

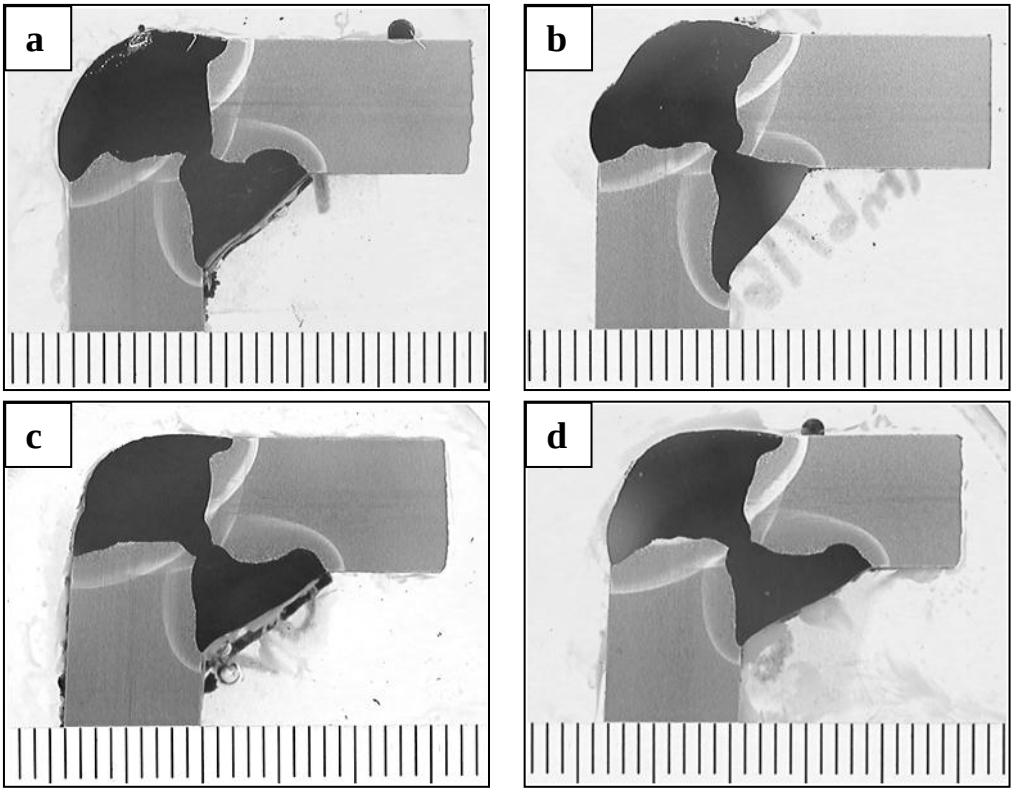

Figure 3-23 Macrophotographs of the 4 pass corner welds deposited with metal-cored consumable employing ambient preheat and various interpass temperature conditions; a - 120°C, b – 160°C, c - 200°C, d - 250°C. Note: scale is in millimetres.

3.2.3.1 Weld thermal history

During welding trials the weld thermal history of all weldments employing the selected interpass temperatures was recorded for both consumables. The results acquired for 1st inner passes are not presented as all of them were deposited separately from the cap passes with preheat temperature of 20°C (ambient) and do not provide any information about the effect of interpass temperature on the properties of the joints.

Figure 3-24 and Figure 3-25 show the weld thermal history of the 4 and 3 cap passes of the corner welds deposited with flux-cored and metal-cored consumable respectively. As expected and evident from the graphs; the cooling rate of the subsequent passes decreased but cooling time increased as a result of increasing the interpass temperature. It is to be noted that the subject of the present study was not to record thermal history directly in the weld metal or coarse-grain HAZ. The recorded thermal history provides the information about the thermal

history experienced by over-tempered HAZ. The temperature was also recorded to monitor the inerpass temperature via a real-time graph and ensure that the subsequent pass was deposited exactly when the required temperature was reached. Weld thermal history was acquired to provide information about effects of various interpass temperatures on cooling rate and cooling times of the over-tempered region of the welded joint.

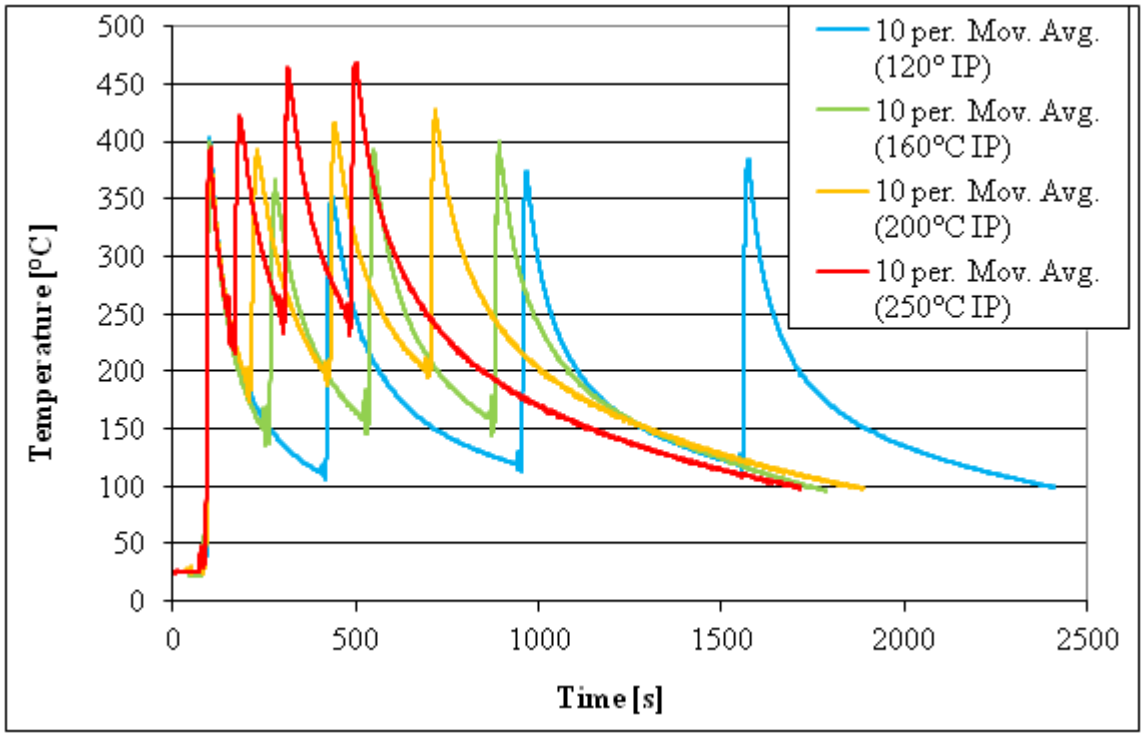

Figure 3-24 Weld thermal history of the 4 cap passes deposited with flux-cored consumable employing ambient preheat and interpass temperatures of 120°C, 160°C, 200°C and 250°C.

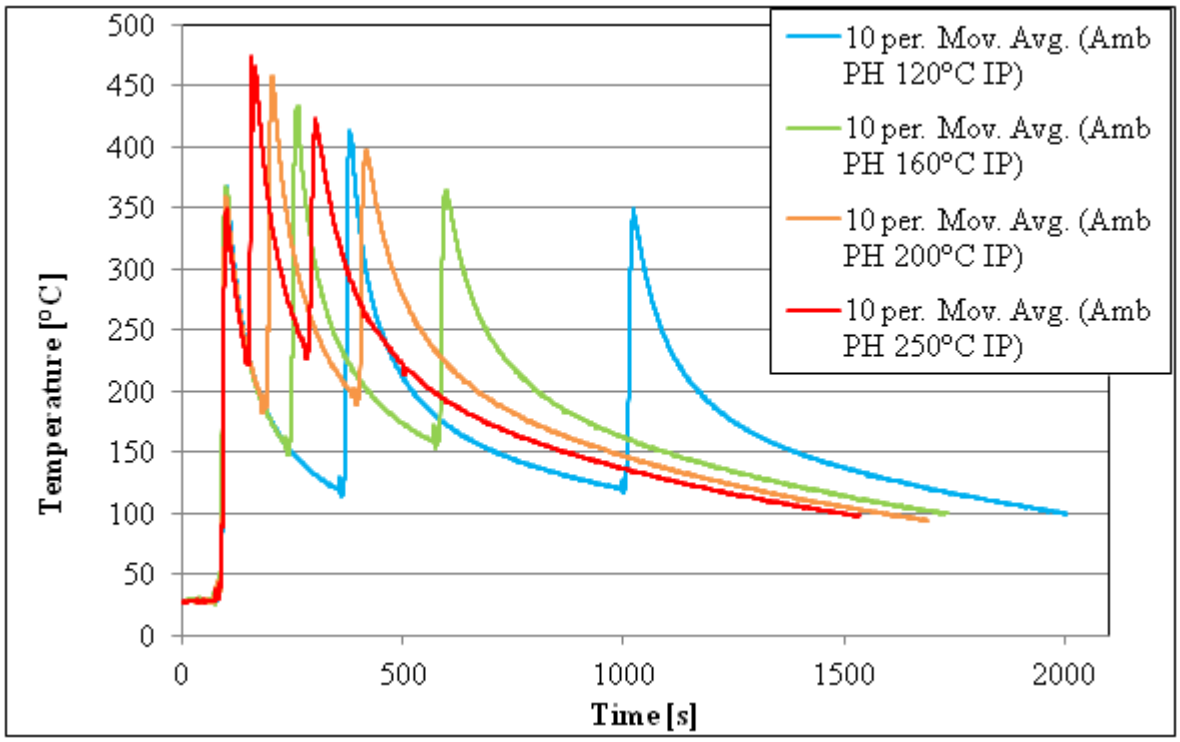

Figure 3-25 Weld thermal history of the 3 cap passes deposited with metal-cored consumable employing ambient preheat and interpass temperatures of 120°C, 160°C, 200°C and 250°C.

The cooling time data presented in Table 3-8 and Table 3-9 for flux-cored and metal-cored consumable respectively show that increasing interpass temperature from 120°C to 250°C reduces the welding time (from the peak temperature of the first cap pass [$t_p(1^{st}$ pass)] until the peak temperature of the final pass is reached [t_p(final pass)]) from 1742 s to 401 s and 923 s to 203 s for flux-cored and metal-cored consumable respectively. These data are particularly significant to industry requirements and are a useful gauge to likely productivity gains during fabrication. Increasing the interpass temperature from 120°C to 200°C resulted in reduction in cooling time of approximately 15 minutes (60%) for the flux-cored consumable and 10 minutes (67%) for the metal-cored consumable. The overall cooling time (from the peak temperature of the first cap pass [$t_p(1^{st}$ pass)] until 100°C was reached after completion of welding [$t_{100°C}$(final pass)]) was gradually reduced from 1904 s to 1400 s with the increase of interpass temperature from 120°C to 250°C for metal-cored consumable. In case of the flux-cored consumable the overall cooling time initially decreased with increasing interpass temperature from 120°C to 160°C but a further increase to 200°C resulted in a slightly longer overall cooling time. This is a consequence of the significantly longer cooling time after deposition of final weld pass when 200°C interpass temperature was employed. Overall

cooling time data is important in assessing the time taken for cooling with respect to diffusion of hydrogen out of the weldment during the welding process.

Table 3-8 Cooling times of the 4 cap passes of the corner weld welded with flux-cored consumable.

Interpass temperature [˚C]	120	160	200	250
Cooling time {t_p(1st pass) to t_p(4th pass)} [sec]	1472	793	617	401
Cooling time {t_p(1st pass) to $t_{100°C}$(4th pass)} [sec]	2302	1642	1769	1615

Table 3-9 Cooling times of the 3 cap passes of the corner weld welded with metal-cored consumable.

Interpass temperature [˚C]	120	160	200	250
Cooling time {t_p(1st pass) to t_p(3rd pass)} [sec]	923	496	315	203
Cooling time {t_p(1st pass) to $t_{100°C}$(3rd pass)} [sec]	1904	1634	1486	1400

3.2.3.2 Weld hardness profiles

Hardness measurement traverses of multipass corner weldments were undertaken in the cap area in two orientations as shown in Figure 2-17 for both consumables. Figure 3-26 - Figure 3-29 present the weld hardness data of the samples welded at ambient (22°C) preheat temperature in combination with 120°C, 160°C, 180°C, 200°C and 250°C interpass temperatures. All zones of the weldment are shown: weld metal (WM), fusion line (FL), heat affected zone (HAZ), over-tempered region (OT) and parent metal (PM). Similarly as with the hardness measured for varying preheat temperature, some scatter was observed in particular in the HAZ which is inherent with this type of micro-hardness indentation and also weld metal hardness show large discrepancies due to the nature of the weld metal microstructure. It is noted that hardness variations across the weld metal was not the subject

of present study. However, the overall hardness trend of the HAZ and over-tempered region can easily be observed. Hardness measured in both orientations displayed similar trends and values for both consumables. To be able to more precisely describe variation in hardness across the welded joint, HAZ the weldment was again divided into two separate areas (refer to 3.2.2.2): inner HAZ and over-tempered (OT) region.

HAZ hardness

It was observed that with an increase in interpass temperature, a gradual decrease in HAZ hardness was found to occur, as a result of slower cooling rates in transformation region promoting formation of softer microstructures. The maximum difference between HAZ hardness at 120°C and 200°C (250°C) was approximately 60 HV (80 HV) and 90 HV (135 HV) for flux-cored consumable measured in A and B orientation respectively. In case of metal-cored consumable it was maximum 40 HV (115 HV) and 130 HV (150 HV) for A and B orientations respectively. In addition, the HAZ widths for all interpass temperatures were very similar, with only slight increases of a maximum 0.5 mm observed in all orientations for both tested consumables. This indicated that an increase in interpass temperature has some softening effect on microstructure but does not affect the HAZ width. Formation of softer microstructures especially in coarse-grained region could have beneficial effects with respect to reducing the potential risk of HACC. Therefore, it appears that neither ballistic protection nor structural integrity would be compromised in this zone.

OT region hardness

The attempt to improve productivity and cost effectiveness through increasing the interpass temperature could lead to undesirable formation of extensively soft and wide areas in the over-tempered region and thus have an adverse effect on ballistic properties. With increasing interpass temperature less scatter was observed within the over-tempered zones and the hardness profiles were found to be almost identical with only very slight decrease in hardness with the increase in interpass temperature to 200°C for both consumables. A urther increase interpass temperature to 250°C resulted in somewhat higher degree of softening; maximum 35 HV and only 20 HV measured for flux-cored and metal-cored consumable respectively. The width of the over-tempered region increased with increasing cooling rate from 120°C to 250°C by 5 mm and 3.5 mm measured in orientation A and B orientation of the joint welded with flux-cored consumable respectively. For metal-cored consumable the width measured in

A orientation was identical for all interpass temperatures and in B orientation increased by 3.5 mm.

In summary, increasing interpass temperature from 120°C to 250°C resulted in a small incremental reduction of overall hardness of the welded joints and slight increase of the width of the over-tempered region. Importantly, the hardnesses obtained 15.9 mm from the weld toe appears close to, or higher than the lowest hardness of 509 HV permitted by MIL- STAN-1185 (AT) [85] in all cases.

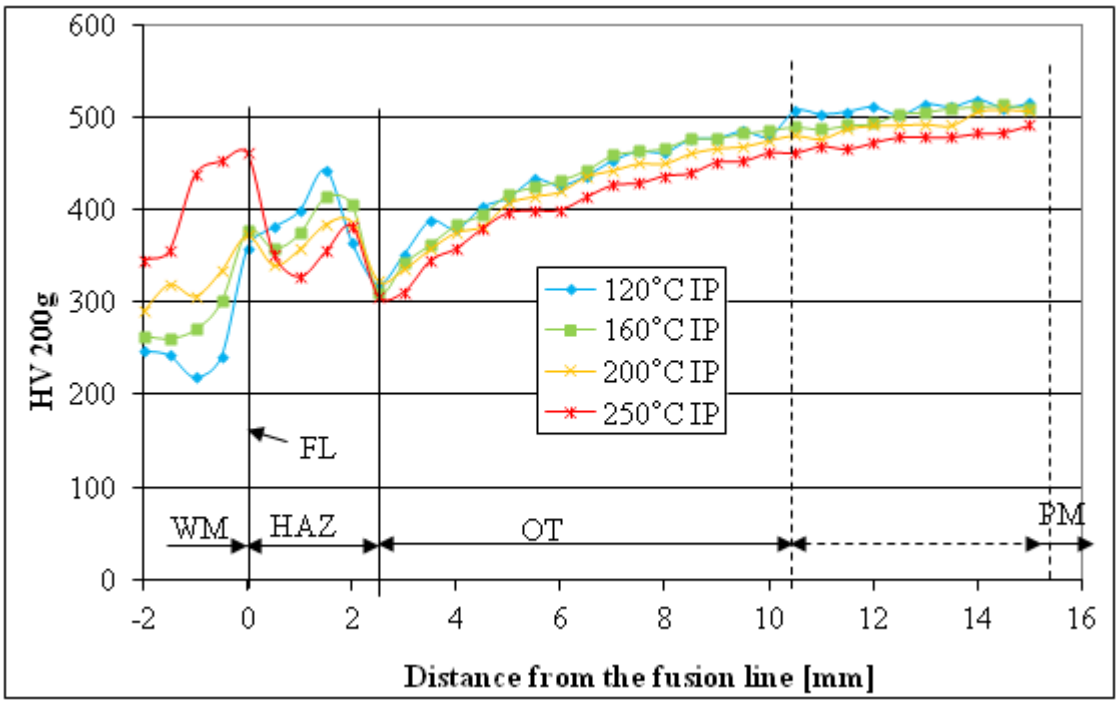

Figure 3-26 Weld hardness profiles measured in A orientation of the 5 pass corner joints welded with flux-cored consumable employing ambient preheat and interpass temperatures of 120°C, 160°C, 200°C and 250°C. Note: Each hardness value represents the average value of the three measurements. Standard deviations for WM, HAZ and OT regions were in the range of ±12 to ±78, ±4 to ±32 and ±0 to ±27 respectively.

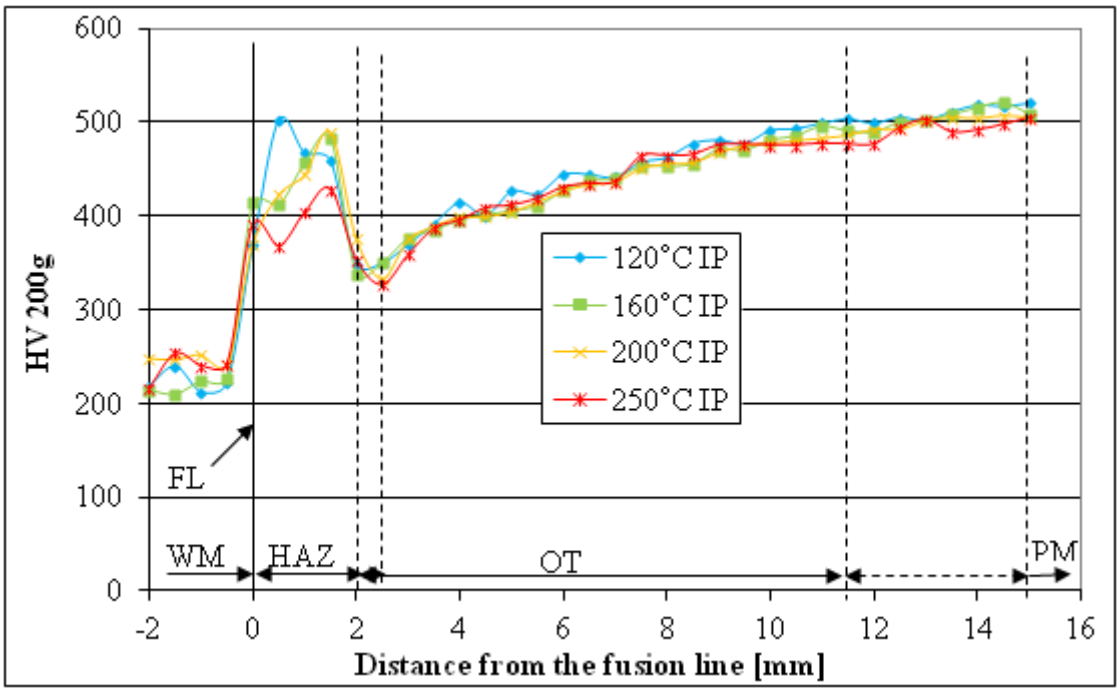

Figure 3-27 Weld hardness profiles measured in B orientation of the 5 pass corner joints welded with flux-cored consumable employing ambient preheat and interpass temperatures of 120°C, 160°C, 200°C and 250°C. Note: Each hardness value represents the average value of the three measurements. Standard deviations for WM, HAZ and OT regions were in the range of ±45 to ±83, ±2 to ±37 and ±1 to ±17 respectively.

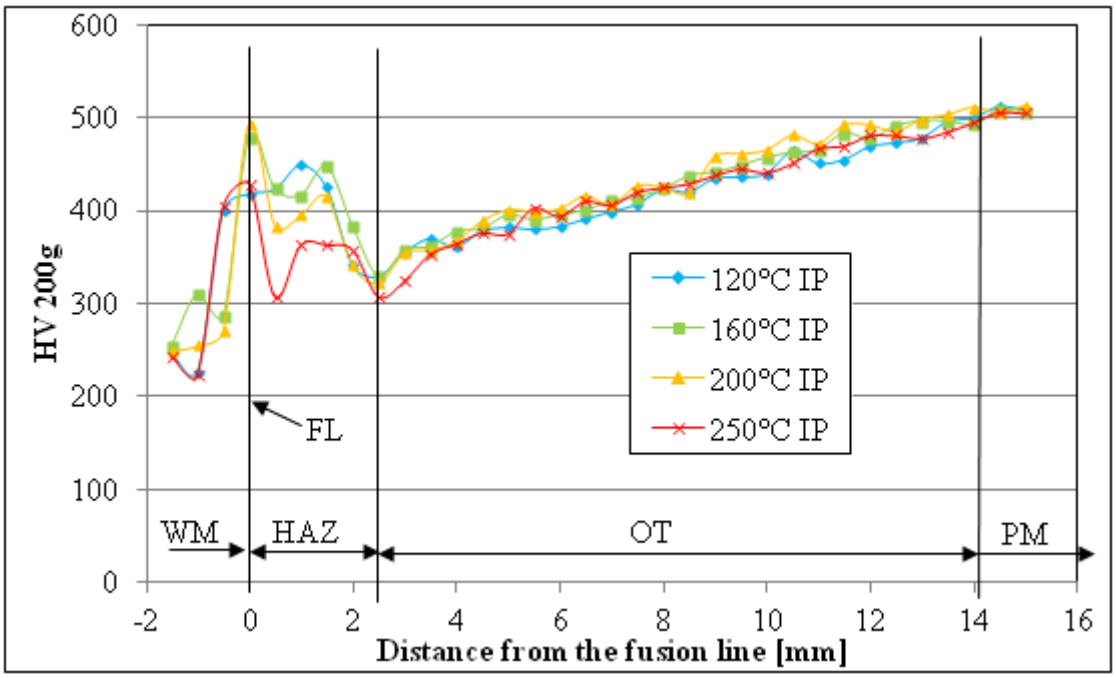

Figure 3-28 Weld hardness profiles measured in A orientation of the 4 pass corner joints welded with metal-cored consumable employing ambient preheat and interpass temperatures of 120°C, 160°C, 200°C and 250°C. Note: Each hardness value represents the average value of the three measurements. Standard deviations for WM, HAZ, OT and PM regions were in the range of ±34 to ±57, ±6 to ±31, ±2 to ±19 and ±1 to ±16 respectively.

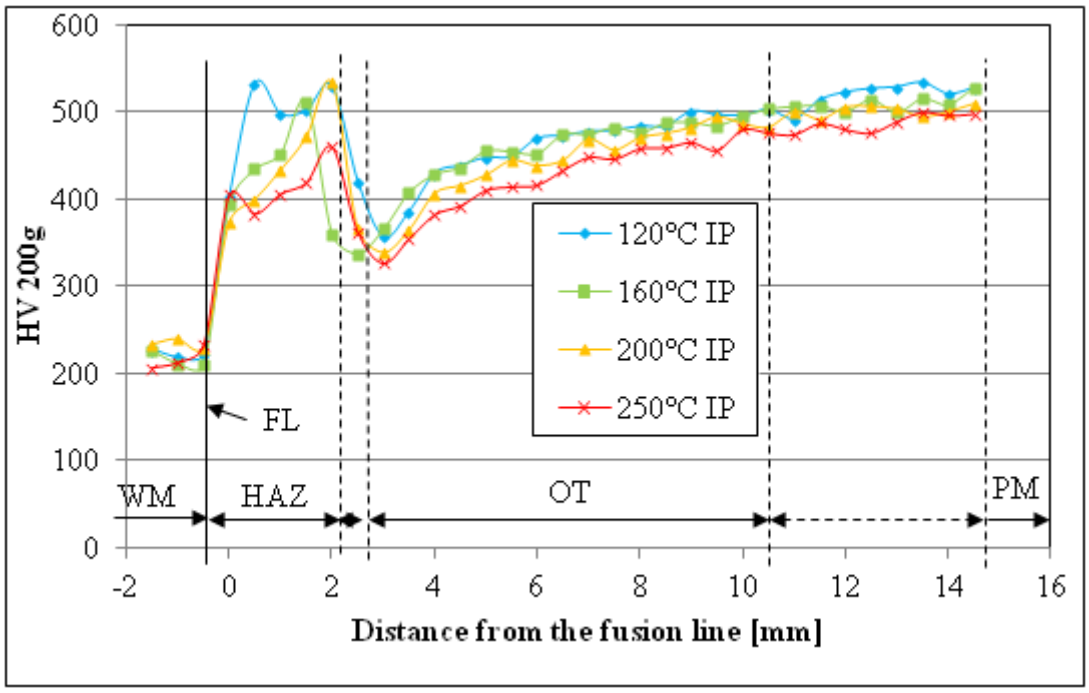

Figure 3-29 Weld hardness profiles measured in B orientation of the 4 pass corner joints welded with metal-cored consumable employing ambient preheat and interpass temperatures of 120°C, 160°C, 200°C and 250°C. Note: Each hardness value represents the average value of the three measurements. Standard deviations for WM, HAZ and OT regions were in the range of ±19 to ±47, ±3 to ±28 and ±2 to ±34 respectively.

3.2.3.3 Metallographic analysis

After hardness testing samples were subjected to metallographic observation to investigate the effect of the selected interpass temperatures on HAZ microstructure. To ensure consistent comparison of the acquired micrographs presented in following section, photos for all the multi-pass corner joints were taken in the same cap area shown in
Figure 3-30. This area was selected because the effect of interpass temperature is amplified as a result of position and sequence of the weld passes.

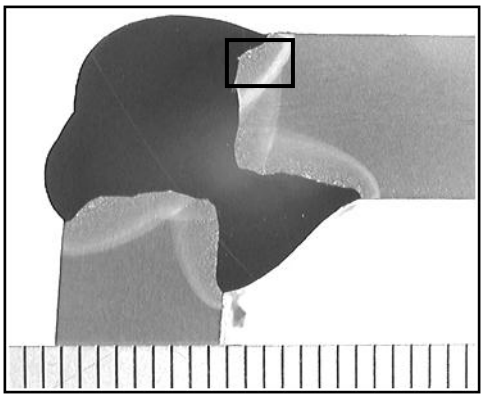

Figure 3-30 Macrograph of multi-pass corner joint showing the area subjected to microstructural investigation.

Low magnification micrographs of each experiment are shown in Figure 3-31 and Figure 3-32 for flux-cored and metal-cored consumable respectively. The micrographs cover weld metal, coarse-grained HAZ, fine-grained HAZ, inter-critical HAZ, over-tempered zone and parent metal. Little increase in HAZ size was observed for both consumables as is consistent with the hardness data and HAZ area measurements presented in previous and following sections. The only noticeable difference in the size of each of these zones was observed for the fine-grain HAZ, which was found to increase slightly with an increasing interpass temperature.

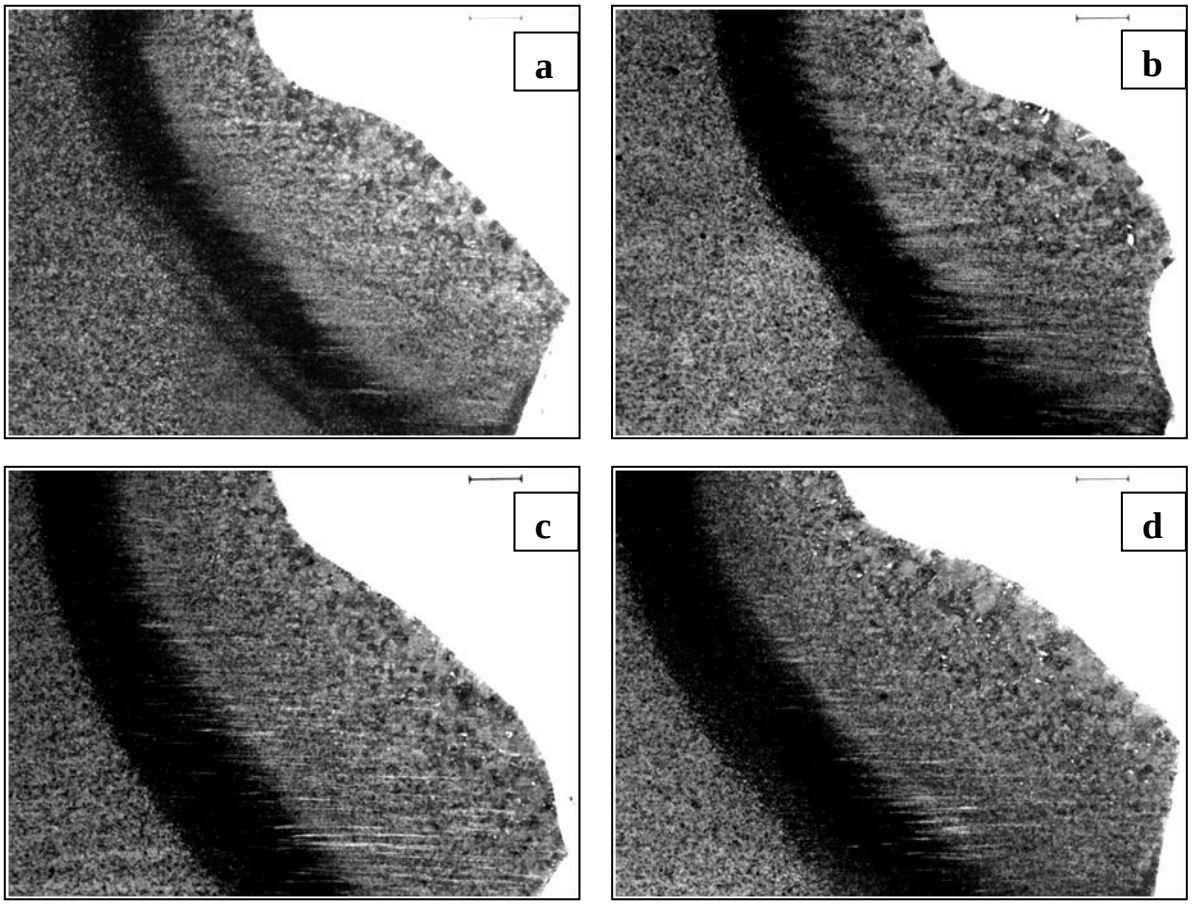

Figure 3-31 Microphotographs depicting different HAZ subzones (from right: weld metal, coarse-grained region, fine-grained region, inter-critical region, over-tempered region) of the 5 pass corner welds deposited with flux-cored consumable employing ambient preheat and various interpass temperatures; a - 120°C, b – 160°C, c - 200°C, d - 250°C. Note: micron bar represents 380 micrometers.

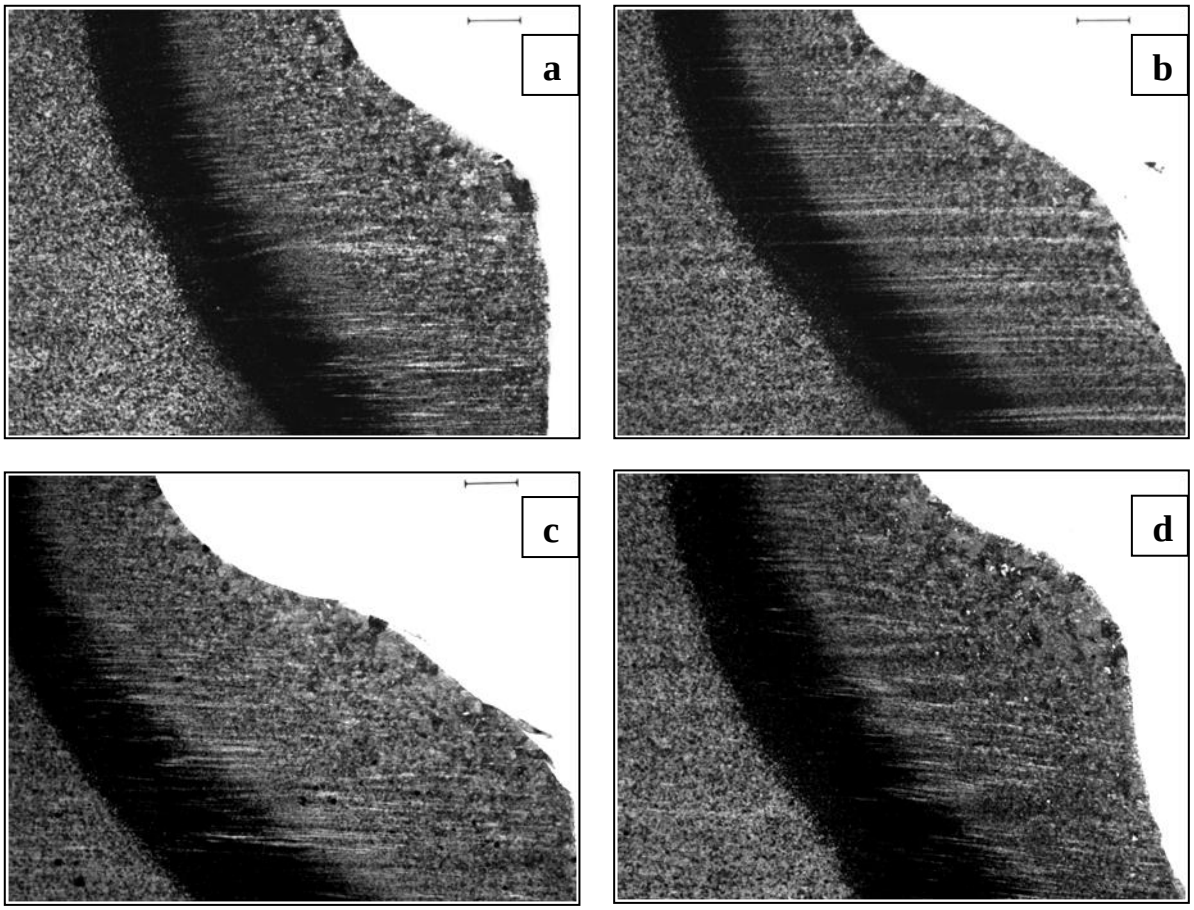

Figure 3-32 Microphotographs depicting different HAZ subzones (from right: weld metal, coarse-grained region, fine-grained region, inter-critical region, over-tempered region) of the 4 pass corner welds deposited with metal-cored consumable employing ambient preheat and various interpass temperatures; a - 120°C, b – 160°C, c - 200°C, d - 250°C. Note: micron bar represents 380 micrometers.

HAZ area measurements for the weldments produced utilising both consumables were calculated using the image analyses program Video Pro 32 and are presented in Table 3-10. HAZ areas were observed to increase slightly with increasing interpass temperature. For example, by increasing the interpass temperature from 120°C to 250°C, an enlargement of the HAZ area was observed to be approximately 9.4% and 8.8% for flux-cored and metal-cored consumable respectively. When compared with weldment produced by normal industry practice (80°C preheat, 120°C interpass temperature) the increase of the HAZ area with increasing interpass temperature to 250° was lower 8.5% and 6.0% for flux-cored and metal-cored consumable respectively. Thus, increasing interpass temperature did not significantly

increase the area of HAZ regions that otherwise be of concern for locations of inhomogenity in the material that could be weak points against ballistic impact.

Table 3-10 Calculated areas of the HAZ as a function of interpass temperature.

	Flux-cored	**Metal-cored**
Preheat/Interpass temperature [°C]	**HAZ Area [mm^2]**	**HAZ Area [mm^2]**
Ambient/120	54.62	55.47
80/120*	55.01	56.93
Ambient/160	56.62	58.48
Ambient/200	58.17	58.96
Ambient/250	59.68	60.34

*current industry practice

Figure 3-33 and Figure 3-34 display the microstructure of the coarse-grained HAZ subzone of the multi-pass corner welds deposited with flux-cored and metal-cored consumable respectively employing 22°C (ambient) preheat and interpass temperatures of 120°C, 160°C, 200°C and 250°C. The coarse-grained subzone experiences the highest temperatures causing extensive grain growth (loss of toughness). Because HHA possesses very high hardenability, the resultant microstructure consists of a mixture of hard brittle phases. The heat introduced into the weldment during deposition of the subsequent passes tempers the original microstructure of the coarse-grain region producing softer structures possessing better toughness. Multiple reheating of the HAZ also results in additional time at high temperatures where the diffusion of hydrogen is accelerated thus results in lower overall levels of the hydrogen present in the weldment. However the HAZ of the final pass remains in untempered condition hence the risk of HACC is increased in this area. The following section focuses on this coarse-grained HAZ subzone since it is the objective of this investigation to develop safe welding procedures that produce HACC free joints. All HAZ subzones are shown in Figure 4-17 and Figure 4-18 where the current industry practice and potential candidate for its replacement are compared in detail. The purpose of the maintaining interpass temperature high is to reduce the cooling rate of the subsequent passes thus reducing the risk of HACC.

The microstructure of the coarse-grained region of the weldments deposited with both consumables followed the same trend of formation of higher volume fraction of softer constituents (upper and lower bainite) with increasing the interpass temperature. Samples for which 120°C interpass temperature was maintained consisted of mixture of lath martensite and upper and quite substantial amount of lower bainite. Ferrite was also present in the form of ferritic laths of upper bainite. Ferrite appears on the photomicrographs as white phase, bainitic laths are dark brown and martensite shows light brown colour. The martensite to bainite (upper + lower) was approximately 40:60 for both consumables. With increasing the interpass temperature to 160°C and 200°C more and more bainite was observed with the martensite to bainite ratio decreasing to approximately 25:75 and 10:90 respectively for flux-cored consumable. In case of metal-cored consumable for these two levels of interpass temperature the martensite to bainite ratio was similar; about 25:75. With increasing interpass temperature even higher to 250°C the martensite content diminished from the microstructure of the coarse-grain region of the weldments produced by flux-cored consumable. The coarse-grain area of the joint produced employing metal-cored consumable still contained around 10% of martensite at this level of interpass temperature. The conditions favoured formation of bainite rather than martensite with the amount of upper bainite prevailing in the microstructure of the joints produced with both consumables. These observations of the formation of softer microstructure in the coarse-grain area are consistent with hardness data presented in previous section.

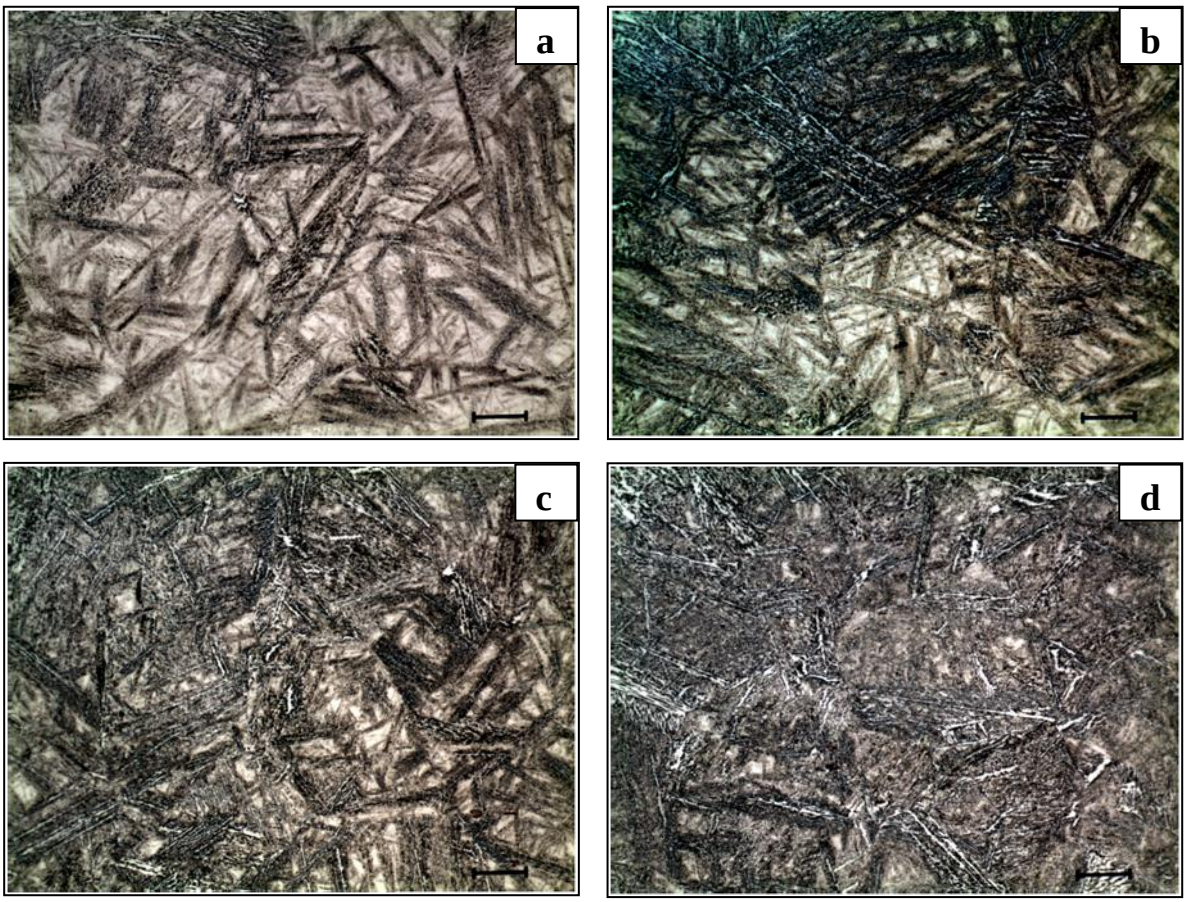

Figure 3-33 Microstructure of the coarse-grained HAZ region of the 5 pass corner welds deposited with flux-cored consumable employing ambient preheat and various interpass temperatures; a - 120°C, b – 160°C, c - 200°C, d - 250°C. Note: micron bar represents 20 micrometres.

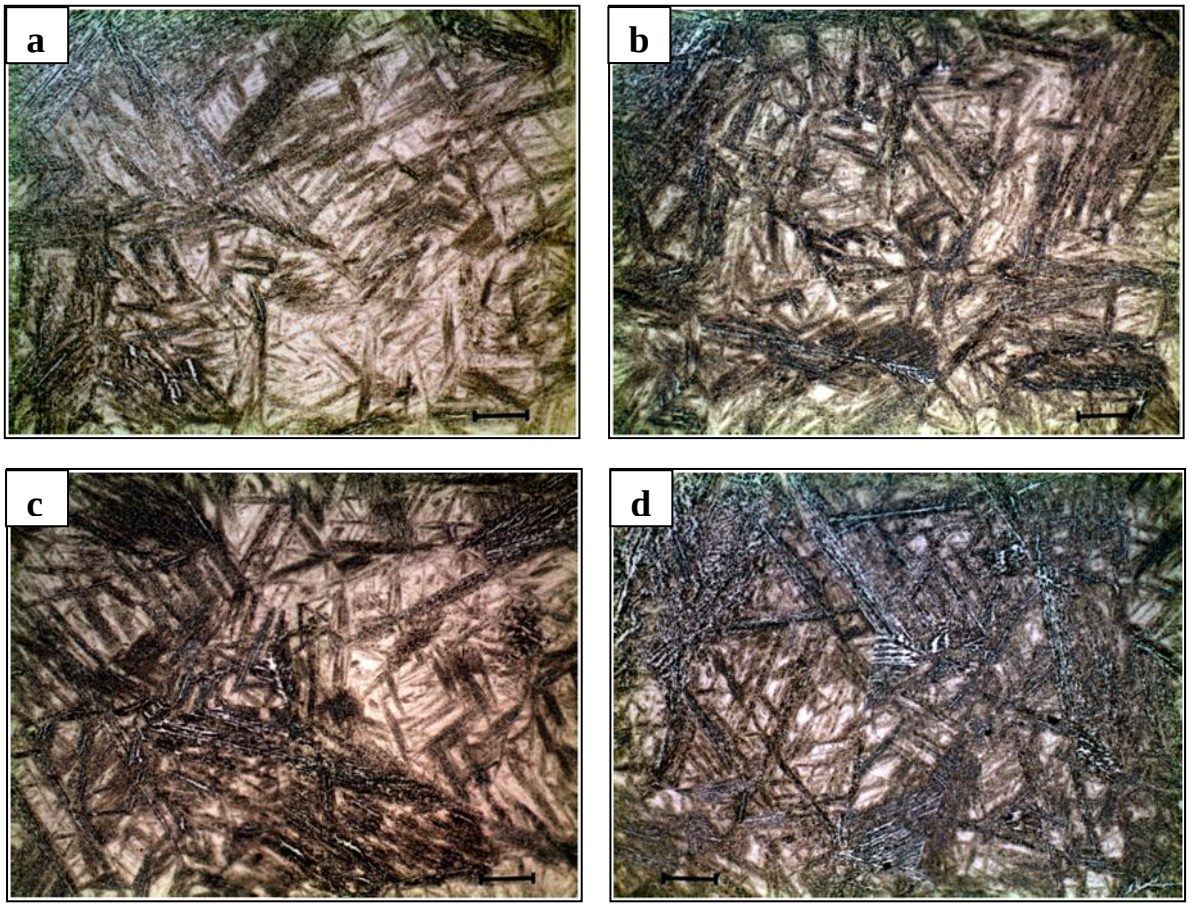

Figure 3-34 Microstructure of the coarse-grained HAZ region of the 4 pass corner welds deposited with metal-cored consumable employing ambient preheat and various interpass temperatures; a - 120°C, b – 160°C, c - 200°C, d - 250°C. Note: micron bar represents 20 micrometers.

When welding high hardness armour steel in Q&T conditions the deposition of multiple passes can result in formation of extensively wide softened regions especially when high interpass temperatures or high heat inputs are employed. Therefore the microstructure of over-tempered region was subjected to close examination. Micrographs of over-tempered regions of the multi pass corner weldments produced by flux-cored and metal cored consumable are presented in Figure 3-35 and Figure 3-36 respectively. The microstructure of the over-tempered zone of all of the investigated weldments consisted predominantly of tempered martensite. Increasing interpass temperature for 120°C to 250°C appears to have little to no effect on the microstructure of over-tempered region of the weldments produced by both tested consumables. This observation is consistent with hardness data presented in previous section.

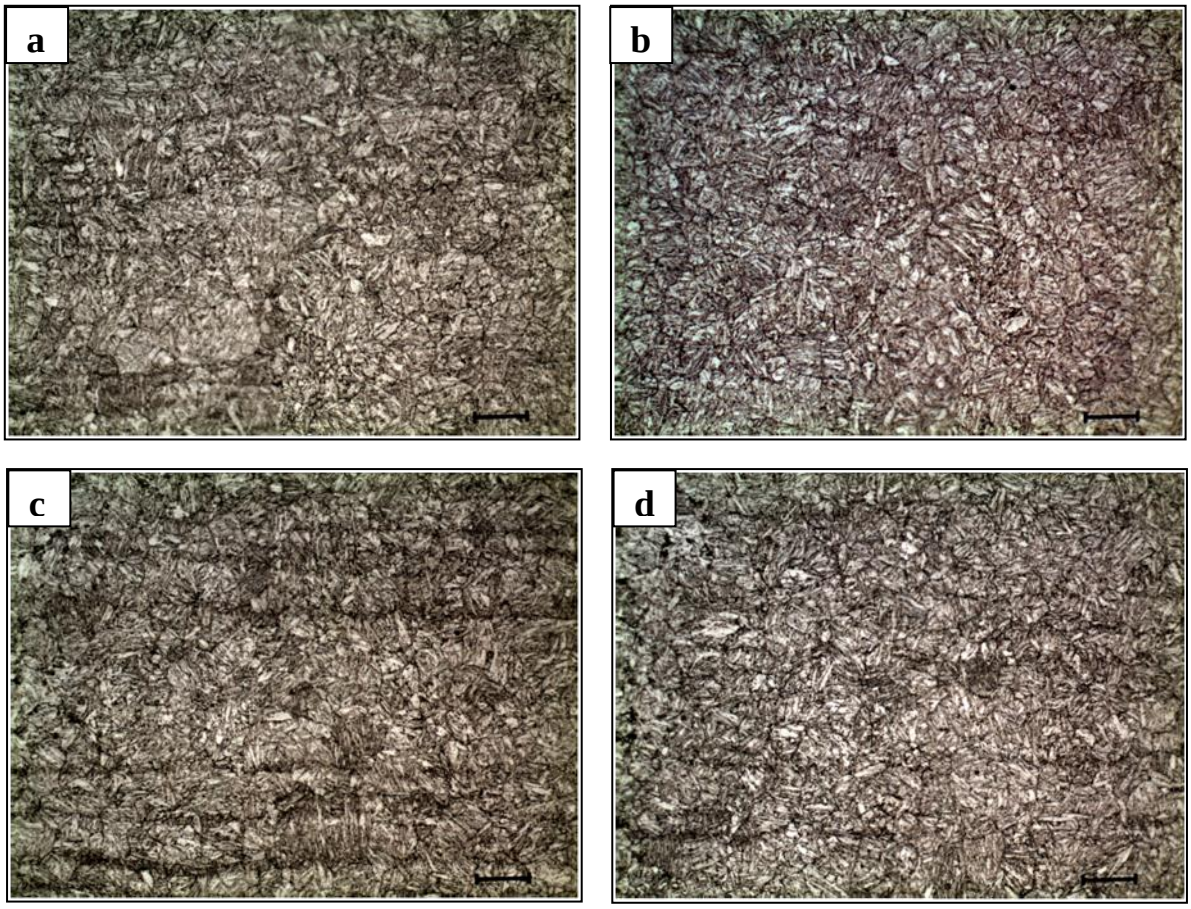

Figure 3-35 Microstructure of the over-tempered HAZ region of the 5 pass corner welds deposited with flux-cored consumable employing ambient preheat and various interpass temperatures; a - 120°C, b – 160°C, c - 200°C, d - 250°C. Note: micron bar represents 20 microns.

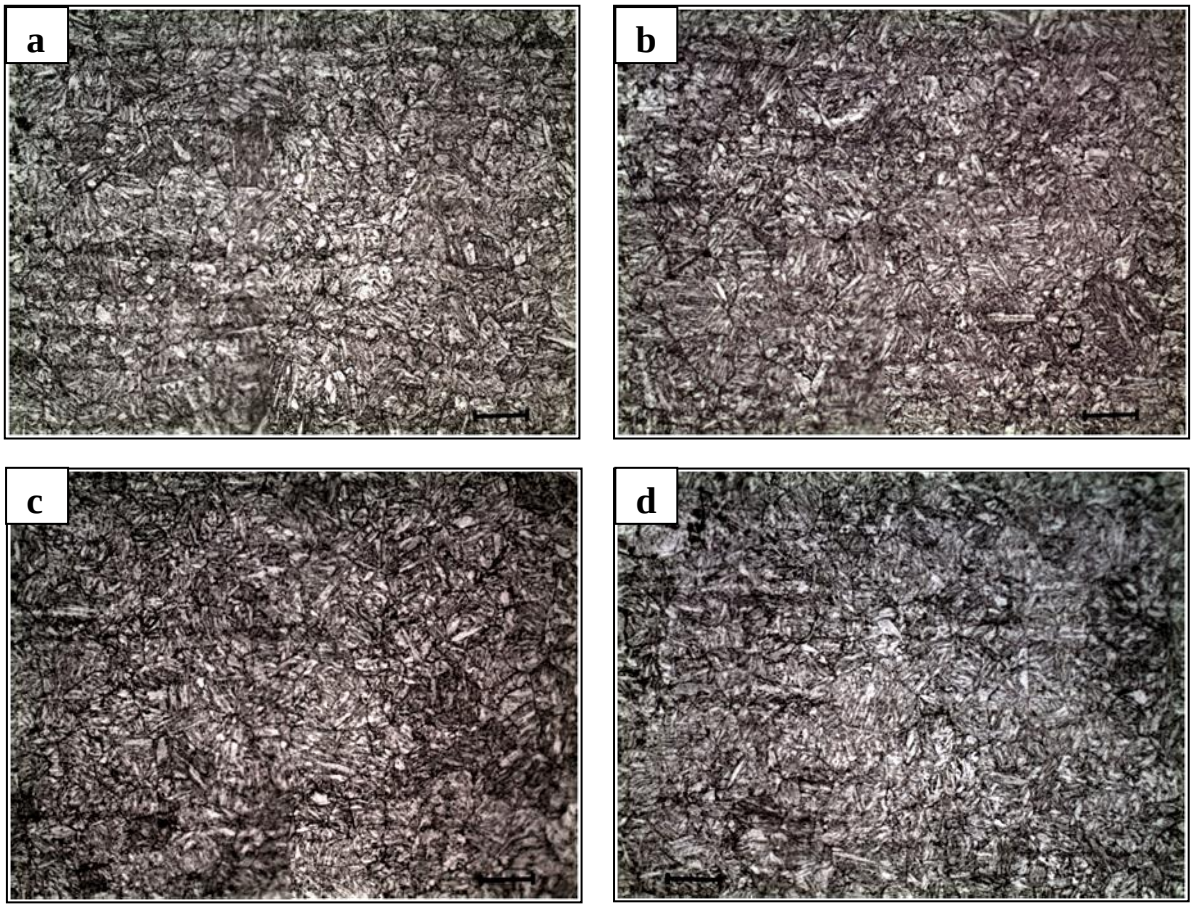

Figure 3-36 Microstructure of the over-tempered HAZ region of the 4 pass corner welds deposited with metal-cored consumable employing ambient preheat and various interpass temperatures; a - 120°C, b – 160°C, c - 200°C, d - 250°C. Note: micron bar represents 20 micrometers.

3.3 FEASIBILITY OF HYBRID LASER-GMAW FOR JOINING HHA STEEL

The objective of this part of the research was to investigate the feasibility of the hybrid laser-GMAW process for welding HHA, and if found feasible, provide recommendations for direction of the future development of the process. Initial testing was carried out to understand the capabilities and limitations of the testing infrastructure available for this investigation and also to develop the skills to operate the apparatus. This involved basic testing conducted predominantly on mild steel, the majority of the results of this preliminary testing is not included in this document. The main aim was to produce the high hardness armour corner joint of similar configuration to the joint used for GMAW trials. Further, to

investigate the microstructure and hardness resulting from this process and assess the suitability of this process for future replacement of conventional multipass GMAW.

3.3.1 Procedure development

Gap between plates

During early testing, it was concluded that hybrid laser-GMAW system in combination 3kW diode laser does not have sufficient power to achieve the required penetration through test plates tacked tight against each other. As a result of insufficient power of the laser source, the gap dividing the HHA plates was introduced to aid the penetration. A series of trials determined the optimum width of the gap to be 1.5 mm.

Table 3-11 lists a summary of the test parameters and results obtained during process development. For tests 1-9 presented in this table, only the hybrid laser-GMAW pass was completed so penetration could be measured without sectioning the weld. For tests 10-11 both weld passes were completed. The inner GMAW pass was deposited first followed by hybrid laser-GMAW pass. In between these two passes the plates were allowed to cool down to ambient temperature of 19°C.

Table 3-11 Summary of the test parameters subjected to optimisation and obtained results.

Test number	Experimental test parameters					Notes
	Overlap [mm]	Gap [mm]	WFS [m/min]	TS [mm/min]	LWD [mm]	
For the following tests only cap hybrid laser-GMAW pass was deposited						
1	5	1	5	380	**0**	Very poor penetration
2	5	1	5	380	**1**	Improved penetration
3	5	1	5	380	**2**	Very poor penetration
4	5	**1.5**	5	380	1	Good penetration
6	5	1.5	**6**	380	1	Poor penetration
7	**3**	1.5	5	380	1	Insufficient penetration
8	3	1.5	5	**300**	1	Improved penetration
9	3	1.5	5	**250**	1	Satisfactory penetration
Following tests included both cap hybrid laser-GMAW and inner GMAW weld pass						
10	3	1.5	5	250	1	Inner pass deposited using flux-cored consumable. Flux trapped in the plate gap.
11	3	1.5	5	250	1	Inner pass deposited using solid consumable. Complete fusion obtained.

WFS - Wire Feed Speed

TS - Travel speed

LWD – Laser to Wire Distance

Laser to wire distance

Tests 1-3 (refer to Table 3-11) showed that the laser to GMAW wire weld pool distance significantly effect depth of penetration. The deepest penetration was obtained when a laser to wire distance of 1mm was employed. Tests 4 and 5 (refer to Table 3-11) indicate that the optimal laser to wire distance will also change depending on wire feed speed. If the wire feed speed is too high too much molten metal is present in the weld pool and interferes with the action of the laser. The initially selected wire feed speed of 5 m/min was found to be optimum. Higher wire feed speeds resulted in insufficient penetration. Lower wire feed speeds were not considered in this investigation as the current geometry requires quite large area to be filled with weld deposit.

Travel speed

After experimental parameters for geometry with 5 mm overlap were optimised to deliver good penetration the overlap was decreased to 3 mm increasing the thickness to be penetrated. Travel speed affects the overall energy delivered into the weldment. The penetration improved when the travel speed was decreased from 380 to 300 mm/min and Test 9 (refer to Table 3-11) showed that it is possible to create a hybrid laser-GMAW pass with sufficient penetration when the travel speed was reduced to 250 mm/min and 1.5 mm gap was present between the plates. Approximately 1.5 mm of plate overlap remained to be filled by the conventional GMAW fillet weld. A macrograph of the weld cross-section of this trial is shown in Figure 3-37.

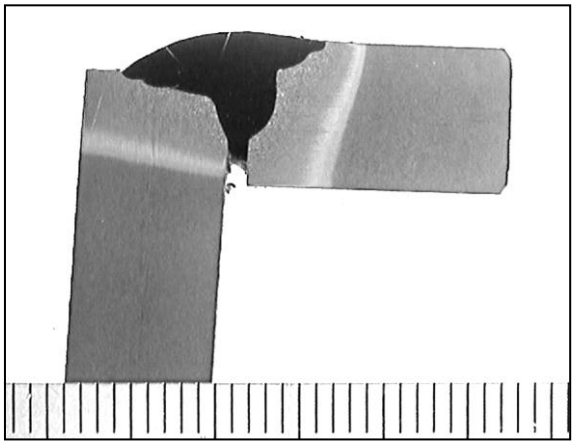

Figure 3-37 Macrograph of the weld cross-section produced with parameters detailed in Table 3-11 - Test 9. Note: Scale is in millimetres.

Test 10 (refer to Table 3-11) was a complete 2 pass joint consisting of both GMAW and hybrid laser-GMAW passes. The inner GMAW fillet run was deposited with the flux cored consumable. As expected, the hybrid laser-GMAW pass did not fuse with the inner GMAW deposit as flux from the first pass was trapped in the gap between the two HHA plates. Due to this fact, the inner pass of the next Test 11 was deposited utilising a solid consumable. The welding parameters used to produce this joint are shown in Table 3-12. A macrograph of the cross-section of this weld is shown in Figure 3-38. From this figure it is obvious that is possible to create a hybrid laser-GMAW joint with close to ideal geometry employing a 3kW diode laser and parameters detailed in Table 3-11 – Test11.

Table 3-12 Welding parameters of GMAW and hybrid laser-GMAW passes used to produce corner joint of suitable geometry.

Pass	Process	Filler	Current [A]	Potential [V]	TS [mm/min]	WFS [m/min]	Shielding gas
1	GMAW	Solid ø1.2	212	26.3	400	9.5	1.5% O_2 in Ar at 20 l/min
2	Laser-GMAW	Solid ø1.2	190	31	250	5	1.5% O_2 in Ar at 20 l/min

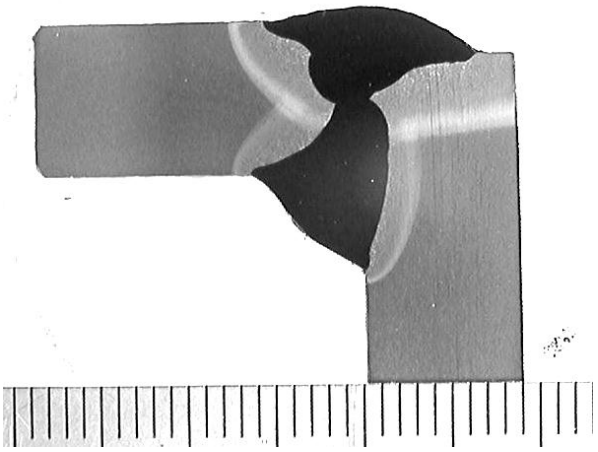

Figure 3-38 Macrograph of the weld cross-section produced with parameters detailed in Table 3-11 - Test 11. Note: Scale is in millimetres.

3.3.2 Hardness measurements

The Hardness of the hybrid laser-GMAW joint was measured and the hardness traverses obtained in A and B orientations are presented in Figure 3-39 and Figure 3-40 respectively. All zones of the weldment are shown: weld metal (WM), fusion line (FL), heat affected zone (HAZ), over-tempered region (OT) and parent metal (PM). The weldment area is again divided into two separate sections: heat-affected zone (HAZ) and over-tempered region as described in section 3.2.2.2.

HAZ hardness

The HAZ hardness measured in both orientations did not exceed the hardness of the original parent HHA steel in Q&T condition. The area possessing highest hardness measured in A orientation was fine-grain sub-zone with hardness of 491 HV with relatively low hardness of 362 HV measured in coarse-grain region. The HAZ hardness measured in B orientation gradually decreased with highest hardness value of 506 HV measured in coarse-grained region. The width of HAZ was measured to be 3.5 mm and 4 mm for A and B orientation respectively. The hardness measured in both orientations followed the same trend of a gradual increase when moving away from inter-critical region.

OT region hardness

The over-tempered region width was measured to be 8.5 mm and 11 mm for A and B orientation respectively. Importantly, in both orientations the value of hardness obtained 15.9 mm from the weld toe appears to be higher than the lowest hardness of 509 HV permitted by MIL- STAN-1185 (AT) [85] Note: MIL- STAN-1185 (AT) [85] states that welds are acceptable (i.e. the welding did not produce excessive HAZ softening) if the structure 15.9 mm from the fusion line possesses hardness of at least 509 HV.

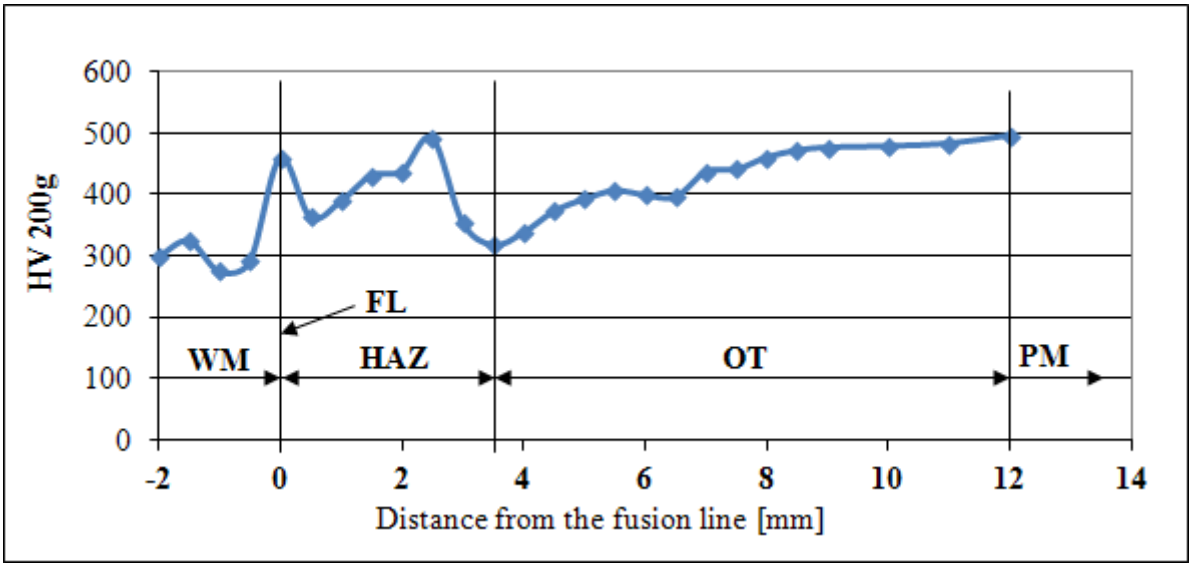

Figure 3-39 Weld hardness profiles measured in the area of hybrid laser-GMAW pass - A orientation. Weld was deposited employing Ambient (19°C) and solid austenitic stainless steel consumable. Note: Each hardness value represents the average value of the three measurements. Standard deviations for WM, HAZ and OT regions were in the range of ±19 to ±73, ±4 to ±24 and ±8 to ±32 respectively.

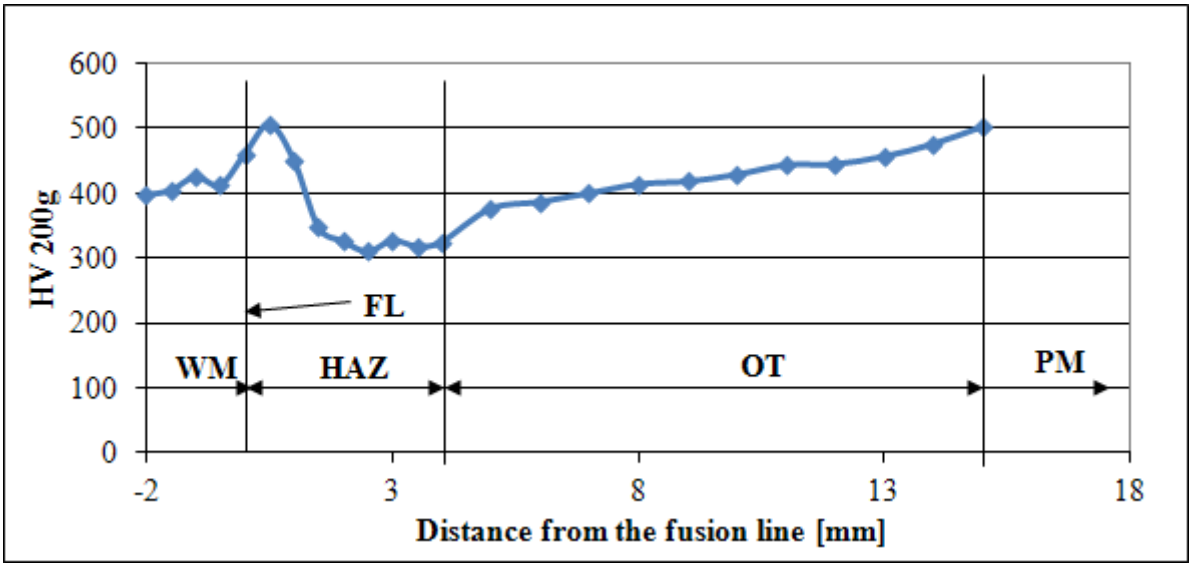

Figure 3-40 Weld hardness profiles measured in the area of hybrid laser-GMAW pass - B orientation. Weld was deposited employing Ambient (19°C) and solid austenitic stainless steel consumable. Note: Each hardness value represents the average value of the three measurements. Standard deviations for WM, HAZ and OT regions were in the range of ±17 to ±63, ±3 to ±16 and ±6 to ±28 respectively.

3.3.3 Metallographic analysis

After hardness testing the sample was subjected to metallographic observation to investigate the effect of the hybrid laser-GMAW process on the microstructure of the HHA joint. The microstructural investigation was carried out in two locations of the weldment as shown in Figure 3-41. Both these areas were examined due to the variations in HAZ of the hybrid laser-GMAW pass produced in the direction parallel and perpendicular to the direction of the laser.

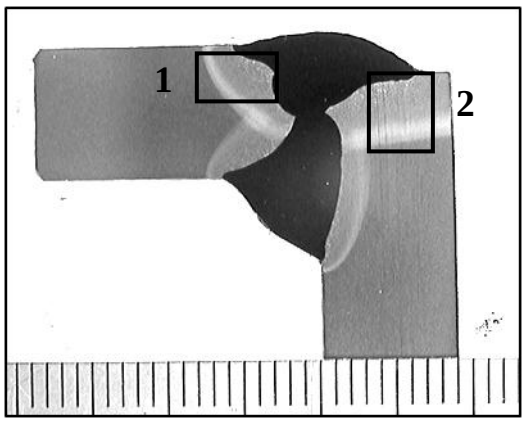

Figure 3-41 Macrograph of the 2-pass corner joint showing the area subjected to microstructural investigation.

From low magnification micrographs displayed in Figure 3-42 it is obvious and it is consistent with the hardness data. The hybrid laser-GMAW pass produced considerably wider HAZ in the direction parallel to the direction of the laser. It was noticed that all sub-zones of the HAZ exhibit increase in width. The HAZ produced in the direction perpendicular to the direction of the laser possesses a shape similar to HAZ produced by conventional GMAW process.

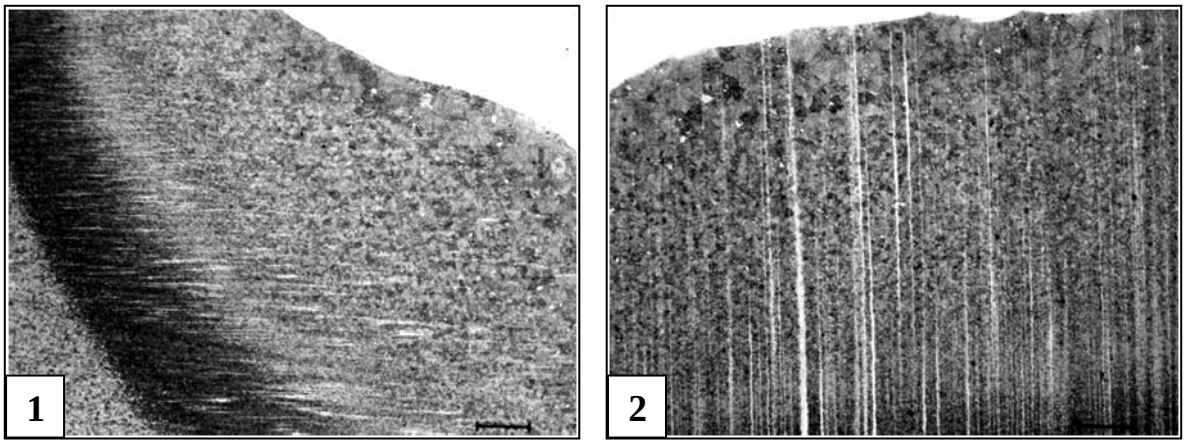

Figure 3-42 Microphotographs depicting different HAZ subzones ((1 - from right): weld metal, coarse-grained region, fine-grained region, inter-critical region, over-tempered region and parent material) and (2 - from the top): weld metal, coarse-grained region, fine-grained region and part of the inter-critical region) of the 2 pass corner joint with 2nd pass deposited utilising hybrid laser-GMAW process. Micrographs marked as 1 and 2 were acquired in corresponding areas shown in Figure 3-41. Micron bar represents 380 micrometers.

Figure 3-43 displays the microstructure of all HAZ subzones of the 2-pass corner weld produced by conventional GMAW (1st pass) and hybrid laser-GMAW process (2nd pass) both deposited employing solid austenitic stainless steel consumable and 23°C (ambient) preheat. Photographs were taken in two orientations as shown in Figure 3-41. The microstructure of the coarse-grain sub-zone in both orientations comprised predominantly of upper and lower bainite and martensite. A small portion of grain-boundary ferrite was also formed close to the fusion line in the orientation perpendicular to the direction of the laser beam. A higher volume fraction of martensite was present in the structure with the amount increasing when moving away from the fusion line. The coarse-grain sub-zone in the orientation parallel to the direction of the laser beam exhibited greater width and softer structures of upper and lower bainite were formed over a larger region at the expense of martensite compared to orientation 1. Mainly upper and lower bainite and martensite but also a small portion of fine grain boundary ferrite was observed in the microstructure of fine-grain region in both orientations with the orientation parallel to the direction of the laser containing higher volume fraction of softer features. From the micrographs it is obvious that inter-critical region in the orientation parallel to the direction of the laser has a much greater width with higher volume fraction of partially transformed constituents of the parent plate original microstructure. The microstructure exhibits mixed mode consisting of newly formed ferrite and bainite and

heavily tempered martensite. The microstructure of the over-tempered regions showed only marginal differences with tempered martensite being the main constituent.

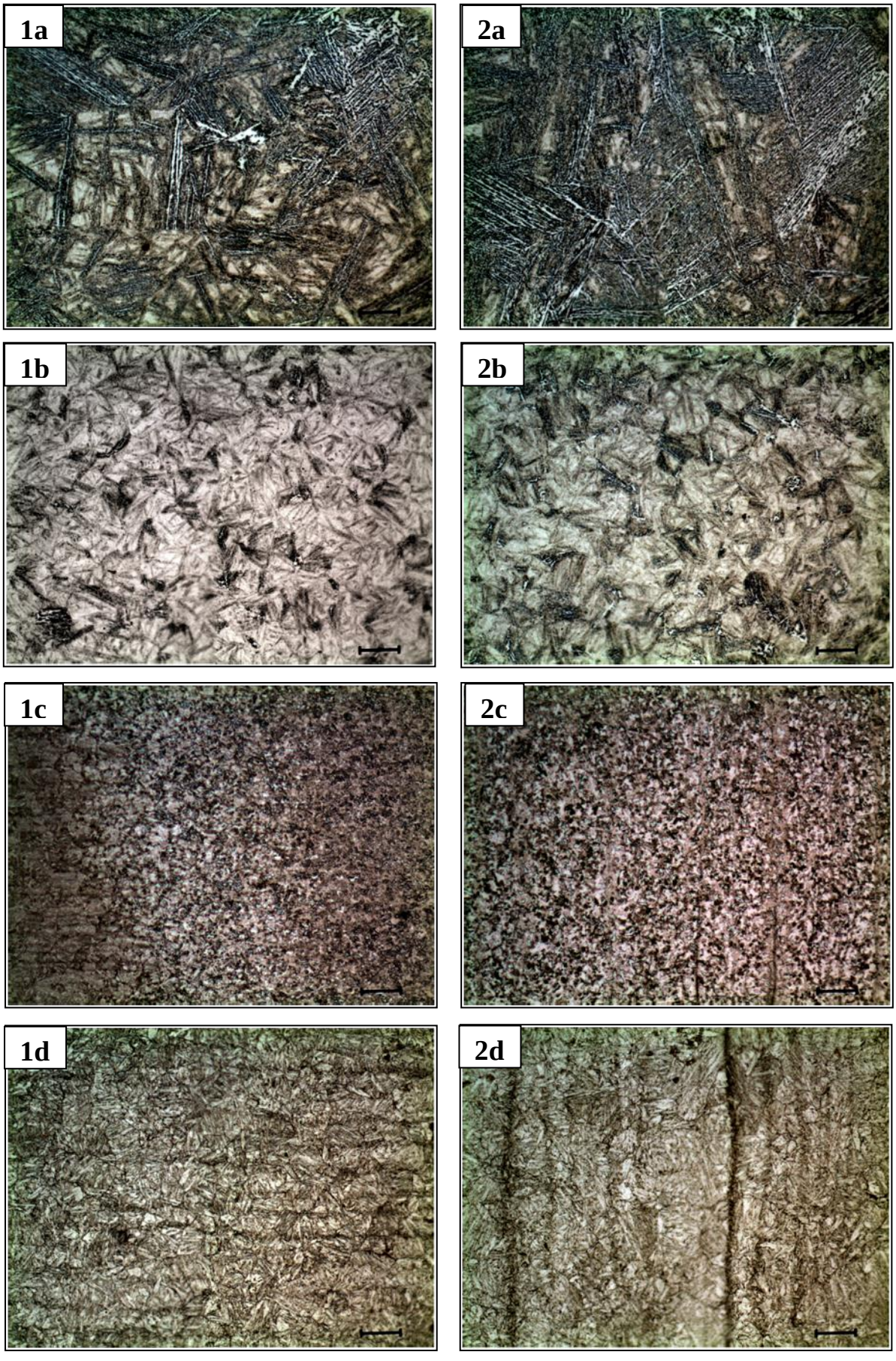
1a
2a
1b
2b
1c
2c
1d
2d

Figure 3-43 Microphotographs showing different HAZ subzones of the 2 pass corner joint with 2nd pass deposited utilising hybrid laser-GMAW process (from top): a - coarse-grained region, b - fine-grained region, c - inter-critical region, d - over-tempered region. Micrographs marked as 1 and 2 were acquired in the cap areas shown in Figure 3-41. Micron bar represents 20 micrometers except of the micrographs picturing inter-critical regions (1c and 2c) where micron bar represents 50 micrometers.

3.4 HYDROGEN TESTING

The main objective of this part of the investigation was to quantify the effect of the previously used ferritic and currently used austenitic welding consumables on the type, level and distribution of the hydrogen across the HHA weldment. A further aim was to investigate the effects of different levels of preheat and also various type of austenitic stainless steel consumable (flux-cored, metal-cored and solid) on hydrogen levels present in the HHA welds.

3.4.1 Deposition of weld metal on test piece assembly

During all welding trials the welding parameters were recorded. The parameters which were held constant for all trials are presented in Table 2-14 and variable welding parameters are displayed in Table 3-13. Every test with selected conditions was performed three times. Macrographs of the representative samples of all trials are shown in Appendix 4. The first series of three trials was also repeated two times to gain confidence in repeatability and consistency of the results. Further, for every residual hydrogen test three samples of weld metal were sectioned out of all three centre pieces welded under the same conditions and were tested for residual hydrogen. Results of both diffusible and residual hydrogen testing showed excellent consistency and repeatability (as can be seen in Appendix 4 Complete results of hydrogen testing trials).

Table 3-13 Variable welding parameters of hydrogen testing welding trials. Note: The values given in table are the average value of three trials welded under the same conditions.

Welding trial ID	**PH [°C]**	**Quench [°C]**	**Shielding gas**	**Flow rate [l/min]**	**Amperage [A]**	**Heat input [kJ/mm]**	**Relative humidity [%]**
FC_ASS_APH_DQ	20	Direct	Argoshield 52	16	215	0.85	48
FC_FER_APH_DQ	24	Direct	Argoshield 52	16	253	0.998	68
FC_ASS(PM+WM)_APH_DQ	22	Direct	Argoshield 52	16	218	0.86	70
FC_ASS_7°CPH_150°CQ	6	150	Argoshield 52	16	215	0.85	86
FC_ASS_80°CPH_150°CQ	80	150	Argoshield 52	16	213	0.84	74
FC_ASS_APH_150°CQ	22	150	Argoshield 52	16	220	0.87	65
MC_ASS_APH_150°CQ	22	150	Stainshield	16	294	1.16	58
S_ASS_APH_150°CQ	21	150	Stainshield	20	245	0.97	60

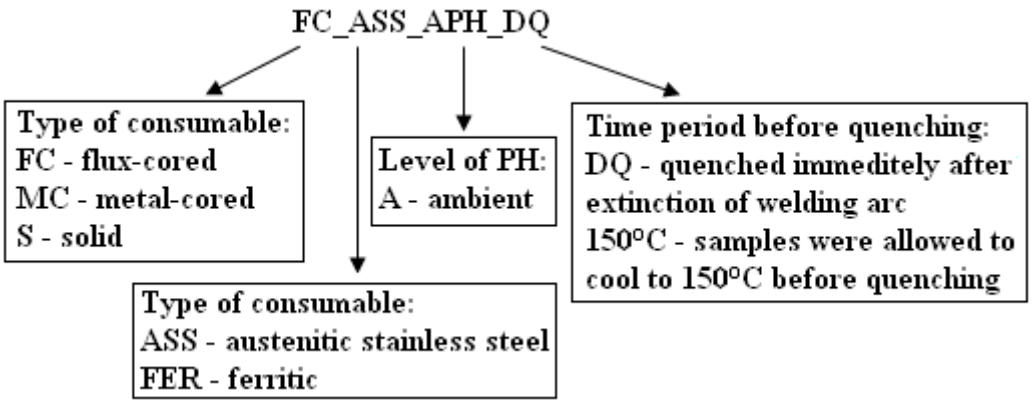

Figure 3-44 Hydrogen welding trials identification explanation.

3.4.2 Effect of welding consumable type on hydrogen level in HHA steel weldment

The measured levels of diffusible and residual hydrogen are presented in Table 3-14. To be able to directly compare the overall amount of hydrogen introduced into the weldment utilising these two ferritic and austenitic stainless steel flux-cored wires, samples were quenched in stirred iced water immediately after extinction of the welding arc. Samples were welded without preheat with ambient temperature of approximately 22°C. The values of 1.3 and 24.3 ml of diffusible hydrogen per 100g of weld metal for austenitic stainless steel and ferritic consumable respectively illustrate the dramatic difference in the amount of diffusible hydrogen present in the weldment. The objective of this study was to measure the diffusible hydrogen levels in HAZ for HHA joints as this part of weldment is highly susceptible to HACC. To prove that all the diffusible hydrogen measured for samples welded with austenitic stainless steel consumable originates from the HAZ only, weld runs employing austenitic stainless steel consumable were also deposited onto 304 austenitic stainless steel base metal. This should, based on the above theory, result in zero diffusible hydrogen. This theory was confirmed as there was no diffusible hydrogen whatsoever released during this testing.

Table 3-14 Levels of diffusible and residual hydrogen measured for austenitic stainless steel (ASS) and ferritic weld metal deposited onto the HHA and also austenitic stainless steel weld metal (WM) deposited onto 304 austenitic stainless steel parent metal (PM). Note: Presented levels of diffusible hydrogen are the average values of three trials and residual weld metal's hydrogen levels the average of nine samples produced under the same conditions.

Consumable	Diffusible H content [ml/100g of WM]	Residual H content [ml/100g of WM]
ASS	1.3	5.8
Ferritic	23.4	0.9
ASS (PM+WM)	0	8

To demonstrate that hydrogen is also present during welding with austenitic stainless steel consumable but is safely "locked" in weld metal, after completion of diffusible hydrogen testing samples were sectioned and weld metal was subjected to residual hydrogen testing. The resulting 5.8 ml of hydrogen per 100 g of weld metal indicates that indeed the hydrogen is "locked" in the microstructure of austenitic stainless steel weld metal. Whereas the low value of 0.9 ml of hydrogen per 100g of ferritic WM suggests that the majority of hydrogen diffused out of the WM / into the HAZ.

3.4.3 Effect of preheat (PH) temperature on hydrogen content in HHA joints welded with flux-cored austenitic stainless steel (ASS) consumable

One objective of this study was to identify the lower safe PH temperature threshold for welding HHA steel with flux-cored ASS consumable that would allow lowering or possibly eliminating the normal PH temperature of 80°C. The measured levels of diffusible and residual hydrogen in the HHA samples welded utilising flux-cored ASS wire employing three different PH temperatures (80°C, Ambient (22°C) and 7°C) are presented in Table 3-15. To be able to compare the influence of various levels of PH on diffusible hydrogen content, samples were allowed to cool down to 150°C after the weld run prior to quenching. The results show that a decrease in the PH temperature from 80°C to 22°C and 7°C resulted in an

increased level of diffusible hydrogen from 0.5 to 0.8 and 1.3 ml of hydrogen per 100g of deposited WM respectively, but the level of the WM's residual hydrogen content decreased from 8.0 to 7.9 and 6.1 ml of hydrogen per 100g of deposited WM respectively.

Table 3-15 Levels of diffusible and residual hydrogen measured for ASS WM deposited onto HHA PM under different PH conditions. Note: Presented levels of diffusible hydrogen are the average values of three trials and residual WM's hydrogen levels the average of nine samples produced under the same conditions.

PH temperature [°C]	Diffusible H content [ml/100g of WM]	Residual H content [ml/100g of WM]
7	1.3	6.1
Ambient (22)	0.8	7.9
80	0.5	8.0

3.4.4 Comparison of hydrogen level of three types of ASS consumable

Levels of diffusible and residual hydrogen contents measured for three different types of ASS wires namely flux-cored, metal-cored and solid wire are displayed in Table 3-16. As expected the highest levels of both diffusible and residual hydrogen were present when employing flux-cored wire. This is due to the presence of the rutile flux the major source of hydrogen contamination. Metal-cored deposits resulted in 38% and 42% reduction of diffusible and residual hydrogen respectively compared to flux-cored welds. Samples produced employing solid wire did not release any diffusible hydrogen at all and the residual hydrogen content was reduced by 53% and 20% compared to flux-cored and metal-cored wires respectively.

Table 3-16 Values of diffusible and residual hydrogen levels measured for three different types of ASS consumable deposited onto HHA. Note: Presented levels of diffusible hydrogen are the average values of three trials and residual WM's hydrogen levels the average of nine samples produced under the same conditions.

ASS consumable type	Diffusible H content [ml/100g of WM]	Residual H content [ml/100g of WM]
Flux-cored	0.8	7.9
Metal-cored	0.5	4.6
Solid	0	3.7

3.5 ASSESSMENT OF RESIDUAL STRESSES

Experimental welding trials were carried out in an attempt to assess the effect of preheat temperature on weld residual stresses. The magnitude of residual stresses was not measured directly but through comparison of the angular distortion of the corner joint resulting from welding.

All joints were tacked at ambient temperature. Weld passes were deposited utilising preheat temperatures of 80°C and 21°C (ambient). Three weldments were produced for both levels of preheat. Only two valid samples that employed 80°C preheat were taken into account for calculation of angular distortion because during the final trial one of the welding fixtures failed allowing the plates to deform upon cooling. The welding trial could not be repeated due to the lack of HHA steel plates. The laser profiles of the first trials employing 80°C and ambient preheat are graphically presented in Figure 3-45. Profiles were acquired after tacking and also after deposition of the single inner pass when the weldment cooled to ambient temperature. Clamps restraining the HHA plates against movement were removed prior profiling. The laser profile of the joints consisted of 239 single points. The trend line was imposed on the straight section of the profiles representing the corner joint. The value of angular distortion was calculated from equations of the trend lines and is presented numerically in Table 3-17.

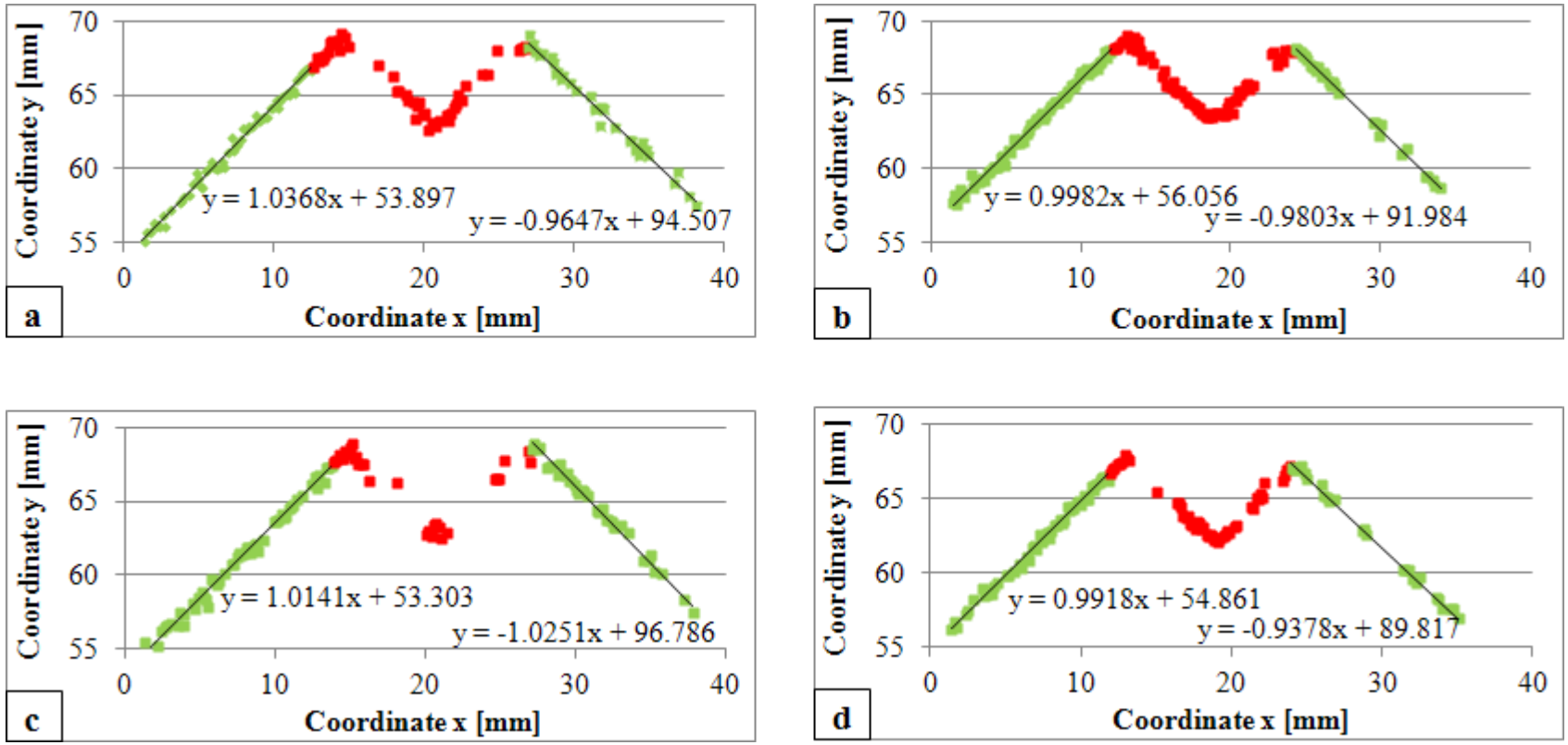

Figure 3-45 Geometry profiles of the first lot of weldments acquired using laser profile sensor. Graphs show equations of the trednlines used to calculate the angles between the HHA plates. a – 80°C preheat, tacked plates, b – 80°C preheat, after deposition of the inner pass, c – 21°C (ambient) preheat, tacked plates, d – 21°C (ambient) preheat, after deposition of the inner pass. Note: laser profiles of remaining weldments are presented in Appendix 6.

Table 3-17 Variation of magnitude of angular distortion of HHA joint as a function of different level of preheat.

Preheat [°C]	**Tack/weld**	**Plate angle [°]**	**Angular distortion [°]**	**Average distortion [°]**
80	Tack 1	90.0	0.6	**0.45**
	Weld 1	89.4		
	Tack 2	90.3	0.3	
	Weld 2	90		
	Tack 3	90.4	-	
	Weld 3	-		
21 (ambient)	Tack 1	91.1	3.2	**2.63**
	Weld 1	87.9		
	Tack 2	91	1.9	
	Weld 2	89.1		
	Tack 3	90.8	2.8	
	Weld 3	88		

The ideal geometry of the corner joint consists of the two adjacent HHA plates set at a 90° angle. The profile of all joints after tacking was considered as reference profile of the joints free from residual stresses. The angle contained by tacked HHA plates was close to 90°. Deposition of the inner weld pass generated uneven thermal gradients resulting in thermal contraction of the weld and HAZ introducing thermal strains in the weldment. After the temperature dropped to ambient and clamps were removed accumulated stresses higher than yield stress of parent material transformed to angular distortion. The reduction of the preheat temperature resulted in higher value of angular distortion. The average value of the measured distortion was 0.45° and 2.63° for joints welded with 80°C and 21°C (ambient) preheat respectively.

4 DISCUSSION

Some discussion of the material presented has been provided in the preceding experimental and results sections but the following section brings together the overall results of the work, their significance and validity in relation to the original objective. It also discusses the sources of error and the validity of the assumptions made.

4.1 CONTINUOUS COOLING TRANSFORMATION BEHAVIOUR OF HHA STEEL

It has previously been recognised that CCT diagrams help to develop safe welding procedures that ensure improved and more consistent properties of the steel welds [19]. For a given chemical composition they identify the relationship between cooling rate, transformation temperature range, resultant microstructure (decomposition products of γ→α transformation) and hardness. Different steels experience diverse difficulties in various locations in the HAZ or weld metal itself when subjected to welding. By designing the appropriate thermal cycle and peak temperature various areas of the heat affected zone can be simulated through dilatometry studies and these help to understand and predict the development of the microstructure under different cooling conditions. One practical advantage of producing such samples is considerably higher volume of material possessing microstructure corresponding to particular area of interest compared to that found in real weldments. In the present investigation the CCT diagram (refer to Figure 3-2) simulating the coarse-grain region of HHA steel was developed. No previous CCT data existed for the steel studied. As is obvious from chemical composition (refer to Table 2-1) the HHA steel studied here possesses very high hardenablity and the microstructure consisted of hard bainitic and martensitic constituents even when slow cooling rates were employed. As expected the transformation temperature range was shifted to lower temperatures with increasing cooling rate due to the formation of low temperature products [77]. In the current work considerable effort was taken to produce reliable CCT diagrams for the steel being evaluated. The validity of the derived diagrams was validated by repeat dilatometry runs and post test metallography.

4.1.1 γ→α phase transformation on cooling

The microstructure of steels is complicated and it is influenced by composition, homogeneity, heat treatment and plate thickness. When steel is subjected to a weld thermal cycle it results in formation of even more complex structures within the HAZ. Phase transformation

occurring on cooling is a more intricate process than the transformation that the steel undergoes during heating due to formation of non-equlibrium phases especially when intermediate and high cooling rates are employed. With increasing cooling rate the diffusion controlled transformation (ferrite + pearlite) is replaced by shear type semi-diffiusionless (bainite) and diffusionless (martensite) transformations [86]. Due to the alloy design and resultant high hardenability of HHA steel the non-equilibrium products form even when slow cooling rates are employed thus the Fe-C equilibrium diagram does not have any practical use when predicting the microstructure produced in welding conditions. Conversely CCT diagrams are designed to provide relevant information about the microstructure and hardness resulting from employing various cooling rates. However before applying the information from CCT diagrams into real welding practice several discrepancies between simulated and real coarse-grain HAZ have to be carefully considered.

4.1.2 Difference in thermal cycle of simulated and real coarse-grain HAZ

The HAZ of the real weld experiences more rapid heating to peak temperature than samples subjected to dilatometry experiments. The average heating time of the coarse-grain region to peak temperature measured for bead-on-plate welds was approximately 1.6 s while due to the limitations of experimental equipment the heating time of dilatometry samples to the selected austenitisation temperature was 27 s. Even though the peak temperature during real welding was measured to be in the range of 1349°C to 1411°C, well above the nominal A_{c1}, the extremely fast heating rate is expected to shift the A_{c1} to a higher temperatures and allows significantly less time for re-austenititsation and homogenisation of austenite through dissolution of inclusions and precipitates. In addition the average time spent at peak temperature of the real welds was measured to be approximately 0.25 s, considerably shorter than during dilatometry simulations (2 s) this would have the effect of suppressing the austenite grain growth. Prior austenite grain size has a significant effect on formation of austenite decomposition products. Fine austenite grains favour formation of bainite and shifts the bainite start temperature to higher values, thus the smaller austenite grains produced in coarse-grain region of real welds can result in higher volume fraction of bainite compared to simulated samples [87]. Unlike bainite the martensite start temperature is only negligibly affected by prior austenite grain size [88]. Shome and Mohanty [89] during their study of continuous cooling transformation behaviour of HSLA-80 and HSLA-100 steel grades

observed that coarse austenite grains promoted formation of lath martensite with larger gaps in between the single laths. However extensively large austenite grains were divided into several sub-grains due to formation of nonparallel variants refining the structure of lath martensite. They also observed formation of higher ratio of lath martensite to bainite and transformation start temperature occurring at lower temperatures with increasing prior austenite grain size due to the reduced amount of nucleation sites. During dilatometry simulations from peak temperature samples were cooled linearly. However, in real welding conditions the coarse-grain HAZ experiences exponential cooling with slower cooling rates through the transformation region (as displayed in Figure 4-1) possibly increasing the transformation start temperature and promoting the formation of softer phases compared to linearly cooled simulated samples. The slower cooling rates through the martensite transformation region create better conditions for auto-tempering of the martensite formed at higher temperatures. If all these differences between simulated and real coarse-grain HAZ are carefully considered the generated CCT diagrams can be of great value in welding metallurgical applications. However, the different conditions experienced during welding (as described above) compared to dilatometry experiments should be considered and taken into account.

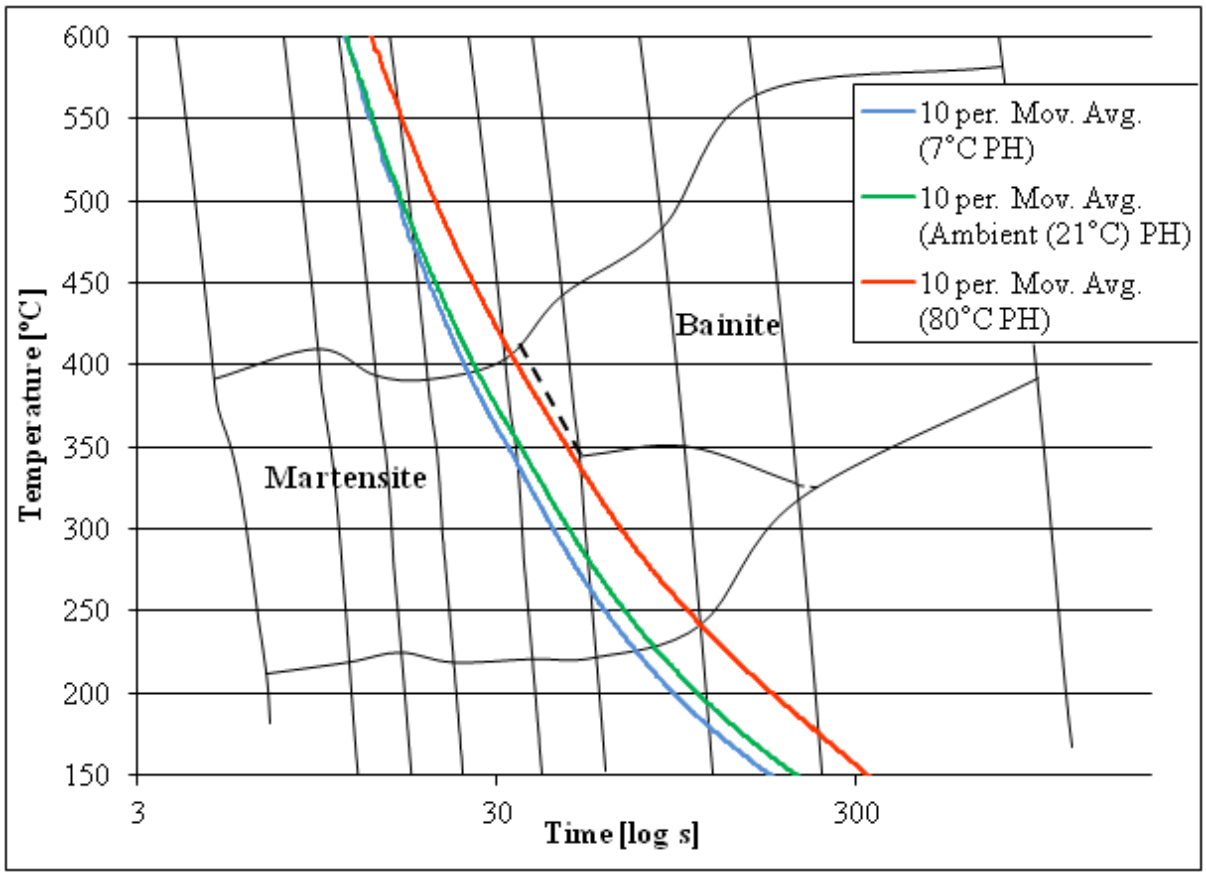

Figure 4-1 CCT diagram showing comparison of cooling conditions through transformation region of simulated dilatometry samples subjected to various cooling rates and actual coarse-grain HAZ of the joints welded with preheats of 7°C, ambient (23°C) and 80°C.

4.1.3 Comparison of coarse-grain HAZ microstructure of the simulated and real weld samples

In this section the comparison of the microstructure between the simulated coarse-grain HAZ (dilatometry samples) and coarse-grain HAZ of the real welds was made. Figure 4-2 displays the microstructure of a dilatometry sample and the coarse-grain HAZs of the singe pass fillet weld welded with flux-cored and metal-cored consumable employing various levels of preheat. The dilatometry sample subjected to a cooling rate (20°C/s) which produced a microstructure most similar to the real welding conditions was selected for this comparison.

Due to the corner joint configuration used for deposition of bead-on-plate welds employing 7°C and 80°C preheat the recorded thermal history of the coarse-grain HAZ is very similar to thermal history of coarse-grain region of single pass fillet weld produced employing the

identical preheat temperatures. For these reasons these thermal profiles were considered when comparing the thermal history of the coarse-grain HAZ of the single pass fillet welds produced with flux-cored consumable with the dilatometry samples. The heat input of the two procedures employing flux-cored and metal-cored consumable is identical thus the recorded thermal history also applies to the single pass fillet welds produced with the metal-cored consumable. The microstructure of the dilatometry sample subjected to 20°C/s cooling rate exhibited greatest similarity to the coarse-grain HAZ of the weldments produced with both tested consumables and levels of preheat.

The cooling curves of the welds preheated to 80°C and 7°C plotted onto the CCT diagram are both located in the martensitic region (refer to Figure 4-1). The cooling time t8/5 of the dilatometry sample (~15 s) was a little longer compared to real welds (t8/5(80°CPH) = 12.6 s and t8/5(7°CPH) = 9 s) thus it is expected that transformation start temperature of the welded specimens was suppressed to slightly lower temperatures. However, the cooling time through transformation region t6/2 of the dilatometry sample that cooled linearly was significantly shorter (~20s) compared to real welds that cooled exponentially (t6/2(80°CPH) = 159 s and t6/2(7°CPH) = 81 s), thus it is expected that bainitic field of the welded specimens was shifted to the left. This consequently resulted in formation of higher volume fraction of bainite of the weld preheated to 80°C compared to simulated dilatometry sample.

Both weldments (flux-cored and metal-cored) produced with 7°C preheat contained less bainitic features compared to joints preheated to 80°C and the microstructure consisted predominantly of martensite. These findings suggest that in real welding conditions the critical cooling rate for formation of 100% martensite is shifted to the left compared to the generated CCT diagram.

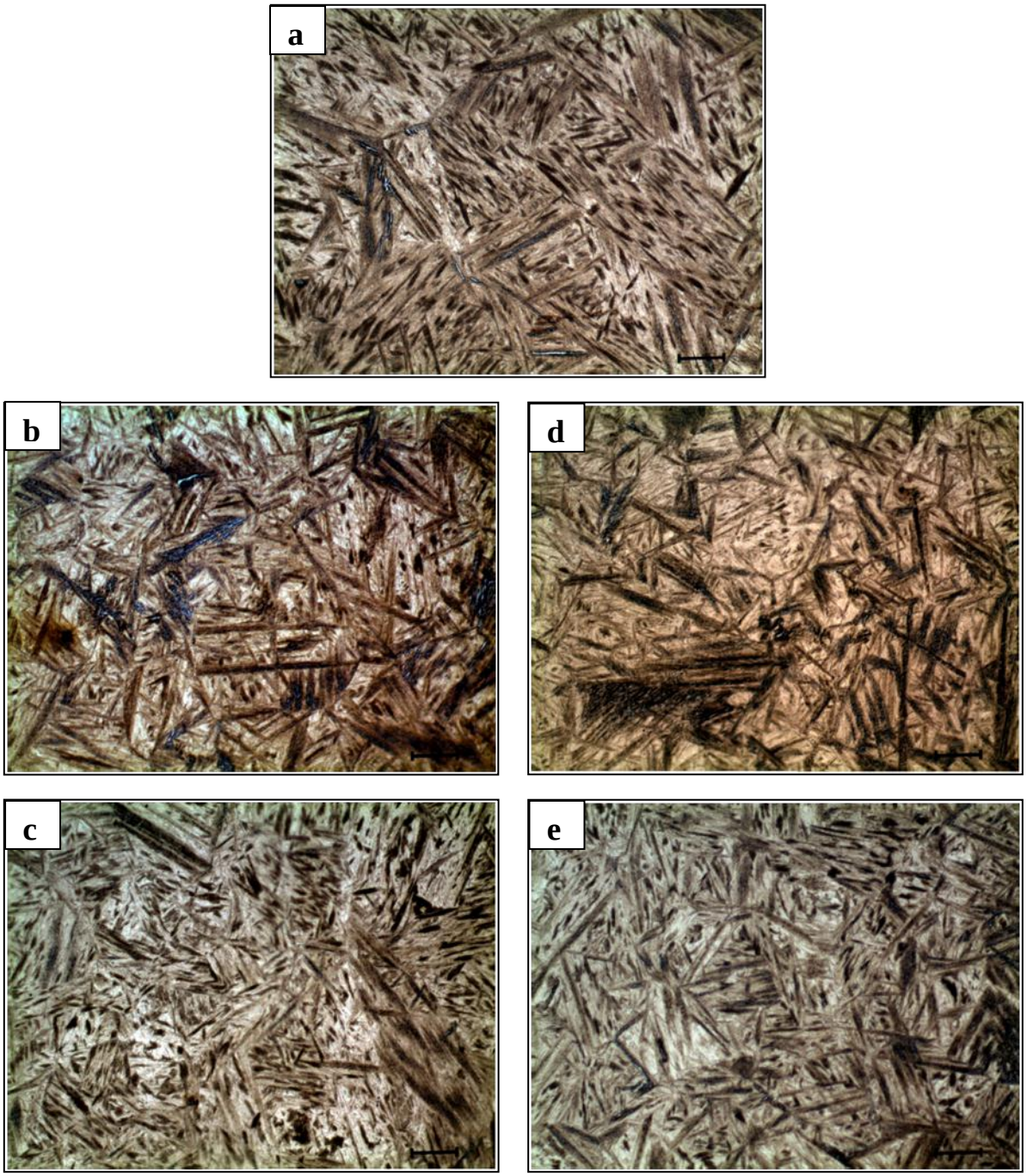

Figure 4-2 Typical microstructure of: a – dilatometry sample subjected to 20°C/s cooling rate; b – coarse-grain HAZ of the 1 pass fillet weld welded with flux-cored consumable and 80°C preheat; c - coarse-grain HAZ of the 1 pass fillet weld welded with flux-cored consumable and 7°C preheat; d - coarse-grain HAZ of the 1 pass fillet weld welded with metal-cored consumable and 80°C preheat; e - coarse-grain HAZ of the 1 pass fillet weld welded with metal-cored consumable and 7°C preheat Note: micron bar represents 20 microns.

The grain size of all simulated dilatometry samples appears to be larger than the grain size obtained in the coarse-grain HAZ of the real welds. This is a result of slower heating rate to the peak temperature and also longer (2 s) hold of simulated samples at peak temperature of 1350°C allowing the time for grain growth. Also microstructural features of coarse-grain HAZ of the real welds are finer compared to simulated samples. This is due to the smaller grain size as the formation of diffusionless (martensite) and semi-diffusionless (bainite) products of $\gamma \rightarrow \alpha$ transformation is constrained by the prior austenite grain boundaries and also due to shorter austenititsation times retaining more precipitates acting as a nucleation sites. This means if the grain size is larger the coarser features may form within the grain.

4.2 GMAW WELDING TRIALS

4.2.1 Optimisation of preheat temperature

Q&T steels in the high hardness condition are not only prone to HAZ and weld metal HACC but also to excessive softening of the HAZ and over-tempered region. To develop welding procedures avoiding both of these phenomena and to produce weldments with the desired properties requires the design of procedures employing parameters from a constrained range particularly when ferritic consumables are used. It is also very important to ensure that in manufacturing practice these restricted procedures are carefully followed. The common practice to avoid HACC is the use of sufficient pre or post heating of the weldment. However, both these treatments represent an additional step in the welding process, significantly reduce productivity and increase fabrication costs. Further, post weld heat treatment is not recommended for Q&T steels due to the possibility of stress relief cracking [27]. Some fabricators adopt an alternative approach and use austenitic stainless steel welding consumables. While this may be expected to relax the very restricted range of process parameters, due to the lack of available data the full benefits of its use are limited by the requirement to strictly follow procedures developed for previously used ferritic consumables. These procedures require preheating of the plates prior welding to 80-120°C. The objective of this investigation was to provide solid evidence that preheating of HHA steel prior to welding can be avoided if austenitic stainless consumables are employed.

A series of welding trials were carried out in order to assess the effect of preheat reduction on susceptibility of HAZ of the HHA weldments produced with flux-cored and metal-cored austenitic stainless steel consumable to HACC. From a manufacturers view point employing ambient preheat temperature would be the most beneficial from both aspects of productivity and cost. The typical ambient temperature experienced at the location of manufacturing plant examined in this study is in the range of 15°C to 30°C. However during severe winter periods ambient temperatures can drop to around 7°C. Therefore to be able to eliminate preheat from manufacturing practice altogether the conditions employing the lowest possible ambient temperature need to be considered. Based on the results presented in section 3.2.2 it was concluded that a minimum temperature of 7°C should be examined as a 'worst case' potential candidate for replacement of currently used preheat of 80°C. A comparison of the hardness and microstructure obtained in the HAZ of the joints preheated to 80°C and 7°C is presented in the following section.

4.2.1.1 Comparison of the hardness profiles

Figure 4-3 - Figure 4-6 present the weld hardness profiles of weldments produced with flux-cored and metal-cored consumable in combination with a preheat of 80°C and 7°C. The hardness was measured in both orientations (refer to Figure 2-14). The general trend of a slight increase in hardness can be observed resulting from faster cooling rates with decreasing preheat temperature from 80°C to 7°C. For hardness evaluation purposes the weldment area was again divided into two separate sections: HAZ and OT region (refer to section 3.2.2.2).

<u>HAZ hardness</u>

In case of flux-cored consumable decreasing the preheat temperature resulted in formation of narrower HAZ. The HAZ width decreased by 0.5 mm in both orientations with lowering preheat temperature from 80°C to 7°C. The size of the HAZ decreased from 2.5 mm to 2mm and from 2 mm to 1.5 mm measured in A and B orientation respectively. The HAZ of the HHA joints is the most susceptible region to HACC thus the reduction in size is considered to be beneficial. The HAZ size of the weldments produced with metal-cored consumable was not affected by lowering the preheat temperature with the constant width of 2 mm measured in both orientations. On lowering the level of preheat the HAZ hardness measured in A orientation increased on average by 30 HV and 40 HV for flux-cored and metal-cored

consumable respectively. B orientation exhibited almost identical hardness values for both tested consumables. The only difference in case of flux-cored consumable was slightly narrower inter-critical region and metal-cored consumable produced 50 HV harder coarse-grain region when employing lower preheat. The coarse-grain region, adjacent to fusion line experiences the highest temperature and the steepest thermal history thus it is the most susceptible to HACC of all HAZ sub-zones. Lowering the preheat temperature from 80°C to 7°C resulted in hardness increase of 36 HV measured in A orientation for flux-cored consumable. Hardness measured in orientation B remained almost identical. Higher degree of hardening was observed for metal-cored consumable with hardness increase of 39 HV and 51 HV measured in A and B orientation respectively. However the risk of HACC is not expected to be higher as the metal-cored consumable introduces lower level of diffusible hydrogen into the weld pool compared to flux-cored consumable.

OT region hardness

The hardness and size variations of the OT region with decreasing preheat temperature from 80°C to 7°C is described in detail in section 3.2.2.2. The OT region was not the area of concern when lowering preheat temperature. In general reducing preheat resulted in narrower OT regions with increased hardness in both orientations for both tested consumables. This is beneficial form ballistic view point as the higher volume of original HHA microstructure with optimum properties was preserved when preheat temperature of 7°C was employed.

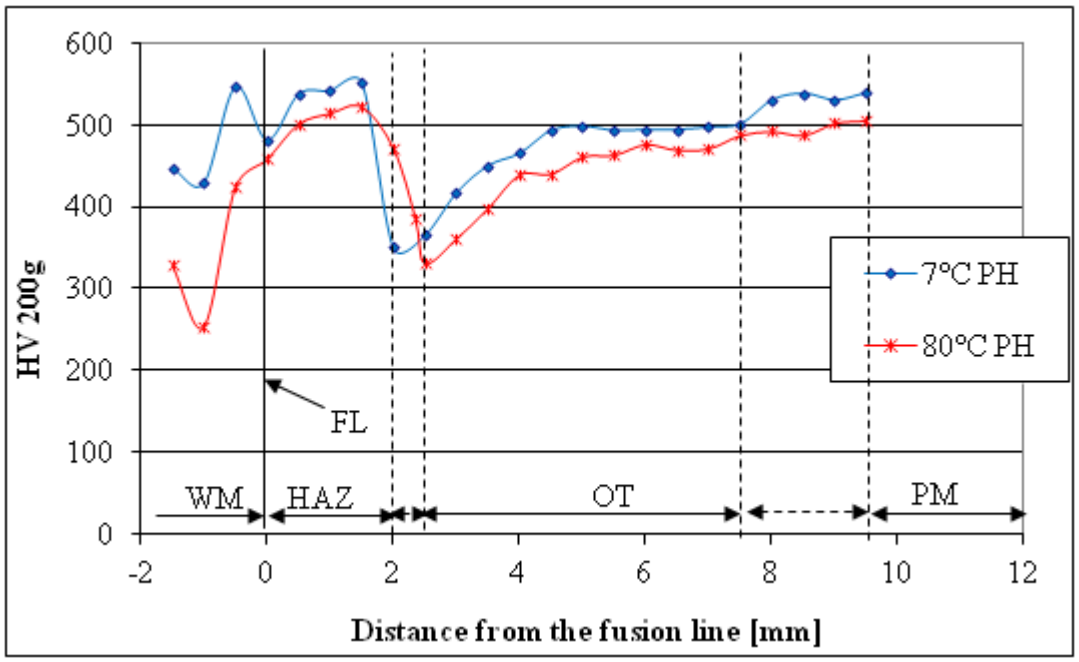

Figure 4-3 Weld hardness profiles measured in A orientation of the 1 pass filet joints welded with flux-cored consumable employing preheat temperatures of 7°C and 80°C. Note: Each hardness value represents the average value of the three measurements. Standard deviations for WM, HAZ and OT regions were in the range of ±23 to ±47, ±5 to ±24 and ±2 to ±19 respectively.

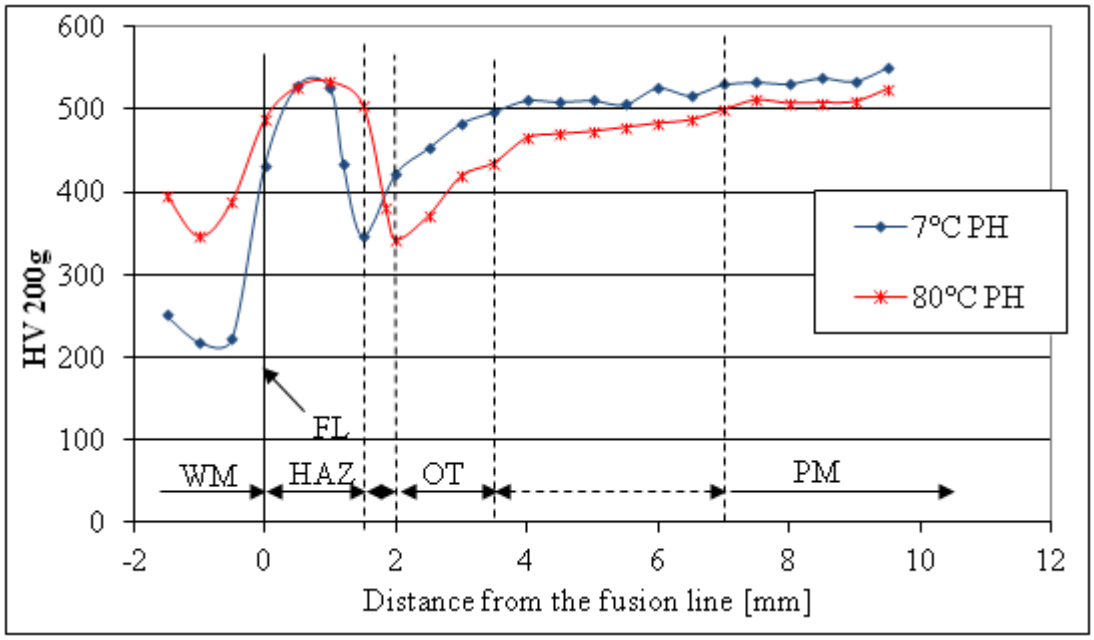

Figure 4-4 Weld hardness profiles measured in B orientation of the 1 pass filet joints welded with flux-cored consumable employing preheat temperatures of 7°C and 80°C. Note: Each hardness value represents the average value of the three measurements. Standard deviations

for WM, HAZ, OT and PM regions were in the range of ±31 to ±37, ±5 to ±17, ±2 to ±25 and ±2 to ±9 respectively.

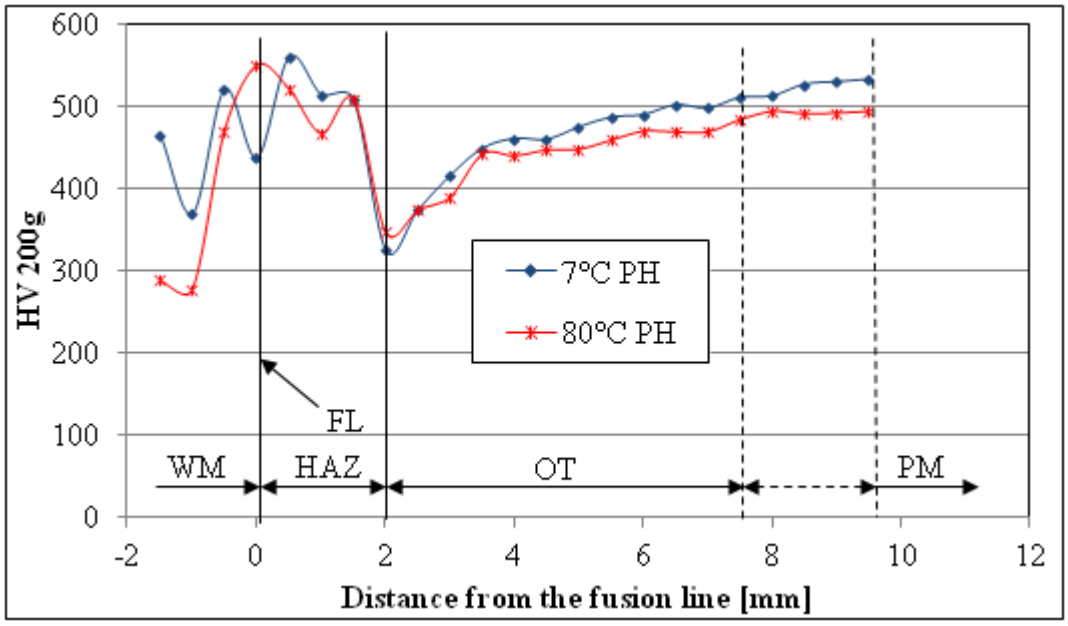

Figure 4-5 Weld hardness profiles measured in A orientation of the 1 pass filet joints welded with metal-cored consumable employing preheat temperatures of 7°Cand 80°C. Note: Each hardness value represents the average value of the three measurements. Standard deviations for WM, HAZ and OT regions were in the range of ±21 to ±81, ±8 to ±23 and ±5 to ±25 respectively.

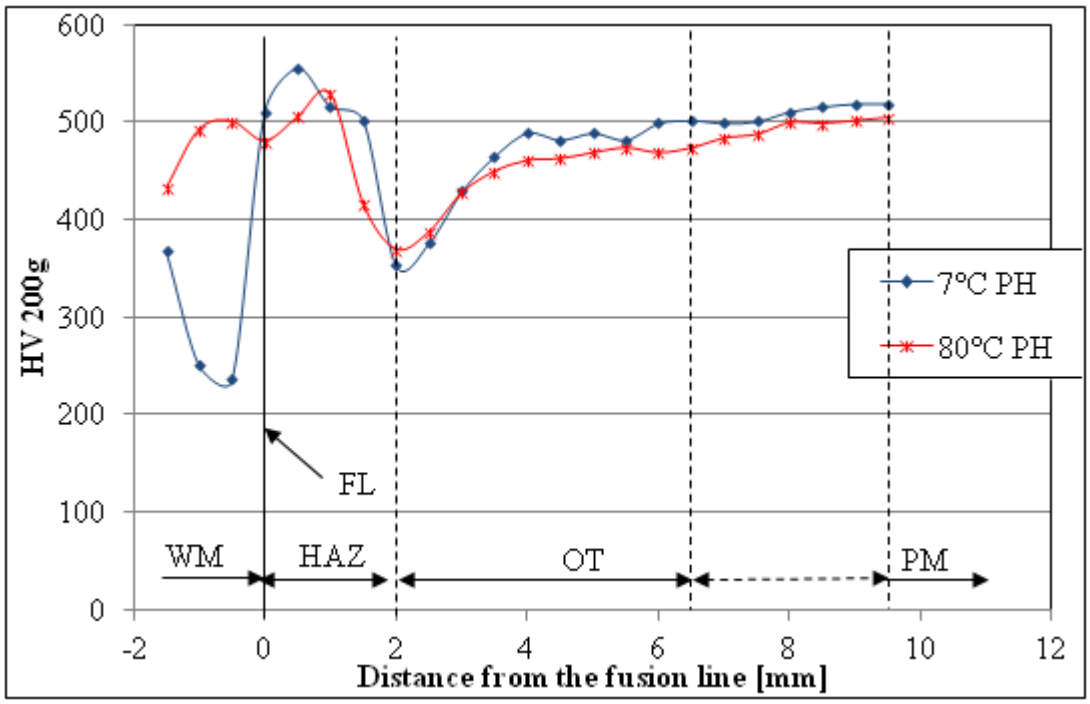

Figure 4-6 Weld hardness profiles measured in B orientation of the 1 pass filet joints welded with metal-cored consumable employing preheat temperatures of 7°C and 80°C. Note: Each hardness value represents the average value of the three measurements. Standard deviations for WM, HAZ and OT regions were in the range of ±34 to ±56, ±5 to ±29 and ±12 to ±14 respectively.

Overall the changes of hardness follow expected trends but the change in HAZ area and relatively small increases in hardness due to the lower preheat temperature are not considered to have a significant effect on the risk of HACC when the other factors discussed below are taken into account.

4.2.1.2 Comparison of the weld microstructure

The aim of preheating the plate prior to welding is to reduce the cooling rate resulting in formation of softer microstructure in the HAZ thus reducing risk of HACC. In the investigated industry application relatively a low preheat temperature of 80°C is employed thus elimination of preheating is not expected to have significant effect on the microstructure formed in the HAZ.

Figure 4-7 and Figure 4-8 display the microstructure of all HAZ subzones (coarse-grain, fine-grain, inter-critical and over-tempered) of the samples produced employing preheat temperatures of 80°C and 7°C welded with flux-cored and metal-cored consumable respectively.

The effect of shorter cooling times with reducing preheat temperature from 80°C to 7°C is the most notable in the coarse-grain region of the HHA joints. The microstructure of the weldments produced employing flux-cored consumable and 80°C preheat exhibited a mixed mode containing upper and lower bainite and martensite. In addition definite ferritic features of upper bainite were present. When the preheat temperature was reduced to 7°C a certain degree of hardening is expected based in the microstructure developed. Increased cooling rate resulted in the formation of a higher volume fraction of lower bainite and martensite and microstructural features became finer. Ferritic features were no longer present. The structure consisted predominantly of martensite. The same trend was observed for weldments produced with metal-cored consumable.

The fine-grain region of all samples consisted of a mixture of lower bainite and martensite. Samples welded with the flux-cored consumable and a preheat of 7°C exhibited a larger amount of harder phases and higher degree of refinement compared to those preheated to 80°C. The fine-grain subzone of the weldments produced with metal-cored consumable employing both preheats appeared to be identical consisting predominantly of martensite.

Decreasing the preheat temperature from 80°C to 7°C resulted in the formation of narrower inter-critical region for both consumables. Fine-grained ferrite, granular bainite and some martensite were observed in the structure of all samples.

The over-tempered sub-zone of all samples had the same appearance with no obvious changes caused by reducing the preheat temperature; they consisted of tempered martensite similar to that of the original parent plate.

Reducing the preheat temperature from 80°C to 7°C resulted in only minor differences in the microstructure of different HAZ sub-zones. The overall trend was formation of slightly higher volume of harder phases with finer microstructural features. Reducing the preheat

temperature also decreases the time spent in the higher temperature range allowing less time for grain growth and coarsening of the original microstructure in the area adjacent to fusion line.

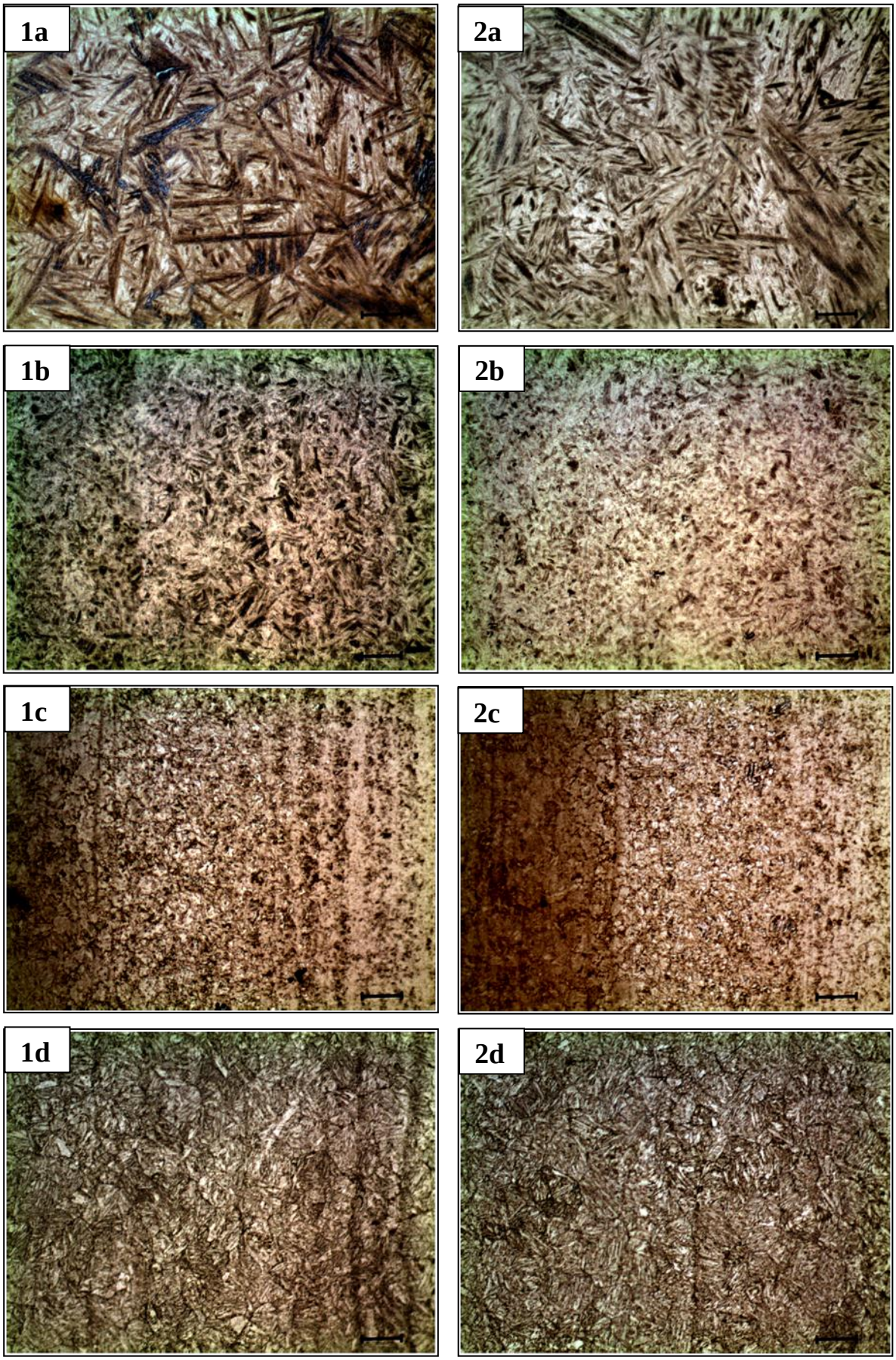
1a
2a
1b
2b
1c
2c
1d
2d

Figure 4-7 Microphotographs showing different HAZ subzones of the 1 pass fillet joint deposited utilising GMAW process in combination with flux-cored austenitic stainless steel consumable (from top): a - coarse-grained region, b - fine-grained region, c - inter-critical region, d - over-tempered region. Micrographs marked as 1 and 2 represent joints welded with 80°C and 7°C preheat respectively. Micrographs were acquired in the cap areas as shown in Figure 3-16. Micron bar represents 20 micrometers except of the micrographs picturing inter-critical regions (1c and 2c) where micron bar represents 50 micrometers.

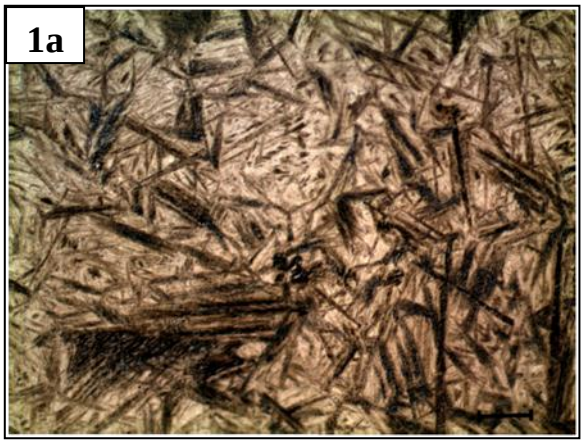
1a

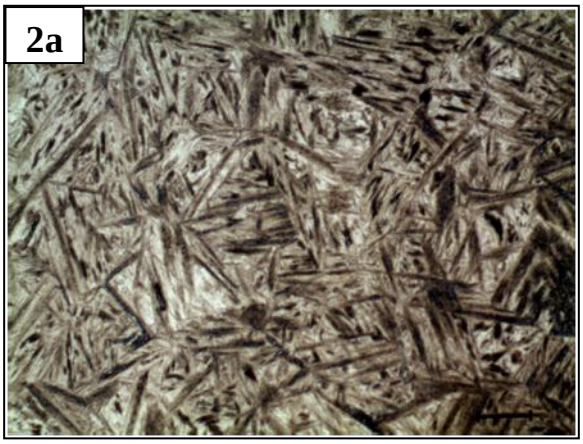
2a

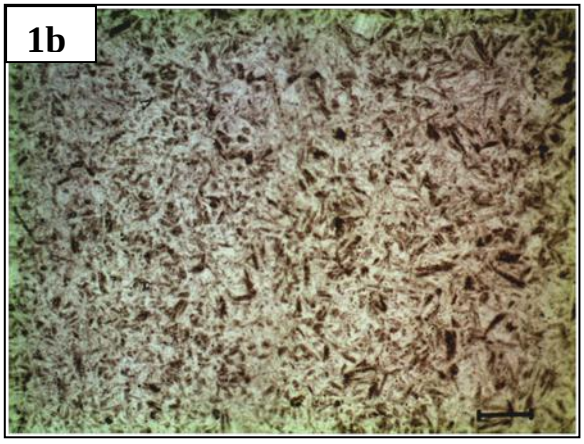
1b

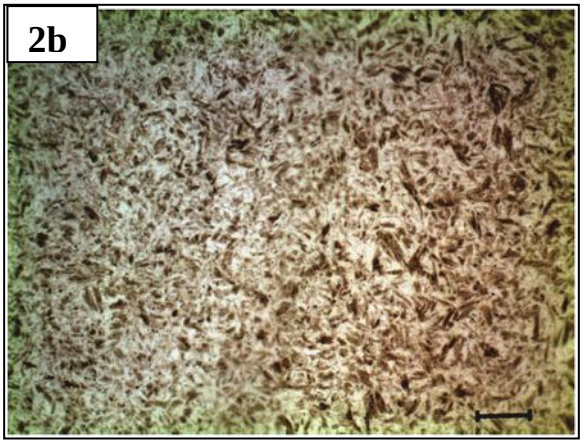
2b

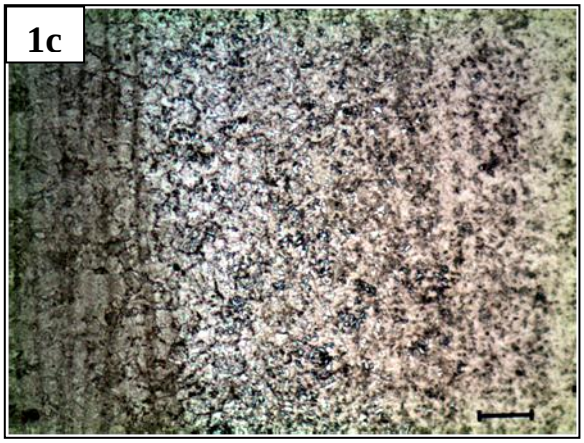
1c

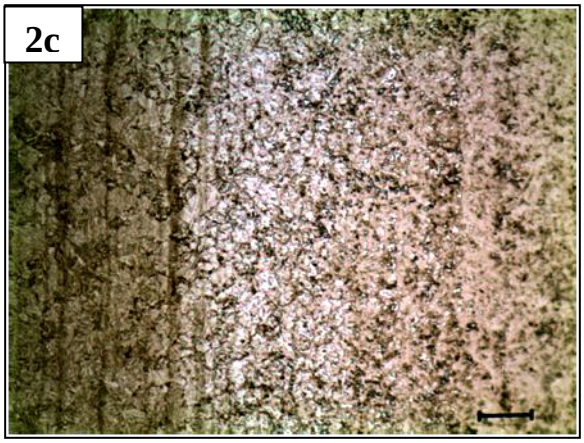
2c

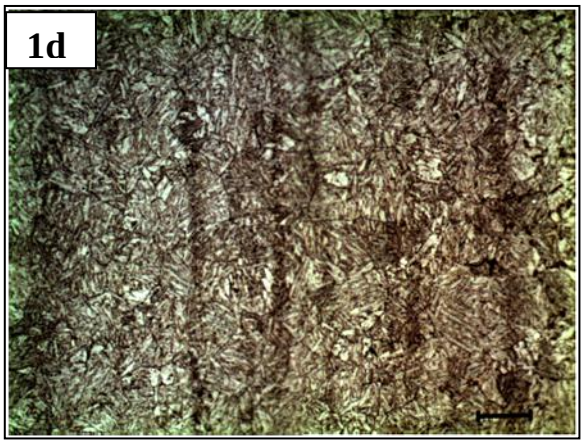
1d


2d

Figure 4-8 Microphotographs showing different HAZ subzones of the 1 pass fillet joint deposited utilising GMAW process in combination with metal-cored austenitic stainless steel consumable (from top): a - coarse-grained region, b - fine-grained region, c - inter-critical region, d - over-tempered region. Micrographs marked as 1 and 2 represent joints welded with 80°C and 7°C preheat respectively. Micrographs were acquired in the cap areas as shown in Figure 3-16. Micron bar represents 20 micrometers except of the micrographs picturing inter-critical regions (1c and 2c) where micron bar represents 50 micrometers.

4.2.1.3 Prediction of HAZ microstructure

It is well accepted that the harder the microstructure obtained in the HAZ the higher the risk of HACC. Martensitic microstructures are particularly susceptible to hydrogen cracking. Arata et al. [90] developed a formula for determination of Vickers hardness value of a fully martensitic microstructure obtained in the HAZ. This formula takes into consideration nothing but the carbon content of the welded steel and is valid for carbon content between 0.07 and 0.53 wt%. This is based on the assumption that carbon has the most significant influence on the hardenablity of the steel out of all alloying elements.

$$HV_{100\%\,martensite} = 835C + 287 \qquad (4.1)$$

where: C is carbon content.

Using this equation the Vickers hardness value of the HAZ of the HHA steel weld containing 100% martensite was calculated to be 537 HV. The microstructure and resultant hardness obtained in the coarse-grained HAZ of the HHA single pass fillet welds are in good agreement with this value.

It is claimed that bainitic microstructures formed in the HAZ are preferred over martensitic structures. Lorenz and Durren [91] proposed the maximum value of carbon equivalent (CE) of the steel to determine when the HAZ does not contain any martensite. This equation is valid for steels with carbon content lower than 0.8 wt%.

$$CE_B = C + \frac{Si}{11} + \frac{Mn}{8} + \frac{Cu}{9} + \frac{Cr}{5} + \frac{Ni}{17} + \frac{Mo}{6} + \frac{V}{5} \quad (4.2)$$

Value of CE_B for HHA was calculated to be 0.7 and based on this equation the HAZ of HHA should not contain any martensite. However the heat input employed in welding of HHA is relatively low resulting in fast cooling rates and the formation of harder phases as seen here.

4.2.1.4 Determination of minimum preheat temperature

When developing safe welding procedures an appropriate minimum level of preheat is commonly established using one of the standard methods. Firstly the level of minimum preheat temperature was determined according to WTIA guidelines - Welding and fabrication of quenched and tempered steel [27]. This method uses P_w index [%] that considers three factors contributing to HACC, hardenability of the steel, diffusible hydrogen content and restraint:

$$P_w = P_{cm} + \frac{H_D}{60} + \frac{R_F}{4000} \quad (4.3)$$

where: H_D is weld metal diffusible hydrogen content [ml/100g], R_F is restraint intensity factor [N/mm^2] (usually less than 40 x plate thickness) and P_{cm} is carbon equivalent formula [%] calculated by the equation:

$$Pcm = C + \frac{Si}{30} + \frac{Mn}{20} + \frac{Cu}{20} + \frac{Ni}{60} + \frac{Cr}{20} + \frac{Mo}{15} + \frac{V}{10} + 5B \quad (4.4)$$

From this the minimum preheat temperature [°C] can be calculated using the formula:

$$T_{P\,min} = 1440P_W - 392 \quad (4.5)$$

According to this method the minimum preheat temperature was determined to be 315°C and 307°C for flux-cored and metal-cored consumable respectively. The level of diffusible hydrogen considered for this calculation was 1.3 ml/100g for flux-cored consumable (refer to

Table 3-14). The overall amount of diffusible hydrogen resulting from welding with metal-cored consumable was not determined experimentally but the level of 1 ml/100g was considered based on the results from hydrogen testing (refer to Table 3-16) where metal-cored deposits released 38% less diffusible hydrogen compared to flux-cored deposits. The value of 1 ml/100g does not correspond to 62% of the amount considered for flux-cored consumable because it also takes into account longer cooling times resulting from deposition of the weld bead using a metal-cored consumable during these tests. The value of the restraint intensity factor considered in this calculation was 40 x actual thickness of the HHA plate (9 mm). The guidelines state that the restraint intensity factor is usually less than 40 x plate thickness. The high value of restraint was considered because during manufacturing of complex structures large, highly stiffened HHA plates may be used thus the level of restraint is high. The minimum levels of preheat calculated using this method are excessively high due to extremely high hardenablitity of HHA steel. This method appears not to be suitable for determination of the minimum preheat temperature for HHA steel weldments and the manufacturers of the Q&T armour steel do not recommend preheating plates of thickness less than 30 mm above 150°C. Employing such a high level of preheat would almost certainly result in deterioration of the HAZ properties which is inadmissible from ballistic protection and also structural view point. The WTIA guidelines [27] for calculation of minimum preheat temperature for Q&T steels use P_{cm} carbon equivalent. This is suitable for majority of Q&T steels because Carbon content is generally well bellow 0.15 wt % (validity range for use of P_{cm}). Further, Q&T alloy design commonly utilizes extremely effective hardening agent Boron and P_{cm} is the only generally used carbon equivalent formulae that considers this element. HHA contains very high carbon content what is believed contributed to the excessive value of recommended preheat temperature calculated using WTIA guidelines.

Several other methods for the avoidance of cold cracks are summarised and compared in technical report ISO/TR 17844 Welding – Comparison of standardised methods for the avoidance of cold cracks [76]. All reported techniques were reviewed and based on the joint geometry and chemical composition and heat treatment of parent HHA steel the so called CET-method (investigations published as IIW-Documents) was selected as the only suitable one to calculate the reference level of preheat. The background of this method is based on data from y-joint and CTS type cracking tests. This method is valid for steels with following chemical composition: 0.05 – 0.32 wt% C, ≤ 0.8 wt% Si, 0.5 – 1.9 wt% Mn, ≤ 1.5 wt% Cr, ≤

0.7 wt% Cu, ≤ 0.75 wt% Mo, ≤ 0.06 wt% Nb, ≤ 2.5 wt% Ni, ≤ 0.12 wt% Ti, ≤ 0.18 wt% V, and ≤ 0.005 wt% B. The determination of the minimum level of preheat ensuring freedom from HACC using this method takes into account influence of hardenability and thickness of the parent plate to be welded, the level of diffusible hydrogen, heat input and residual stresses. The effect of these factors is combined in the formula:

$$T_p = T_{pCET} + T_{pd} + T_{pHD} + T_{pQ} \tag{4.6}$$

where: T_p is the minimum preheat temperature [°C], T_{pCET} is minimum preheat temperature component [°C] calculated based on carbon equivalent, T_{pd} is minimum preheat temperature component [°C] reflecting the thickness of the parent plate, T_{pHD} is minimum preheat temperature component [°C] calculated based on weld diffusible hydrogen content and T_{pQ} is minimum preheat temperature component [°C] calculated based on process heat input.

The single components for determination of minimum preheat temperature are determined as follows:

1 $$T_{pCET} = 750CET - 150 \tag{4.7}$$

where: CET is carbon equivalent in [%] derived from chemical composition of the parent plate and calculated using formula:

$$CET = C + \frac{Mn + Mo}{10} + \frac{Cr + Cu}{20} + \frac{Ni}{40} \tag{4.8}$$

2 $$T_{pd} = 160 \tan(^{d}/_{35}) - 110 \tag{4.9}$$

where: d is plate thickness [mm].

3 $$T_{pHD} = 62HD^{0.35} - 100 \tag{4.10}$$

where: HD is diffusible hydrogen content [ml/100g of weld metal] determined according to EN ISO 3690 (Australian equivalent is AS/NZS 3752:2006)

4 $$T_{pQ} = (53CET - 32)Q - 53CET + 32 \quad (4.11)$$

where: Q is process heat input [10^3. N.m.mm^{-1}] calculated in accordance with EN 1011-1 and 2 calculated using formula:

$$Q = k\frac{IU}{v}10^{-3} \quad (4.12)$$

where: k is heat transfer efficiency (0.8 for GMAW), I is welding current [A], U is voltage [V] and v is welding travel speed [mm.s^{-1}].

The effect of residual stresses on the minimum preheat temperature is not directly quantified for different applications as the knowledge in this area is only qualitative. The residual stresses of magnitude of the yield strength of the parent or weld metal have been assumed when developing this formula. It is however recommended that higher minimum preheat temperature should be used in case of welding highly restraint structures [76].

Using the CET-method the minimum preheat temperature was calculated to be 78°C and 72°C for flux-cored and metal cored consumable respectively. The levels of diffusible hydrogen of the two consumables used in this calculation were identical to the levels used in the calculations according the WTIA recommendations. The calculated minimum level of preheat is in good agreement with the one commonly used in the industry practice. However, ISO/TR 17844 [76] document further states that preheat can be considerably reduced when an austenitic stainless steel consumable is used as a result of better strain condition and hydrogen distribution across the weldment. Lower levels of preheat are also permissible for multipass welding if adequately high interpass temperature is maintained in between the deposition of the single passes assisting the diffusion of hydrogen out of the areas of previous passes. Unfortunately the 'considerable' reduction in preheat suggested by the CET method is not quantified. The target application of this investigation is a multi-pass HHA corner joint.

The upper interpass temperature threshold was also identified in this study as a part of optimisation of the current welding procedure. It was found that interpass temperature can be increased from 120°C to 200°C without negatively affecting hardness in the HAZ and over-tempered region. Thus it is expected that employing higher interpass temperature would

reduce the risk of HACC in the cap area of the weldment. However the 1st inner pass is deposited separately and the joint is allowed to cool down to ambient temperature before deposition of the remaining cap passes. Additionally the findings of this investigation of minimum safe level of preheat would be applied not only to the multipass corner joint but to all standard HHA joints welded with austenitic stainless steel consumable.

From a microstructural view point decreasing the preheat temperature from 80°C to 7°C produces slightly harder structures. However (coarse-grain) HAZ of the weldments produced employing both levels of preheat comprises of hard and brittle bainitic and martensitic constituents. The difference between the two levels of preheat is that joint simulating ambient preheat temperature of 7°C contains higher martensite to bainite ratio compared to the one welded utilising 80°C preheat. in addition the HAZ hardness of the joints welded employing both preheats is very high, well about the level considered to be safe from HACC view point. The AS/NZS: standard: Structural steel welding – Welding of high strength quenched and tempered steels standard [41] states that even when welding Q&T steels employing low hydrogen consumable, the maximum allowable HAZ hardness ensuring freedom from HACC is 450 HV. This critical hardness value is considered when welding utilising ferritic consumable. However, the industry procedures previously used for welding HHA steel employed ferritic consumable in combination with 80°C that resulted in HAZ hardness levels above 500 HV without occurrence of HACC. Even higher hardness obtained in the HAZ as a result of elimination of preheat is expected to be compensated by the ability of austenitic stainless steel weld metal to accommodate higher hydrogen and stress levels.

There are no guidelines for calculation minimum preheat temperature for welding ferritic steels with an austenitic stainless steel consumable thus the minimum level of preheat for these applications was determined experimentally. The results of the different preheat trials suggest that lowering preheat temperature all the way down to 7°C does not have a significant effect on microstructure and hardness obtained in the HAZ. But before the lower level of preheat can be adopted by the industry all the remaining factors contributing to HACC (diffusible hydrogen and residual stresses) have to be properly assessed.

4.2.2 Optimisation of interpass temperature

In case of multi-pass welding maintaining adequately high interpass temperature in between deposition of single passes has a similar effect to preheating the plate prior to welding. The same restrictions as for minimum preheat temperature apply for minimum interpass temperature. The minimum level of interpass temperature should be calculated using the same formula (4.6) as for calculation of minimum preheat temperature. However there are no guidelines for determination of maximum interpass temperature. In these circumstances the level of maximum allowable interpass temperature can only be determined experimentally for each intended application based on the microstructure formed in the HAZ.

A series of welding trials were carried out in order to assess the effect of increasing interpass temperature on HAZ harness and microstructure of the multi-pass HHA weldments produced with flux-cored and metal-cored austenitic stainless steel consumables. From a productivity view point reducing the waiting times is beneficial but requires the highest practical interpass temperature to be used. The limitation on this upper temperature is achievment of the required joint properties without undue loss of strength and hardness. Based on the results presented in section 3.2.3 it was concluded that interpass temperature of 200°C would be ideal candidate for replacement of the current interpass temperature of 120°C for both flux-cored and metal-cored consumable. The comparison of hardness and microstructure obtained in the HAZ of the multipass joints produced employing current industry practice of 80°C preheat in combination with 120°C interpass temperature (further referred to as “current weld”) and optimised procedure utilising ambient preheat in combination with 200°C interpass temperature (further referred to as “optimised welds”) was undertaken and is discussed in the following section.

For reference the macrographs of the cross-sections of the HHA weldments deposited simulating current industry practice and proposed level of preheat and interpass temperature produced with flux-cored and metal-cored consumable are presented in Figure 4-9 and Figure 4-10 respectively.

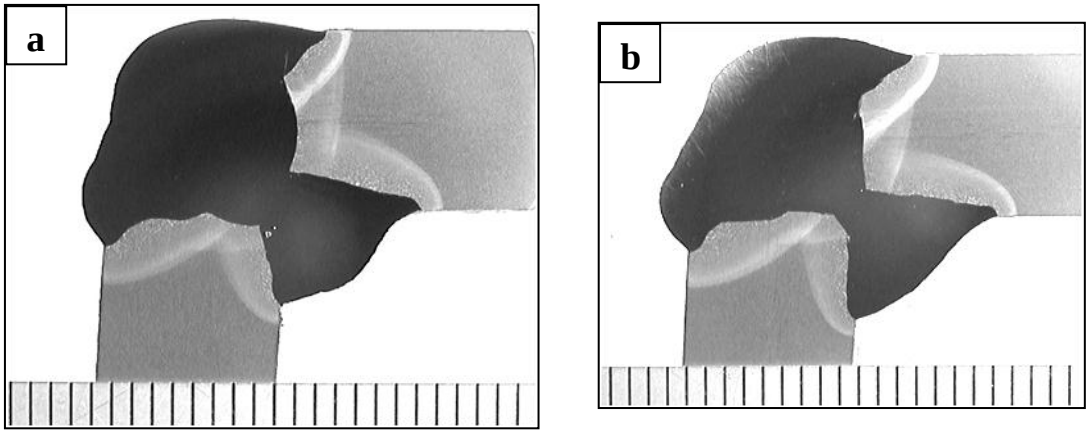

Figure 4-9 Macrophotographs of the 5 pass corner welds deposited with flux-cored consumable; a – "current weld" and b – proposed "optimised weld". Note: scale is in millimetres.

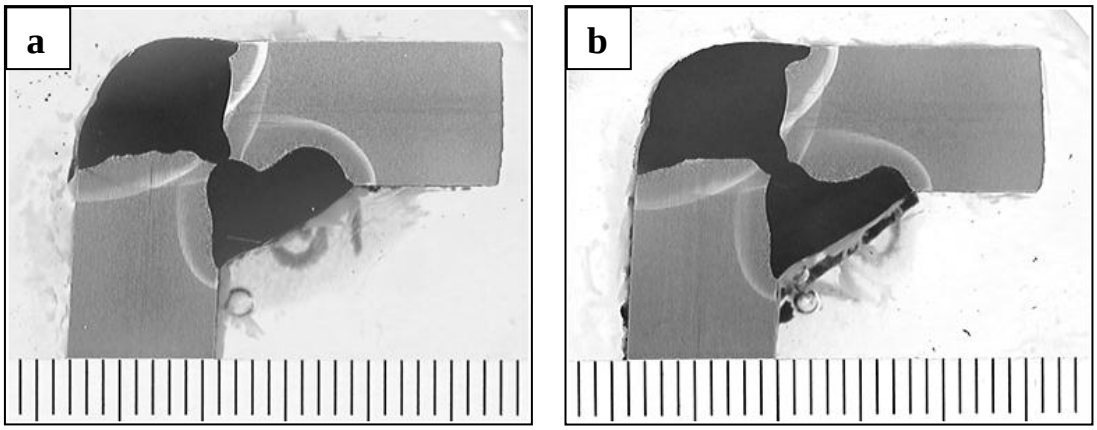

Figure 4-10 Macrophotographs of the 4 pass corner welds deposited with metal-cored consumable; a – "current weld" and b – proposed "optimised weld". Note: scale is in millimetres.

4.2.2.1 Comparison of hardness profiles

Figure 4-11 - Figure 4-14 show the weld hardness profiles of the "current" and "optimised welds" produced with flux-cored and metal-cored consumables measured in both orientations (refer to Figure 2-17). The general trend of a slight increase of the over-tempered region width can be observed resulting from reduced cooling rates with increasing interpass temperature from 120°C to 200°C. The weldment area was again divided into two separate sections: HAZ and OT region (refer to section 3.2.2.2).

HAZ hardness

Even though “current welds” were preheated to 80°C the hardness obtained in the coarse-grained HAZ region was slightly higher than the hardness of “optimised weldments” in both orientations and for both investigated consumables. The hardness of the fine-grain region measured in B orientation increased for both consumables. The HAZ width measured in A orientation remained constant and in orientation B increased by 0.5 mm for both consumables.

OT region hardness

Hardness of over-tempered region measured in both orientations of both current and optimised weldments produced with flux-cord consumable was almost identical. Minor increase in OT region width of 1 mm and 0.5 mm measured in A and B orientation respectively was observed in case of optimised welds. A certain degree of over-tempered zone softening of approximately 35 HV measured in A orientation resulted from employing higher interpass temperature in the case of joints produced with the metal-cored consumable. Hardness profiles measured in B orientation were also almost identical for both current and optimised welds. The slight increase of the over-tempered region width of 3 mm and 1 mm measured in A and B orientation respectively was measured for weldments produced employing higher interpass temperature.

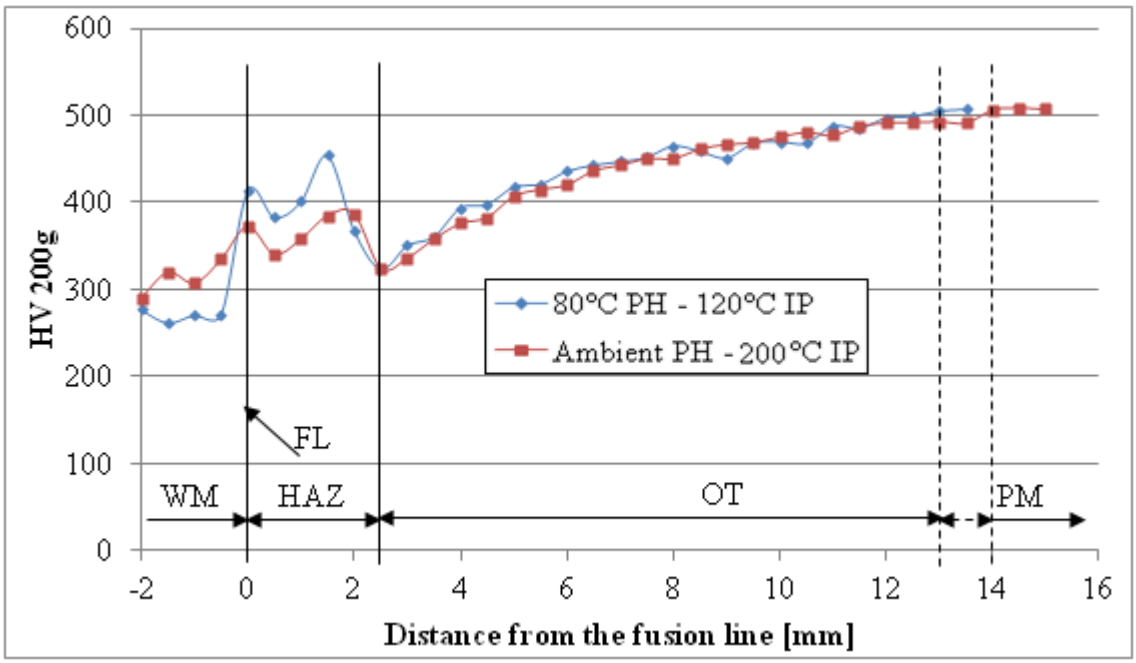

Figure 4-11 Weld hardness profiles measured in A orientation of the 5 pass corner joints welded with flux-cored consumable employing currently used preheat and interpass temperatures of 80°C and 120°C respectively and proposed optimised procedure with Ambient preheat and 200°C interpass temperature. Note: Each hardness value represents the average value of the three measurements. Standard deviations for WM, HAZ, OT and PM regions were in the range of ±12 to ±63, ±6 to ±29, ±0 to ±25 and ±2 to ±17 respectively.

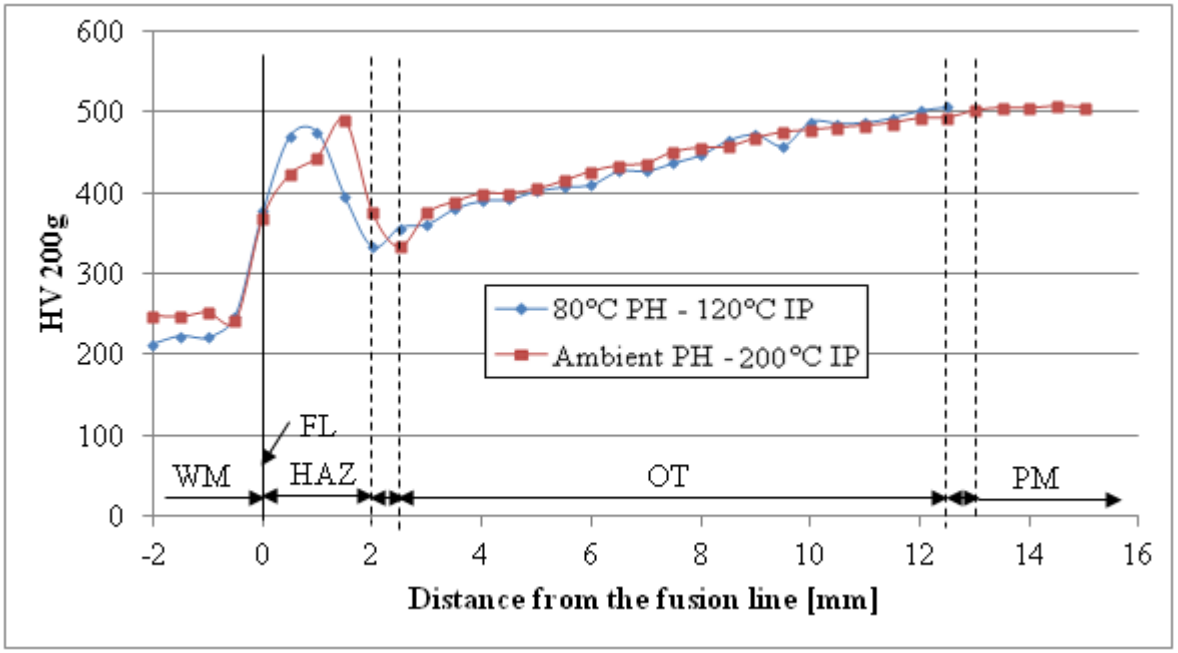

Figure 4-12 Weld hardness profiles measured in B orientation of the 5 pass corner joints welded with flux-cored consumable employing currently used preheat and interpass

temperatures of 80°C and 120°C respectively and proposed optimised procedure with Ambient preheat and 200°C interpass temperature. Note: Each hardness value represents the average value of the three measurements. Standard deviations for WM, HAZ, OT and PM regions were in the range of ±45 to ±71, ±4 to ±31, ±1 to ±22 and ±0 to ±14 respectively.

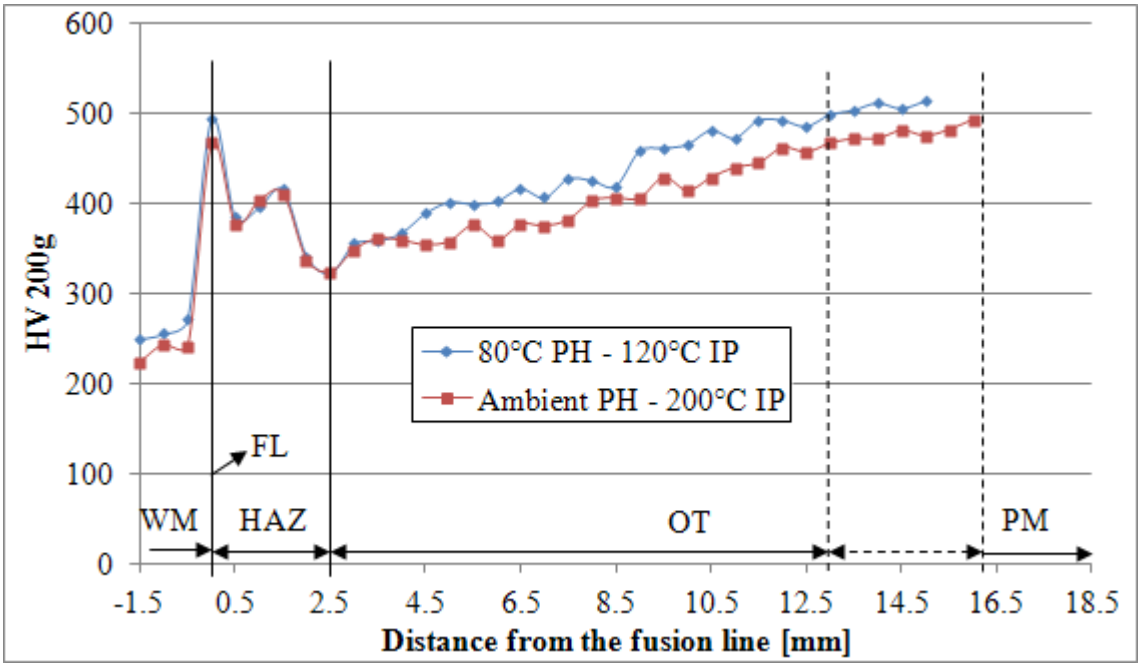

Figure 4-13 Weld hardness profiles measured in A orientation of the 4 pass corner joints welded with metal-cored consumable employing currently used preheat and interpass temperatures of 80°C and 120°C respectively and proposed optimised procedure with Ambient preheat and 200°C interpass temperature. Note: Each hardness value represents the average value of the three measurements. Standard deviations for WM, HAZ, OT and PM regions were in the range of ±34 to ±52, ±6 to ±29, ±2 to ±17 and ±3 to ±25 respectively.

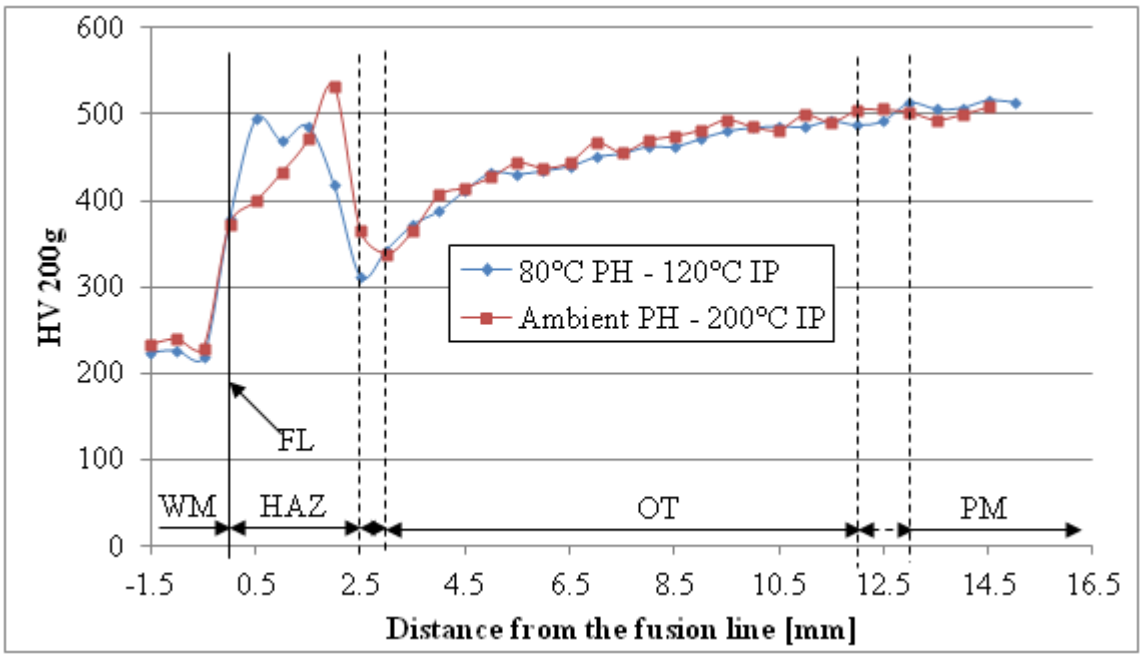

Figure 4-14 Weld hardness profiles measured in B orientation of the 4 pass corner joints welded with flux-cored consumable employing currently used preheat and interpass temperatures of 80°C and 120°C respectively and proposed optimised procedure with Ambient preheat and 200°C interpass temperature. Note: Each hardness value represents the average value of the three measurements. Standard deviations for WM, HAZ, OT and PM regions were in the range of ±21 to ±47, ±3 to ±24, ±2 to ±39 and ±4 to ±19 respectively.

4.2.2.2 Comparison of HAZ microstructure

Figure 4-15 and Figure 4-16 show low magnification micrographs of the HAZ of the multi-pass corner joints welded utilising current and optimised preheat and interpass temperatures deposited with flux-cored and metal-cored consumable respectively. The micrographs were acquired in the cap area as shown in

Figure 3-30 corresponding to hardness orientation B. A slight increase of HAZ width particularly the inter-critical region of the samples welded with optimised preheat and interpass temperatures can be observed from presented micrographs.

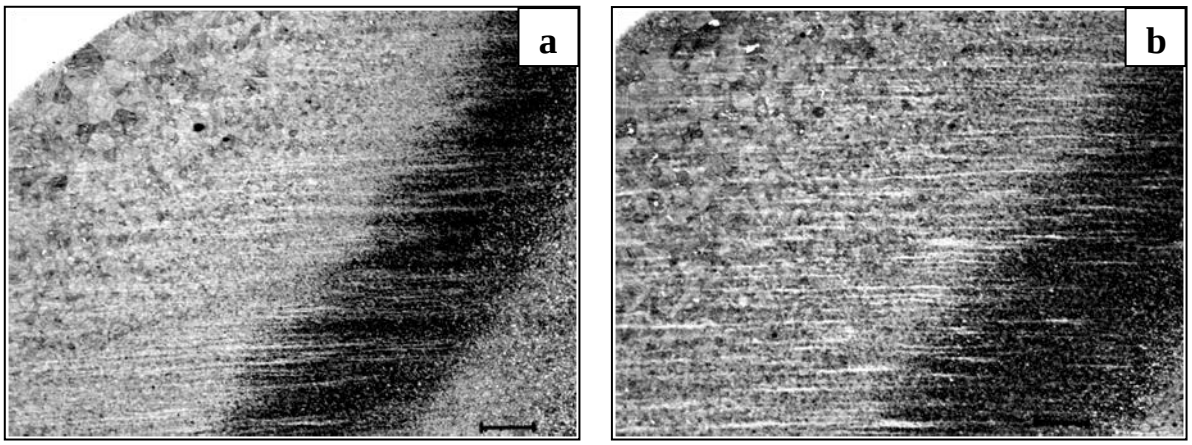

Figure 4-15 Microphotographs depicting different HAZ subzones (from right: weld metal, coarse-grained region, fine-grained region, inter-critical region, over-tempered region) of the 5 pass corner welds deposited with flux-cored consumable employing: a – "current" and b – "optimised" preheat and interpass temperature respectively. Note: micron bar represents 200 micrometers.

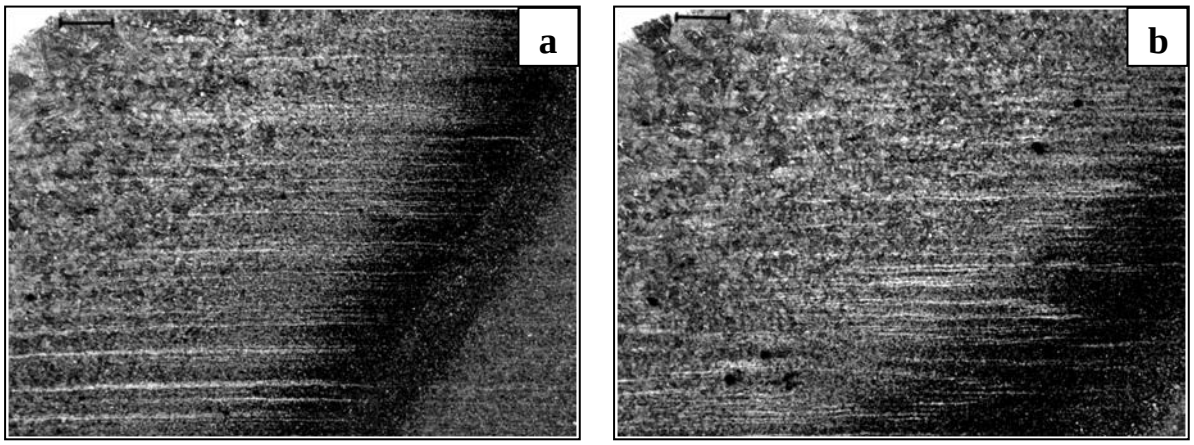

Figure 4-16 Microphotographs depicting different HAZ subzones (from right: weld metal, coarse-grained region, fine-grained region, inter-critical region, over-tempered region) of the 4 pass corner welds deposited with metal-cored consumable employing: a – "current" and b – "optimised" preheat and interpass temperature respectively. Note: micron bar represents 200 micrometers.

The main concern when employing higher interpass temperatures for welding HHA steel is formation of wide extensively softened areas in the over-tempered region that could compromise the ballistic performance of the welded structure. Conversely the resulting prolonged cooling times favour the diffusion of the hydrogen from the HAZ of the previous pass and also temper its rehardened HAZ area thus reducing the risk of HACC. These effects

compensate for the possible effects of employing the proposed lower level of preheat for multi-pass joints.

Figure 4-17 and Figure 4-18 display the microstructure of all HAZ subzones (coarse-grain, fine-grain, inter-critical and over-tempered) of the samples welded with “current” and “optimised” levels of preheat and interpass temperature and produced with flux-cored and metal-cored consumable respectively.

The coarse-grain region of all HHA weldments exhibited a mixed mode microstructure containing upper (ferritic) and lower bainite and martensite. The effect of longer cooling times as a result of increased interpass temperature can be clearly seen in this region. The microstructure of the “optimised” weldments deposited with both consumables consisted of a much higher volume fraction of softer phases (upper and lower bainite) extending further away from fusion line compared to current welds. This observation is consistent with hardness data presented in previous section

The fine-grain region of all samples consisted of mixture of upper and lower bainite and martensite. Few very fine grains of grain boundary ferrite were also observed. Only marginal differences were observed in this region for the samples welded with flux-cored consumables. The samples welded with a metal-cored consumable utilising the “optimised” preheat and interpass temperature exhibited higher amount of harder phases and higher degree of refinement compared to the “current” weld. In general fine-grain region of all samples consisted predominantly of martensite.

Increasing the interpass temperature from 120°C to 200°C resulted in the formation of a wider inter-critical region for both consumables. Fine-grained ferrite, granular bainite and some martensite were observed in the structure of all samples.

The over-tempered sub-zone of all produced samples had the same appearance with no obvious changes caused by employing current and optimised levels of preheat and interpass temperature and consisted of tempered martensite of the original parent plate.

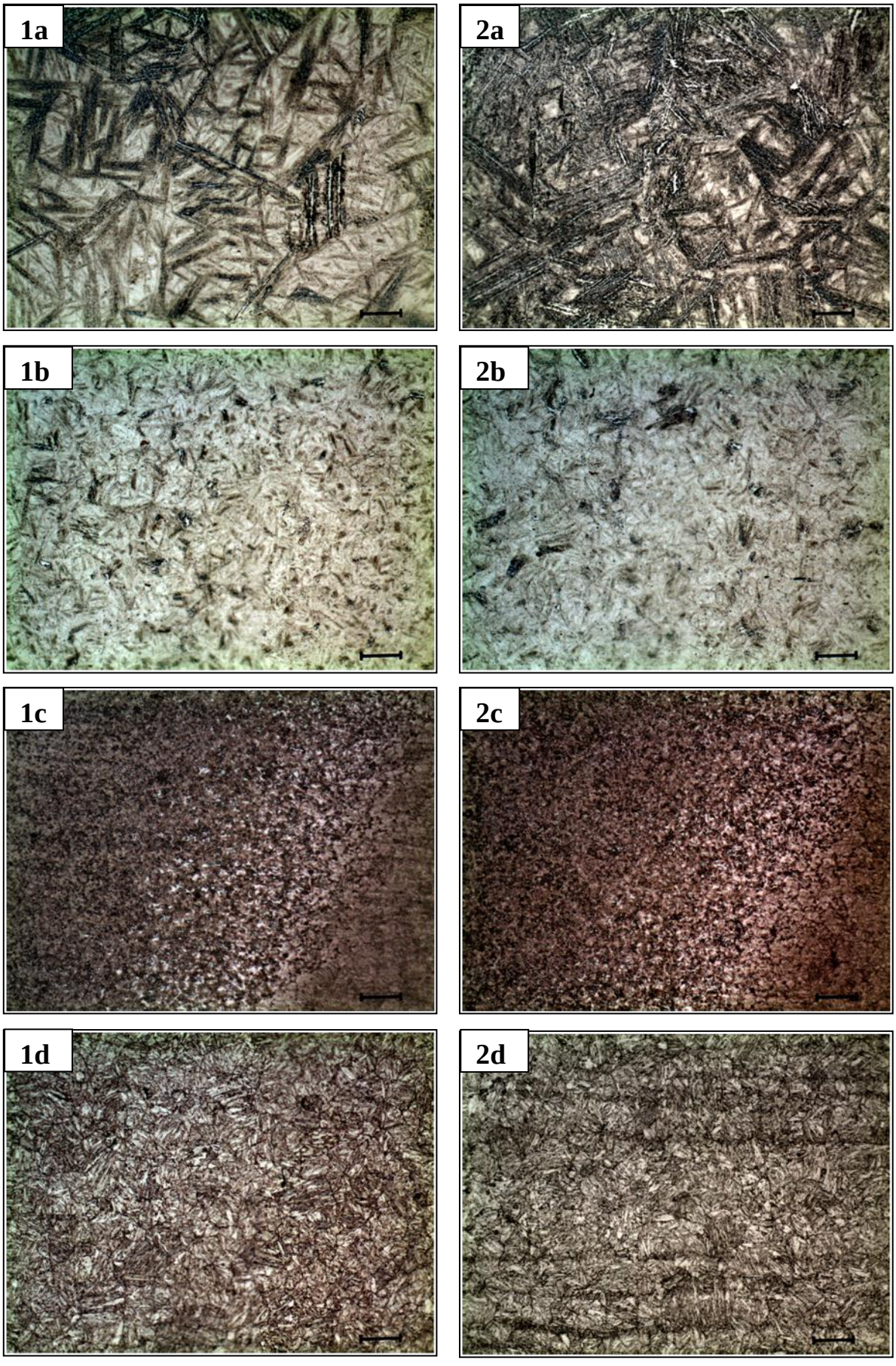
1a
2a
1b
2b
1c
2c
1d
2d

Figure 4-17 Microphotographs showing different HAZ subzones of the 5 pass corner joint deposited utilising GMAW process in combination with flux-cored austenitic stainless steel consumable (from top): a - coarse-grained region, b - fine-grained region, c - inter-critical region, d - over-tempered region. Micrographs marked as 1 and 2 represent current and optimised welds respectively. Micrographs were acquired in the cap areas as shown in Figure 3-30. Micron bar represents 20 micrometers except of the micrographs picturing inter-critical regions (1c and 2c) where micron bar represents 50 micrometers.

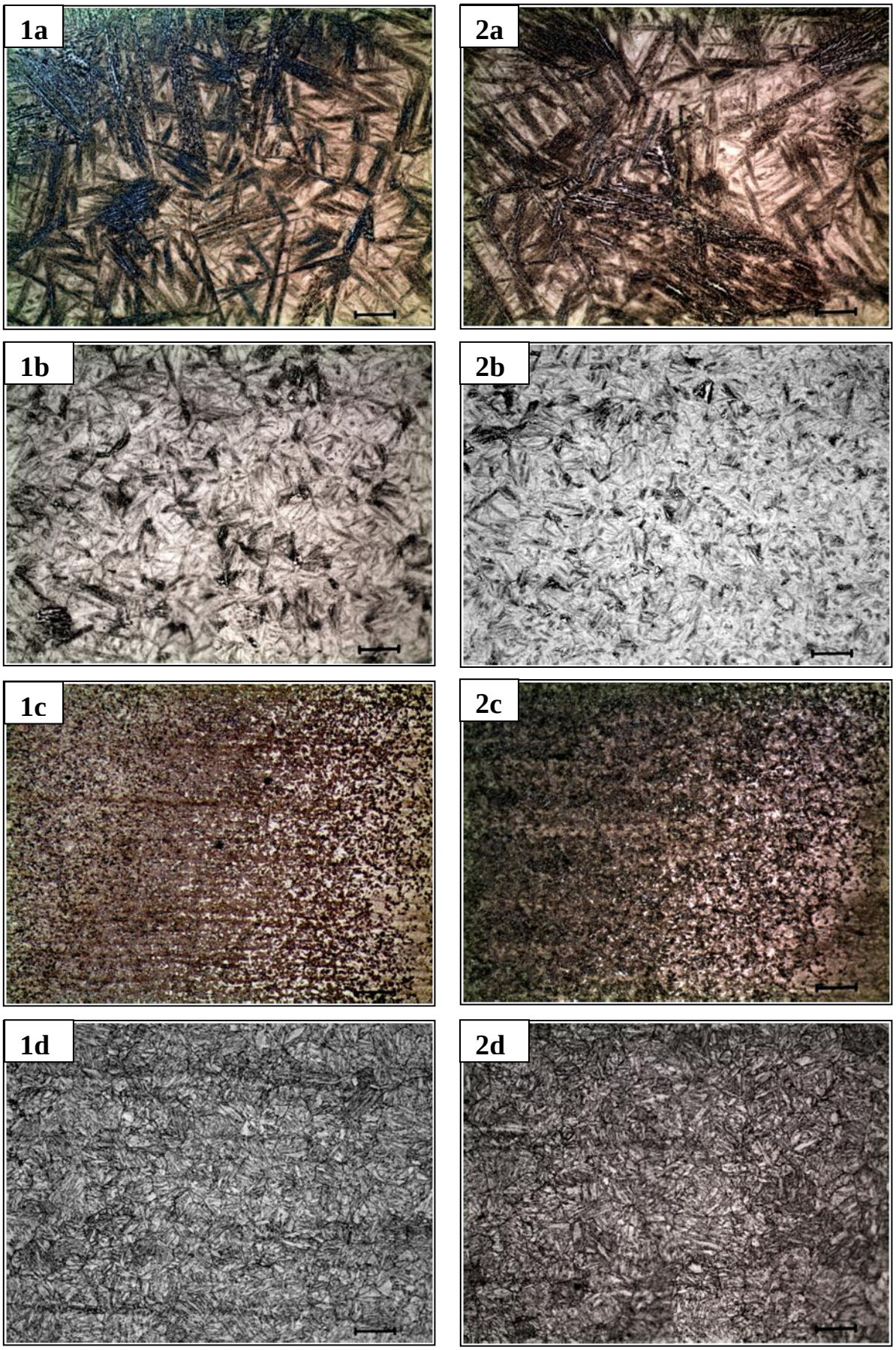
1a
2a
1b
2b
1c
2c
1d
2d

Figure 4-18 Microphotographs showing different HAZ subzones of the 4 pass corner joint deposited utilising GMAW process in combination with metal-cored austenitic stainless steel consumable (from top): a - coarse-grained region, b - fine-grained region, c - inter-critical region, d - over-tempered region. Micrographs marked as 1 and 2 represent current and optimised welds respectively. Micrographs were acquired in the cap areas as shown in Figure 3-30. Micron bar represents 20 micrometers except of the micrographs picturing inter-critical regions (1c and 2c) where micron bar represents 50 micrometers.

Data acquired from conducted welding trials suggest that by implementing the proposed ambient preheat and 200°C interpass temperature significant productivity improvement can be achieved without compromising ballistic integrity of the HHA weldments. Hardness results show that employing higher interpass temperature actually improves the hardness in the coarse-grain HAZ sub-zone effectively reducing the risk of HACC. Further there was little to no softening observed in the over-tempered area of the optimised welds and hardness attained 15.9 mm from the weld toe appears to be higher than the lowest hardness of 509 HV permitted by MIL- STAN-1185 (AT) [85].

4.3 FEASIBILITY OF HYBRID LASER-GMAW PROCESS FOR JOINING HHA STEEL

LH welding combines laser welding with conventional GMAW in a synergic process to combine the advantages and overcome disadvantages of the two single welding processes. If implemented, these advantages include, but are not limited to increasing speed of welding, superior penetration and gap brigeability, reduction in amount of welding time and consumable used, reduction in the number of weld passes, potential for improvement of HAZ size and reduction of fabrication costs. However, it is important that weldments fabricated by this process possess good materials properties and can compare with those currently produced by the conventional GMAW process. The comparison between the current 5-pass GMAW technique and a 2-pass hybrid laser-GMAW procedure is discussed in following section.

4.3.1 Comparison of corner joints produced by 2-pass hybrid laser-GMAW and current 5-pass GMAW procedure

A comparison between the current FCAW multi-pass and the hybrid laser-GMAW two pass procedure has been made and the comparative results are presented in Table 4-1. The time, consumable length, and weld volume has been calculated per one meter of the joint and does not account for preheat time, time needed to remove the slag from the surface of the bead or time waiting to achieve interpass temperature. These values suggest that a 36% decrease in welding time and a 56% decrease in the amount of consumable used would result from using the hybrid laser-GMAW process for deposition of the outer cap pass. However, this would be offset by an increase in the amount of HHA plate required as there is more overlap in hybrid laser-GMAW joints.

Table 4-1 Comparison of the time spent in deposition, consumable usage and total volume of the weld for current 5-pass FCAW and investigated 2-pass hybrid laser-GMAW procedure.

Process	Pass	TS [mm/min]	WFS [m/min]	Time [s]	Consumable [m]	Weld volume[1] [mm^3]
FCAW	1	400	9.5	150	23.8	22900
	2	500	11.0	120	22.0	21100
	3	500	9.5	120	19.0	18200
	4	550	9.5	109	17.3	16600
	5	550	9.5	109	17.3	16600
			Total	**608**	**99.4**	**95400**
GMAW +Laser-GMAW	1	400	9.5	150	23.8	26400
	2	250	5.0	240	20.0	22200
			Total	**390**	**43.8**	**48600**
			Difference	**218**	**55.6**	**46800**

Note: 85% deposition efficiency for flux-cored wire and 98% deposition efficiency for solid wire were assumed. The overall time taken for the laser weld is around 64% of that required for the a GMAW only technique. It should also be noted that the consumable is costly and the 50% saving in usage is significant.

4.3.1.1 Comparison of the weld metal and HAZ areas

The HHA steel in as supplied Q&T condition has the desired mechanical properties but the welding process not only alters the original microstructure of the parent plate but also creates a weld metal deposit with properties which are different from the parent HHA plate. For this reason it is considered beneficial to employ welding procedures with a reduced number of weld passes and thus minimised HAZ area. Weld metal and HAZ zone areas of the joints produced by both processes were compared. For reference, the cross sections of both welds produced by hybrid laser-GMAW process and also the current FCAW procedure are shown in Figure 4-19. An outline of the base material, weld material, and HAZ of the two welds is shown in Figure 4-20. From the diagrams it can be seen that weld produced with hybrid laser-GMAW has a wider HAZ in both vertical and horizontal HHA plates compared to the conventional GMAW joint. The overall weld area is much larger in case of a conventional GMAW joint, thus the weldment produced by the hybrid laser-GMAW process has much larger proportion of the original HHA plate this should be beneficial in terms of ballistic protection. The HAZ produced by inner passes is of similar size. It should be noted that laser power source available for this investigation did not have sufficient power to achieve the required penetration therefore slower welding speeds had to be employed increasing the overall heat input and creating wider HAZ. Initial bead-on-plate welding trials conducted on mild steel suggested that laser source was not able to create a keyhole and achieve the deep penetration typical for laser welds. Figure 4-21 – a shows cross-section of BOP 3kW laser only weld, welded at 400mm/min travel speed. Figure 4-21 - b shows a macrograph of the 4.5 kW CO_2 laser weld published in literature [34] which demonstrates the typical laser shape and much deeper penetration resulting from presence of a keyhole effect during welding. It is noted that the weld speed of 800mm/min was employed, double the value possible in this work and this created a narrower weld bead, HAZ and over-tempered region. The results published in the same paper [34] also suggests that full penetration of bead-on-plate welds on 7 mm mild steel plate is possible using the hybrid laser-GMAW method and a powerful 4.5kW CO_2 laser. Thus it is expected that welding procedures utilising a higher power laser source could produce faster welding speeds and minimise the HAZ area.

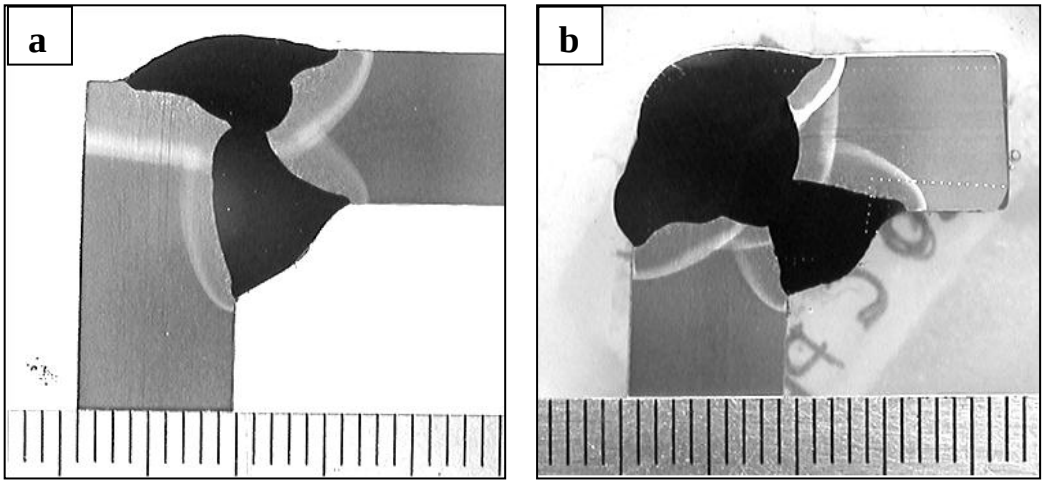

Figure 4-19 Macrographs of the weld cross-sections of the joints produced by: a – 1st pass GMAW process in combination with solid austenitic stainless steel consumable, 2nd pass hybrid laser-GMAW process in combination with solid austenitic stainless steel consumable; b - current 5-pass FCAW procedure. Note: Scale is in milimentres.

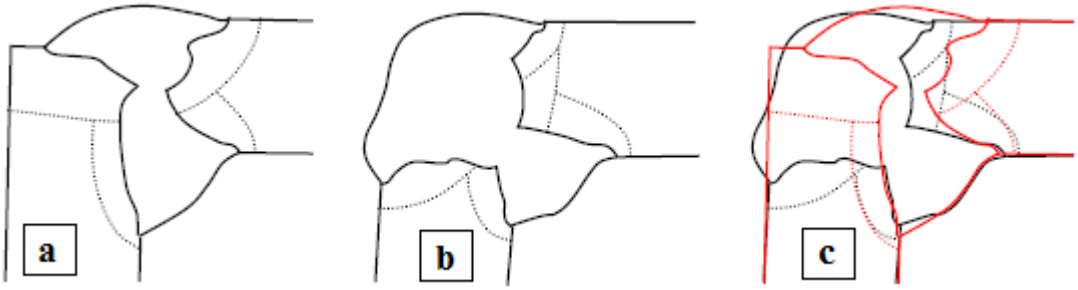

Figure 4-20 Comparison of weld cross-sections outlining areas of the weld metal and HAZ of welds produced by: a – investigated GMAW+ hybrid-GMAW laser process employing ambient (19°C) preheat; b - current FCAW procedure utilising 80°C preheat and 120°C inter-pass temperature; c – overlap of the two former ones.

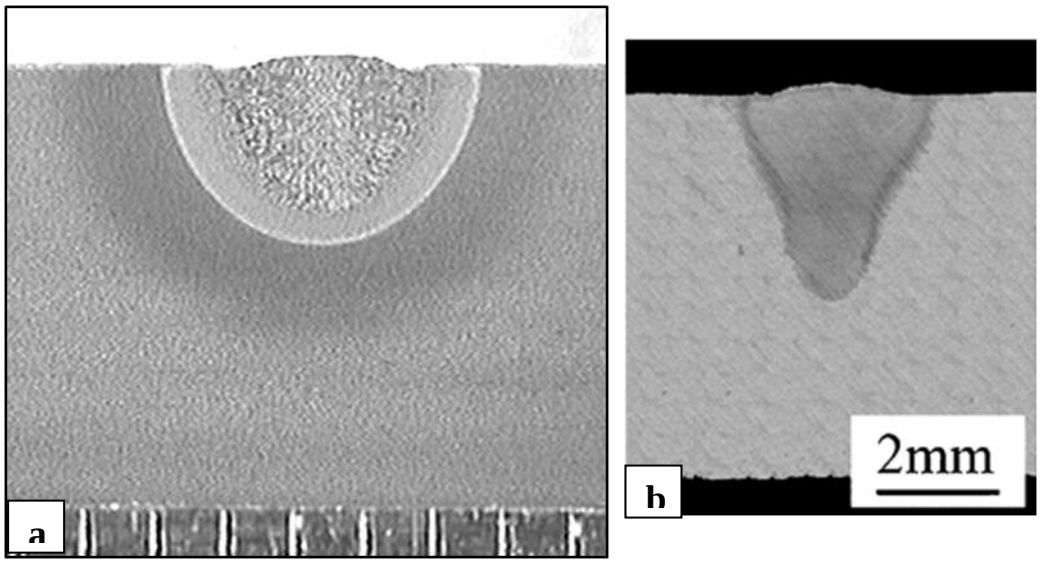

Figure 4-21 Marographs showing the different shape of laser welds deposited onto mild steel without filler material employing following parameters: a – 3 kW diode laser power source; Travel speed = 400 mm/min; Base metal thickness = 9 mm. Note: Scale is in milimetres; b – 4.5 kW CO_2 laser power source; Travel speed = 800 mm/min; Base metal thickness = 7 mm.

4.3.2 Ideal joint geometry

The 1.5 mm gap used here between the two HHA plates increases the total area of weld metal. For this reason there is insufficient weld metal to cover the cap area of the weldment. An attempt has been made to produce a weldment with the same parameters as test 11 (Table 3-11) but without the gap separating the HHA plates (refer to Figure 4-22). Full penetration of the joint was not achieved due to insufficient laser power as already discussed but the cap area was covered with weld metal all the way to the edge creating a complete joint. The higher power laser power source would not only solve the penetration issues and minimise the HAZ but also produce a joint with adequate geometry.

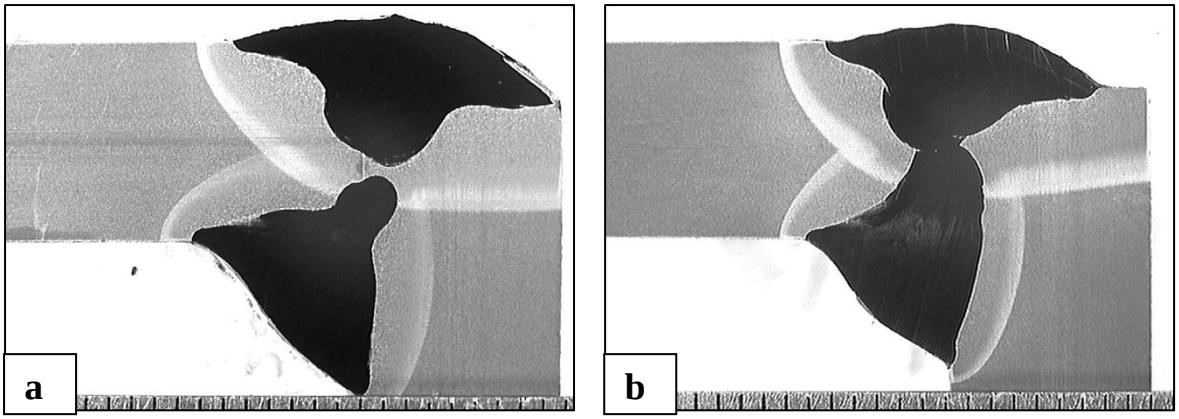

Figure 4-22 Macrophotographs of the hybrid laser-GMAW joints produced with the same welding parameters: a - zero gap in between the two HHA plates, b - 1.5 mm gap in between the two HHA plates.

4.3.3 Hardness profiles

As is obvious from the term HHA (high hardness armour) hardness is critical property ensuring good performance against possible ballistic attack. Also the hardness obtained in HAZ area, particularly the coarse-grain region is a good indication of the susceptibility to HACC.

The hardness of the samples produced with both procedures was measured in the same areas as shown in Figure 2-17 and Figure 2-23 for the current GMAW and novel hybrid laser-GMAW process respectively. The hardness profiles show the distinction in the different HAZ subzones and the hardness trend they follow through over-tempered region to unaffected parent material.

Figure 4-23 shows the hardness profile of the cap area - orientation A. It can be seen that the HAZ resulting from the hybrid laser-GMAW process was 1 mm wider compared with current GMAW procedure. The fine-grained HAZ of both joints developed the highest hardness value of 454 and 490 HV/200 g for current and hybrid laser-GMAW process respectively. Besides these two discrepancies the hardness profiles were very similar and the unaffected parent material extended 12 mm from the fusion line for both procedures, thus the ballistic performance in this area does not appear to be compromised.

As seen from the hardness traverses measured in B orientation (Figure 4-24) the HAZ of the hybrid laser-GMAW joint is only 0.5 mm wider, and the coarse-grain is only approximately 30 HV units harder than the one produced by conventional GMAW procedure. The over-tempered region of the hybrid laser-GMAW joint shows higher degree of softening by average of approximately 50 HV units compared to GMAW weldment. Importantly the hardness of the over-tempered region of the GMAW weldment reaches the values of unaffected parent metal 4 mm earlier than the hybrid laser-GMAW joint. This is undesirable from the ballistic view point as the attempt is to minimise the HAZ to enhance the ballistic properties of the welded structure. However, the weld metal area of the hybrid laser-GMAW weld is considerably smaller, compared to GMAW joint, improving the ballistic protection. Employing higher power laser allowing faster welding speeds for this application has the potential to improve the HAZ properties further.

Hardness profiles measured in the area of the inner pass (orientation C) are presented in Figure 4-25. The hardness profiles of the HAZ of both samples are almost the same and the HAZ width is identical. The over-tempered region of the GMAW pass of the hybrid laser-GMAW joint is 0.5 mm wider and shows slightly higher degree of softening by an average of approximately 30 HV units due to the use of solid consumable involving higher values of current during welding.

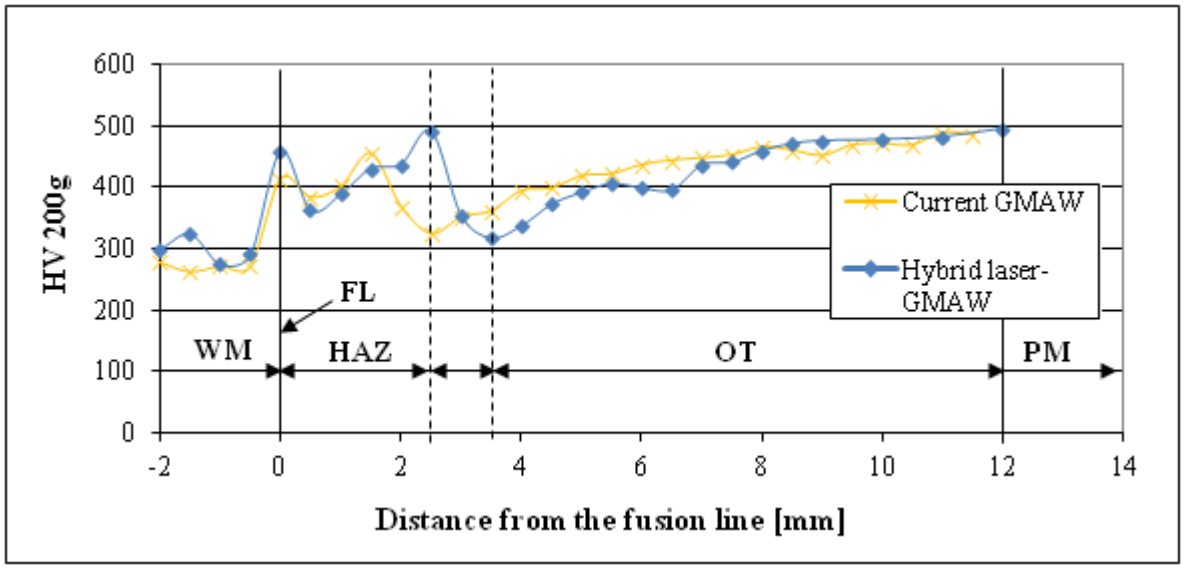

Figure 4-23 Weld hardness profiles of the joints produced by current GMAW procedure and investigated hybrid laser-GMAW (LH) process. Hardness was measured in the area of the cap pass – orientation A. Note: Each hardness value represents the average value of the three

measurements. Standard deviations for WM, HAZ and OT regions were in the range of ±19 to ±73, ±2 to ±24, ±2 to ±17 and ±3 to ±32 respectively.

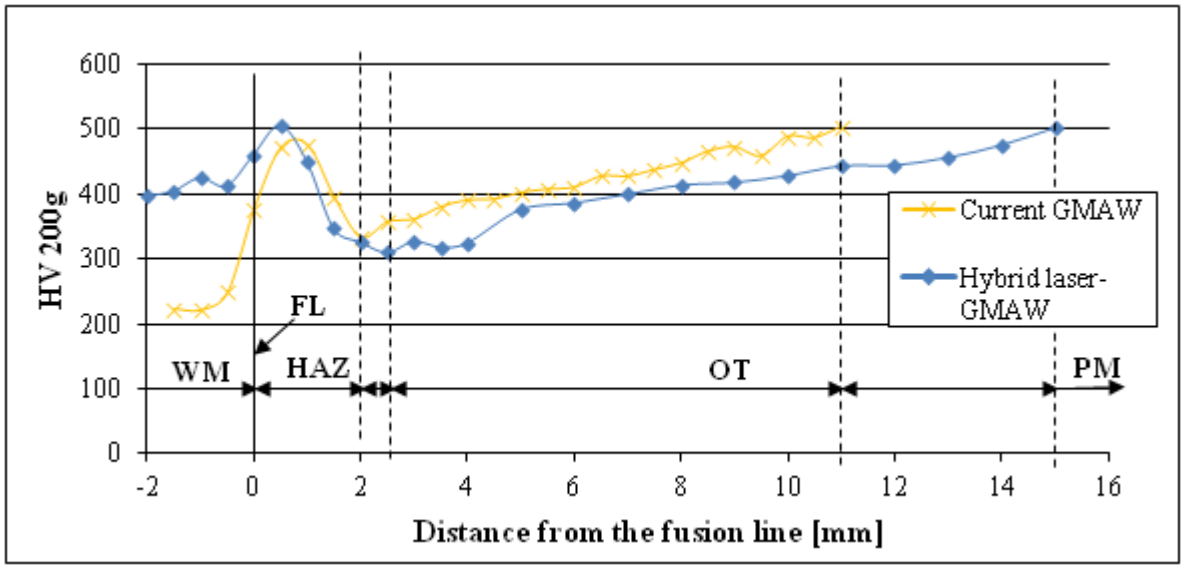

Figure 4-24 Weld hardness profiles of the joints produced by current GMAW procedure and investigated hybrid laser-GMAW (LH) process. Hardness was measured in the area of the cap pass – orientation B. Note: Each hardness value represents the average value of the three measurements. Standard deviations for WM, HAZ and OT regions were in the range of ±17 to ±67, ±3 to ±27 and ±6 to ±31 respectively.

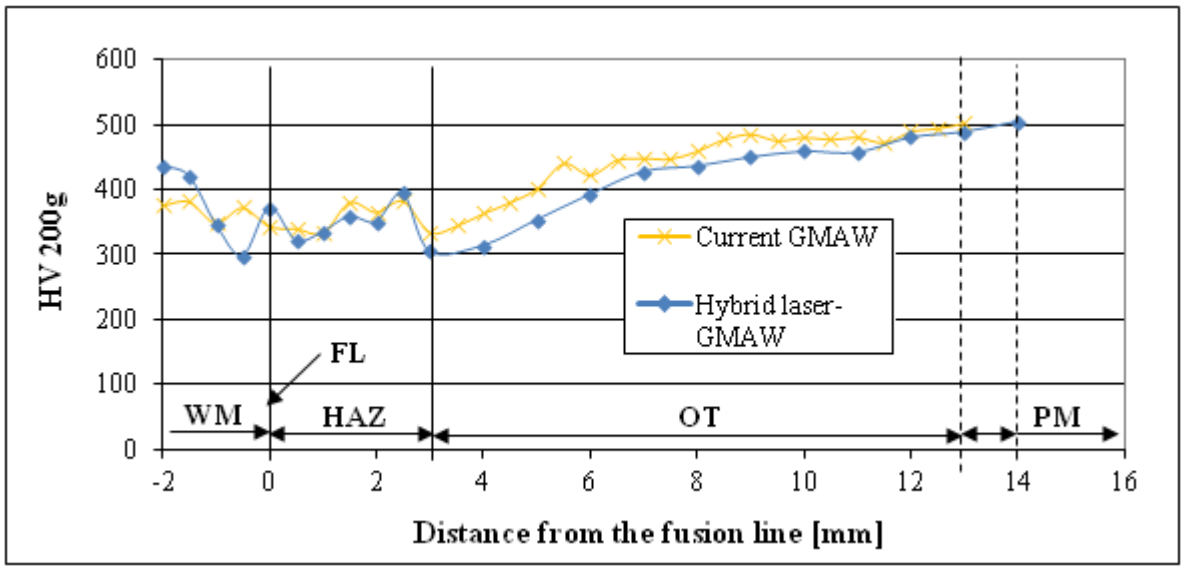

Figure 4-25 Weld hardness profiles of the joints produced by current GMAW procedure and investigated hybrid laser-GMAW process. Hardness was measured in the area of the inner pass – orientation C. Note: Each hardness value represents the average value of the three

measurements. Standard deviations for WM, HAZ, OT and PM regions were in the range of ±16 to ±74, ±4 to ±36, ±3 to ±18 and ±1 to ±18 respectively.

4.3.4 Comparison of HAZ microstructure

The microstructure obtained in the HAZ is a crucial factor when assessing the suitability of a welding process for a given application. It determines not only properties of the heat affected area itself but also influences the overall performance of the welded structure. The resultant HAZ microstructure is a function of a combination of factors like the chemical composition of the parent steel, welding process used, heat input and number and location of the weld passes. The HAZ microstructure of the 5-pass corner joint produced by the current GMAW process employing flux-cored austenitic stainless steel consumable in combination with 80°C preheat and 120°C interpass temperature and the HAZ of the hybrid laser-GMAW process employing solid austenitic stainless steel consumable in combination with ambient preheat was investigated and compared. The relevant findings are discussed in the following section.

Figure 4-26 displays low magnification micrographs of the HAZ of the corner joints welded utilising current GMAW and hybrid laser-GMAW processes. The micrographs were acquired in the cap area as shown in Figure 3-41 corresponding to hardness orientation A and B. From these micrographs it can be seen that hybrid laser-GMAW produced significantly wider HAZ area compared to the conventional GMAW process.

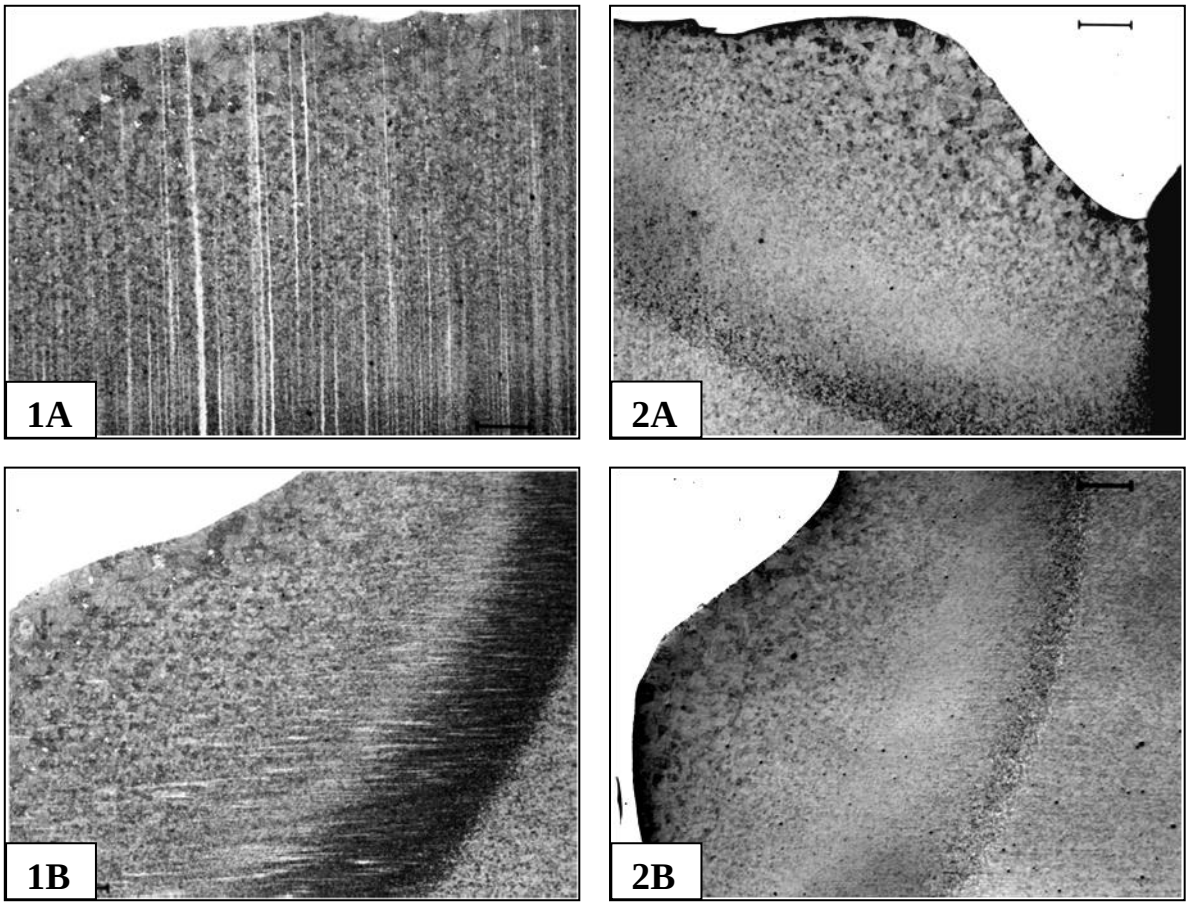

Figure 4-26 Microphotographs depicting different HAZ subzones (weld metal, coarse-grained region, fine-grained region, inter-critical region, over-tempered region) of the corner welds. Photos marked as 1A and 1B display microstructure of 2-pass hybrid laser-GMAW joint acquired in the cap area corresponding to hardness orientation A and B respectively. Photos marked as 2A and 2B display microstructure of 5-pass GMAW joint acquired in the cap area corresponding to hardness orientation A and B respectively Note: micron bar represents 380 micrometers.

Figure 4-27 displays the microstructure of all HAZ subzones (coarse-grain, fine-grain, inter-critical and over-tempered) of the joints produced by conventional procedure currently used in the industry practice and the hybrid laser-GMAW technique acquired in the cap area corresponding to hardness orientation A.

Due to the orientation of the laser beam during welding more heat was introduced into the weldment in the direction parallel to the laser resulting in the formation of a significantly wider HAZ; all sub-zones exhibited greater width compared to the weld produced by the conventional GMAW process. Coarse-grain area of both weldments consisted of upper and

lower bainite and martensite. Both joints also contained significant ferritic features which were, in the case of weld produced by the conventional GMAW process, concentrated mainly in the vicinity of fusion line whereas in case of the hybrid weld these features extended considerably further. The main difference was that coarse-grain region of conventional weld was heavily tempered by the heat introduced by subsequent passes while in case of hybrid welding it remained in original untempered condition. The heat introduced by subsequent passes was sufficient to heavily temper the microstructure of the fine-grain region of the conventional weld producing a microstructure consisting predominantly of tempered martensite, tempered upper and lower bainite and a few grains of polygonal ferrite. The microstructure obtained in the fine-grain region of the hybrid weld was in untempered condition and comprised mainly of martensite, upper and lower bainite and a small amount of randomly distributed grains of polygonal ferrite. The inter-critical region of both welds comprised fine-grained ferrite, granular bainite and some martensite. The width of this region produced by the hybrid process was considerably greater. The microstructure of over-tempered regions of the two weldments showed only marginal differences with tempered martensite being the main constituent.

Figure 4-28 shows the microstructure of all HAZ subzones (coarse-grain, fine-grain, inter-critical and over-tempered) of the joint produced by the conventional procedure currently used in the industry and the hybrid laser-GMAW technique; these images were acquired in the cap area corresponding to hardness orientation B.

This part of the hybrid laser-GMAW joint was predominantly influenced by the GMAW component of the synergic process and in case of the weld produced by conventional GMAW it was the HAZ area created by the final pass (no subsequent passes that would temper this region were deposited) thus the HAZ of both joints possessed similar nature and shape. However the higher overall combined heat of the laser beam and welding arc together with much slower welding speed resulted in formation of a wider HAZ and higher volume fraction of softer constituents in the sub-zones of a hybrid laser-GMAW joint.

The microstructure of the coarse-grain subzone of both welds consisted of upper and lower bainite, martensite and bainitic ferrite. A few randomly distributed grains of polygonal ferrite were observed in the structure of the hybrid laser-GMAW joint. The weldment produced by

conventional GMAW welding contained a higher volume fraction of harder constituents (martensite and lower bainite) in the coarse-grain zone compared to the hybrid weld. The microstructure produced in the fine-grain region of both welds comprised a mixture of martensite, upper and lower bainite and few grains of polygonal ferrite. Again the structure of the hybrid laser-GMAW joint contained a higher volume fraction of the softer phases (upper bainite and bainitic ferrite) compared to weldment produced by the conventional process. The microstructure in the inter-critical region of both weldments was very similar exhibiting fine-grained ferrite, granular bainite and some martensite. Due to the higher heat input of a hybrid laser-GMAW joint the inter-critical region exhibited greater width compared to the inter-critical region produced by conventional welding process. The over-tempered sub-zone of both weldments appeared identical and consisted predominantly of tempered martensite.

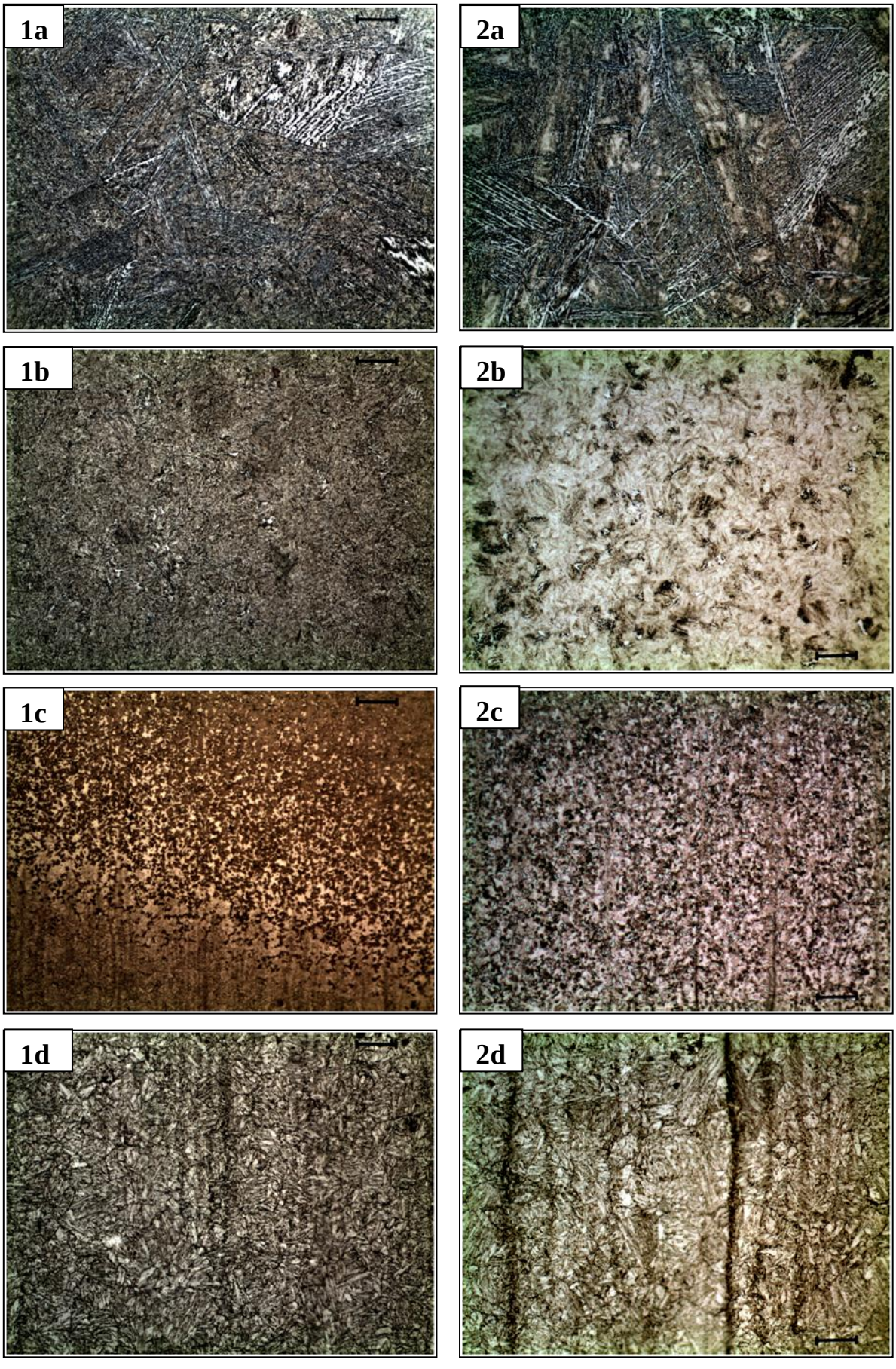
1a
2a
1b
2b
1c
2c
1d
2d

Figure 4-27 Microphotographs showing different HAZ subzones of the corner joint (from top): a - coarse-grained region, b - fine-grained region, c - inter-critical region, d - over-tempered region. Micrographs marked as 1 represent 5 pass corner joint deposited utilising current industry. Micrographs marked as 2 represent 2 pass joints deposited utilising hybrid laser-GMAW Micrographs were acquired in the cap areas corresponding to hardness orientation A. Micron bar represents 20 micrometers except of the micrographs picturing inter-critical regions (1c and 2c) where micron bar represents 50 micrometers.

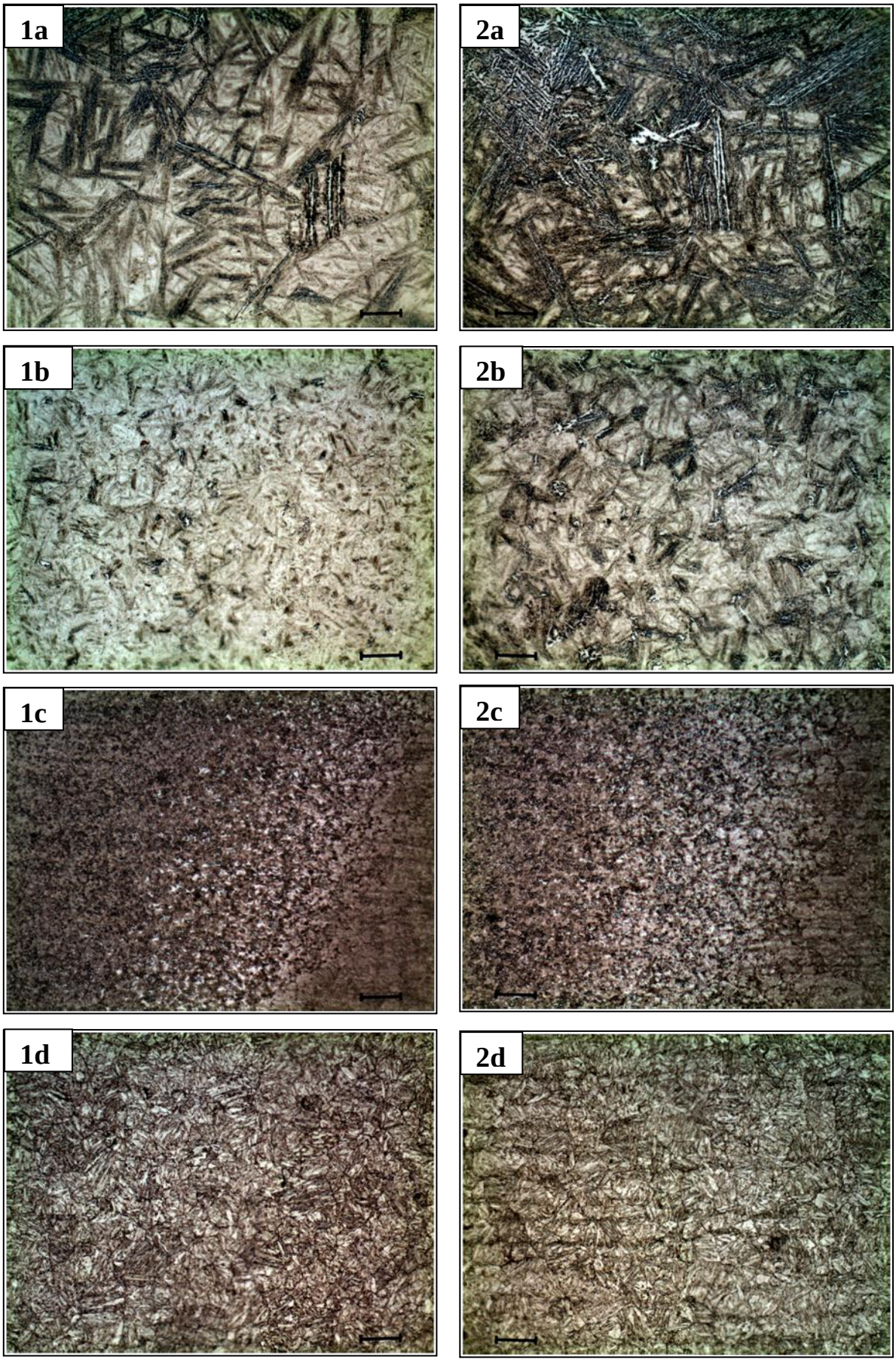
1a
2a
1b
2b
1c
2c
1d
2d

Figure 4-28 Microphotographs showing different HAZ subzones of the corner joint (from top): a - coarse-grained region, b - fine-grained region, c - inter-critical region, d - over-tempered region. Micrographs marked as 1 represent 5 pass corner joint deposited utilising current industry. Micrographs marked as 2 represent 2 pass joints deposited utilising hybrid laser-GMAW Micrographs were acquired in the cap areas corresponding to hardness orientation B. Micron bar represents 20 micrometers except of the micrographs picturing inter-critical regions (1c and 2c) where micron bar represents 50 micrometers.

4.3.5 Susceptibility of hybrid laser-GMAW to HACC

Implementing the hybrid laser-GMAW process in production also has the potential to reduce the risk of HACC in the HHA weldments [92]. This process utilises solid austenitic stainless steel consumable that according to data acquired from weld hydrogen testing presented in section 3.4.4 results in zero weld diffusible hydrogen content, practically ruling out the risk of HACC. The laser beam and welding arc operate in one weld pool under common shielding atmosphere thus the diffusible hydrogen content of hybrid laser-GMAW joints is not expected to by higher than diffusible hydrogen content of single GMAW. However the overall energy of the hybrid laser-GMAW process can be much higher than that of single GMAW resulting in formation of bigger weld pool thus increasing the active area for hydrogen intake. Blomquist et al. [93] measured the diffusible hydrogen content of hybrid laser-GMAW and conventional GMAW joints welded utilising a ferritic consumable. From the data acquired they concluded that hybrid laser-GMAW results in much lower level of diffusible hydrogen compared to GMAW. Further, the weld residual stresses in the hybrid laser-GMAW joint are expected to be lower compared to conventional GMAW. This theory is supported by the results obtained by Colegrove et al. [94] where hybrid laser-GMAW produced lower tensile longitudinal residual stresses in the weld metal and HAZ compared to GMAW. Additionally the region of tensile residual stresses was reported to be narrower when joints were produced using hybrid laser-GMAW. The magnitude of thermal contraction of austenitic weld metal is relative to its volume thus the hybrid laser-GMAW process that uses 56% less filler material to deposit the cap pass will lead to reduced overall shrinkage and consequently to lower stresses resulting from welding.

4.4 HYDROGEN TESTING

The objective of this study was to demonstrate that the use of austenitic stainless steel consumable is satisfactory measure to prevent HACC in HHA steel weldments by controlling the diffusible hydrogen levels, thus preheating plate prior to welding (carried out in the industry due to rigorous adherence to welding procedures developed for previously used ferritic consumable) can be avoided. A series of experiments was performed in effort to quantify the effect of different types of consumable and various preheat condition on the amount and distribution of hydrogen in HHA. The relevant findings of the hydrogen testing are discussed in the following sections.

4.4.1 Effect of welding consumable type on hydrogen level in HHA steel weldment

From the values of diffusible hydrogen measured for austenitic stainless steel and ferritic filler deposited onto the HHA test piece assembly presented in Table 3-14 it can be seen that utilising a ferritic consumable resulted in 18 times higher level of diffusible hydrogen compared to that produced with the ASS wire. During this testing samples were quenched immediately after extinction of the welding arc. The measured amounts were 24.3 and 1.3 ml of hydrogen per 100 g of weld metal. The specification AS 2203.1 ETP-GCp-W503ACM1H10 for the ferritic consumable VERTICOR 3XP includes the designation H10, which means that this consumable should not introduce more than 10 millilitres of hydrogen per 100g of deposited weld metal (according to the consumable manufacturer typically 5.0-6.0 ml of hydrogen per 100g of deposited weld metal, when Argoshield 52 is employed as a shielding gas as in this investigation). The extremely high value found here could be a result of hydrogen pick-up due to inappropriate storage of the filler spool in non sealed environment (the original manufacturer's package had however never been opened) over a long period of time of approximately 5-6 years. As mentioned before, both consumables (austenitic stainless steel and ferritic wires) are seamed wires and contain rutile flux, thus are highly prone for hydrogen pick-up from surrounding atmosphere. However, according to results published by M. Pitrun [95] diffusible hydrogen levels of 17 ml per 100 g of weld metal were measured for identical "fresh" consumable VERTICOR 3XP - H10, similar welding parameters (Stickout:15 mm, Heat input: 1.26 kJ/mm) and identical shielding gas (Argoshield 52 - 25% CO_2 in Ar). This result indicates that the investigated ferritic consumable introduces

somehow higher levels of hydrogen into the weldment than is expected from the specification. The austenitic stainless steel consumable was also stored in non-sealed environment for time period of approximately 3 years. Thus, it is expected that "fresh" properly stored consumables would introduce lower hydrogen levels. Therefore, these results could be taken as the worst case scenario.

The total amount of hydrogen evolved from the sample welded with austenitic stainless steel originated from the HAZ. Whereas, in the case of the ferritic deposit the measured diffusible hydrogen evolved from weld metal and HAZ, both of which are susceptible to HACC. To minimise the risk of HACC in the weld metal, a ferritic consumable with under matching strength was utilised to join the HHA plates before the introduction of the austenitic consumable. The consumable with under-matching strength has a lower alloy content than the HHA parent metal, thus on cooling after welding the $\gamma \rightarrow \alpha$ transformation occurs at higher temperatures resulting in evolution of the diffusible hydrogen from weld metal to HAZ, thus significantly increasing the risk of HACC in the HAZ. On the contrary the austenitic weld metal does not undergo a phase transformation. Upon transformation the HAZ becomes oversaturated with hydrogen that is induced to diffuse towards weld metal that sustains much higher solubility and lower diffusivity compared to the HAZ and has the ability to accommodate much higher levels of hydrogen. Also the test results suggest that diffusion of hydrogen is promoted from susceptible HAZ to weld metal. From the gathered data it can be concluded that the risk of HACC in the weldments deposited with an austenitic stainless steel consumable is greatly reduced compared to the joints welded with a ferritic consumable. It can be concluded that hydrogen migrates to the austenitic phase due to the higher solubility and lower diffusion rate of hydrogen in austenite compared to ferrite.

4.4.2 Effect of preheat temperature on hydrogen content in HHA joints welded with flux-cored austenitic stainless steel consumable

In the previous section the effect of ferritic and austenitic stainless steel consumables on the level of hydrogen introduced into the weldment was discussed. In order to justify the elimination of preheat the effect of three different preheat temperatures on the amount of diffusible hydrogen present in the HAZ and the amount of residual hydrogen present in weld metal were studied.

The increase in diffusible hydrogen content from 0.5 to 0.8 and 1.3 ml of hydrogen per 100 g of deposited weld metal with decreasing preheat temperature from 80°C to 22°C (ambient) and 7°C is a result of reduced cooling time in the temperature range associated with highly effective hydrogen diffusion out of the weldment.

The nature of austenite promotes hydrogen diffusion from HAZ to weld metal where it becomes effectively trapped. In other words the microstructure of the austenitic stainless steel weld metal having high solubility and very low diffusivity of hydrogen acts like a hydrogen sink. Therefore reduced cooling times (less time for evolution of hydrogen from HAZ into weld metal) as a consequence of lowering preheat temperature resulted in lower levels of weld metal residual hydrogen content.

The level of diffusible and residual hydrogen in the sample under cooled to 7°C and allowed to cool down to 150°C was actually slightly higher than the amount present in the sample that was quenched immediately after extinction of welding arc. This a consequence of the water condensation on the plates to be welded due to the high ambient temperature and temperature of the plate being lower than the dew point. During welding this excess moisture is dissociated in welding arc environment and partially absorbed into the weld pool, thus a lower level of hydrogen is expected when the temperature of the steel plate and the ambient temperature are identical. Savage et al. [96] found that when the water vapour was present in the welding arc it resulted in higher hydrogen levels than when the same quantity of hydrogen gas was added

4.4.3 Comparison of hydrogen level of three types of ASS consumable

Different welding applications require different types of austenitic stainless steel wire. Currently manual and semi-automatic GMAW in combination with flux-cored wire are predominantly used to join HHA steel. For the future automation of the current process metal-cored consumables offer an optimum solution. In addition advanced process control techniques in combination with solid wire are currently under investigation. The structure and the chemical composition of the three types of wire are different hence levels of hydrogen introduced into the weldment are expected to vary. If the current procedures were to be

followed all these applications would require preheating prior to welding. The aim was to demonstrate that the risk of HACC diminish when moving from flux-cored to metal-cored and solid wires.

As expected the measured amount of hydrogen both diffusible and residual was highest in the case of flux-cored consumable. This is a result of the presence of rutile flux prone to pick up moisture from the environment. The structure of the wire also contains a seam facilitating the transfer of moisture into the inner core if consumable is stored inappropriately.

The very low levels of hydrogen both diffusible and residual measured for metal-cored consumable are attributed to the absence of the flux and seamless structure of external metallic sheath of the wire eliminating hydrogen pick-up by the inner core.

The zero diffusible and very low levels of weld metal residual hydrogen measured for solid wire deposits are attributed to combination of solid structure of the wire lacking the inner core and low hydrogen welding process. These conditions practically rule out the risk HACC.

4.4.4 Summary of hydrogen testing

The residual hydrogen values measured for austenitic stainless steel deposits reflect the amount of residual hydrogen (trapped, molecular, and combined) and also the diffusible hydrogen present in the bcc lattice. The diffusion rate of hydrogen in austenite is very slow thus all the hydrogen measured in the weld metal can be considered as residual thus safe from the HACC view point.

It was previously recognized that diffusion of hydrogen is the most effective at high temperatures and the majority of diffusible hydrogen diffuses out of the weld in few seconds after it solidifies [97, 98]. Additionally hydrogen evolves from the start of the weld while the rest of the weld is still being deposited. Small variation of the time period from the extinction of the welding arc until the welded sample is quenched can significantly affect the results, thus it is extremely difficult to quantify the absolute amount of hydrogen introduced into the weldment by a particular consumable however the control of the trials ensured the results were comparable.

Various literature sources consider different levels of hydrogen to be safe from HACC view point. Basu [99] concluded that when welding armour grades of Q&T steels, the hydrogen content introduced by any consumable should not be higher than 4 ml per 100 g of deposited weld metal. Specifications published by American Society of Mechanical Engineers [100] state that in order to ensure freedom from HACC the maximum allowable diffusible hydrogen level in low alloy low hydrogen ferritic consumables is 4 ml of hydrogen per 100 g of weld metal. Holsberg et al. [101] claimed that when welding high strength steels the maximum permissible hydrogen content introduced into the weldment is in the range between 5-2 ml of hydrogen per 100 g of weld metal. Latter two values are considered for welding utilising ferritic consumable. Hence somewhat higher values of hydrogen initially introduced into the weld pool are expected to be safe when an austenitic consumable is used.

Based on above criteria for allowable diffusible hydrogen content all levels of preheat and all types of austenitic stainless steel consumable are safe from HACC view point.

4.5 RESIDUAL STRESSES

The formation of residual stresses in the weld metal and surrounding areas is an inevitable side effect of fusion welding processes. The weld thermal cycle induces thermal expansion and contraction in all three primary axes. Normally there are no forces acting against volume changes in the through thickness orientation; however the expansion and contraction in the transverse and longitudinal direction is restrained [81]. Accumulated strains are either relieved through distortion or in case of thicker highly restrained structures transform into residual stress.

It is widely accepted that tensile residual stresses approaching the material yield stress form parallel to the weld seam as a result of thermal contraction of the metal constrained by bulk (cold) adjacent material that did not achieve yield point strain during the thermal cycle [81]. The type and distribution of longitudinal residual stresses tend to be invariant and magnitude often approaches the yield stress of the parent metal. Whereas transverse residual stresses vary with different welding processes and parameters [66]. Preheating plates prior to welding also reduces weld residual stresses.

Direct measurement of residual stresses was not carried out in the present work since the sample size was unrepresentative of the fully restrained final structure, however the distortion of small test samples was taken as a comparative indication of the likely residual stress which would be produced by the various process variants investigated.

The results of this work show an agreement with this generally accepted theory. From the acquired data it was concluded that reducing preheat temperature leads to formation of higher level of strains. This was deducted from the values of angular distortion measured from the joints welded at 80°C and 21°C preheat utilising identical welding parameters. Welding distortion takes place when strains resulting from thermal shrinkage are too high and cannot be accommodated by elastic deformation. Angular distortion occurs as a consequence of the transverse strains exceeding the yield point of the metal resulting from uneven thermal expansion and contraction of the material due to uniform thermal gradients [81]. The average value of distortion of a corner (90°) joint was 0.45° and 2.63° for plates preheated to 80°C and ambient (21°C) temperature respectively. The lower level of distortion of the HHA joint preheated to 80°C is attributed to less rapid thermal gradients and slower cooling rate.

During welding and subsequent cooling HHA plates were highly restrained, thus the strains generated during welding could not produce geometric deformation but were transformed into weld residual stresses. After completion of cooling to room temperature clamps were released (the force acting against deformation forces was no longer present) allowing the stresses to alter the original geometry. Austenitic weld metal has a much lower yield stress (530 MPa for flux-cored consumable TETRA S used in this investigation) than HHA (1400 MPa) therefore the accumulated stresses in the weldment were accommodated by the weld metal.

The level of preheat currently used for HHA joints welded with austenitic stainless steel consumables was originally designed for use in combination with ferritic consumable. Austenite has considerably higher coefficient of thermal contraction than ferrite (typically 18 and 14 x 10^{-6} /°C in the range of 1°C – 100°C for austenitic and ferritic steel respectively) the overall contraction is higher than that of ferrite but austenitic weld metal possesses increased ability to yield and hence compensate for the thermal contraction resulting in limited residual

stresses compared to ferritic weld metal [102]. Due to these phenomena the residual stresses in joints welded with austenitic consumable are likely to be lower than when ferritic consumables are employed. In addition, on cooling the HAZ of the HHA parent material undergoes martensitic transformation that is accompanied by volume expansion which to certain extent compensates the thermal shrinkage. Francis [103] concluded that when the martensitic transformation occurs at low temperatures lower stress build-up can be expected. This is a result of higher stresses present in the structure at lower temperatures favouring the formation of transformation texture and anisotropic dimensional changes accommodating the strains thus reducing the residual stresses. During the dilatometry and high temperature and confocal microscopy experiments it was found that HHA steel experiences martensitic transformation at relatively low temperature range of 400°C - 200°C when cooling rates representing real welding conditions are employed.

5 CONCLUSIONS

The objectives of this work have been achieved resulting in optimised welding procedures for HHA steel.

Based on the research work described in this document the following conclusions have been made:

1) It has been demonstrated that due to the 1. transformation characteristics of the ferritic HAZ and austenitic weld metal; 2. higher solubility and lower diffusivity of hydrogen in austenite compared to ferrite, the majority of hydrogen diffuses into the weld metal where it is safely "locked" and therefore is not available to contribute to HAZ HACC. Hence, if HHA steel is welded utilising ASS consumable preheating is not necessary.
2) Both, total weld hydrogen content and HAZ diffusible hydrogen content decrease from flux-cored to metal cored and solid consumable. Additionally, the use of solid ASS consumable results in zero diffusible hydrogen in HAZ.
3) When welding HHA steel, increasing interpass temperature up to 250°C does not result in detrimental HAZ softening.
4) Proposed optimised preheat and interpass temperatures significantly reduce the time required to produce a weldment, if applied in the welding fabrication practices.
5) To improve cost efficiency of welding fabrication, safe welding procedures developed for welding ferritic parent metal with ASS consumable previously should be reviewed and proposed optimised preheat and interpass temperatures should be incorporated.
6) The proposed approach based on the difference in transformation temperature of WM and HAZ (refer to publication "Weld metal hydrogen assisted cold cracking in high strength low alloy steels" enclosed in Appendix 7) can be used for future assessment of hydrogen control in steel welding.
7) Further, the proposed optimised preheat and interpass temperatures facilitate the automation (decrease the cost and complexity and improve the productivity) therefore encourage implementing innovation into the welding fabrication.
8) The results of the research work studying the feasibility of the hybrid laser-GMAW process have shown that:
    a) It is possible to produce a hybrid laser-GMAW on high strength Q&T plate at close to the ideal geometry using a 3 kW diode laser.

b) Hardness profiles measured in the area of both cap and inner pass are almost identical
c) The CGHAZ hardness of the hybrid laser-GMAW weldment in area of the inner as well as outer pass was very similar to joint welded using current FCAW process.
d) The hybrid laser-GMAW joining process reduced welding time by 36% and consumable usage by 56% over the current FCAW procedure. (Note: Only time spent in actual deposition of the weld is considered.)
e) The hybrid laser-GMAW technique significantly reduces the number of weld runs required and therefore considerably improves welding economics.

Based on these findings it was concluded that the Hybrid laser-GMAW process is feasible for joining HHA.

From the entire family of commercially produced high strength Q&T steels HHA possesses a highest carbon content, carbon equivalent, hardenability and thus it is the most difficult to weld hence the findings of this research work can be applied to all high strength Q&T steels.

Industry partner wishes to implement outcomes of this research work into the manufacturing practice and is currently waiting for approval from Defence Science and Technology Organisation (DSTO).

Findings regarding optimised preheat and interpass temperatures for welding of high strength Q&T steels presented above are also being reviewed by DSTO and Australian Standard Committee to be incorporated into standard AS/NZS 1554.4 - Structural steel welding - Welding of high strength quenched and tempered steels and also relevant defence standard.

6 REFERENCES

1. Zahn, B.R., *The future combat system: Minimizing risk while maximizing capability*. 2000: Carlisle Barracks, PA, US. p. 1-49.
2. Børvik, T., S. Dey, and A.H. Clausen, *Perforation resistance of five different high-strength steel plates subjected to small-arms projectiles.* International Journal of Impact Engineering, 2008. In Press, Accepted Manuscript.
3. Gooch, W.A., et al. *Ballistic testing of swedish steel armox plate for U.S. armor applications*. in *21st international symposium on Ballistics*. 2004. Adelaide, Australia.
4. Gooch, W.A., et al. *Ballistic testing of australian bisalloy steels for armor applications*. in *23rd international symposium on ballistics*. 2007. Tarragona, Spain.
5. Rapacki, E.J., et al., *Armor steel hardness influence on kinetic energy penetration*, in *15th International Symposium on Ballistics*. 1995: Jerusalem, Israel. p. 323-330.
6. Prifti, J.J., R. Squillacioti, and R. Cellitti, *Improved rolled homogeneous armor (IRHA) steel through higher hardness*. 1997, U. S. Army Research Laboratory: Aberdeen. p. 49.
7. Maweja, K. and W. Stumpf, *The design of advanced performance high strength low-carbon martensitic armour steels: Part 1. Mechanical property considerations.* Materials Science and Engineering: A, 2008. **485**(1-2): p. 140-153.
8. Srivathsa, B. and N. Ramakrishnan, *Ballistic performance maps for thick metallic armour.* Journal of Materials Processing Technology, 1999. **96**(1-3): p. 81-91.
9. U.S. Department of Defense, *MIL-A-12560H - Armor plate, steel, wrought, homogeneous*. 1990: Washington, D.C.
10. U.S. Department of Defense, *MIL-A-46100D - Armor plate, steel, wrought, high hardness*. 1988: Washington, D.C.
11. Australian Department of Defence, *Australian defence standard, DEF (AUST) 8030, Rolled armour plate, steel (3-35 mm)*. 2005.
12. UK Ministry of Defence, *UK defence standard, DEF STAN 95-24, Armour plate, Steel (3-160 mm)*. 2004.
13. Yurioka, N., Suzuki, H., *Hydrogen assisted cracking in C-Mn and low alloy steel weldments.* International Materials Reviews, 1990. **35**(4): p. 217-249.
14. Williams, J.G., *New alloy design perspectives for high strength steels*. 2008, BluescopeSteel: Wollongong. p. 1-14.
15. Barbaro, F.J., et al., *Sulphide inclusions in low manganese steels*. 2008, BluescopeSteel: Wollongong. p. 1-13.
16. Suzuki, S. *Microalloy precipitation control in development of TMCP*. 2005. New York, NY 10016-5990, United States: American Society of Mechanical Engineers.
17. Rao, T.V.L.N., et al., *On mixed upper bainite-martensite in an AISI 4330 steel exhibiting an uncommonly improved strength-toughness combination.* Scripta Metallurgica et Materialia, 1990. **24**(7): p. 1323-1328.
18. Bowie, G.F., et al., *The influence of micro titanium additions on the weld heat affected zone hardness of C-Mn structural steels*, in *International Conference Welding 90* 1990: Geestacht, Germany. p. 219.
19. Harrison, P.L. and R.A. Farrar, *Application of continuous cooling transformation diagrams for welding of steels.* International Materials Reviews, 1989. **34**(1): p. 35-51.
20. Zhang, Z. and R.A. Farrar, *An atlas of continuous cooling transformation (CCT) diagrams applicable to low carbon low alloy weld metals* 1995, London: Institute of Materials. 95.

21. Payares-Asprino, M.C., H. Katsumto, and S. Liu, *Effect of martensite start and finish temperature on residual stress development in structural steel welds.* Welding Journal (Miami, Fla), 2008. **87**(11): p. 279-289.
22. Hornbogen, E., *Effect of variables on maternesitic transformation temperatures.* Acta Metallurgica, 1985. **33**(4): p. 13-28.
23. Suzuki, S., et al. *Low Temperature Type New TMCP Steel Plate for LPG Carriers*. in *4th International Offshore and Polar Engineering Conference*. 1994. Osaka, Japan.
24. Andrews, K.W., *Empirical formulae for the calculation of some transformation temperatures* J. Iron Steel Institute, 1965. **203**: p. 721-727.
25. Alkemade, S.J., *The weld cracking susceptibility of high hardness armour steel*. 1996, Defence Science and Technology Organisation. p. 24.
26. Magudeeswaran, G., V. Balasubramanian, and G. Madhusudhan Reddy, *Hydrogen induced cold cracking studies on armour grade high strength, quenched and tempered steel weldments.* International Journal of Hydrogen Energy, 2008. **33**(7): p. 1897-1908.
27. WTIA, *WTIA Technical Note No. 15 - Welding & fabrication of quenched and tempered steel* 1996, WTIA.
28. Cooper, N., R. Murray, and R. Aubrey, *Welding in armour plate - Fabrication for the fighting forces.* Welding and Metal Fabrication, 2001. **69**.
29. ESAB. *Advantages and Disadvantages of Metal Cored Wires*. 2011 [cited 2011 22.3.2011]; Available from: http://www.esabna.com/us/en/education/knowledge/fillermetals/Advantages-and-Disadvantages-of-Metal-Cored-Wires.cfm.
30. Lincoln Electric, *Pulsed spray metal transfer*, Educational publication, 2004. p. 1-8.
31. Reutzel, E.W., et al. *Laser-GMA hybrid welding: Process monitoring and thermal modeling*. 2005. Pine Mountain, GA, United states: ASM International.
32. Staufer, H., M. Rührnößl, and G. Miessbacher, *LaserHybrid Welding and LaserBrazing: State of the Art in Technology and Practice by the Examples of the Audi A8 and VW-Phaeton*. 2004, Fronius: Wels. p. 1-10.
33. Reutzel, E.W., et al., *Hybrid laser-GMA welding for improved affordability*. Journal of Ship Production, 2008. **24**(2): p. 72-81.
34. Gao, M., et al., *Microstructure characteristics of laser-MIG hybrid welded mild steel.* Applied Surface Science, 2008. **254**(18): p. 5715-5721.
35. Herbert, S., *Laser-hybrid welding of ships.* Welding Journal (Miami, Fla), 2004. **83**(6): p. 39-43.
36. Thomy, C. and F. Vollertsen. *Dynamic behaviour of CO2 laser GMA hybrid welding*. in *Laser Materials Processing Conference*. 2006: ICALEO.
37. Fronius, *High-performance welding: LaserHybrid, TimeTwin Digital, strip-wire, large-diameter wires*. 2003, Wels: Fronius International GMBH.
38. Feliman, A. and V. Kujanpaa, *The effect of shielding gas composition on welding performance and weld properties in hybrid CO2 laser-gas metal arc welding of carbon manganese steel.* Journal of Laser Applications, 2006. **18**(1): p. 12-20.
39. Kah, P., A. Salminen, and J. Martikainen, *The analysis of shielding gases in laser-arc hybrid welding processes.* Proceedings of the Institution of Mechanical Engineers, Part B: Journal of Engineering Manufacture, 2011. **225**(7): p. 1073-1082.
40. Tani, G., et al., *The influence of shielding gas in hybrid LASER-MIG welding.* Applied Surface Science, 2007. **253**(19): p. 8050-8053.
41. *Joint Standards Australia/Standards New Zealand Committee WD-003, AS/NZS 1554.4:2010: Structural steel welding - Welding of high strength quenched and*

tempered steels, 2010, Standards Australia (Sydney) and Standards New Zealand (Wellington).
42. SSAB, *Armox welding recommendations*. 2005, SSAB Oxelosund AB: Oxelosund, Sweden.
43. Magudeeswaran, G., et al., *Effect of welding consumables on tensile and impact properties of shielded metal arc welded high strength, quenched and tempered steel joints.* Science and Technology of Welding and Joining, 2008. **13**(2): p. 97-105.
44. Magudeeswaran, G., V. Balasubramanian, and G. Madhusudhan Reddy, *Effect of welding consumables on hydrogen induced cracking of armour grade quenched and tempered steel welds.* Ironmaking and Steelmaking, 2008. **35**(7): p. 549-560.
45. Bailey, N., et al., *Welding steels without hydrogen cracking*. 2nd ed. 1993, Cambridge: Woodhead Publishing Limited.
46. Murugananth, M., et al., *Mathematical Modelling of Weld Phenomena 6*, ed. B.H.K.D. H. Vol. 6. 2002, London: Institute of Materials, Minerals and Mining 1135.
47. Toriano, A.R., *The role of H and other interstitials in the mechanical behaviour in metals.* Transaction of the ASM, 1960. **52**: p. 54-80.
48. Olson, D.L. and S. Liu, *The physical and chemical behaviour of steel welding consumables*, in *4th International Conference on Trends in Welding Research*. 1996: Gatlinburg. p. 299-307.
49. Self, J.A., et al., *Phase transformation and alloy stability in Fe-Mn-Ni-Cr-Al weld metal*, in *Proceedings of Alternate alloying for environmental resistance*. 1987. p. 37-46.
50. Wang, W.W., et al. *Use of martensite start temperature for hydrogen control*. 1996. Cleveland, OH, USA: Minerals, Metals & Materials Soc (TMS).
51. Lancaster, J.F., *Metallurgy of welding* 6th ed. 1999, Cambridge :: Abington.
52. Hart, P.H.M. *Hydrogen cracking - its causes, costs and future occurrence*. in *1st International Conference on Hydrogen Cracking in Pipeline Girth Welds*. 1999. Wollongong.
53. Boellinghaus, T., H. Hoffmeister, and A. Dangeleit, *A scatterband for hydrogen diffusion coefficients in micro-alloyed and low carbon structural steels.* Welding in the World, 1996. **37**(1): p. 16-23.
54. Nolan, D. and M. Pitrun, *Diffusible hydrogen testing in Australia.* Welding Research Abroad, 2005. **51**(2): p. 45-51.
55. Gedeon, S.A. and T.W. Eagar, *Thermomechanical analysis of hydrogen absorption in welding.* Welding Journal (Miami, Fla), 1990. **69**(7): p. 264-271.
56. Engelhard, W.J., D.L. Olson, and B. Mishra. *Dissolution of Gaseous Hydrogen in High Strength Steels at Elevated Temperatures*. 1998. Rosemont, IL, United states: ASM International.
57. Howden, D.G., *Behaviour of hydrogen in arc weld pools*, in *Weld pool chemistry and metallurgy international conference*. 1980: London. p. 205-215.
58. Jargelius, R.F.A. and Fun-Cun-Gan, *The influence of hydrogen on the mechanical properties and microstructure of stainless steels*, in *International Conference on Stainless Steels*. 1991, ISIJ: Chiba. p. 692-699.
59. Louthan, M.R. and G.R. Cannell, *Impact of H2 in shielding gas for welding austenitic stainless steels.* Welding Journal (Miami, Fla), 2005. **84**(4): p. 38-40.
60. Vilginate, G.N., et al., *Hydrogen induced cracking tests of high strength steels and nickel-iron base alloys* 1996.
61. Chen, Z., et al., *Effect of Structures Formed in HAZ on behaviour of Hydrogen Diffusion and Properties for Ultra High Strength Steel 30CrMnSiNi2A*, 1986. Gatlinburg, TN, USA: ASM Int.

62. Maroef, I.S. and D.L. Olson. *Evaluation of Hydrogen Trapping for Hydrogen Management in Steel Welding*. 2002. Phoenix, AZ, United states: ASM International.
63. Odengard, O., G.M. Evans, and N. Christensen, *Apparent diffusivity of hydrogen in multi-run weld arc deposits.* Metal Construction, 1971. **3**(2): p. 47-49.
64. Kim, J.S., et al., *Microstructural influences on hydrogen delayed fracture of high strength steels.* Materials Science and Engineering A, 2009. **505**(1-2): p. 105-110.
65. Dong, P., J. Zhang, and M.V. Li. *Computational modeling of weld residual stresses and distortions - an integrated framework and industrial applications*. 1998. San Diego, CA, USA: ASME.
66. Masubuchi, K., *Control of distortion and shrinkage in welding.* Welding Research Council Bulletin, 1970.
67. Matsuda, F., et al., *Effect of transformation expansion restraint stress of weldment in relation to cold cracking of high strength steels* Transactions of JWRI (Japanese Welding Research Institute), 1982. **11**(2): p. 57-65.
68. Madhusudhan Reddy, G. and T. Mohandas, *Influence of welding process and residual stress on ballistic performance.* Journal of Materials Science Letters, 1996. **15**(18): p. 1633-1635.
69. Park, M.J., et al., *Residual stress measurement on welded specimen by neutron diffraction.* Journal of Materials Processing Technology, 2004. **155-156**(1-3): p. 1171-1177.
70. Onsien, M.I., M. M'Hamdi, and O.M. Akselsen, *Residual stresses in weld thermal cycle simulated specimens of X70 pipeline steel.* Welding Journal (Miami, Fla). **89**(6): p. 127s-132s.
71. Yurioka, N., *Physical metallurgy of steel weldability.* ISIJ international, 2001. **41**(6): p. 566-570.
72. *AS/NZS 1554. 1:2004 Structural steel welding Part 1: Welding of steel structures*. 2004, Standards of Australia.
73. Yurioka, N., et al., *Prediction of HAZ hardness of transformable steels.* Metal Construction, 1987. **19**(4): p. 217r-223r.
74. BisalloySteelGroup, *Bisplate technical guide*. 2008: Wollongong. p. 1-46.
75. Yurioka, N. and T. Kasuya, *Chart method to determine necessary preheat in steel welding.* Welding in the World, Le Soudage Dans Le Monde, 1995. **35**(5): p. 327-334.
76. *ISO/TR 17844:2004 (E): Welding — Comparison of standardised methods for the avoidance of cold cracks*, WEE/17, Editor. 2004: Geneva.
77. Bhadeshia, H.K.D.K. and R.W.K. Honeycombe, *STEELS: Microstructure and Properties*. 3rd ed. Materials Characterization, ed. B. Ralph. Vol. 59. 2008, Amsterdam: Elsevier. 348.
78. Cottrell, C.L.M., *Assessment of Weldability by Rapid Dilatation Tests.* Journal of the Iron and Steel Institute, 1953. **174**(53): p. 17-24.
79. Funderburg, R.S., *The importance of interpass temperature.* Welding innovation, 1998. **15**(1): p. 31-32.
80. Gao, M., X.Y. Zeng, and Q.W. Hu, *Effects of welding parameters on melting energy of CO2 laser–GMA hybrid welding.* Science and Technology of Welding and Joining, 2006. **11**(5): p. 517-522.
81. WTIA, *Distortion control in shipbuilding*. 2006, Welding technology institute of Australia: Newington. p. 7.
82. Kennedy, I.J., *Development of Continuous Cooling Diagrams for Quenched and Tempered Steels Containing Molybdenum and Chromium*, in *Materials Engineering*. 1995, University of Wollongong: Wollongong. p. 88.

83. Kiefer, J.H., *Effects of welding parameters on FCAW HAZ cooling*, in *International Conference on The Metallurgy, Welding, and Qualification of Microalloyed (HSLA) Steel Weldments*, J.T. Hickey, Howden, D.G., Randall, M. D, Editor. 1990, AWS Miami Florida: Houston, Texas.
84. TechnicalCommiteeCEN/TC121"Welding", *EN 1011-2 Welding - Recommendations for welding of metallic materials - Part 2: Arc welding of ferritic steels*, E.C.f. Standardization, Editor. 2001: Brussels. p. 1-67.
85. U.S.DepertmentofDefense, *MIL-STD-1185, Department of defense manufacturing process strandard: Welding, High Hardness Armor* 1973, Department of Defense: Washington, DC.
86. Krauss, G., *Principles of heat treatment of steel*, ed. M. Park. 1980, Ohio: ASM International. 291.
87. *ASM handbook; v.9: Metallography and microstructure*, in *Scitech Book News*. 2005, Book News, Inc.: United States, Portland.
88. Zhao, J., *Continuous cooling transformations in steels.* Materials Science and Technology, 1992. **8**(11): p. 997-1003.
89. Shome, M. and O.N. Mohanty, *Continuous cooling transformation diagrams applicable to the heat-affected zone of HSLA-80 and HSLA-100 steels.* Metallurgical and Materials Transactions A: Physical Metallurgy and Materials Science, 2006. **37**(7): p. 2159-2169.
90. Arata, Y., et al., *Weldability concept on hardness prediction.* Transactions of JWRI (Japanese Welding Research Institute), 1979. **8**(1): p. 43-52.
91. Lorenz, K. and C. Düren, *Evaluation of Large Diameter Pipe Steel Weldability by Means of the Carbon Equivalent*, in *International Conference on Steels for Linepipe and Fittings*. 1981, Metals Society: London. p. 322-332.
92. Defalco, J., *Practical applications for hybrid laser welding.* Welding Journal (Miami, Fla), 2007. **86**(10): p. 47-51.
93. Blomquist, P.A., S.E. Ferree, and B.M. Marx. *Diffusible hydrogen characteristics of Hybrid Laser Arc Welding (HLAW)*. 2009. Orlando, FL, United states: Laser Institute of America.
94. Colegrove, P., et al., *Welding process impact on residual stress and distortion.* Science and Technology of Welding and Joining, 2009. **14**(8): p. 717-725.
95. Pitrun, M., *The effect of welding parameters on levels of diffusible hydrogen in weld metal deposited using gas shielded rutile flux cored wires*, in *Department of Materials Engineering - Faculty of Engineering*. 2004, University of Wollongong3: Wollongong. p. 339.
96. Savage, W.F., E.F. Nippes, and E.I. Husa, *HYDROGEN-ASSISTED CRACKING IN HY-130 WELDMENTS.* Welding Journal (Miami, Fla), 1982. **61**(8): p. 233-s-242-s.
97. Terasaki, T., et al., *An analysis on specimen size for determination of diffusible hydrogen in weld metal.* Trans. Japan Welding Society 1986. **17**(1): p. 93-101.
98. Hooijmans, J.W. and G. Den Ouden, *Model of hydrogen absorption during GTA welding.* Welding Journal (Miami, Fla), 1997. **76**(7): p. 264.s-268.s.
99. Basu, B., *Special Considerations for Use of High Strength Steel Weldments* in *National Conference on "Welding-Productivity & Quality"*, A.K. Shah, Editor. 2007: Ambarnath, India. p. 73-78.
100. ASME, *Specifications for low alloy steel electrodes for shielded metal arc welding*, in *ASME boiler pressure vessel code*. 2007, American Society of Mechanical Engineers. p. 105-107.
101. Holsberg, P.W. and R.J. Wong, *Welding of HSLA-100 for Naval Applications.* Weldability of Materials, 1990: p. 219-239.

102. Bhadeshia, H.K.D.H., *Developments in martensitic and bainitic steels: Role of the shape deformation.* Materials Science and Engineering A, 2004. **378**(1-2 SPEC. ISS.): p. 34-39.
103. Francis, J.A., H.K.D.H. Bhadeshia, and P.J. Withers, *Welding residual stresses in ferritic power plant steels.* Materials Science and Technology, 2007. **23**(9): p. 1009-1020.

APPENDICES

APPENDIX 1

Certificate of chemical analysis of HHA steel.

BLUESCOPE STEEL

Laboratory Services
Central Laboratory (30)
For: Kembla Steelworks
PO Box 1854
Wollongong NSW 2500
Telephone: 02 4275 7422
Facsimile: 02 4275 3429
BlueScope Steel (AIS) Pty Limited
ABN 19 000 019 625
Enquiries: Metals Analysis ext 7432

CERTIFICATE OF ANALYSIS

Lab Reference: M09/0323

Charge to: 202060

Job Description: Square test sample off cuts
Specification:
Sender's Ref.: UOW
Purchase Order:
Client: Product Application
Central Lab

Certificate Issued: 17/04/09
Samples Received: 17/04/09
Date Sampled: 17/04/2009

Phone: 3405

Attention: Frank Barbaro

Fax:

Lab N°:	M09/0323/1	M09/0323/2
Sample Id:	1	2
Heat N°:		
C	0.26	0.27
P	0.015	0.014
Mn	0.29	0.30
Si	0.30	0.32
S	0.0025	0.0025
Ni	0.17	0.19
Cr	1.05	1.05
Mo	0.25	0.25
Cu	0.018	0.019
Al	0.046	0.059
Sn	<0.002	<0.002
Nb	0.004	0.003
Ti	0.021	0.023
V	0.039	0.040
B tot	0.0015	0.0011
Ca	0.0009	0.0007
N	0.0044	0.0049
Verified By	JPL	JPL

NT=Not Tested. *Samples tested have been supplied by the customer.* *All elements reported as % m/m unless otherwise stated.*

Test Method: Analysis by Atomic Emission Spectroscopy (MA-LABS-OES-05).

Copy to:

Approved By:
John Palinkas
Senior Analyst

Page 1 of 1

APPENDIX 2

Example of the robot programme used for investigation of the optimum interpass temperature of the five pass corner weldment welded with flux-cored consumable.

```
%%%
 VERSION:1
  LANGUAGE:ENGLISH
%%%

MODULE HHAS1011
  CONST robtarget StartPoint3:=[[750.89,-815.04,379.24],[0.926998,0.000746,-0.375067,-
7.9E-05],[-1,1,-2,0],[9E+09,9E+09,9E+09,9E+09,9E+09,9E+09]];
  !welddata: [wd_speed, delay_distance, org_wd_speed]
  PERS welddata wd:=[50,0,30];
  PERS welddata wd_1:=[45,0,30];
  PERS welddata wd_2:=[50,0,30];
  PERS welddata wd_3:=[50,0,30];
  PERS welddata wd_4:=[55,0,30];
  PERS welddata wd_5:=[55,0,30];
  !not Used
  CONST speeddata v2:=[2,500,5000,1000];
  !weavedata: [shape, type, cycle, width, height, dwell_left, dwell_center, dwell_right,
wv_dir,
  !          wv_tilt, wv_ori, wv_bias, wv_sync_left, wv_sync_right, org_wv_width,
org_wv_height, org_wv_bias]
  PERS weavedata wv_1:=[0,0,0,0,0,0,0,0,0,0,0,0,0,0,0];
  !seamdata: [purge_time, preflow_time, ign_move_delay, scrape_start, heat_speed,
heat_time,
  !          heat_distance, cool_time, fill_time, postflow_time]
  PERS seamdata sm_1:=[0,0,0,0,0,0,0,0,0,0];
  PERS robtarget StartPoint1:=[[749,-815.03,381.22],[0.901,0.1804,-0.3663,0.0722],[-1,1,-
2,0],[9E+09,9E+09,9E+09,9E+09,9E+09,9E+09]];
```

```
  PERS robtarget EndPoint1:=[[751.5,-595.35,381],[0.901,0.1804,-0.3663,0.0722],[-1,1,-
2,0],[9E+09,9E+09,9E+09,9E+09,9E+09,9E+09]];
  PERS robtarget StartPoint2:=[[547.58,-831.69,372.88],[0.908458,0.182112,-
0.369114,0.072768],[-1,0,-2,0],[9E+09,9E+09,9E+09,9E+09,9E+09,9E+09]];
  PERS robtarget EndPoint2:=[[550.23,-552.18,371.69],[0.908419,0.182183,-
0.369172,0.072783],[-1,0,-2,0],[9E+09,9E+09,9E+09,9E+09,9E+09,9E+09]];
  PERS robtarget
CurrentPos:=[[0,0,0],[0,0,0,0],[0,0,0,0],[9E+09,9E+09,9E+09,9E+09,9E+09,9E+09]];
  PERS robtarget StartPoint:=[[465.64,-747.41,871.75],[0.901,0.1804,-0.3663,0.0722],[-2,1,-
2,0],[9E+09,9E+09,9E+09,9E+09,9E+09,9E+09]];
  PERS robtarget WeldStart:=[[547.58,-831.69,372.88],[0.908458,0.182112,-
0.369114,0.072768],[-1,0,-2,0],[9E+09,9E+09,9E+09,9E+09,9E+09,9E+09]];
  PERS robtarget WeldEnd:=[[550.261,-552.3,373.4],[0.901,0.1804,-0.3663,0.0722],[-1,1,-
2,0],[9E+09,9E+09,9E+09,9E+09,9E+09,9E+09]];
  PERS robtarget FindPointStart:=[[540.136,-552.3,376.4],[0.901,0.1804,-0.3663,0.0722],[-
1,1,-2,0],[9E+09,9E+09,9E+09,9E+09,9E+09,9E+09]];
  PERS robtarget FindPointEnd:=[[560.136,-552.3,376.4],[0.901,0.1804,-0.3663,0.0722],[-
1,1,-2,0],[9E+09,9E+09,9E+09,9E+09,9E+09,9E+09]];
  PERS robtarget TouchPoint:=[[550.261,-552.326,376.374],[0.908427,0.181908,-
0.36929,0.0727717],[-1,0,-2,0],[9E+09,9E+09,9E+09,9E+09,9E+09,9E+09]];
  VAR dionum WeldEnable:=low;
  PERS num TestPos:=0;
  PERS num RunProg:=0;
  PERS num WeldEnableNum:=0;
  PERS num ExecProg:=0;
  PERS num WeldEnableNumF:=0;
  VAR num RTestPos:=0;
  VAR num RRunProg:=0;
  VAR num Rtack:=0;
  VAR num RWeldEnableNum:=0;
  VAR num RWeldType:=0;
  VAR num Xoffs:=0;
  VAR num Yoffs:=0;
```

```
VAR num Zoffs:=0;
VAR num StickOut:=0;

PROC main()
  WHILE TRUE DO
    MoveJ StartPoint,v200,fine,F_Weldgun;
    ConfL\Off;
    !set up fronius welder for manual control
    SetDO doMode0,0;
    SetDO doMode1,0;
    SetDO doMode2,1;
    ! Ask user which pass to run
    TPReadFK RRunProg,"Pass #","Pass 1","Pass 2","Pass 3","Pass 4","Pass 5";
    ! Ask user if if welding should be enabled (for program testing)
    TPReadFK RWeldEnableNum,"Activate Welding","","","","Yes","No";
    IF RWeldEnableNum=4 THEN
      WeldEnable:=high;
    ELSE
      WeldEnable:=low;
    ENDIF
    IF RRunProg=1 THEN
      TPReadFK Rtack,"Tack of Weld","","","","Tack","Weld";
      IF Rtack=4 THEN
        MoveL Offs(StartPoint1,-100,0,100),v200,fine,F_Weldgun;
        MoveL StartPoint1,v50,fine,F_Weldgun;
        SetAO aoArcCorrection,-3;
        SetAO aoPower,37;
        SetDO doArcOn,WeldEnable;
        ArcL\Off,Offs(StartPoint1,0,5,0),v500,sm_1,wd_1,wv_1,fine,F_Weldgun;
        MoveL Offs(StartPoint1,-100,0,100),v50,fine,F_Weldgun;
        MoveJ StartPoint,v200,fine,F_Weldgun;
        MoveL Offs(EndPoint1,-100,0,100),v200,z50,F_Weldgun;
        MoveL EndPoint1,v50,fine,F_Weldgun;
```

```
    SetDO doArcOn,WeldEnable;
    ArcL\Off,Offs(EndPoint1,0,-5,0),v500,sm_1,wd_1,wv_1,fine,F_Weldgun;
    MoveL Offs(EndPoint1,-100,0,100),v50,z50,F_Weldgun;
  ENDIF
  IF Rtack=5 THEN
    MoveL Offs(StartPoint1,-100,0,100),v200,fine,F_Weldgun;
    MoveL Offs(StartPoint1,0,0,0),v50,fine,F_Weldgun;
    SetAO aoArcCorrection,-3;
    SetAO aoPower,37;
    SetDO doArcOn,WeldEnable;
    ArcL\Off,Offs(EndPoint1,0,0,0),v500,sm_1,wd_1,wv_1,fine,F_Weldgun;
    MoveL Offs(EndPoint1,-100,0,100),v200,z50,F_Weldgun;
  ENDIF
ENDIF
IF RRunProg>=2 THEN
  TPReadFK RWeldType,"Weld Type","","Find Plt","Full","1st Half","2nd Half";
  IF RWeldType=3 THEN
    WeldStart:=StartPoint2;
    WeldEnd:=EndPoint2;
  ENDIF
  IF RWeldType=4 THEN
    WeldStart:=StartPoint2;
    WeldEnd:=EndPoint2;
    WeldEnd.trans:=WeldStart.trans+(WeldEnd.trans-WeldStart.trans)*0.45;
  ENDIF
  IF RWeldType=5 THEN
    WeldStart:=StartPoint2;
    WeldStart.trans:=WeldStart.trans+(WeldEnd.trans-WeldStart.trans)*0.55;
    WeldEnd:=EndPoint2;
  ENDIF
  IF RWeldType=2 THEN
    RRunProg:=0;
    RWeldEnableNum:=0;
```

```
  FindPointStart:=Offs(StartPoint2,-10,0,3);
  FindPointEnd:=Offs(StartPoint2,10,0,3);
  MoveL Offs(FindPointStart,-100,0,100),v200,fine,F_Weldgun;
  MoveL FindPointStart,v200,fine,F_Weldgun;
  SetDO doTouch,high;
  SearchL\Stop,diCurrentFlow,TouchPoint,FindPointEnd,v2,F_Weldgun;
  SetDO doTouch,low;
  MoveL Offs(FindPointStart,-100,0,100),v200,fine,F_Weldgun;
  StartPoint2.trans.x:=TouchPoint.trans.x;
  MoveL StartPoint,v200,fine,F_Weldgun;
  FindPointStart:=Offs(EndPoint2,-10,0,3);
  FindPointEnd:=Offs(EndPoint2,10,0,3);
  MoveL Offs(FindPointStart,-100,0,100),v200,fine,F_Weldgun;
  MoveL FindPointStart,v200,fine,F_Weldgun;
  SetDO doTouch,high;
  SearchL\Stop,diCurrentFlow,TouchPoint,FindPointEnd,v2,F_Weldgun;
  SetDO doTouch,low;
  MoveL Offs(FindPointStart,-100,0,100),v200,fine,F_Weldgun;
  EndPoint2.trans.x:=TouchPoint.trans.x;
ENDIF
IF RRunProg=2 THEN
  StickOut:=0;
  Xoffs:=0-(0.707*StickOut);
  Yoffs:=0;
  Zoffs:=0+(0.707*StickOut);
  wd:=wd_2;
  SetAO aoArcCorrection,-3;
  SetAO aoPower,37;
ENDIF
IF RRunProg=3 THEN
  StickOut:=0;
  Xoffs:=-3.5-(0.707*StickOut);
  Yoffs:=0;
```

```
    Zoffs:=0+(0.707*StickOut);
    wd:=wd_3;
    SetAO aoArcCorrection,-3;
    SetAO aoPower,37;
  ENDIF
  IF RRunProg=4 THEN
    StickOut:=0;
    Xoffs:=-2.3-(0.707*StickOut);
    Yoffs:=0;
    Zoffs:=4+(0.707*StickOut);
    wd:=wd_4;
    SetAO aoArcCorrection,-3;
    SetAO aoPower,37;
  ENDIF
  IF RRunProg=5 THEN
    !not used
    StickOut:=0;
    Xoffs:=-1.5-(0.707*StickOut);
    Yoffs:=0;
    Zoffs:=6+(0.707*StickOut);
    wd:=wd_5;
    SetAO aoArcCorrection,-3;
    SetAO aoPower,37;
  ENDIF
  IF RRunProg<>0 THEN
    MoveL Offs(WeldStart,-100,0,100),v200,fine,F_Weldgun;
    MoveL Offs(WeldStart,Xoffs,Yoffs,Zoffs),v50,fine,F_Weldgun;
    SetDO doArcOn,WeldEnable;
    ArcL\Off,Offs(WeldEnd,Xoffs,Yoffs,Zoffs),v500,sm_1,wd,wv_1,fine,F_Weldgun;
    MoveL Offs(WeldEnd,-100,0,100),v200,fine,F_Weldgun;
  ENDIF
ENDIF
RRunProg:=0;
```

```
      RWeldEnableNum:=0;
    ENDWHILE
    MoveL StartPoint1,v1000,z50,F_Weldgun;
    MoveJ EndPoint1,v1000,z50,F_Weldgun;
  ENDPROC
ENDMODULE
```

APPENDIX 3

Typical dilatation curves for each cooling rate acquired during dilatometry experiments.

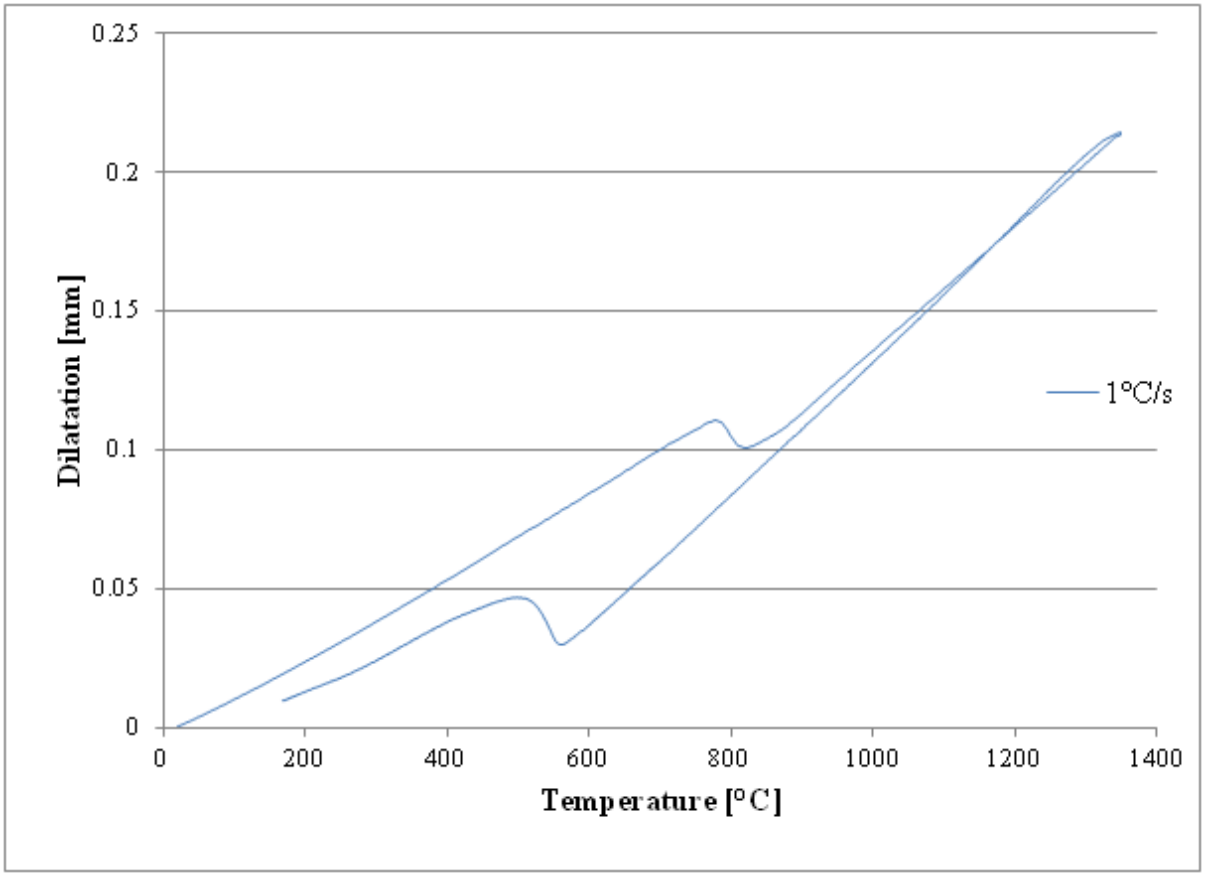

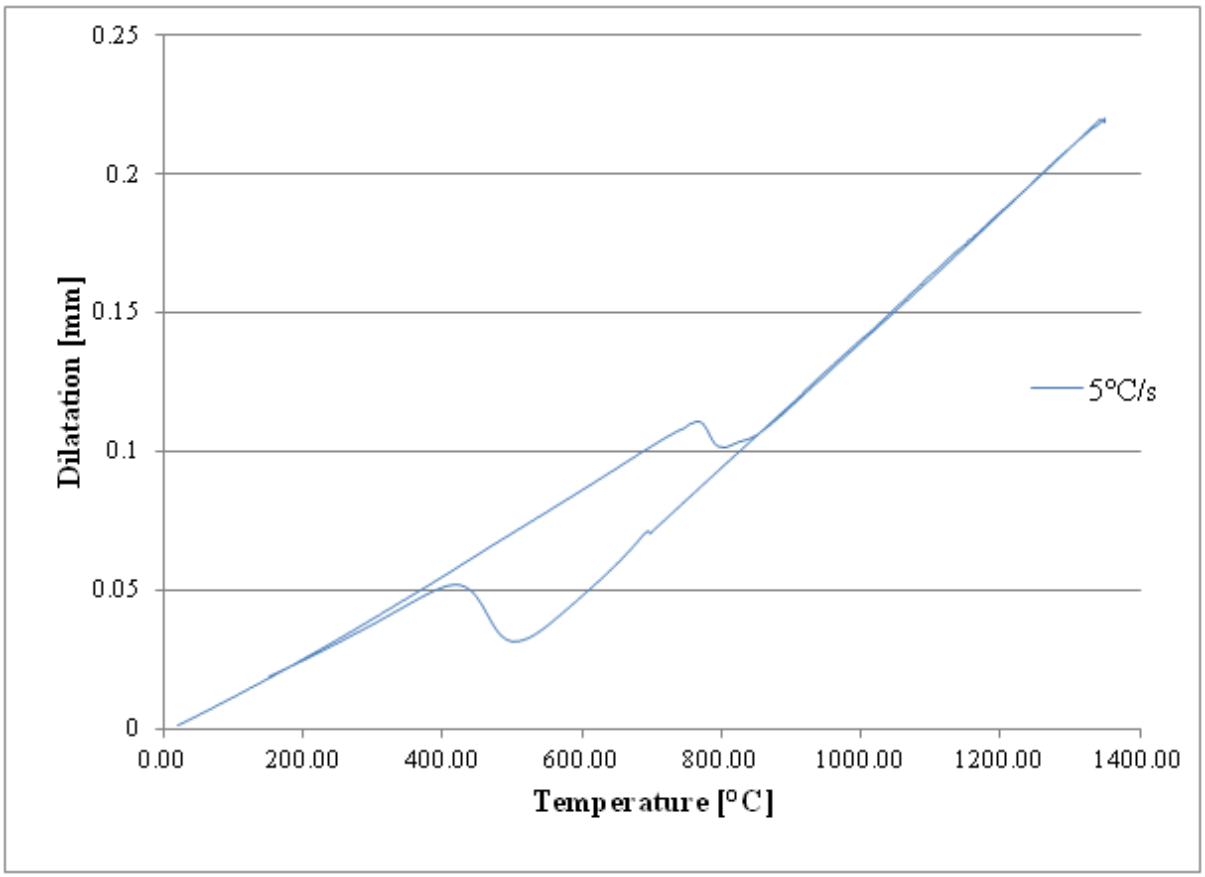
0.25
0.2
0.15
0.1
0.05
0
Dilatation [mm]
0.00
200.00
400.00
600.00
800.00
1000.00
1200.00
1400.00
Temperature [°C]
5°C/s

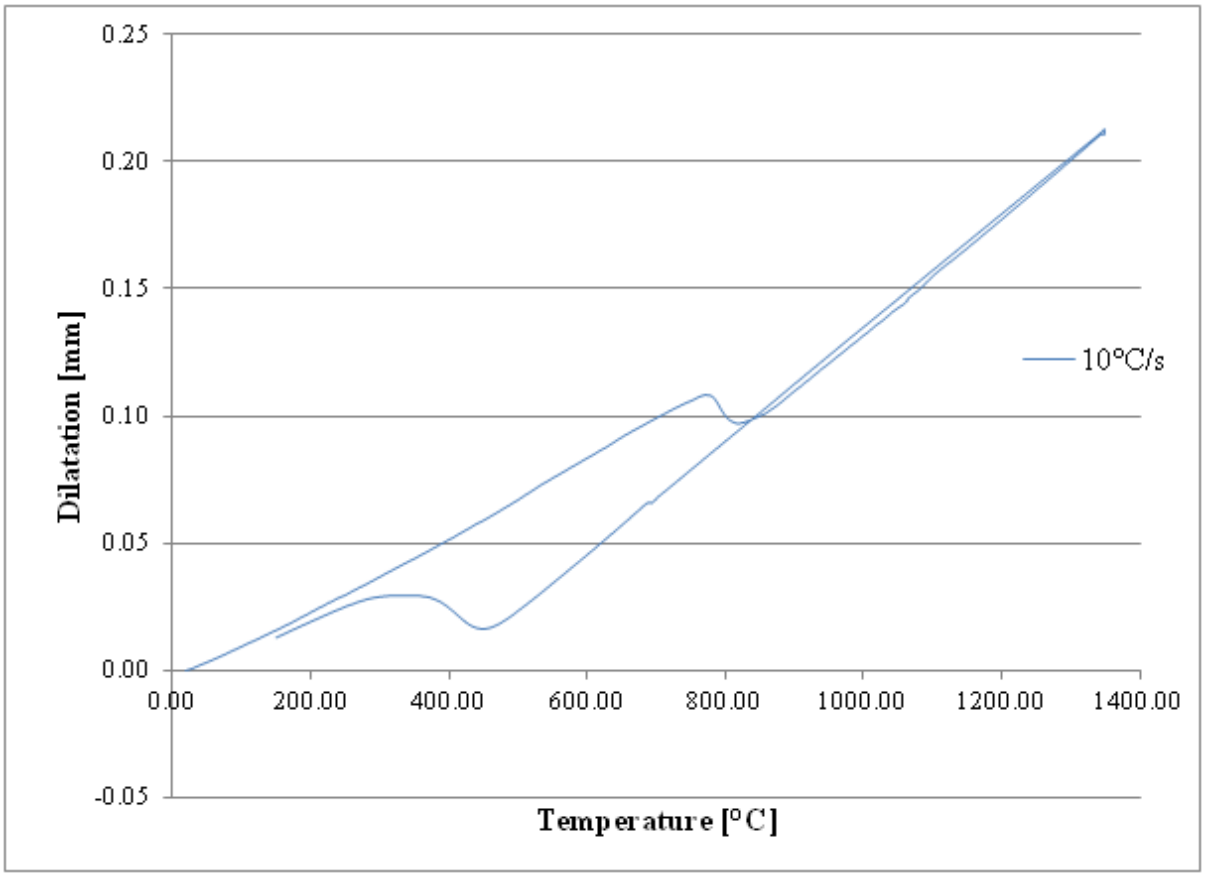
0.25
0.20
0.15
0.10
0.05
0.00
-0.05
Dilatation [mm]
0.00
200.00
400.00
600.00
800.00
1000.00
1200.00
1400.00
Temperature [°C]
10°C/s

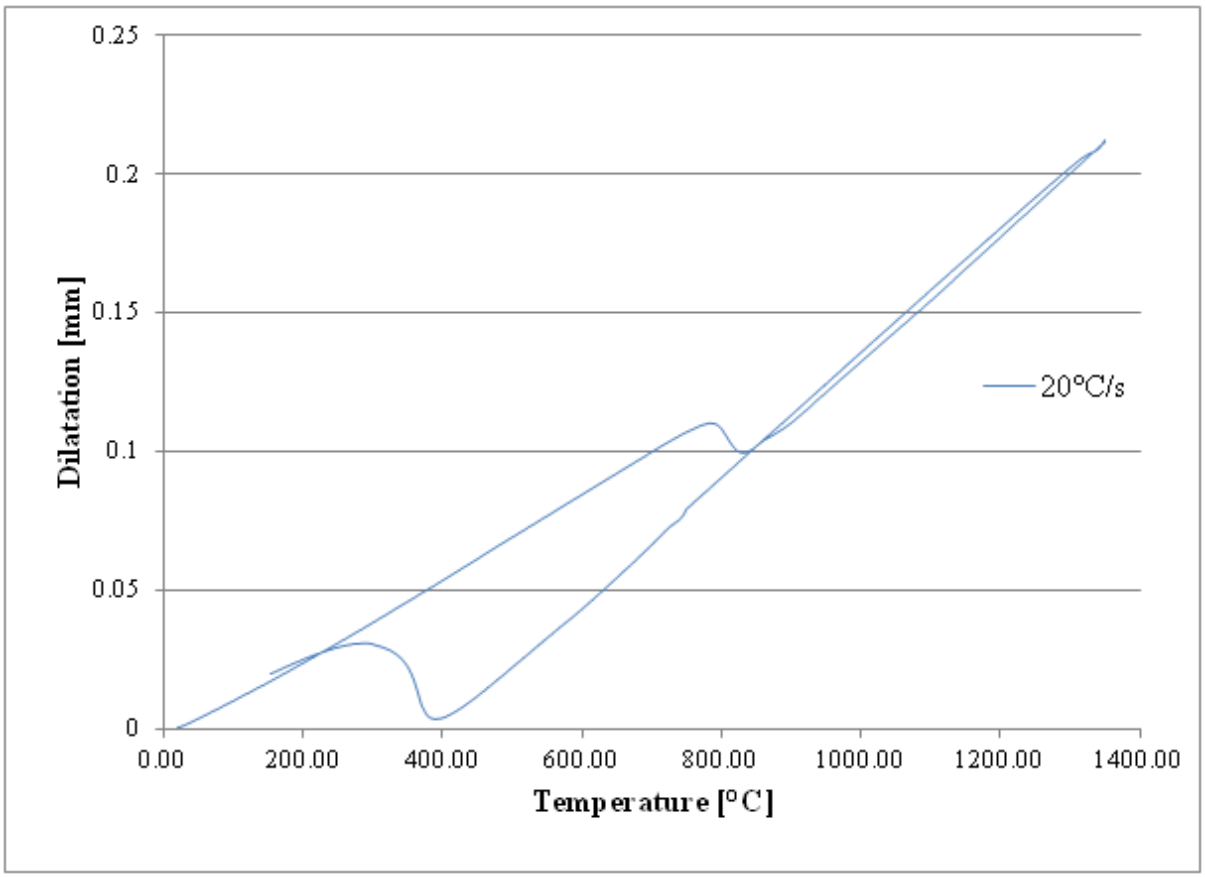
0.25
0.2
0.15
0.1
0.05
0
Dilatation [mm]
20°C/s
0.00
200.00
400.00
600.00
800.00
1000.00
1200.00
1400.00
Temperature [°C]

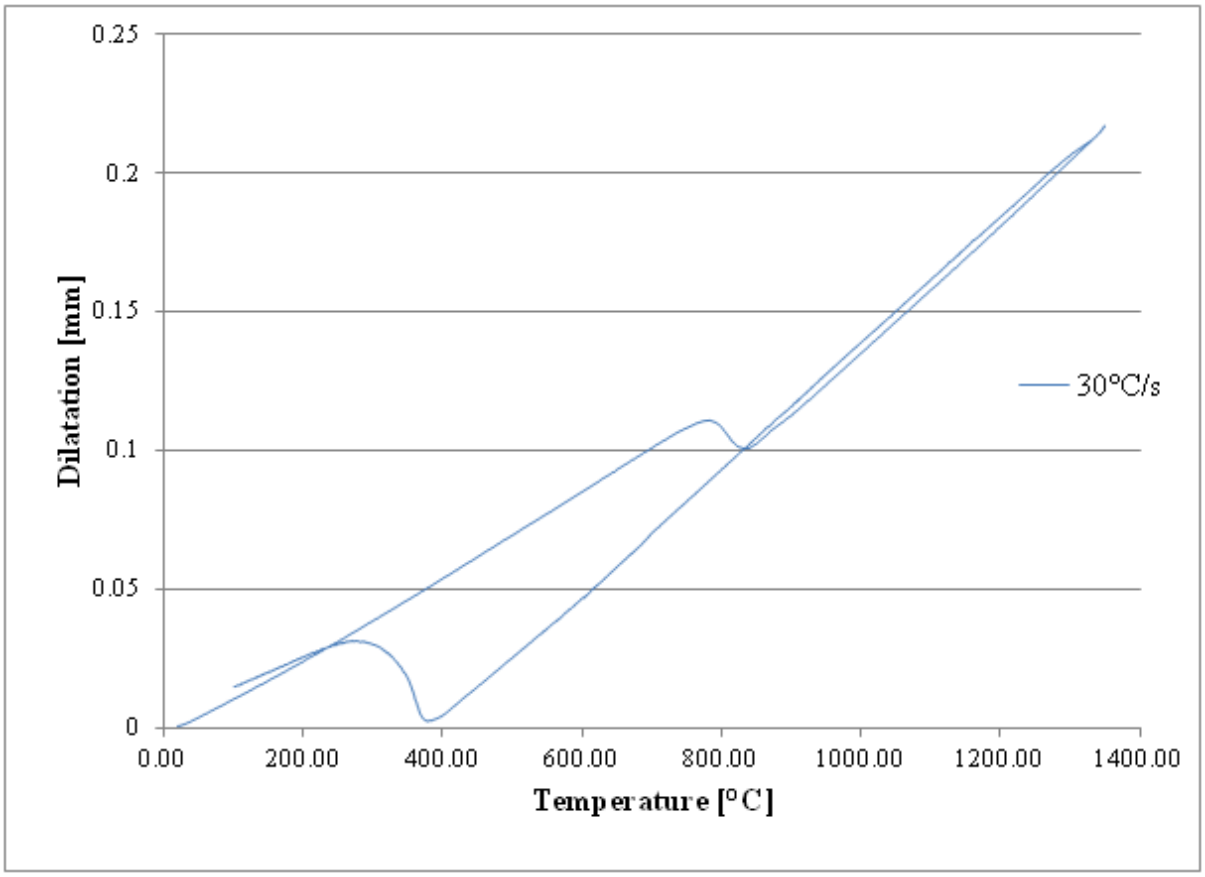
0.25
0.2
0.15
0.1
0.05
0
Dilatation [mm]
30°C/s
0.00
200.00
400.00
600.00
800.00
1000.00
1200.00
1400.00
Temperature [°C]

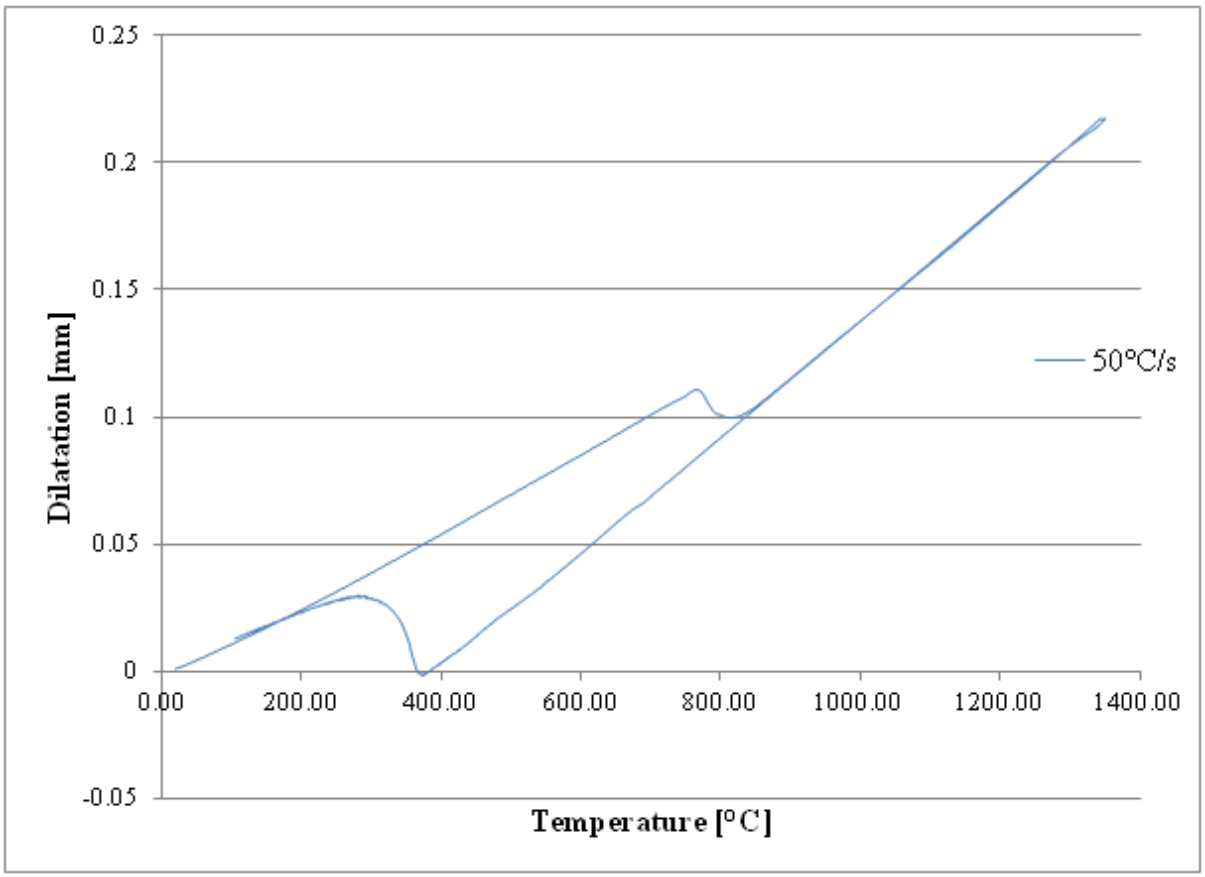
0.25
0.2
0.15
0.1
0.05
0
-0.05
Dilatation [mm]
0.00
200.00
400.00
600.00
800.00
1000.00
1200.00
1400.00
Temperature [°C]
50°C/s

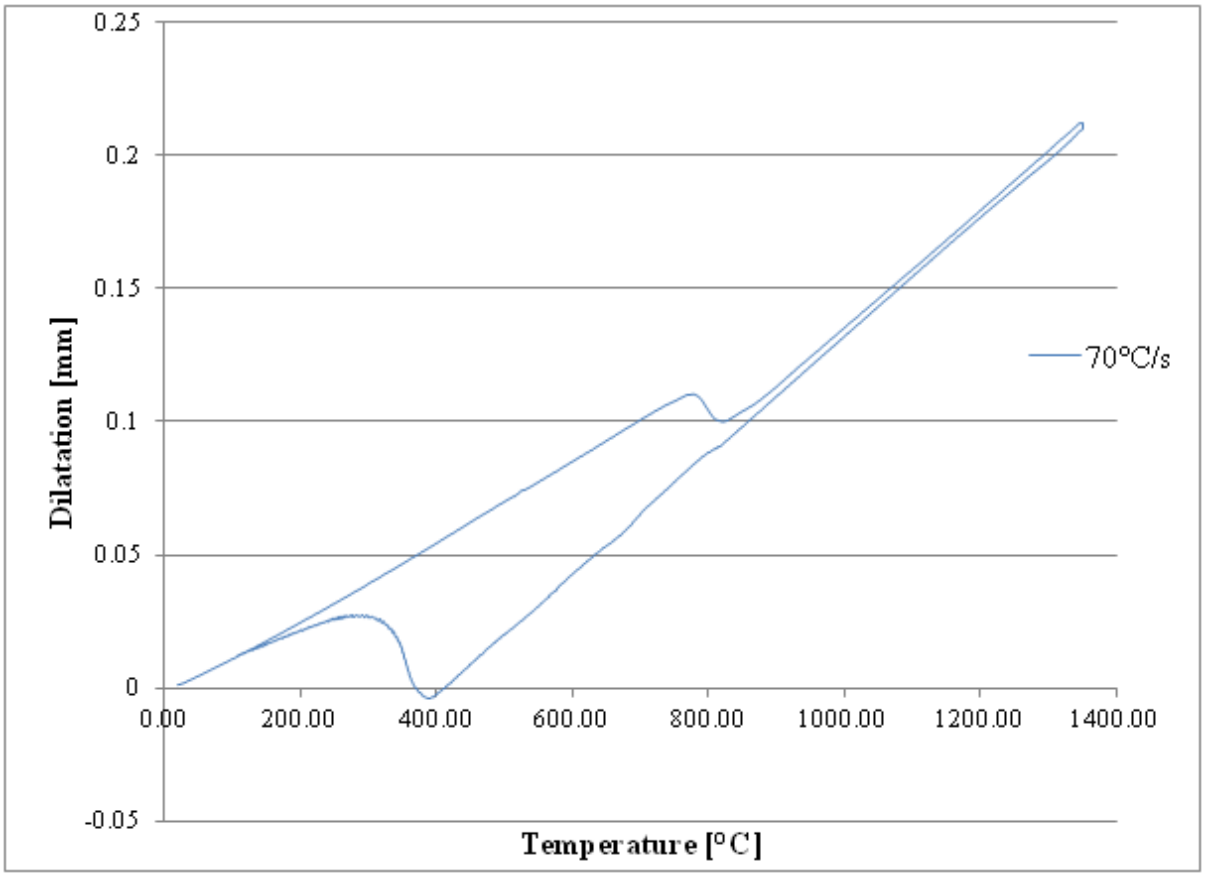
0.25
0.2
0.15
0.1
0.05
0
-0.05
Dilatation [mm]
0.00
200.00
400.00
600.00
800.00
1000.00
1200.00
1400.00
Temperature [°C]
70°C/s

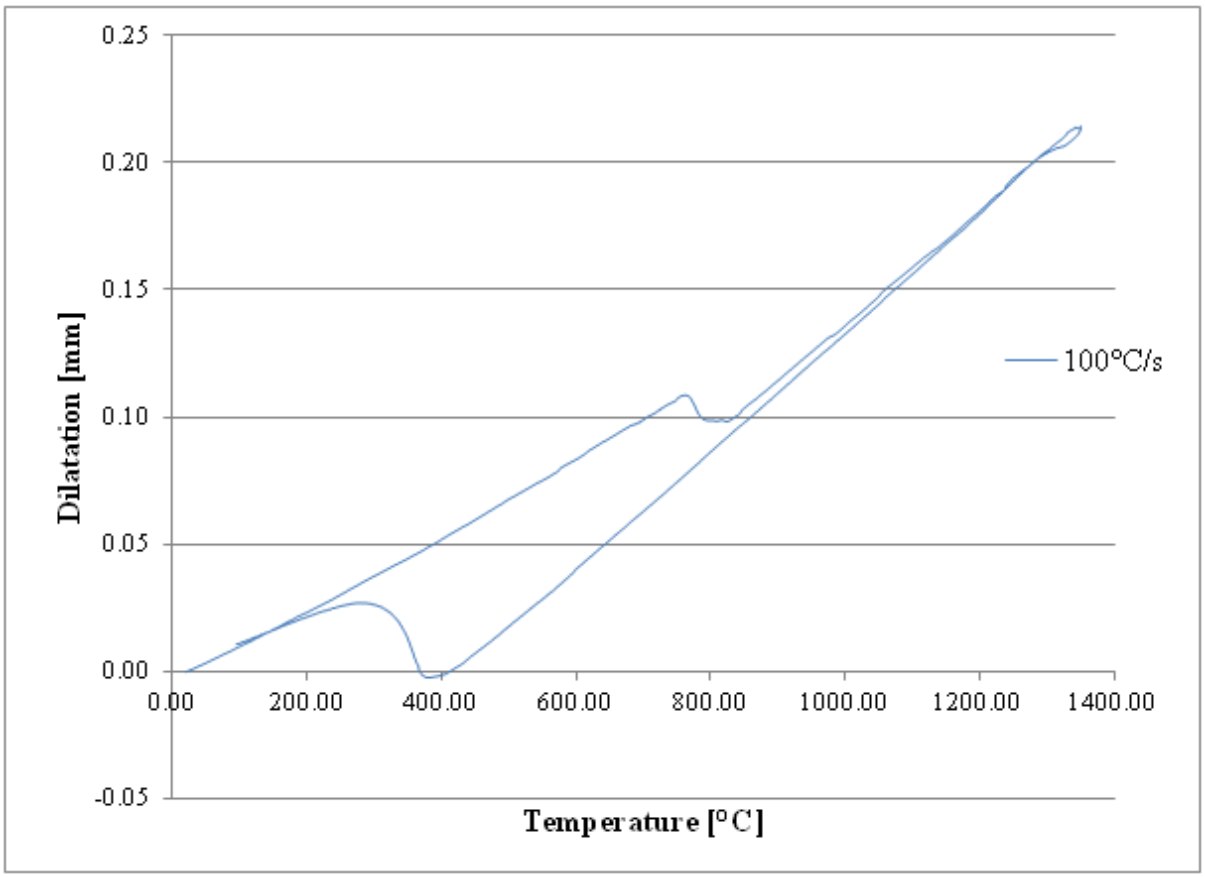
0.25
0.20
0.15
0.10
0.05
0.00
-0.05
Dilatation [mm]
0.00
200.00
400.00
600.00
800.00
1000.00
1200.00
1400.00
Temperature [°C]
100°C/s

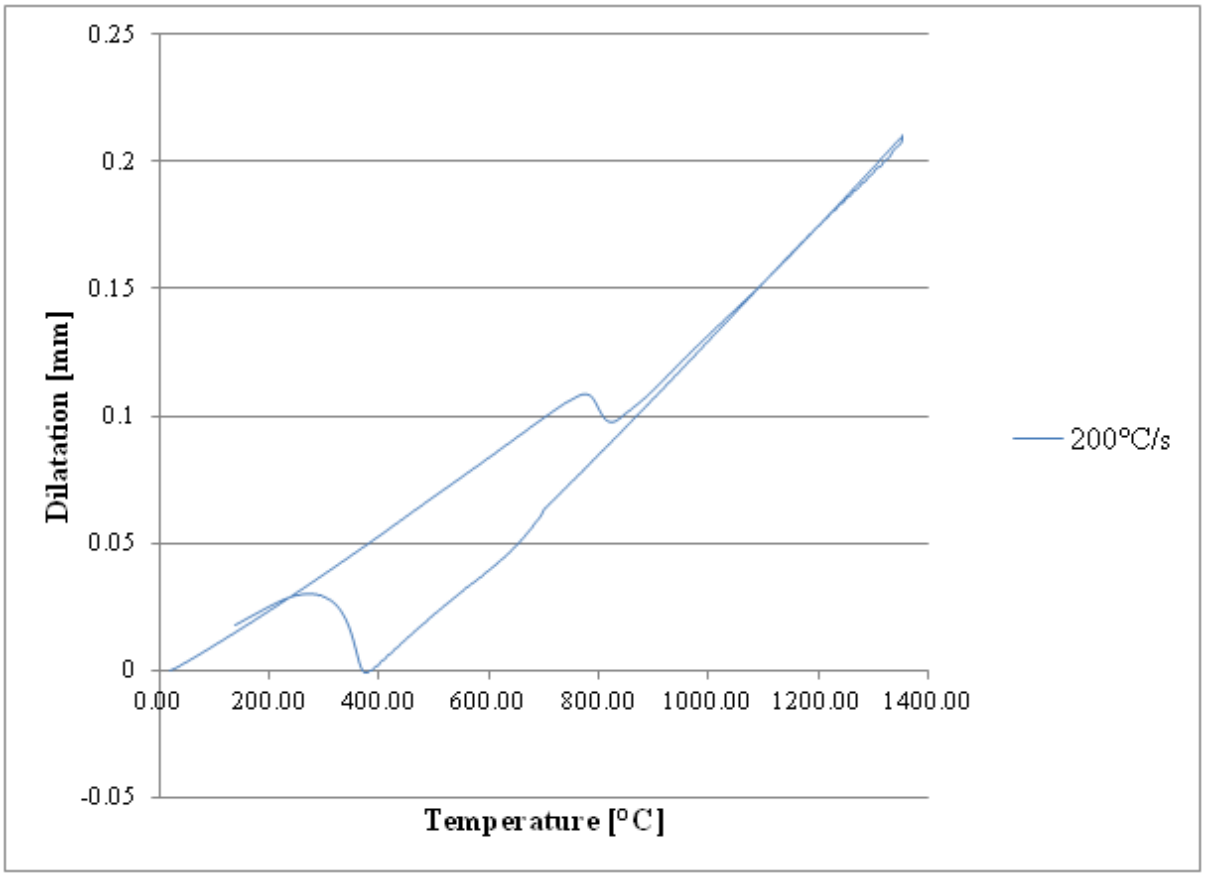
0.25
0.2
0.15
0.1
0.05
0
-0.05
Dilatation [mm]
0.00
200.00
400.00
600.00
800.00
1000.00
1200.00
1400.00
Temperature [°C]
200°C/s

APPENDIX 4

Complete results of hydrogen testing trials.

Diffusible hydrogen was determined using the "collection of hydrogen over mercury" method. Residual hydrogen was determined using "inert gas melt extraction" method. Residual hydrogen value in ppm acquired from the testing equipment was converted to ml/100g of WM using the calculations described in section 2.6.3. The same sample identification as described in Figure 3-44 was used.

Table below shows hydrogen testing results acquired in order to determine: The level of diffusible hydrogen in weld HAZ welded with ferritic and ASS consumable.

Sample ID	Diffusible H content [ml/100g of WM]	Residual H content [ppm]	Residual H content * [ml/100g of WM]
Initial hydrogen testing trials of the 3 samples (A,B,C)			
FC-ASS-APH-DQ-A	1.1	5.8	6.92
FC-ASS-APH-DQ-B	1.3	5.03	6
FC-ASS-APH-DQ-C	1.4	4.56	5.44
ASS-DQ_INITIAL_TRIAL_average	1.3	5.13	6.12
Initial hydrogen testing under the same conditions was repeated to assure acquired data were consistent. Diffusible hydrogen content is expressed as only one value per sample. After completion of diffusible hydrogen testing each sample was sectioned and three separate samples of WM were subjected to residual hydrogen testing. Therefore three residual hydrogen values are stated per one sample.			
FC-ASS-APH-DQ-D1		4.75	5.67
FC-ASS-APH-DQ-D2		5.22	6.23
FC-ASS-APH-DQ-D3		5.2	6.21
D average	1.3	5.06	6.04
FC-ASS-APH-DQ-E1		NT	
FC-ASS-APH-DQ-E2		NT	
FC-ASS-APH-DQ-E3		4.77	5.69
E average	1.3	4.77	5.69
FC-ASS-APH-DQ-F1		4.68	5.58
FC-ASS-APH-DQ-F2		4.77	5.69
FC-ASS-APH-DQ-F3		4.77	5.69
F average	1.2	4.74	5.65
FC-ASS-APH-DQ_average	1.3	4.86	5.79
FC-FER-APH-DQ-G1		0.52	0.62
FC-FER-APH-DQ-G2		0.74	0.88

FC-FER-APH-DQ-G3		0.76	0.91
G average	24.21	0.67	0.80
FC-FER-APH-DQ-H1		0.64	0.76
FC-FER-APH-DQ-H2		0.78	0.93
FC-FER-APH-DQ-H3		0.64	0.76
H average	21.45	0.69	0.82
FC-FER-APH-DQ-I1		0.94	1.12
FC-FER-APH-DQ-I2		0.9	1.07
FC-FER-APH-DQ-I3		0.78	0.94
I average	24.42	0.87	1.04
FC-FER-APH-DQ_average	23.36	0.74	0.89
S-ASS(PM&WM)-APH-DQ-V1		NT**	
S-ASS(PM&WM)-APH-DQ-V2		NT	
S-ASS(PM&WM)-APH-DQ-V3		NT	
V average	0	-	-
S-ASS(PM&WM)-APH-DQ-X1		6.7	8
S-ASS(PM&WM)-APH-DQ-X2		6.7	8
S-ASS(PM&WM)-APH-DQ-X3		NT	
X average	0	6.7	8
S-ASS(PM&WM)-APH-DQ-Y1		NT	
S-ASS(PM&WM)-APH-DQ-Y2		NT	
S-ASS(PM&WM)-APH-DQ-Y3		NT	
Y average	0	-	-
S-ASS(PM&WM)-APH-DQ_average	0	6.7	8

*Calculated for normal conditions - 20°C, 101kPa.
**Not tested.

Table below shows hydrogen testing results acquired in order to determine: The level of diffusible hydrogen in weld HAZ of the samples welded with flux-cored ASS consumable under different PH conditions.

Sample ID	Diffusible H content [ml/100g of WM]	Residual H content [ppm]	Residual H content * [ml/100g of WM]
FC-ASS-7PH-150Q-Z1		5.8	6.9
FC-ASS-7PH-150Q-Z2		5.8	6.9
FC-ASS-7PH-150Q-Z3		6.2	7.4
Z average	1.29	5.9	7.1
FC-ASS-6PH-150Q-AA1		5.3	6.3
FC-ASS-6PH-150Q-AA2		5.5	6.6
FC-ASS-6PH-150Q-AA3		5	6

AA average	0.998	5.3	6.3
FC-ASS-6PH-150Q-BB1		4	4.8
FC-ASS-6PH-150Q-BB2		4.5	5.4
FC-ASS-6PH-150Q-BB3		3.8	4.5
BB average	1.61	4.1	4.9
ASS-7PH-150Q_average	1.299	5.1	6.1
FC-ASS-APH-150Q-J1		6.7	8
FC-ASS-APH-150Q-J2		NT	
FC-ASS-APH-150Q-J3		6.2	7.4
J average	0.96	6.45	7.7
FC-ASS-APH-150Q-K1		6.6	7.88
FC-ASS-APH-150Q-K2		6.9	8.23
FC-ASS-APH-150Q-K3		6.5	7.76
K average	0.78	6.67	7.96
FC-ASS-APH-150Q-L1		6.9	8.23
FC-ASS-APH-150Q-L2		6.6	7.88
FC-ASS-APH-150Q-L3		6.8	8.11
L average	0.81	6.77	8.07
ASS-APH-150Q_average	0.85	6.63	7.91
FC-ASS-80PH-150Q-M1		6.9	8.23
FC-ASS-80PH-150Q-M2		6.1	7.28
FC-ASS-80PH-150Q-M3		NT	
M average	0.64	6.5	7.76
FC-ASS-80PH-150Q-N1		6.6	7.88
FC-ASS-80PH-150Q-N2		7.6	9.07
FC-ASS-80PH-150Q-N3		7.4	8.83
N average	0.498	7.2	8.59
FC-ASS-80PH-150Q-O1		6.5	7.76
FC-ASS-80PH-150Q-O2		6.5	7.76
FC-ASS-80PH-150Q-O3		6	7.2
O average	0.5	6.3	7.57
ASS-80PH-150Q_average	0.55	6.7	7.97

*Calculated for normal conditions - 20°C, 101kPa.
**Not tested.

Table below shows hydrogen testing results acquired in order to determine: The level of diffusible hydrogen in weld HAZ welded with 3 different types of ASS consumable, namely flux-cored, metal-cored and solid.

Sample ID	Diffusible H content [ml/100g of WM]	Residual H content [ppm]	Residual H content * [ml/100g of WM]
MC-ASS-APH-150Q-P1		4.6	5.489
MC-ASS -APH-150Q-P2		4.6	5.489
MC-ASS -APH-150Q-P3		4.9	5.85
P average	0.51	4.7	5.61
MC-ASS -APH-150Q-Q1		3.5	4.18
MC-ASS -APH-150Q-Q2		3.4	4.06
MC-ASS -APH-150Q-Q3		3.6	4.296
Q average	0.498	3.5	4.18
MC-ASS -APH-150Q-R1		3.3	3.94
MC-ASS -APH-150Q-R2		3.6	4.296
MC-ASS -APH-150Q-R3		3.5	4.18
R average	0.36	3.47	4.14
ASS(MC)-APH-150Q_average	0.46	3.89	4.64
S-ASS-APH-150Q-S1		2.9	3.46
S-ASS -APH-150Q-S2		13.6***	
S-ASS -APH-150Q-S3		2.8	3.34
S average	0	2.85	3.4
S-ASS -APH-150Q-T1		2.9	3.46
S-ASS -APH-150Q-T2		3.1	3.699
S-ASS -APH-150Q-T3		3.3	3.94
T average	0	3.1	3.70
S-ASS -APH-150Q-U1		3.3	3.94
S-ASS -APH-150Q-U2		3.3	3.94
S-ASS -APH-150Q-U3		3.4	4.06
U average	0	3.33	3.98
ASS(S)-APH-150Q_average	0	3.09	3.69

*Calculated for normal conditions - 20°C, 101kPa.

***Not included for calculation due to extremely different value compared to the other two samples of WM sectioned out of the same coupon.

APPENDIX 5

Macrographs of cross sections of the representative samples from each trial:

a - FC_ASS_APH_DQ; b - FC_FER_APH_DQ; c - FC_ASS(PM+WM)_APH_DQ; d - FC_ASS_APH_150°CQ; e - FC_ASS_80°CPH_150°CQ; f - FC_ASS_7°CPH_150°CQ; g - MC_ASS_APH_150°CQ, h - S_ASS_APH_150°CQ. Note: the scale is in millimetres.

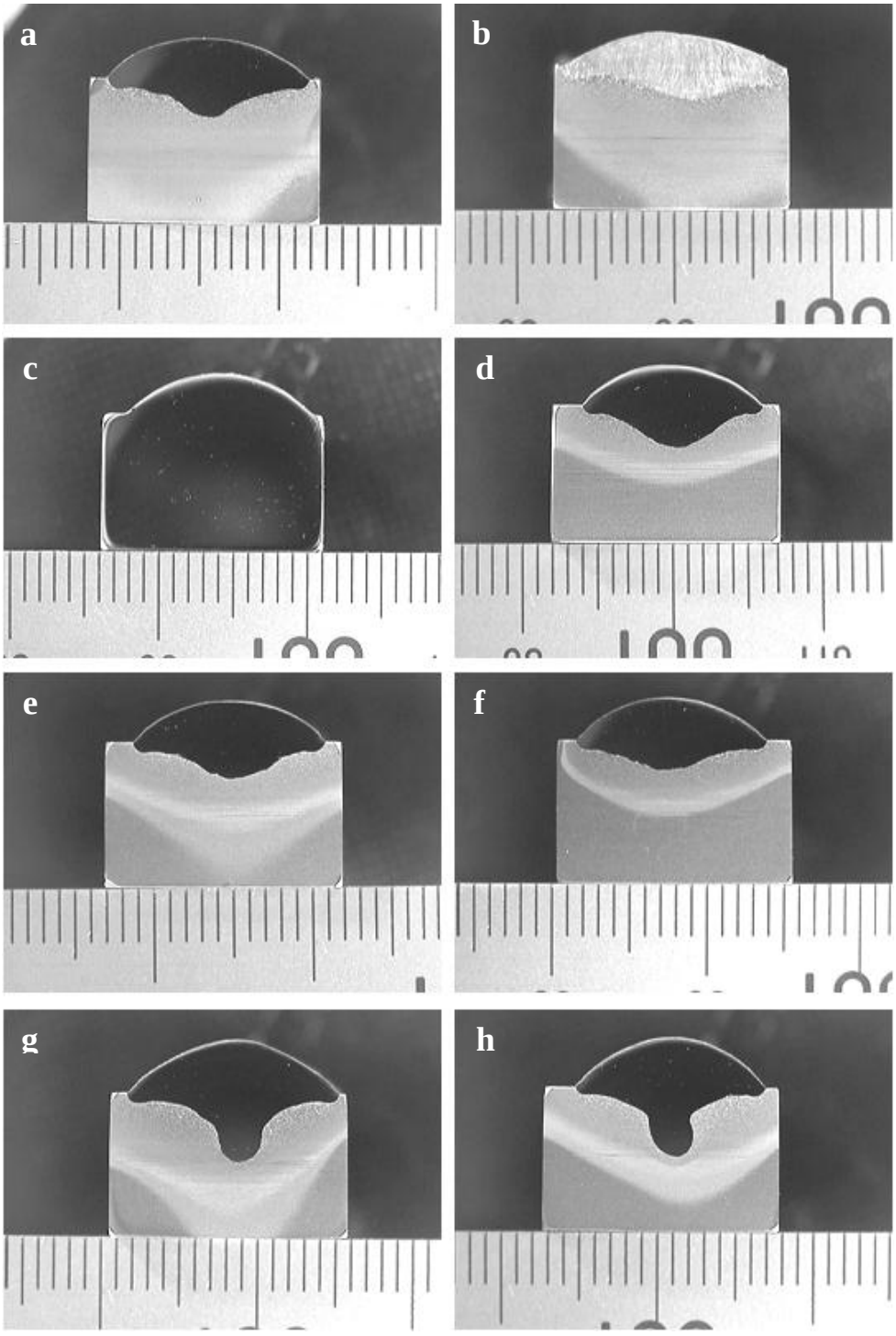

APPENDIX 6

Geometry profiles of the remaining weldments acquired using laser profile sensor.

Graphs show equations of the trednlines used to calculate the angles between the HHA plates: a – 80°C preheat (Trial 2) tacked plates, b – 80°C preheat (Trial 2) after deposition of the inner pass;

c – 21°C (ambient) preheat (Trial 2), tacked plates, d – 21°C (ambient) preheat (Trial 2), after deposition of the inner pass; e – 21°C (ambient) preheat (Trial 3), tacked plates, f – 21°C (ambient) preheat (Trial 3), after deposition of the inner pass.

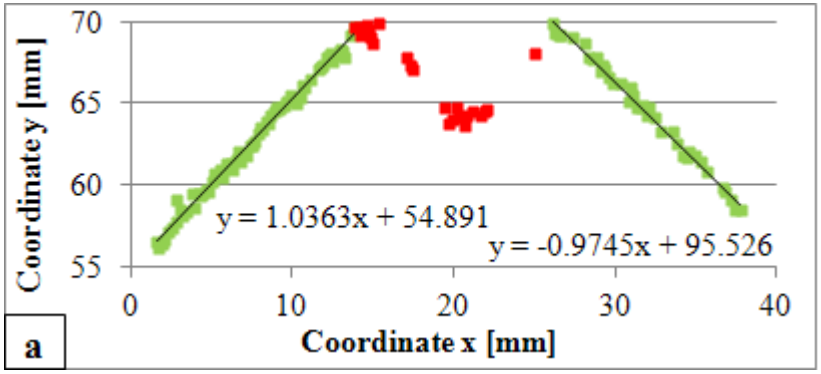

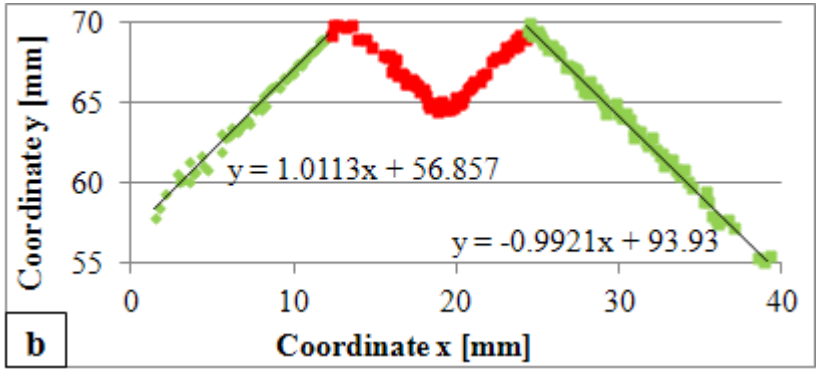

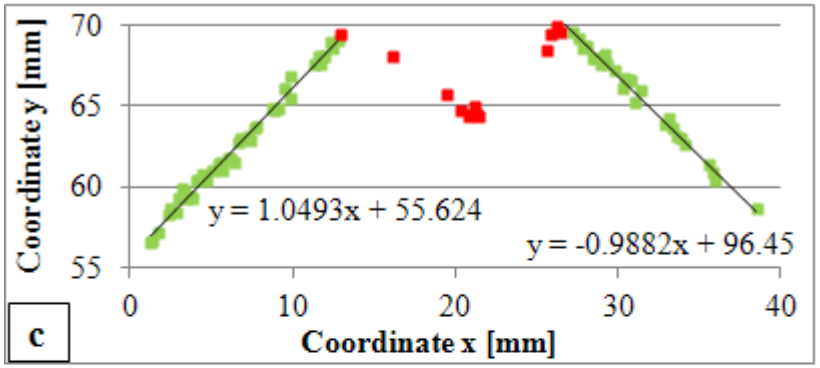
Coordinate y [mm]
70
65
60
55
0
10
20
30
40
Coordinate x [mm]
y = 1.0493x + 55.624
y = -0.9882x + 96.45
c

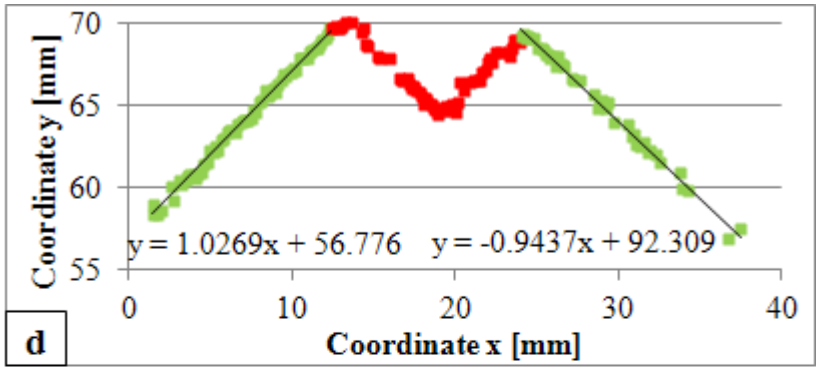
Coordinate y [mm]
70
65
60
55
0
10
20
30
40
Coordinate x [mm]
y = 1.0269x + 56.776
y = -0.9437x + 92.309
d

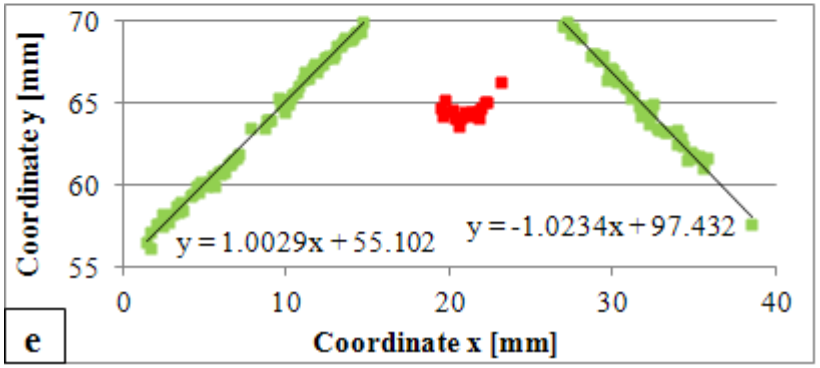
Coordinate y [mm]
70
65
60
55
0
10
20
30
40
Coordinate x [mm]
y = 1.0029x + 55.102
y = -1.0234x + 97.432
e

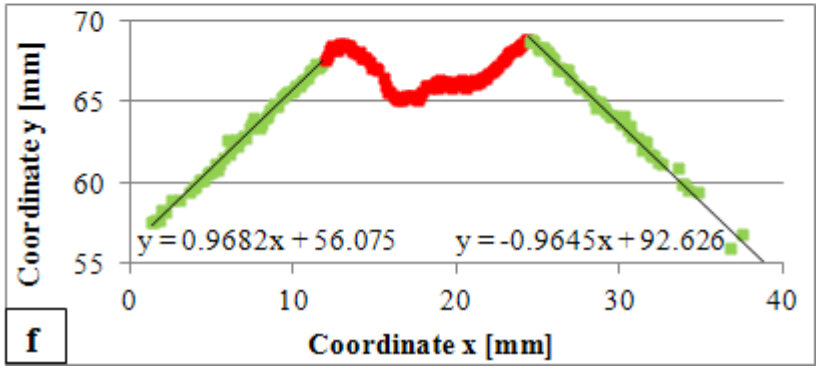
Coordinate y [mm]
70
65
60
55
0
10
20
30
40
Coordinate x [mm]
y = 0.9682x + 56.075
y = -0.9645x + 92.626
f

APPENDIX 7 – PUBLICATIONS

A STUDY OF THE CONTINUOUS COOLING BEHAVIOUR AND EFFECT OF PREHEAT AND INTERPASS TEMPERATURE ON THE HAZ OF HIGH STRENGTH QUENCHED AND TEMPERED STEEL

Authors: Lenka Kuzmikova, Mark Callaghan, Nathan Larkin, Robert Scott, Robert De Jong, Huijun Li, and John Norrish

This paper has been presented at 63rd Annual Assembly & International Conference of the International Institute of Welding, Doc IX-2352-10, 2010, Istanbul, Turkey.

ABSTRACT

In this study, the continuous cooling phase transformation behaviour of a quenched and tempered armour steel was investigated. A continuous cooling transformation diagram was constructed providing valuable information for predicting microstructural evolution and mechanical properties at different cooling rates during actual welding fabrication. Welding trials were carried out utilising a flux-cored arc welding technique in combination with an austenitic stainless steel consumable. The effect of various preheat and interpass temperatures on cooling rate and consequently on the heat affected zone microstructure and mechanical properties of multipass welds were investigated.

IIW-Thesaurus keywords: Continuous cooling transformation diagram; Hydrogen induced cold cracking; Quenched and tempered plate; High strength steel; Welding; Preheat temperature; Interpass temperature.

1 INTRODUCTION

Welding is the main fabrication technique for joining high strength quenched and tempered (Q&T) armour steel plates for land-based vehicles. The chemistry and heat treatment of armour steels are designed to deliver optimum ballistic protection against specified threats, thus any microstructural changes during fabrication are undesirable. However, when steel is subjected to welding, the area surrounding the weld pool, known as the heat affected zone (HAZ), undergoes complex thermal cycles which cause microstructural changes in the material. The extent and character of these changes depend on thermal cycles experienced and may lead to such undesired effects such as HAZ softening (or hardening) and hydrogen induced cold cracking (HICC). These phenomena are detrimental to the ballistic performance of armour steels, as well as introducing fabrication issues that affect the overall structural integrity of the vehicle.

The degree in which the HAZ softens depends on chemical composition, thermal cycle and kinetics of the phase transformation [1]. Whether HICC will occur relies on three aspects occurring in concert, these being formation of a susceptible microstructure; type (tensile) and magnitude of residual stresses, and level of diffusible hydrogen entering the weld pool [2]. Cracks typically form in the coarse-grained (CG) sub-zone of the HAZ, which have been exposed to temperatures between 1100°C to 1450°C [3]. It has been shown that the risk of CGHAZ cracking is linearly related to the $\gamma \rightarrow \alpha$ transformation temperature, as well as to the

martensite finish (M_f) temperature during transformation, both of which may be predicted from experimental cooling curves [4].

Novel improved alloy design, as well as continuous industry demands for improving welded joint quality, increasing production outputs and lowering costs during fabrication, have indicated the necessity for research in the area of weldability of Q&T armour steels. Multi-pass gas metal arc welding (GMAW) is one process used in fabricating these materials. Two areas of optimisation during welding are plate preheating temperature and interpass temperature. The armour plate is preheated prior to welding to eliminate the risk of HICC in weldments, by removing moisture from the plate surface, decreasing cooling rate after welding (allowing longer time for hydrogen to diffuse out of the weldment, especially considerable in the case of ferritic consumables), and reducing residual stresses imposed on the weldment as a result of thermal shrinkage on cooling as well as creating a far less susceptible microstructure. Conversely, preheating represents an additional step in the welding process, significantly reducing productivity and increasing fabrication costs.

Further, in order to minimise the risk of HICC, the minimum interpass temperature is usually identical to the minimum preheat temperature. From a productivity view point, it is beneficial to permit the highest interpass temperature possible, whilst producing a weldment with optimised materials properties. Moreover, it is essential to determine the upper interpass temperature threshold for a given heat input, which prevents formation of excessively wide softened areas of HAZ, with loss of both strength and hardness [5].

Hence, it is important to understand and quantify the effect of welding thermal cycles, as well as optimise welding parameters, to produce weldments of the desired microstructure and mechanical properties for armour steels. In this paper, a continuous cooling transformation (CCT) diagram was constructed for an armour steel, providing extremely valuable information for predicting microstructural evolution and mechanical properties at numerous cooling rates during actual welding fabrication. The effect of a number of preheating and interpass temperatures on cooling rate, HAZ microstructure evolution and consequently mechanical properties of multi-pass welds was analysed.

2 EXPERIMENTAL PROCEDURES

2.1 Materials

The steel grade investigated in this work complies with Australian specification DEF AUST 8030 [6] and belongs to a family of Q&T steels for armour applications. The chemical composition (max) of the investigated armour steel is listed in Table 1. The microstructure of the plate in the green feed as well as Q&T condition is shown in Figure 1. The microstructure of the plate in Q&T condition consists of tempered martensite with an average hardness of 542 HV20.

Table 1. Chemical composition of steel in wt % max.

Element	C	P	Mn	Si	S	Ni	Cr	Mo
Wt% max	0.32	0.02	0.4	0.35	0.005	0.35	1.15	0.3

Element	Cu	Al	Nb	Ti	V	B	CE_{IIW}
Wt% max	0.2	0.06	0.005	0.03	0.05	0.002	0.72

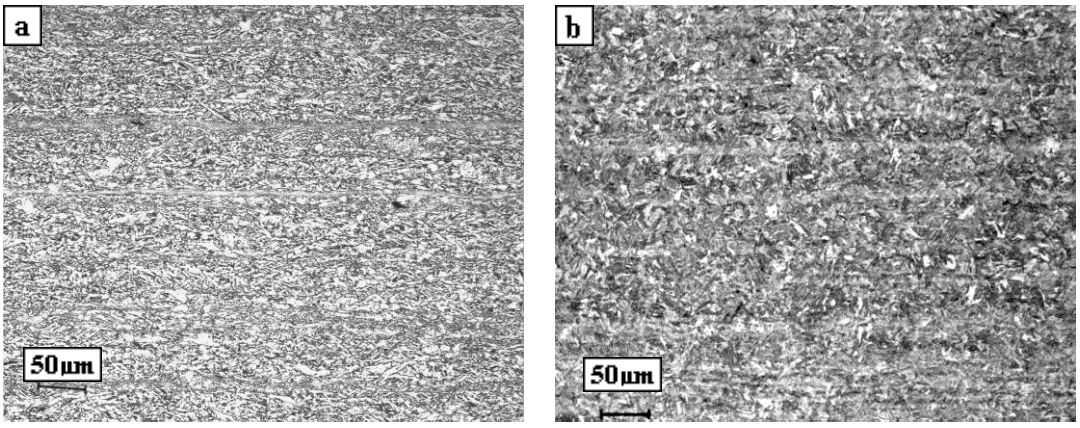

Figure 1. Microstructure of investigated steel: a – in green feed (as-rolled) condition, b – in Q&T condition.

The alloying design of this steel utilises the novel low manganese approach [7] in order to reduce centreline segregation of MnS inclusions and thus improve mechanical properties and weldability. The steel is microalloyed with Nb, Ti, V, and B in order to increase hardenability and enhance the HAZ properties.

2.2 Dilatometry experiments

Samples for dilatometry tests were machined from hot rolled plate in the green feed condition. Samples were 10 mm long hollow cylinders with a 5 mm diameter and 0.75 mm wall thickness. Experiments were carried out in the vacuum chamber of a Theta II thermo-mechanical simulator. An S-type thermocouple was spot-welded in the middle of the sample to the outer surface to ensure good temperature control. High vacuum was generated in the dilatometer chamber in order to protect the surface of the samples from oxidation. After a stable vacuum was achieved, samples were heated at rate of 50°C/s to the austenitisation temperature of 1350ºC (to simulate CGHAZ subzone), held for 5 seconds and then cooled to 100ºC using 9 different cooling rates, namely 1°C/s, 5°C/s, 10°C/s, 20°C/s, 30°C/s, 50°C/s, 70°C/s, 100°C/s, and 200ºC/s. Samples were then mounted in epoxy resin and prepared according to standard procedures for Vickers microhardness measurements and metallographic examination using optical microscopy.

2.3 Preheat temperature experiments

Samples were welded employing robot-controlled flux-cored arc welding (FCAW) technique in combination with austenitic stainless steel (ASS) consumable. The welding trials utilised a multipass corner joint configuration which consisted of two steel plates of dimensions 400 mm x 100 mm x plate thickness, welded in a horizontal/vertical position. Test plates were preheated to three different temperatures - ambient (24°C), 80°C and 200°C - using an electric resistance heating blanket. After deposition of the first fillet pass, samples were

allowed to cool down to room temperature. Before deposition of the remaining cap passes, plates were again preheated to the aforementioned preheat temperatures. Interpass temperature was kept constant (120°C) for all three trials. To achieve precise temperature control during preheating and to acquire weld thermal profiles, two K-type thermocouples were spot-welded to the middle of the plate surface, approximately 10 mm from the edge. After completion of the final pass, samples were sectioned, mounted in epoxy resin and prepared according to standard procedures for Vickers microhardness measurements and metallographic examination. The orientation of hardness testing traverses is shown in Figure 2.

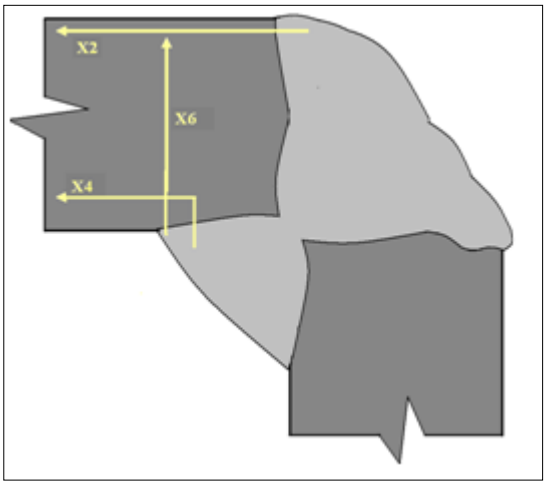

Figure 2. Orientation of hardness testing traverses.

2.4 Interpass temperature experiments

For these experiments, the plates were prepared in the same manner as described in section 2.3. However, for these trials, the interpass temperature was varied and the preheat was kept constant (ambient 24°C). Three different interpass temperatures - 120°C, 160°C and 200°C - were used in this investigation.

3 RESULTS AND DISCUSSION

3.1 Dilatometry

3.1.1 CCT diagram

Figure 3 shows CCT diagram of the investigated material constructed from dilatation curves acquired during dilatometry experiments. From this diagram, it can be seen that transformation start and finish temperatures decrease noticeably with increasing cooling rate, up to 30°C/s then plateau out. The transformation occurs approximately in the 200°C range with all cooling rates.

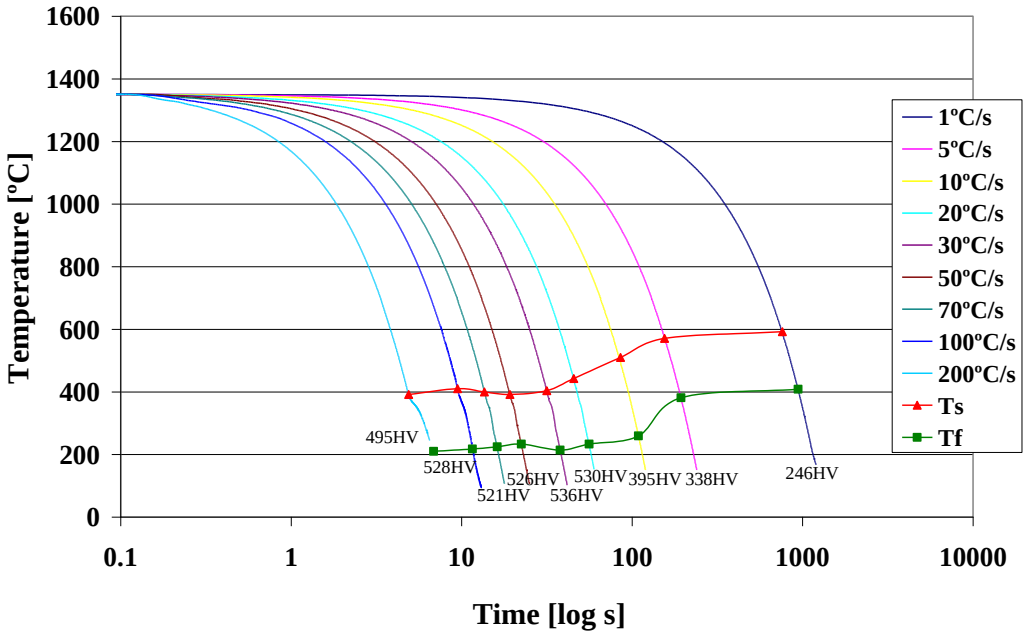

Figure 3. CCT diagram of the investigated steel. Ts – transformation start temperature, Tf – transformation finish temperature. Hardness measurements for each cooling rate are also shown.

3.1.2 Hardness

In Figure 4, the relationship between hardness and cooling rate is shown. Hardness rapidly increases with increasing cooling rate to 30°C/s. This is due to the high amount of martensite formation occurring in the microstructure of the steel as a consequence of increased cooling rate. It was found that further increasing the cooling rate resulted in a hardness plateau. The carbon equivalent of the steel is relatively high (CE_{IIW} average 0.6), thus as expected achieved hardness values are high even when slow cooling rates are employed. This confirms that the steel has good hardenability over a wide range of cooling rates. At cooling rates representative of real weld conditions (20°C/s to 30°C/s), correlations with hardness measurements showed that peak hardenability was reached. Correspondence between transformation temperature and hardness was also observed. Transformation temperature was found to decrease, while hardness increased with increasing cooling rate from 1°C/s to 30°C/s.

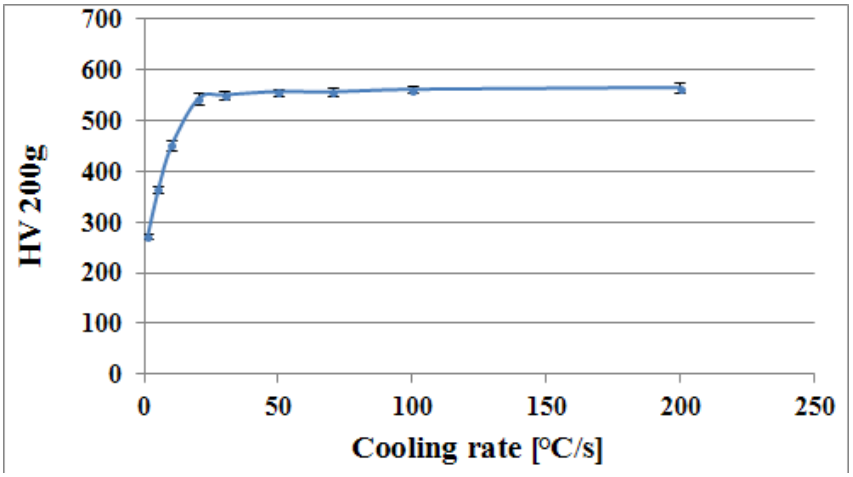

Figure 4. Average measured microhardness of dilatometry samples with respect to cooling rates.

3.1.3 Microstructural characterisation

Figure 5 displays the microstructural evolution of dilatometry samples formed at cooling rates of 5°C/s, 30°C/s and 100°C/s. Ferritic laths of upper bainite can be observed in the microstructure, formed during 5°C/s cooling, formation of which is strongly suppressed in favour of a lower bainite-martensite mixture with increasing cooling rate. It is evident that increasing the cooling rate favours formation of harder structures and a fully martensitic structure was obtained at higher cooling rates as seen in Figures 5c. Large grains similar to those found in the coarse-grained heat affected zone (CGHAZ) in real welding conditions are observed in the microstructure formed under all cooling rates, as a result of the high austenitising temperature (1350°C).

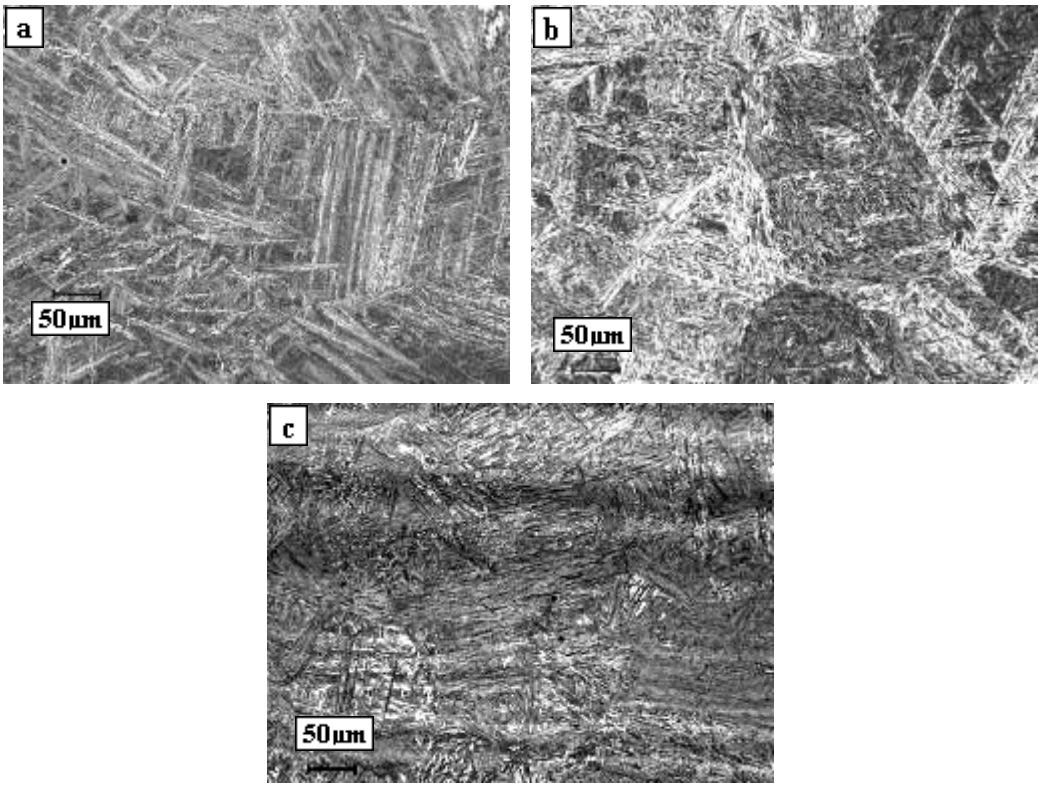

Figure 5. Microstructures of dilatometry samples subjected to slow, medium and fast cooling rate: a – 5°C/s; b – 30°C/s; c – 100°C/s.

3.2 Effect of preheat temperature

3.2.1 Weld thermal profiles

Cooling time from the peak temperature to 100°C was measured for all preheat temperatures and is presented in Table 2 and representative weld thermal profiles are shown in Figure 6. As expected, cooling rate decreased with increasing preheat temperature. It was found that the cooling time for the ambient preheated plate was half the time taken for cooling at a preheat of 80°C and one third the time taken for cooling at a preheat of 200°C. Employing lower temperatures of preheat results in significant time and cost savings in welding practice. Furthermore, possible removal of preheat would remove the whole technological step from industry practice, resulting in highly optimised manufacturing process. However, further in-depth research on the amount of diffusible hydrogen present in weldments should be carried out in order to confirm the safety of the proposed preheat exclusion.

Table 2. Cooling time of the first passes from the peak temperature to 100°C for plates preheated to Ambient (24°C), 80°C and 200°C. t_p – time when the peak temperature was reached; $t_{100°C}$ – time when the 100°C was reached.

Preheat temperature [°C]	Ambient (24)	80	200
Cooling time (t_p to $t_{100°C}$) [sec]	303	597	917

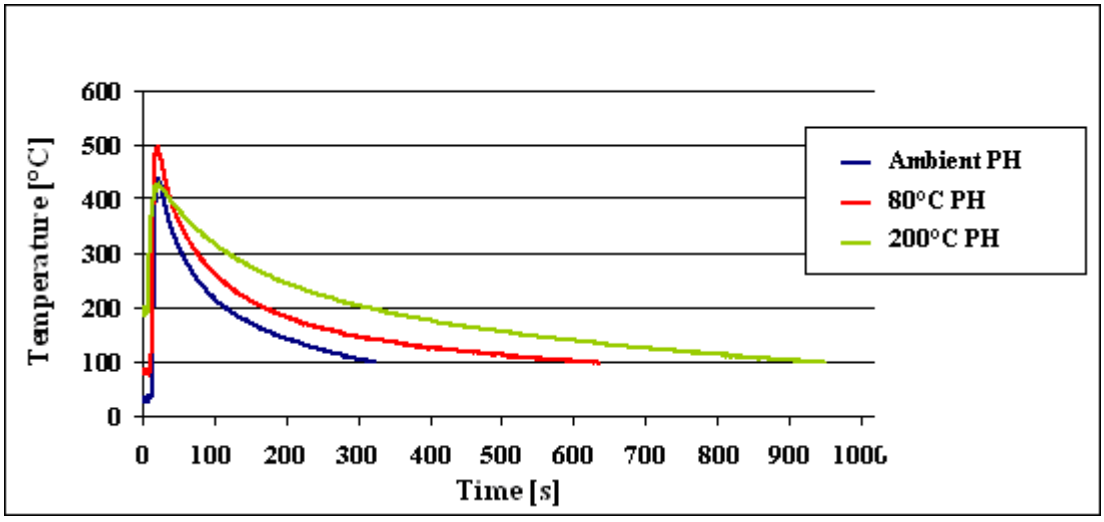

Figure 6. Thermal profiles of the 1st weld passes, indicating the decrease in cooling rate with increasing preheat temperature.

3.2.1 Hardness

Figure 7 represents the weld hardness profiles. From graphs in Figures 7b and c, an increase in HAZ hardness and a decrease in HAZ width are observed as the preheat temperature is lowered. This is due to the formation of harder microstuctures as a result of reduced cooling times. Low hydrogen welding processes is employed in order to ensure that the hydrogen present is at a level lower than the critical level (in terms of HICC formation).

In addition, the austenitic weld metal's bcc lattice can accommodate a higher level of hydrogen without risk of cracking. Further, the weld metal does not undergo $\gamma \rightarrow \alpha$ transformation, thus restricts evolution of hydrogen into the more critical HAZ. It is well known that austenitic consumables lessen this phenomenon, in comparison with ferritic consumables.

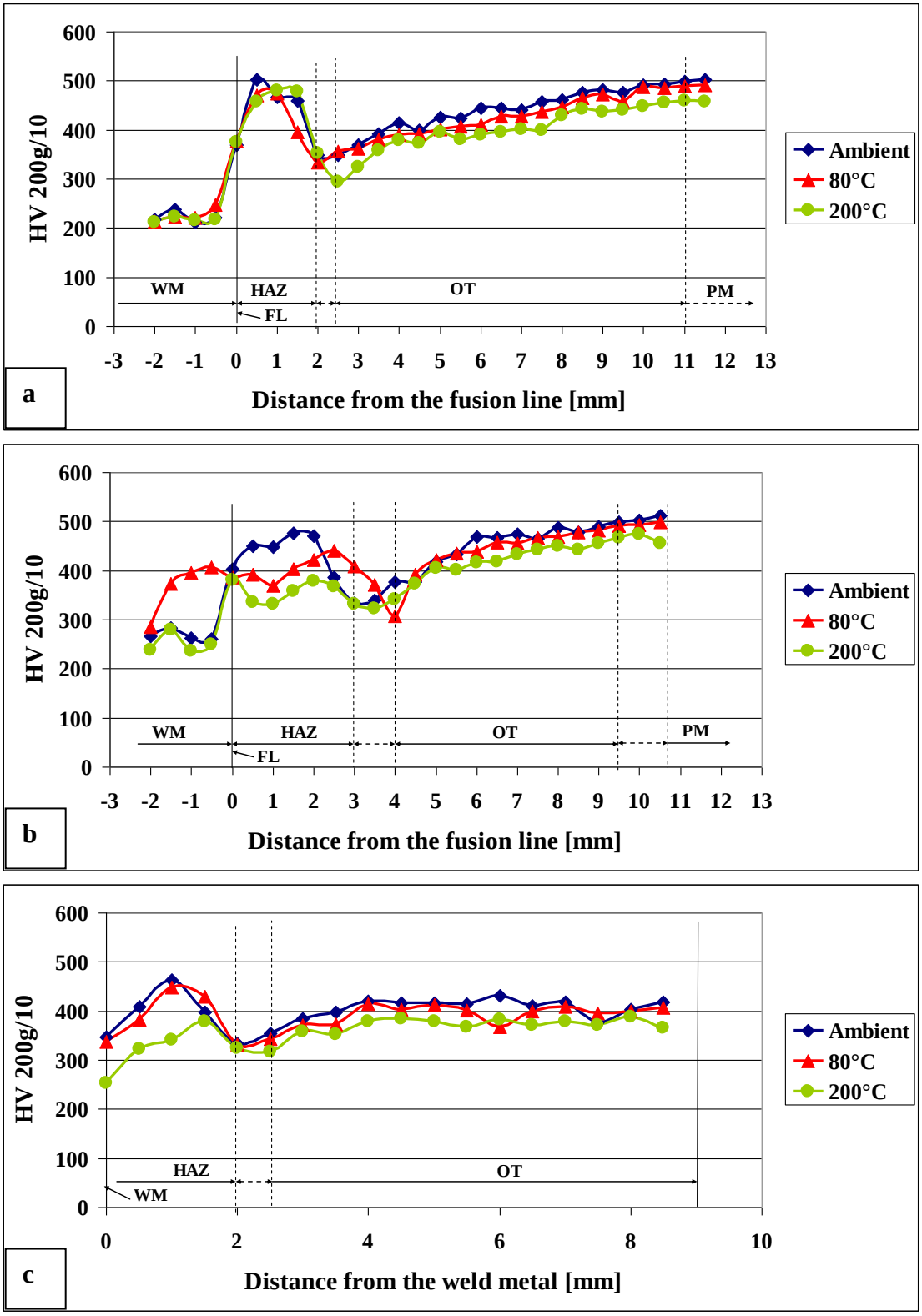

Figure 7. Weld hardness profiles employing ambient (24°C), 80°C and 200°C preheats, measured in: a – X2 orientation, b – X4 orientation, c – X6 orientation. Orientations are defined in Figure 2.

A slight enlargement of the overall HAZ area with increasing preheat temperature is shown in Table 3. HAZ hardness measured in the X2 orientation is almost identical for all three samples. This is a consequence of maintaining constant interpass temperature, resulting in similar cooling rates and thus the microstructure and hardness were similar. The over-tempered (OT) region hardness profiles followed the same trend in all three orientations. Hardness slightly decreases with increasing preheat temperature.

Table 3. Increase in HAZ area with increasing preheat temperature**.**

Preheat temperature [°C]	**HAZ area [mm^2]**
Ambient (24)	54.6
80	55
200	57.8

3.3 Effect of interpass temperature

3.3.1 Weld thermal profiles

The cooling time data presented in Table 4 and the thermal profiles shown in Figure 8, show that increasing interpass temperature reduces the welding time (from beginning the welding process until the peak temperature of the final pass is reached). Overall cooling time (from the beginning of the welding process until 100°C is reached after completion of welding) is reduced with the increase of interpass temperature from 120°C to 160°C, but a further increase to 200°C results in a slightly longer cooling time. This is a consequence of the significantly longer cooling time after deposition of final weld pass. A comparison of the cooling times indicates that a 160°C interpass temperature is the most beneficial from a productivity view point.

Table 4. Cooling times recorded employing 120°, 160°C and 200°C interpass temperatures. t_0 – time at start of the welding; t_p – time when the peak temperature was reached; $t_{100°C}$ – time when the 100°C was reached.

Interpass temperature [°C]	120	160	200
Cooling time (t_0 to t_p final pass) [s]	1580	870	720
Cooling time (t_0 to $t_{100°C}$) [s]	2410	1770	1880

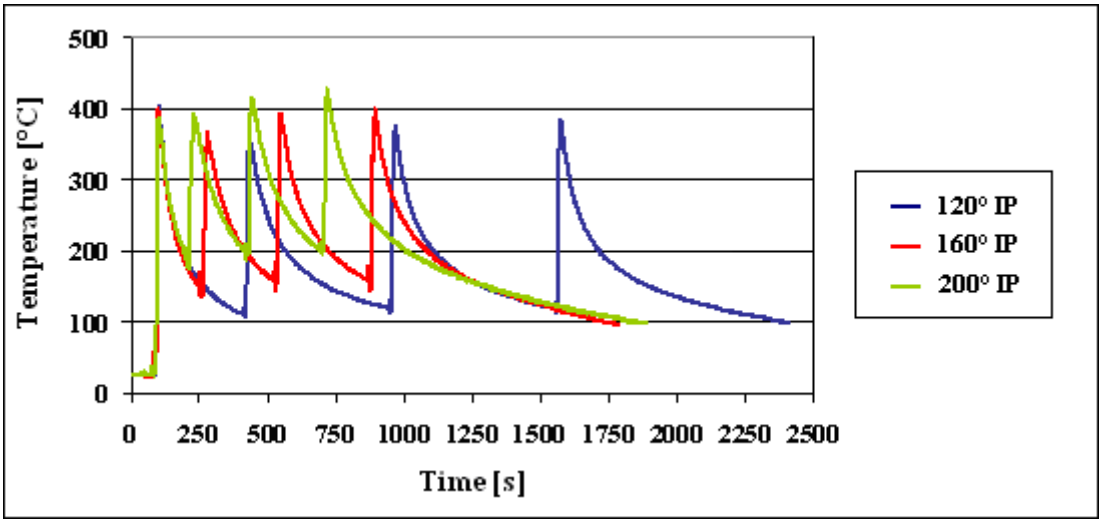

Figure 8. Thermal profiles of the cap passes employing 120°C, 160°C and 200°C interpass temperatures. IP – interpass temperature.

3.3.2 Hardness

Figure 9 presents weld hardness profiles of the samples at ambient (24°C) preheat in combination with 120°C, 160°C and 200°C interpass temperatures. From the graphs, it can be seen that the hardness of both the HAZ and OT regions measured in all orientations are almost identical for all interpass temperatures. This indicates that increasing interpass temperature from 120°C to 200°C does not have a significant effect on the resultant microstructure and hence the hardness of the HAZ. Furthermore, the HAZ width has not increased significantly, thus neither ballistic protection nor structural integrity is compromised.

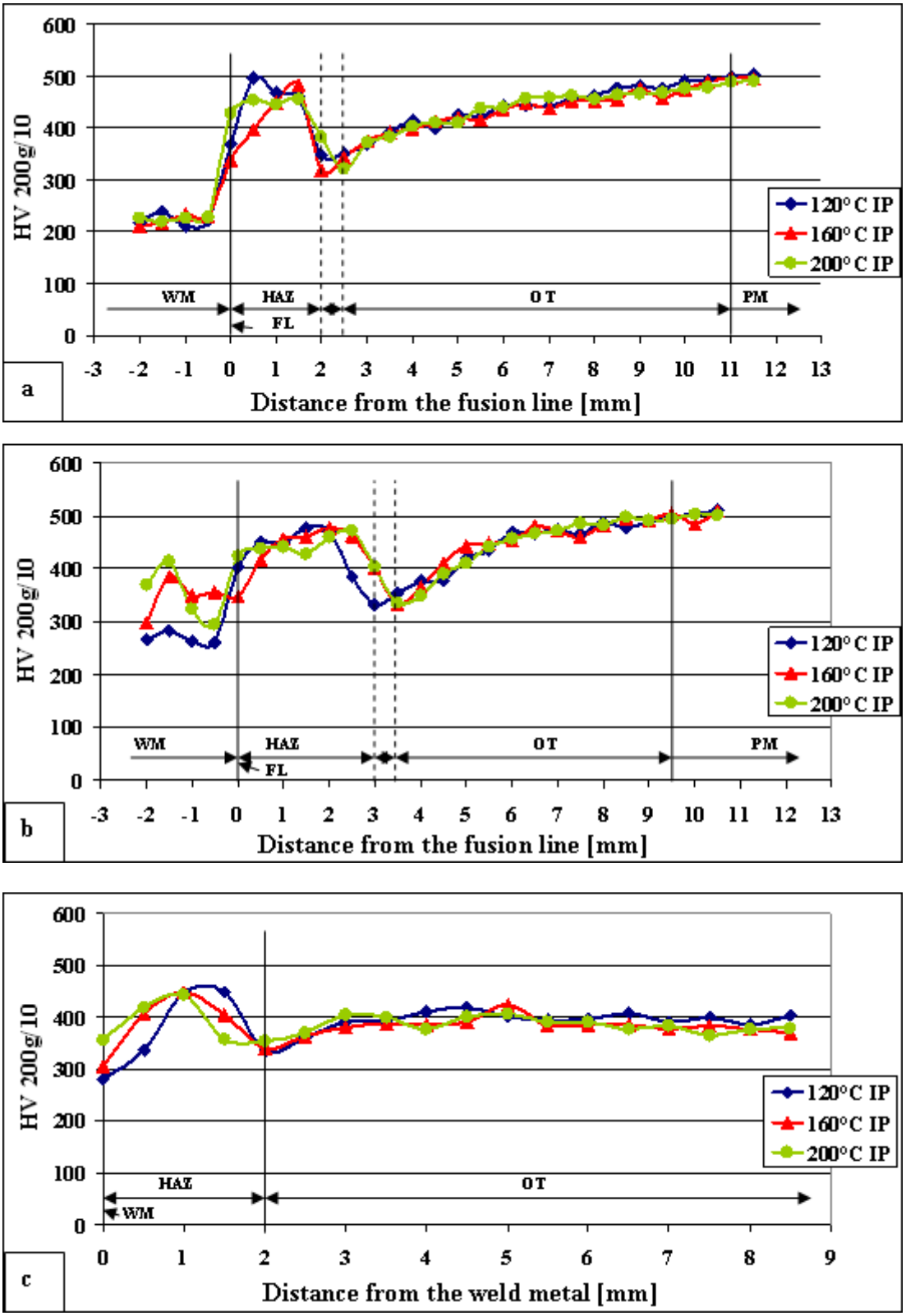

Figure 9. Weld hardness profiles employing 120°C, 160°C and 200°C interpass temperatures, measured in: a – X2 orientation, b – X4 orientation, c – X6 orientation. Orientations are defined in Figure 2. IP – interpass temperature.

A minor increase in overall HAZ area with increasing interpass temperature is presented in Table 5. Importantly, hardness obtained 15.9 mm from the weld toe is higher than the lowest hardness of 509 HV permitted by MIL-A-46100 [8] in all cases.

Table 5. HAZ area as a function of interpass temperature.

Interpass temperature [°C]	**HAZ area [mm^2]**
120	54.6
160	56.6
200	58.2

4 CONCLUSIONS

1) Dilatometry experiments showed that higher cooling rates resulted in the formation of higher fractions of hard structural phases with a fully martensitic structure for a 200°C/s cooling rate. Hardness significantly increases and transformation temperature range significantly decreases with increasing cooling rate up to 30°C/s and with further increasing cooling rate both characteristics plateau out. Results confirm that the steel possesses good hardenability over a wide range of cooling rates. At cooling rates representative of real multipass weld conditions, hardness measurements of dilatometry samples showed that peak hardenability was reached.

2) The HAZ hardness of the steel decreased and width increased, with increasing preheat temperature. Increasing the preheat temperature reduces the cooling rate thus allowing more time for hydrogen to diffuse out of the weldment. This is particularly important for the first fillet pass which is not reheated to the same extent as remaining cap passes. Hardness results indicate that welding without preheating does not significantly increase risk of HICC (given the restraint is a constant) as HAZ peak hardness of the first pass deposited with ambient preheat is lower than peak hardness reached in the cap area where 120°C interpass temperature was maintained.

3) Hardness of the HAZ and OT region remained almost identical for all three interpass temperatures employed. Cooling time from the beginning of the welding process until the peak temperature of the final pass was reached decreases with increasing interpass temperature. Time necessary to cool down to 100°C after completion of welding decreases with increasing interpass temperature from 120°C to 160°C but slightly increases with further increase in temperature to 200°C. This indicates that employing 160°C interpass temperature is the most beneficial from a productivity view point.

4) The nature of an austenitic stainless steel filler has the potential to remove the preheat requirement, which would allow great benefits during welding fabrication in terms of time and costs for industry. However, further in-depth research on the amount of diffusible hydrogen present in weldments should be carried out in order to confirm the safety of the proposed welding procedures and quantitatively assess the viability of the welding parameters.

5 ACKNOWLEDGEMENTS

The authors acknowledge the support of the Defence Materials Technology Centre (DMTC), which was established and is supported by the Australian Government's Defence Future Capability Technology Centre (DFCTC) initiative. The authors gratefully acknowledge the support of Thales Group, Bisalloy Steels Ltd and Bluescope Steel Ltd, for providing the steel test plates and samples, as well as beneficial discussions and guidance on this work. NSW science linkage grant from the NSW Government is acknowledged, for resource contribution to the lean automation workcell in which this work was conducted.

6 REFERENCES

[1] Magudeeswaran, G., V. Balasubramanian, and G. Madhusudhan Reddy, *Hydrogen induced cold cracking studies on armour grade high strength, quenched and tempered steel weldments.* International Journal of Hydrogen Energy, 2008. **33** (7): p. 1897-1908.

[2] Alkemade, S.J., *The weld cracking susceptibility of high hardness armour steel*. 1996, Defence Science and Technology Organisation. p. 24.

[3] Harrison, P.L. and R.A. Farrar, *Application of continuous cooling transformation diagrams for welding of steels.* International Materials Reviews, 1989. **34** (1): p. 35-51.

[4] Cottrell, C.L.M.:J. Iron Steel Institute, 1953, **174**, 17.

[5] Funderburg, R.S, *The importance of interpass temperature.* Welding Innovation, 1998. **15** (1): p. 31-32.

[6] Defence, AU., *Australian defence standard, DEF (AUST) 8030, Rolled armour plate, steel (3-35 mm)*. 2005.

[7] Williams, J.G., *New alloy design perspectives for high strength steels*. 2008, BluescopeSteel: Wollongong. p. 1-14.

[8] Defense, U.S., *MIL-A-46100, Armor plate, steel, wrought, high hardness*. 1988: Washington, D.C.

RESEARCH TO ESTABLISH A SYSTEMATIC APPROACH TO SAFE WELDING PROCEDURE DEVELOPMENT USING AUSTENITIC FILLER MATERIAL FOR FABRICATION OF HIGH STRENGTH STEEL

Authors: Lenka Kuzmikova,John Norrish,Huijun Li,Mark Callaghan.

This paper has been presented at16th International Conference on the Joining of Materials, 2011, Helsinki, Denmark.

ABSTRACT

High strength, thermo-mechanically treated steels often require very careful control of welding procedures to ensure freedom from hydrogen assisted cold cracking (HACC) in the weld metal and heat affected zone (HAZ) whilst avoiding undue loss of heat affected zone strength. In practice this leads to restricted operating envelopes and the requirement for rigorous procedure management. An alternative approach is the use of austenitic welding consumables but whilst this may be expected to expand the process parameter envelope its use is often restricted by adherence to procedures previously developed for ferritic consumables. The current paper describes the research undertaken to establish a systematic approach to the development of optimum, cost effective procedures for welding high strength quenched and tempered steel with an austenitic filler.

1 BACKGROUND

High strength, high hardness, thermo-mechanically treated steels are used extensively in wear resisting applications for materials handling and mining and as armour in defence applications. In most cases it is necessary to fabricate the material by welding. During welding the materials may however be subject to loss of heat affected zone hardness if overheated and hydrogen assisted cold cracking if strength matching ferritic filler materials are used with insufficient pre or post heat. The operating tolerance band when using ferritic fillers is therefore very narrow. In repair situations it has been common to use austenitic fillers to reduce the risk of HACC particularly when the parent material has a high carbon equivalent and close procedural controls are difficult to achieve. The present work was carried out to investigate the feasibility of developing less constrained welding procedures when welding with austenitic fillers.

The risk of HACC is related to three factors, figure 1:

1) The presence of hydrogen
2) A susceptible microstructure
3) Stress

All of these three must act in concert to cause HACC if any one of the factors is absent hydrogen cracking will not occur.

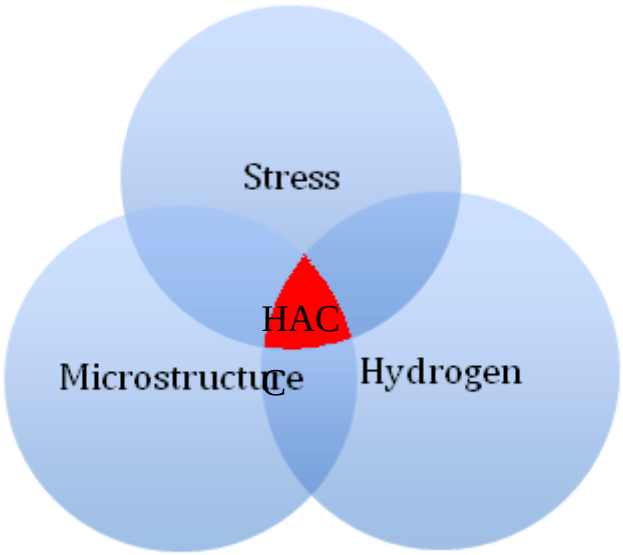

Figure 1 Basic factors responsible for hydrogen assisted cold cracking (HACC).

Stress is almost unavoidable in welded joints due to the contraction stresses and restraint. The level of stress may increase due to the joint design and section thickness. Joint design and welding sequence may be modified to decrease stress but it must be assumed that in more complex fabrications sufficient stress is available to contribute to HACC.

Martensitic structures are normally considered to be susceptible microstructures. Since high hardness is usually a design requirement for use of such materials it is common for the carbon equivalents to be high and normal base microstructures are bainitic or martensitic. Whilst this factor cannot be eliminated there is another issue related to microstructural transformation which influences the hydrogen distribution. If a ferritic filler is used the relative time between transformation of the filler and heat affected zone determines the direction of hydrogen diffusion: the solubility of hydrogen in the molten pool and the high temperature austenitic phase is high but it is much lower in the lower temperature ferritic or martensitic microstructure. If the filler material transforms before the austenitised area of the heat affected zone during cooling of the weld zone any hydrogen in the weld will be 'pumped' into the heat affected zone of the parent material. One obvious way to prevent this 'pumping effect is to use an austenitic filler. In the current investigation a high strength steel was welded with both ferritic and austenitic fillers.

2 METHODOLOGY

The high strength steel used was typical of those used for high hardness wear plate. Its chemical composition is listed in Table 1. The alloying design utilises the novel low manganese approach [1] in order to reduce centreline segregation of MnS inclusions and thus improve mechanical properties and weldability. The steel is microalloyed with Nb, Ti, V, and B in order to increase hardenability and enhance the HAZ properties.

Table 1. Chemical composition of investigated steel in wt% max.

Element	C	P	Mn	Si	S	Ni	Cr	Mo
Wt% max	0.32	0.02	0.4	0.35	0.005	0.35	1.15	0.3

Element	Cu	Al	Nb	Ti	V	B	CE_{IIW}
Wt% max	0.2	0.06	0.005	0.03	0.05	0.002	0.72

After hot rolling the plate is subjected to heat treatment process which consists of two phases: rapid water-quenching from austenite field which results in the formation of untempered martensite and subsequent low temperature tempering which improves the plate's toughness while maintaining high level of hardness. The tempering temperature is based on desired balance between hardness and toughness required for particular application. The microstructure of the investigated plate in Q&T condition consists of tempered martensite with an average hardness of 542 HV20.

Transformation temperature

The continuous cooling transformation behavior of the steel chosen was studied in previous work [2]. It was found that peak hardenability is reached at cooling rates representative of real welding conditions (cooling at 20°C/s to 30°C/s) in the temperature range of 800-200°C. At these cooling rates the austenite to martensite transformation takes place over a range of 200°C with transformation start and finish temperatures being approximately 410°C and 205°C respectively.

Hydrogen investigation

The objective of the tests reported below was to investigate the difference in hydrogen distribution when ferritic and austenitic consumables were used, the effect of preheat (PH) and type of wire on weld hydrogen levels.

Samples were produced using austenitic AWS A5.22 E308 MoT1 type flux-cored wire, an AWS A5.9 EC308Mo type metal-cored wire, an AWS A5.9 ER(307) solid wire and ferritic flux-cored wire complying with AWS A5.20 E71T-1. Both flux cored wires have a similar rutile flux core since it is recognised that the flux system used can have a major influence on the level of hydrogen in weld metal and also its diffusivity.

A robotic GMAW system was utilised to deposit consistent single weld beads onto the test piece assembly clamped in a copper jig. The welding jig is shown in figures 2 and 3. Samples were not degassed prior to welding (as normally required in the relevant standard) in order to simulate the real welding conditions in industry. Preheating was carried out utilising an electric resistance heating blanket and undercooling of the test piece assembly to 7°C was achieved using dry ice (solid CO_2). After deposition of the weld beads, samples were quenched in stirred iced water and transferred in to the bath of liquid nitrogen. Samples were observed for uniform heat-tinting on the reverse side of the test piece assembly and the total length and centre piece to weld crater distance were measured. The run-on and run-off pieces were broken off and centre piece was thoroughly cleaned with a steel wire brush. The intervals spent outside the liquid nitrogen did not exceed 15s.

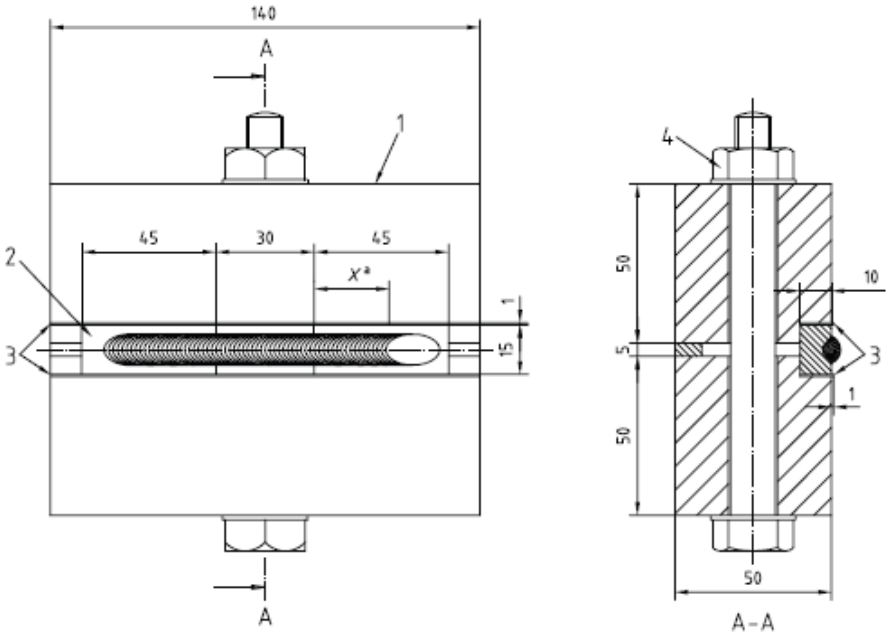

Figure 2 The standard diffusible hydrogen weld test jig assembly.

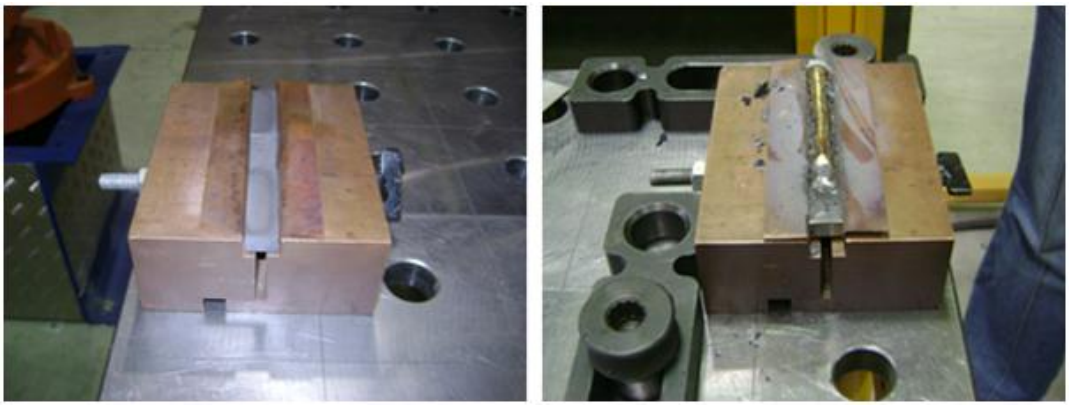

Figure 3 Welding fixture with test piece assembly before the deposition of the single weld and immediately after deposition of test run.

Parameters that were kept constant for all trials are shown in table 1. Variable welding parameters are displayed in table 2..

Table 1 Welding parameters common to all welding trials.

Welding parameter	Value
Travel speed	400 mm/min
Wire feed speed	9.5 m/min
Stick out	16 mm
Voltage	26.3 V
Polarity	DC+
Wire diameter	1.2 mm

Table 2 Variable welding parameters. Note: The values given in table are the average value of three trials welded under the same conditions.

Welding trial ID	PH [°C]	Quench [°C]	Shielding gas	Flow rate [l/min]	Amperage [A]	Heat input [kJ/mm]	Relative humidity [%]
FC_ASS_APH_DQ	20	Direct	Argoshield 52	16	215	0.85	48
FC_FER_APH_DQ	24	Direct	Argoshield 52	16	253	0.998	68
FC_ASS(PM+WM)_APH_DQ	22	Direct	Argoshield 52	16	218	0.86	70
FC_ASS_7°CPH_150°CQ	6	150	Argoshield 52	16	215	0.85	86
FC_ASS_80°CPH_150°CQ	80	150	Argoshield 52	16	213	0.84	74
FC_ASS_APH_150°CQ	22	150	Argoshield 52	16	220	0.87	65
MC_ASS_APH_150°CQ	22	150	Stainshield	16	294	1.16	58
S_ASS_APH_150°CQ	21	150	Stainshield	20	245	0.97	60

Figure 4 Welding trials identification explanation.

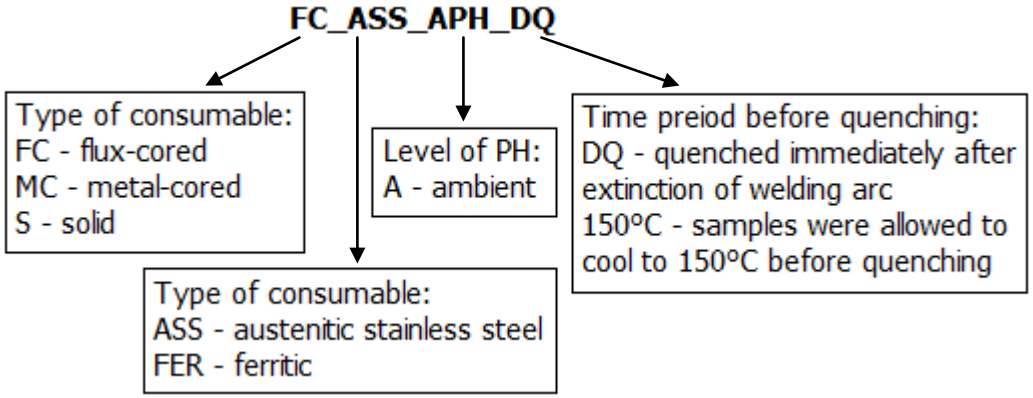

2.1 Diffusible hydrogen testing

Various test methods for determination of diffusible hydrogen content were reviewed. The 'Reference test method' - collection of hydrogen over mercury was selected to measure the diffusible hydrogen content present in the weldments. The gas collection apparatus is shown in figure 4. Testing was performed according to the AS/NZS 3752:2006 standard with few minor modifications. Every test was repeated three times for consistency. The first series of experiments was carried out twice in order to test the welding procedure as well as hydrogen measurement apparatus.

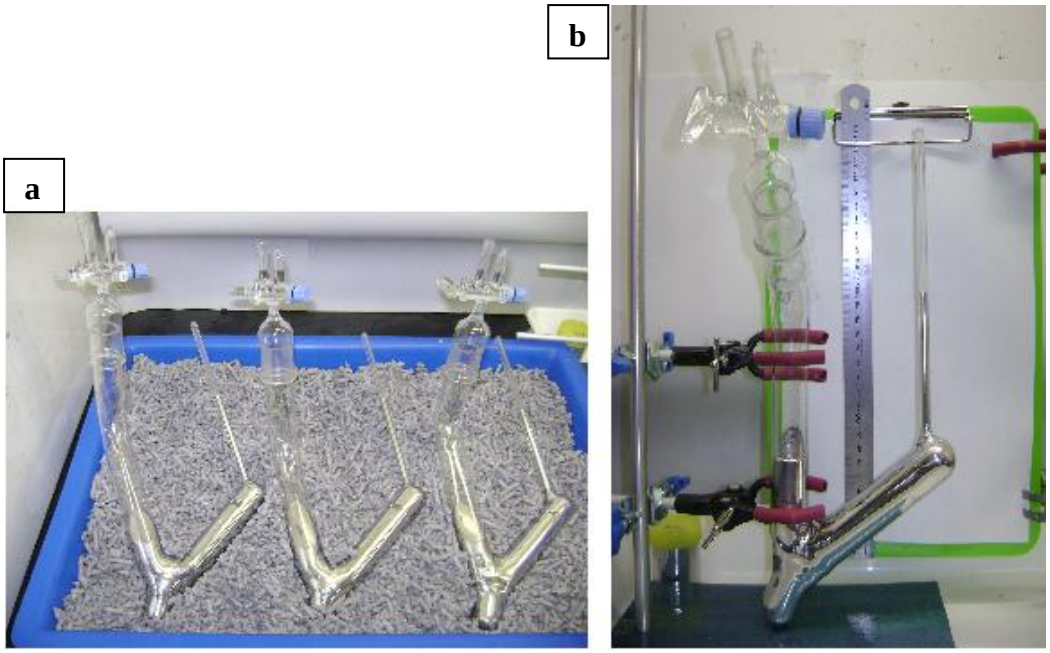

Figure 4 a –Test pieces submerged in mercury in evacuated Y-tube, b- Y-tube during measurement of the volume of evolved hydrogen.

Before transferring the test samples from liquid nitrogen into the y-tube containing mercury and evacuating the inner space, samples were placed into an acetone bath, allowed to rise to room temperature and dried with a jet of air. Samples were left undisturbed in the y-tube for 7 days at room temperature (around 20°C) to allow the majority of diffusible hydrogen to evolve and collect in capillary tube. The readings of atmospheric temperature and pressure were taken every day prior measuring the volume of hydrogen. The volume of the evolved hydrogen was corrected to standard temperature and barometric pressure measured and calculated by the equation:

$$V = \frac{273(P - H)(\pi r^2 C)}{760(273 + T)100}$$

where: V – volume of collected hydrogen at STP in millilitres; P – barometric pressure in mm of Hg; H – is the differential head of mercury between the two limbs of the y-tube in mm; C – length of the gas column above the mercury in mm; r – inner radius of capillary tube in mm; T – ambient temperature at the time of hydrogen measurements in °C.

The weight of the test pieces was determined before the deposition of the weld bead (m_1) and also after completion of diffusible hydrogen testing (m_2) to nearest 10mg.The volume of diffusible hydrogen H_D in ml at STP per 100g of weld metal (WM) was calculated from the equation:

$$H_D = V\frac{100}{(m_2 - m_1)}$$

2.2 Residual hydrogen testing

Various methods of testing residual hydrogen content were also reviewed. The inert gas melt extraction method was selected because it is a rapid process and has a proven reliability. Testing was carried out according to the AS/NZS 1050 standard. The Eltra ONH-2000 total hydrogen testing facility used is shown in figure 5.

After completion of diffusible hydrogen testing, three slices transverse to the longitudinal axis of each centre piece were sectioned utilising a precision cutting machine. The weld metal was separated from the rest of the sample using a grinding wheel. In between grinding steps, samples were cooled in water to prevent heating due to friction and possible loss of residual hydrogen. The resultant samples of weld metal of approximately 1g were washed in acetone, dried and subjected to residual hydrogen testing.

Figure 5 Eltra ONH-2000 - Inert gas melt extraction test facility.

During the test samples were heated to melting temperature to release all residual hydrogen (in case of ASS WM residual hydrogen = diffusible hydrogen in austenite fcc lattice + hydrogen trapped in strong traps). The hydrogen is transported by the carrier gas to the analyser to determine its quantity in ppm. The volume of residual hydrogen in ppm was converted to ml/100g of WM at "normal" atmospheric pressure of 101325 Pa and a temperature of 20°C.

6.1.1 Conversion of ppm to ml of hydrogen per 100g of WM

$$\mathrm{m} = 1\mathrm{ppm\ of\ H} = 0.1\mathrm{mg\ of\ H\ in\ 100g\ of\ WM}$$

$$\mathrm{V[ml\ ofH\ per\ 100g\ of\ WM]} = {}^{\mathrm{m}}/_{\rho}$$

where, V = volume of the gas, m = weight of the gas, ρ = density of the gas.

The density of hydrogen was calculated from the equation of state of an ideal gas:

$$\mathrm{pV} = \mathrm{NkT}$$

where: p = atmospheric pressure, N = number of particles in the gas, k = Boltzmann constant = 1.38×10^{-23} N.m.K^{-1} and T = temperature.

The formula for calculation of the number of particles:

$$\mathrm{N} = \mathrm{nN_A} = {}^{\mathrm{m}}/_{\mathrm{M_m N_A}}$$

where: n = amount of substance, N_A = Avogadro constant = $6.03.10^{23}$ mol^{-1}, M_m = molar mass.

Then,

$$\mathrm{pV} = {}^{\mathrm{m}}/_{\mathrm{M_m R_m T}}$$

where: R_m = molar gas constant = 8.316 N.m.K^{-1}mol^{-1}.

Then, the density of hydrogen can be calculated:

$$\rho = {}^{\mathrm{m}}/_{\mathrm{V}} \rightarrow \rho = {}^{\mathrm{pM_m}}/_{\mathrm{R_m T}}$$

3 RESULTS

Every test was performed three times. The first series of three trials was also repeated twice to gain confidence in the repeatability and consistency of the results. Further, for every residual hydrogen test, three samples of weld metal were sectioned from all three samples welded under the same conditions and were tested for residual hydrogen. Results of both diffusible and residual hydrogen testing showed excellent consistency and repeatability.

3.1 Effect of welding consumable type on hydrogen

Measured levels of diffusible and residual hydrogen are presented in table 3. To be able to directly compare the overall amount of hydrogen introduced into the weldment utilising ferritic and ASS flux-cored wires, samples were quenched in stirred iced water immediately after extinction of the welding arc. Samples were welded without preheat with ambient temperature of approximately 22°C. It was found that the ferritic consumable resulted in a diffusible hydrogen level approximately 18 times greater than that produced by the austenitic wire. The ferritic consumable was expected to produce around 6 to 10 ml/100g .The extremely high value recorded is thought to be due to hydrogen pick-up during prolonged inappropriate storage of the consumable although the original manufacturer's package had never been opened. However, the austenitic consumable was not stored in sealed environment for approximately 3 years. Thus, it is expected that to certain degree "fresh" properly stored consumables would result in lower hydrogen levels and these results could be taken as a 'worst case' scenario. To prove that all the diffusible hydrogen measured for samples welded with austenitic consumable originates only from the HAZ, the austenitic consumable was also deposited onto 304 austenitic plate. This should, based on the above theory, result in zero diffusible hydrogen. This theory was confirmed as there was no diffusible hydrogen whatsoever released during this testing.

Table 3 Levels of diffusible and residual hydrogen measured for ASS and ferritic WM deposited on the investigated steel and also ASS WM deposited on 304 ASS. Note: Presented levels of diffusible hydrogen are the average values of three trials and residual WM's hydrogen levels the average of nine samples produced under the same conditions.

Consumable	Diffusible H content [ml/100g of WM]	Residual H content [ml/100g of WM]
Austenitic	1.3	5.8
Ferritic	23.4	0.9
Austenitic (PM+WM)	0	8

To demonstrate that hydrogen is also present during welding with the austenitic consumable but is safely "locked" in the weld metal, the previous diffusible hydrogen test samples were sectioned and the weld metal was subjected to residual hydrogen testing. The value of 5.8 ml of hydrogen per 100g in the austenitic weld metal indicates that the hydrogen is indeed "locked" within in the microstructure. Whereas the low value of 0.9 ml/100g in the ferritic weld metal indicates that the majority of hydrogen has diffused out of the weld / into the HAZ.

3.2 Effect of preheat temperature on hydrogen content

A further objective of the project was to justify reducing or possibly eliminating the recommended preheat temperature of 80°C when welding this type of high strength steel joint when using an austenitic consumable. To be able to compare the influence of various levels of preheat on diffusible hydrogen content, samples were allowed to cool down to 150°C after

welding and prior to quenching. Measured levels of diffusible and residual hydrogen of the samples welded with an austenitic filler wire at three different preheat temperatures are shown in table 4. The results show that a decrease in the preheat temperature from 80°C to 7°C resulted in an increased level of diffusible hydrogen from 0.5 to 1.3 ml/100g but decreased the level of weld metal residual hydrogen content from 8.0 to 6.1 ml/100g. The increase in diffusible hydrogen content with decreasing preheat temperature is probably the result of reduced cooling time in the temperature range associated with highly effective hydrogen diffusion out of the weldment.

Table 4 Levels of diffusible and residual hydrogen measured for ASS WM deposited on the investigated steel PM under different PH conditions. Note: Presented levels of diffusible hydrogen are the average values of three trials and residual WM's hydrogen levels the average of nine samples produced under the same conditions.

PH temperature [°C]	Diffusible H content [ml/100g of WM]	Residual H content [ml/100g of WM]
7	1.3	6.1
Ambient (22)	0.8	7.9
80	0.5	8.0

The austenitic weld structure promotes hydrogen diffusion from HAZ to weld metal where it becomes effectively trapped. In other words the austenitic weld metal microstructure having a high solubility and very low diffusivity of hydrogen acts like hydrogen sink. Therefore reduced cooling times (less time for evolution of hydrogen from HAZ into the weld metal) as a consequence of lowering the preheat temperature resulted in lower levels of weld metal residual hydrogen content.

3.3 Comparison of hydrogen levels for three types of austenitic consumables

The levels of diffusible and residual hydrogen contents measured for three different types of austenitic wires namely flux-cored, metal-cored and solid wire are displayed in table 5. As expected the highest levels of both diffusible and residual hydrogen were present when employing flux-cored wire. This is due to the presence of the rutile flux, probably the major source of hydrogen contamination. Metal-cored weld deposits resulted in 38% and 42% reduction of diffusible and residual hydrogen respectively. Very low levels of hydrogen both diffusible and residual were expected due to the absence of the flux and seamless structure of external metallic sheath of the wire eliminating hydrogen pick-up by the inner core. Samples produced employing solid wire did not release any diffusible hydrogen at all and the residual hydrogen content was reduced by 53% and 20% compared to flux-cored and metal-cored wires respectively.

Table 5 Values of diffusible and residual hydrogen levels measured for three different types of ASS consumable deposited on investigated stel. Note: Presented levels of diffusible hydrogen are the average values of three trials and residual WM's hydrogen levels the average of nine samples produced under the same conditions.

ASS consumable type	Diffusible H content [ml/100g of WM]	Residual H content [ml/100g of WM]
Flux-cored	0.8	7.9
Metal-cored	0.5	4.6
Solid	0	3.7

4 CONCLUSIONS

From this study it may be concluded that:

1. The use of ferritic consumable with rutile flux type can introduce high levels of hydrogen into the weldment. The low solubility and high diffusivity of hydrogen in the ferritic lattice promotes the transfer of hydrogen into the susceptible HAZ on cooling.

2. When an austenitic consumable is used the majority of the hydrogen introduced into the weldment is contained in the weld metal and does not diffuse into the HAZ or surrounding atmosphere. On the contrary diffusible hydrogen evolves from the HAZ, (which with decreasing temperature becomes heavily oversaturated), into the surrounding atmosphere or into the weld metal.

3. The entire diffusible hydrogen measured in the samples with austenitic weld deposits originated from HAZ.

4. The diffusible hydrogen content of the samples welded with austenitic consumables increased with decreasing preheat temperature. Residual hydrogen levels however increased with increasing preheat temperature indicating that on cooling hydrogen diffuses from supersaturated HAZ into the weld metal.

5. Lowering the preheat temperature from 80°C to 7°C for welding these high strength steels with austenitic consumable resulted in slightly higher level of diffusible hydrogen, but diffusion of this hydrogen is promoted from the HAZ to the weld metal, greatly reducing the risk of HACC compared to a ferritic consumable.

6. Both the diffusible and residual hydrogen levels were decreased when moving from flux-cored to metal-cored and solid austenitic consumable. With zero diffusible hydrogen measured for solid ASS consumable deposited onto investigated steel.

ACKNOWLEDGMENTS

This work was mainly supported by the Defence Materials Technology Centre (DMTC), which was established and is supported by the Australian Government's Defence Future

Capability Technology Centre (DFCTC) initiative. Great support was also obtained from BlueScope Steel Ltd; who provided the apparatus for diffusible hydrogen measurements and performed the residual hydrogen testing. Special thanks are due to Dr Frank Barbaro for his advice and Rudy Drmota for sharing the skills necessary to perform diffusible hydrogen testing. Thales Group is acknowledged for providing the steel plate and welding consumables. NSW science leverage grant from the NSW Government is acknowledged, for resource contribution to the lean automation workcell in which the welding work was conducted.

References

1. Williams, J.G., New alloy design perspectives for high strength steels. 2008, BluescopeSteel Report: Wollongong. p. 1-14.
2. Kuzmikova L., Callaghan M., Larkin N., Scott R., De Jong R., Li H., Norrish J., A Study of a Continuous Cooling Behaviour & Effect of Preheat & Interpass Temperature on the HAZ of High Strength Quenched and Tempered Steel. Doc IX-2352-10. Paper presented in commission IX the IIW Annual Assembly, Istanbul, July 2010.

INVESTIGATION INTO FEASIBILITY OF HYBRID LASER-GMAW PROCESS FOR WLEIDNG HIGH STRENGTH QUENCHED AND TEMPERED STEEL

Authors: Lenka Kuzmikova, Nathan Larkin, Zengxi Pan, Mark Callaghan, Huijun Li and John Norrish

This paper was published in Australasian Welding Journal (AWJ), 2012, Vol. 57 (first quarter), pp. 43-48

ABSTRACT

In this study, the feasibility of hybrid laser-gas metal arc welding process for replacement of conventional flux-cored arc welding procedure for welding high strength quenched and tempered steel was investigated. Experimental work focused on optimisation of process parameters to produce joint with desired properties. Hardness of the weld heat affected zone produced by both processes has been measured. Productivity and cost effectiveness of both processes were compared. It was concluded that hybrid laser-gas metal arc welding process is suitable for welding high strength quenched and tempered steel.

KEYWORDS: high strength quenched and tempered steel, flux-cored arc welding, hybrid laser-gas metal arc welding, heat affected zone, productivity.

1 INTRODUCTION

In manufacturing of heavy high strength steel structures innovative approaches are essential to satisfy the continuous drive to deliver improved quality and productivity outputs at a lower cost. To ensure better product performance and weight to strength ratio the manufacturer of quenched and tempered (Q&T) plate recently adopted novel improved alloy design. Another area of possible improvement is the welding process.

The chemistry and heat treatment of high strength Q&T steels are designed to deliver optimum properties, thus any microstructural changes during fabrication are undesirable. However, when steel is subjected to welding, the area surrounding the weld pool, known as the heat affected zone (HAZ), undergoes complex thermal cycles which alter original microstructure of the material. The extent and characteristics of these changes depend on nature and number of thermal cycles experienced, and may lead to such undesired effects such as HAZ softening (or hardening) and hydrogen assisted cold cracking (HACC). To preserve original properties of the steel plate, it is beneficial to employ welding procedures with optimised heat inputs and if possible, minimum number of weld passes.

Flux-cored arc welding (FCAW) is a widely used fabrication technique for joining high strength Q&T steel plates. The disadvantage of using flux-cored wires is that in multi-pass welding the slag formed on the surface of the bead needs to be removed before deposition of subsequent passes, this is ineffective in terms of both productivity and cost. What is more, the flux also has the potential to pick-up hydrogen from the surrounding atmosphere if the consumable is stored inappropriately or over a long period of time. This hydrogen may be absorbed in the weld pool, increasing the risk of HACC. Welding of thicker plates almost always requires multiple passes as the FCAW procedure gives relatively low penetration, the

seam depth being a function of the heat conduction [33]. Welding of thicker sections with one pass would be possible by employing slower welding speeds, but this would result in even higher heat input and inadmissibly wide and soft HAZ.

The required deep penetration could be achieved by using the laser welding process. However, laser welding alone is not the most suitable option for welding of high strength Q&T steels in a production environment. Whilst it is a high productivity low heat input process, it produces narrow heat affected zones and steep spatial and temporal temperature gradients that often result in brittle microstructures susceptible to HACC. Laser welding also produces welds with a high ratio between welding depth and seam width. It consequently results in a slim weld seam and a poor gap bridging capability [31, 32]. Due to this phenomenon, laser beam welding requires high precision during edge preparation and set-up.

Hybrid laser-gas metal arc welding (GMAW) which utilises synergy between laser beam and welding arc has the potential to offer the ideal solution for welding high strength Q&T steels. It couples the benefits and largely overcomes the disadvantages of the two individual processes [4]. During hybrid laser-GMAW process a smaller weld pool is formed in comparison with the FCAW technique. This results in lower heat input and consequently a narrower HAZ. The HAZ hardness of laser welded area (in laser welding alone possesses high hardness and has increased susceptibility to HACC) is tempered by subsequent GMAW pass [3]. The HAZ properties can be further improved by reduction of weld passes what would also lead to significant time and cost savings. Additionally, hybrid laser-GMAW process in utilises solid austenitic stainless steel consumable that according to data from weld hydrogen testing [5] results in zero weld diffusible hydrogen content, practically ruling out the risk of HACC, common defect experienced when welding high strength Q&T steels.

A comparison of weld seam geometries is shown for laser, laser hybrid and GMAW welding in Figure 1. Gao et al. [34] described characteristic laser hybrid weld as a ‘wine-cup’ shape which consists of wider (arc) zone above the narrow (laser) zone. These two zones differ from each other by alloying elements distribution, microstructure, hardness and the width of HAZ. Observed dissimilarities are attributed to the difference of temperature gradient, crystallizing and the effects of arc pressure on the molten pool between laser zone and arc zone.

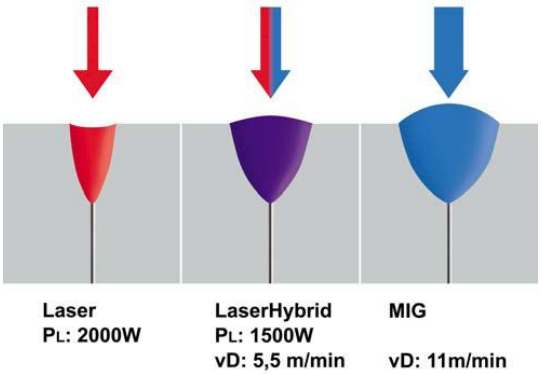

Figure 1 Comparison between the seam geometry of laser, GMAW and hybrid laser-GMAW weld seams with the same penetration depth and the same welding speed [3].

Advantages of hybrid laser-GMAW process over currently used FCAW are summarised as follows:

- Reduction of the number of weld passes

- Reduction in the amount of used filler material
- Significantly improved cost effectiveness and production times
- Potential improvement of joint hardness and minimisation of HAZ
- Reduced risk of HACC

To achieve synergy between laser and arc to produce joints with optimal geometry and properties, process parameters such as laser to wire distance, welding and wire feed speed, welding torch angle have to be carefully selected. Work presented in this paper details the findings of feasibility testing and direction for future work to optimise and develop the hybrid laser-GMAW process for future replacement of currently used FCAW for welding high strength Q&T steel.

2 EXPERIMENTAL

2.1Experimental equipment

This experimental work was completed using the robot controlled GMAW process to produce inner pass and hybrid laser-GMAW test bed to deposit outside cap pass. Hybrid laser-GMAW test bed utilises a 3kW diode laser power source, a GMAW power source and wire feeder, and a lathe bed capable of motion in 2 degrees of freedom. Lathe provides precise positioning system and movement of work piece during welding. A picture of the test bed is shown in Figure 2.

The laser beam is delivered through an optical fibre into a 50mm collimator and a 200mm lens. Significant practical advantage of utilising diode laser in combination with optic fibre is ability to easily position and move the laser torch making it ideal candidate for industrial use and automation.

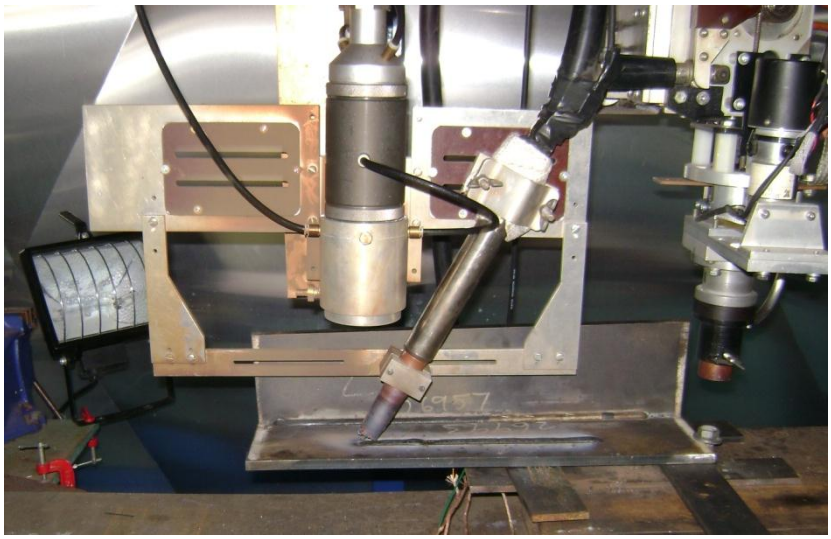

Figure 2 Hybrid laser-GMAW set-up.

2.2 Ideal Joint Geometry

The target of this work is to develop the hybrid laser-GMAW process to produce joints with geometry as shown in Figure 3.

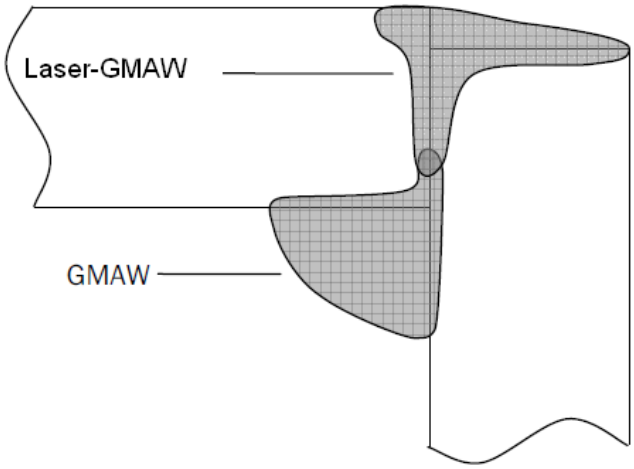

Figure 3 Ideal geometry of the hybrid Laser-GMAW joint.

Weld test sections were prepared by tacking 300x100x8.5 high strength Q&T test plates, with the specified geometry parameters, on the inside corner. It is to be noted that test plates were sectioned using water jet cutter and no edge preparation was done prior to welding. The inner pass was deposited first followed by the outer cap pass.

Initial testing was conducted to understand the capability and limits of the testing infrastructure. Following work focused on optimisation of process parameters to obtain full penetration and good fusion in the welded joint. Welding parameters common to all trials are presented in Table 1.

Table 1 Parameters common to all welding trials

Welding parameter	**Value**
Laser power	3 kW
Hybrid Laser-GMAW filler material	ø1.2 mm solid austenitic stainless steel wire
Hybrid Laser-GMAW shielding gas	1.5% O_2 in Ar at 20 l/min
Hybrid Laser-GMAW voltage	30 V
Laser focal point	2 mm under plate surface
GMAW filler material	ø1.2 mm solid austenitic stainless steel wire
GMAW shielding gas	1.5% O_2 in Ar at 20 l/min
GMAW voltage	26.3 V
GMAW wire feed speed	9.5 m/min

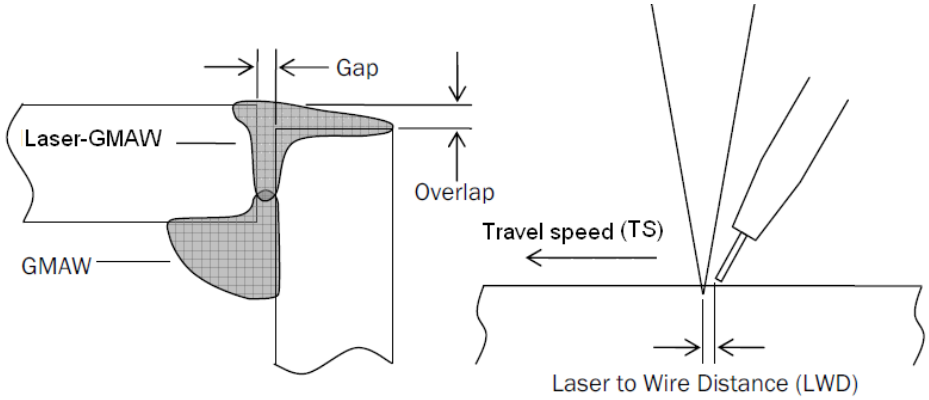

Figure 4 Diagram of experimental parameters.

3 RESULTS

3.1 Gap between plates

During initial testing (Test 1-3, Table 2), it was concluded that 3kW laser does not have sufficient power to achieve required penetration through test plates tacked tight against each other. As a result of that, the gap dividing the test plates was introduced to aid the penetration. Series of trials carried out determined the optimum width of the gap to be 1.5mm. Literature [6] suggests that full penetration of bead-on-plate weld on 7 mm plate of mild steel is possible employing a higher power laser.

3.2 Laser to wire distance

Tests 1-3 (Table 2) also revealed that the depth of penetration is significantly affected by varying laser to GMAW wire distance. The best penetration was obtained employing 1mm laser to wire distance. Test 6 (Table 2) indicates that the optimal laser to wire distance will change depending on wire feed speed.

3.3 Travel speed

After experimental parameters for geometry with 5 mm overlap were optimised to deliver full penetration the overlap was decreased to 3 mm increasing the thickness to be penetrated. Travel speed affects the overall energy delivered into the weldment. The penetration improved when the travel speed was decreased from 380 to 300 mm/min and Test 9 (Table 2) showed that it is possible to create a hybrid laser-GMAW joint with close to ideal geometry when the travel speed was reduced to 250 mm/min and 1.5mm gap was present between the plates. A macro of the weld cross-section of this trial is shown in Figure 5.

Table 2 Summary of the test parameters subjected to optimisation and obtained results.

Test number	Experimental test parameters					Notes
	Overlap [mm]	Gap [mm]	WFS [m/min]	TS [mm/min]	LWD [mm]	
1	5	0	5	380	**0**	Very poor penetration
2	5	0	5	380	**1**	Improved penetration
3	5	0	5	380	**2**	Very poor penetration
4	5	**1**	5	380	1	Improved penetration
5	5	**1.5**	5	380	1	Full penetration

6	5	1.5	**6**	380	1	Poor penetration
7	**3**	1.5	5	380	1	Insufficient penetration
8	3	1.5	5	**300**	1	Improved penetration
9	3	1.5	5	**250**	1	Satisfactory penetration

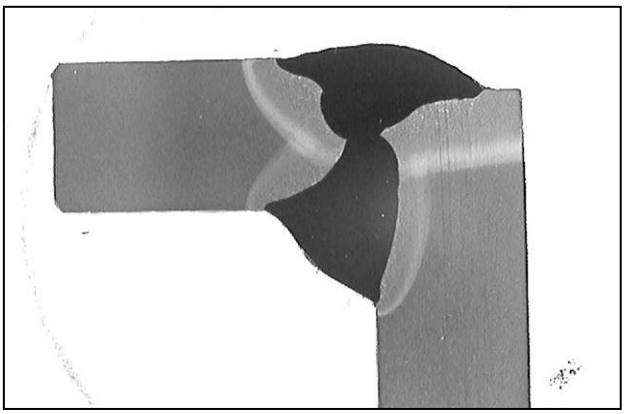

Figure 5 Macro of the weld cross-section produced with parameters detailed in Table 2 – Test 9.

3.4 Comparison with current procedure

A comparison between the current FCAW multi-pass and the investigated hybrid laser-GMAW two pass procedure has been made in

Table 4-1 Comparison of the time spent in deposition, consumable usage and total volume of the weld for current 5-pass FCAW and investigated 2-pass hybrid laser-GMAW procedure.

Process	Pass	TS [mm/min]	WFS [m/min]	Time [s]	Consumable [m]	Weld volume1 [mm3]
FCAW	1	400	9.5	150	23.8	22900
	2	500	11.0	120	22.0	21100
	3	500	9.5	120	19.0	18200
	4	550	9.5	109	17.3	16600
	5	550	9.5	109	17.3	16600
			Total	**608**	**99.4**	**95400**
GMAW +Laser-GMAW	1	400	9.5	150	23.8	26400
	2	250	5.0	240	20.0	22200
			Total	**390**	**43.8**	**48600**
			Difference	**218**	**55.6**	**46800**

Note: 85% deposition efficiency for flux-cored wire and 98% deposition efficiency for solid wire were assumed. The overall time taken for the laser weld is around 64% of that required for the a GMAW only technique. It should also be noted that the consumable is costly and the 50% saving in usage is significant.

6.1.1.1 Comparison of the weld metal and HAZ areas

The HHA steel in as supplied Q&T condition has the desired mechanical properties but the welding process not only alters the original microstructure of the parent plate but also creates a weld metal deposit with properties which are different from the parent HHA plate. For this reason it is considered beneficial to employ welding procedures with a reduced number of weld passes and thus minimised HAZ area. Weld metal and HAZ zone areas of the joints produced by both processes were compared.. The time, consumable length, and weld volume has been calculated per one meter of the joint and does not account for preheat time, time needed to remove the slag from the surface of the bead or time waiting to achieve interpass temperature. These values suggest that a 36% decrease in welding time and a 56% decrease in the amount of consumable used would result from using the hybrid laser-GMAW process for deposition of the outer cap pass.

Table 3 Comparison of the time spent in deposition, consumable usage and total wolume of the weld for current FCAW and investigated hybrid laser-GMAW procedure.

Process	Welding time [s]	Consumable usage [m]	Volume of the weld [mm^3][1]
FCAW	608	99.4	95400
Hybrid laser-GMAW	390	43.8	49500
Difference	**218**	**55.6**	**45900**

[1] 85% efficiency for flux-cored wire and 100% efficiency for solid wire were assumed.

Comparison of the HAZ size has also be made. For reference, the cross section of a weld produced with the current FCAW procedure as shown in Figure 6. An outline of the base material, weld material, and HAZ is shown in Figure 7. From the diagrams it can be seen that weld produced with hybrid laser-GMAW has a much smaller HAZ in the base material shown in the vertical direction. This is offset by a larger HAZ in the base material shown in the horizontal direction. The HAZ from the inner passes is of similar size.

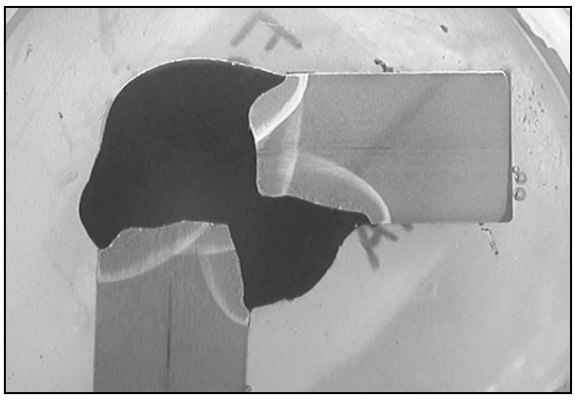

Figure 6 Weld cross-section of the joint produced by current FCAW procedure.

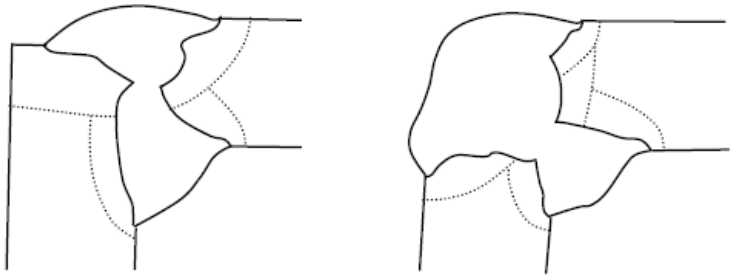

Figure 7 Comparison of weld cross-sections of current FCAW and investigated hybrid laser-GMAW procedures outlining areas of the weld metal and HAZ.

3.4 Hardness testing

Hardness of the samples produced with both procedures was measured 2 mm under plate's surface. Figure 8 presents hardness profile of the cap area. It can be seen that the HAZ resulting form hybrid laser-GMAW process was 1 mm wider compared to FCAW procedure. The hardness profiles were almost identical and the the unaffected parent material was distant 12 mm from the fusion line for both procedures. Hardness profiles measured in the area of inner pass are presented in Figure 9. Hardness of the HAZ of both samples is very similar with slightly wider over tempered region produced by GMAW resulting form higher welding current.

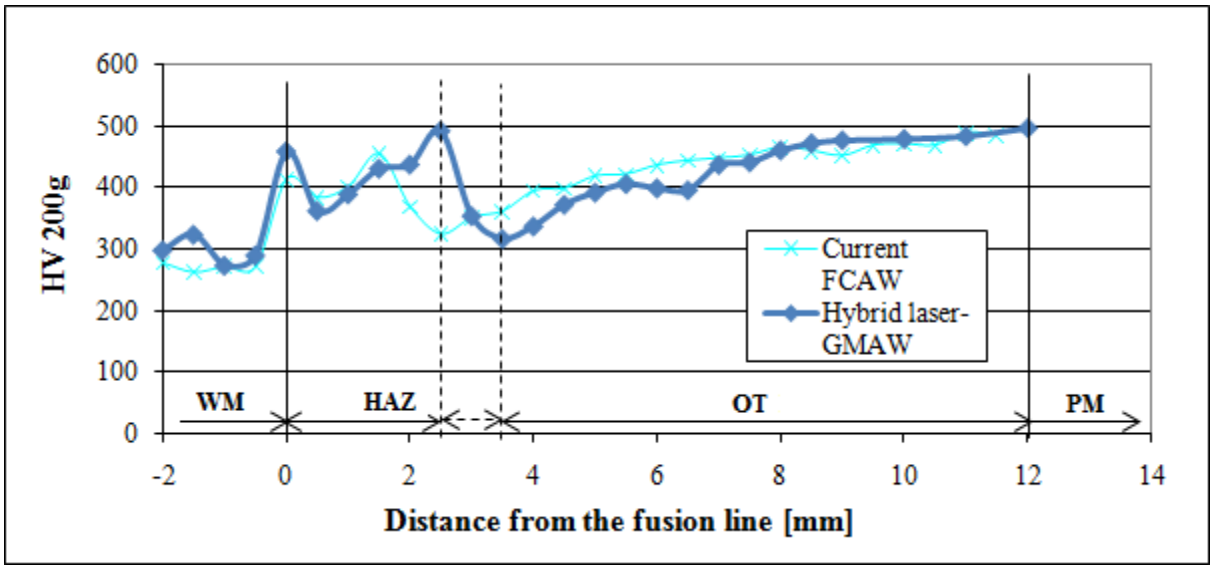

Figure 8 Weld hardness profiles measured on the outer surface of the cap passes.

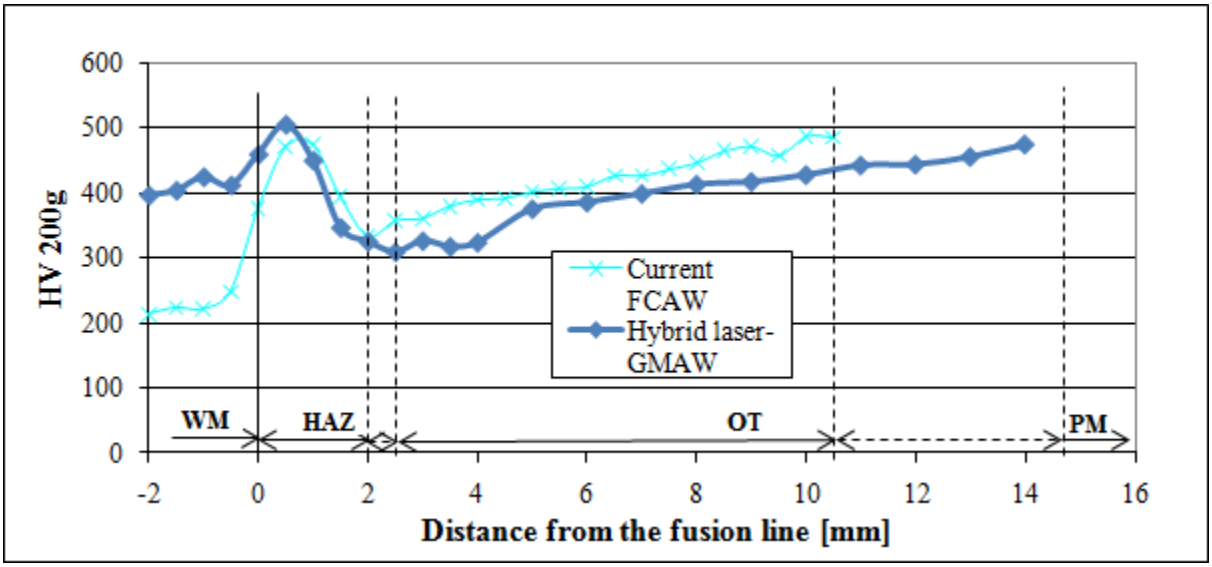

Figure 9 Weld hardness profiles measured on the inner surface of inner pass.

4 CONCLUSIONS AND RECOMMENDATIONS

Feasibility testing of hybrid laser-GMAW process on high strength Q&T plate has been conducted and the following conclusions have been made:

1. It is possible to produce a hybrid laser-GMAW on high strength Q&T plate at close to the ideal geometry using a 3 kW diode laser.
2. The distance between the laser focal point and the wire affects the penetration depth of the resultant weld significantly.
4. The hybrid laser-GMAW joining process reduced welding time by 36% and consumable usage by 56% over the current FCAW procedure. (Note: Only time spent in actual deposition of the weld is considered.)
5. The HAZ of the hybrid laser-GMAW weld showed an increase in size in the direction perpendicular to the laser, and smaller in the direction of the laser.
6. Hardness profiles measured in the area of both cap and inner pass are almost identical. Inner pass deposited with GMAW process possesses slightly wider over tempered region.

To be able successfully implement hybrid laser-GMAW process into industry practice yielding all the potential benefits this process offers, further work is required. Additional testing will be completed on this process to understand limits of operating parameters and optimisation for industry use. Areas for further investigation include:

- Offsetting the GMAW bead from the laser to minimise the size of the HAZ produced in the direction perpendicular to the laser.
- Minimising the plate gap required by the process to obtain full penetration welds.
- Investigate the effect of using a higher power laser.
- Implementing welding robotic arm to carry the hybrid laser-GMAW set-up.

Acknowledgement

This work was mainly supported by the Defence Materials Technology Centre (DMTC), which was established and is supported by the Australian Government's Defence Future Capability Technology Centre (DFCTC) initiative.

References

[1] Reutzel, E.W., et al., *Hybrid laser-GMA welding for improved affordability.* Journal of Ship Production, 2008. **24**(2): p. 72-81.
[2] Reutzel, E.W., et al. *Laser-GMA hybrid welding: Process monitoring and thermal modeling*. 2005. Pine Mountain, GA, United states: ASM International.
[3] Staufer, H., M. Rührnößl, and G. Miessbacher, *LaserHybrid Welding and LaserBrazing: State of the Art in Technology and Practice by the Examples of the Audi A8 and VW-Phaeton*. 2004, Fronius: Wels. p. 1-10.
[4] Gao, M., X.Y. Zeng, and Q.W. Hu, *Effects of welding parameters on melting energy of CO2 laser–GMA hybrid welding.* Science and Technology of Welding and Joining, 2006. **11**(5): p. 517-522.
[5] Kuzmikova, L., et al., *Hydrogen testing of the weldments deposited employing ferritic and various types of austenitic stainless steel consumable under different preheat conditions*. 2010, University of Wollongong: Wollongong. p. 1-16.
[6] Gao, M., et al., *Microstructure characteristics of laser-MIG hybrid welded mild steel.* Applied Surface Science, 2008. **254**(18): p. 5715-5721.

WELD METAL HYDROGEN ASSISTED COLD CRACKING IN HIGH STRENGTH LOW ALLOY STEELS

Authors: Lenka Kuzmikova, Frank Barbaro, John Norrish, Huijun Li

This paper has been presented at International conference of South East Asia Iron and Steel Institute, 2012, Nusa Dua, Bali.

ABSTRACT

High strength low alloy steels have provided significant benefits to the safe and economic fabrication of modern steel structures. Steel consumption has been optimized but most importantly the associated reduction in carbon content has reduced the risk of hydrogen assisted cold cracking (HACC) in the weld heat affected zone (HAZ) and thus improved fabrication procedures. Unfortunately the issue of HACC is now more likely to manifest itself in the weld metal. Although there are reliable procedures available to avoid HACC in the HAZ there is no such guidance for HACC in the weld metal.

The role of hydrogen in this phenomenon is crucial and until now little has been known about the distribution of hydrogen following completion of welding. This investigation, using different weld consumables and novel hydrogen analysis techniques has provided an insight to the diffusion of hydrogen. It is shown that an austenitic weld metal, or a weld metal that transforms after the HAZ will provide a sink for hydrogen and so reduce the level of hydrogen in the adjacent HAZ. It is concluded that this mechanism may contributes to an increased risk of HACC in a susceptible weld metal.

KEYWORDS: weld metal, hydrogen assisted cold cracking, high strength low alloy, HAZ, hydrogen diffusion,

1 INTRODUCTION

High strength low alloy steels have provided significant benefits to the safe and economic fabrication of modern steel structures. Steel consumption has been optimized but most importantly the associated reduction in carbon content of these modern steels has reduced the risk of HAZ HACC to very low levels. Unfortunately the issue of HACC is now more likely to manifest in the weld metal.

The factors controlling the occurrence of HAZ HACC are well known and have been sufficiently quantified to develop procedures that minimize its occurrence. The controlling factors are microstructure, stress and the presence of hydrogen, which are depicted in Figure 1.

Unfortunately, at present the occurrence of WMHACC cannot be predicted by utilization of the HAZ-HACC avoidance parameters and WMHACC is occurring in microstructures with hardness levels significantly lower than that observed in the HAZ. One theory for the shift in

location of HACC from the HAZ to the WM is believed to be associated with the difference in their austenite to ferrite transformation temperature. In conventional high carbon steels, the HAZ can transform at quite low temperatures, presumably after the weld metal, thus providing a sink for hydrogen to effuse from the weld metal.

This is a significant effect because the solubility of the hydrogen, generated during welding, is greater in the high temperature austenite phase, as shown in Figure 2. When the austenite to ferrite transformation in the HAZ occurs after the weld metal, the hydrogen that is rejected in the transformed weld metal can continue to diffuse into the adjacent HAZ that is still in its austenitic state. This mechanism is depicted in Figure 3

So now, in modern low carbon steels, when the HAZ transforms at a higher temperature, ie prior to the weld metal, the hydrogen is unable to effuse from the weld metal. The weld metal must therefore accommodate the entire amount of hydrogen generated during welding. The difference in transformation temperature of the weld metal and HAZ therefore determines the direction of diffusion, or "pumping", of hydrogen in the weld metal generated by the welding process.

In order to appreciate the role of hydrogen in WMHACC, it is important to evaluate the transformation characteristics in the HAZ of the base steel and in the weld metal, and also assess the distribution of hydrogen following welding. Until now experimental evaluation of hydrogen distribution, has proved difficult. However, a novel approach using different combinations of weld metals and base plates along with different hydrogen analysis techniques has provided an insight that may ultimately lead to a better understanding of the role of hydrogen in WMHACC.

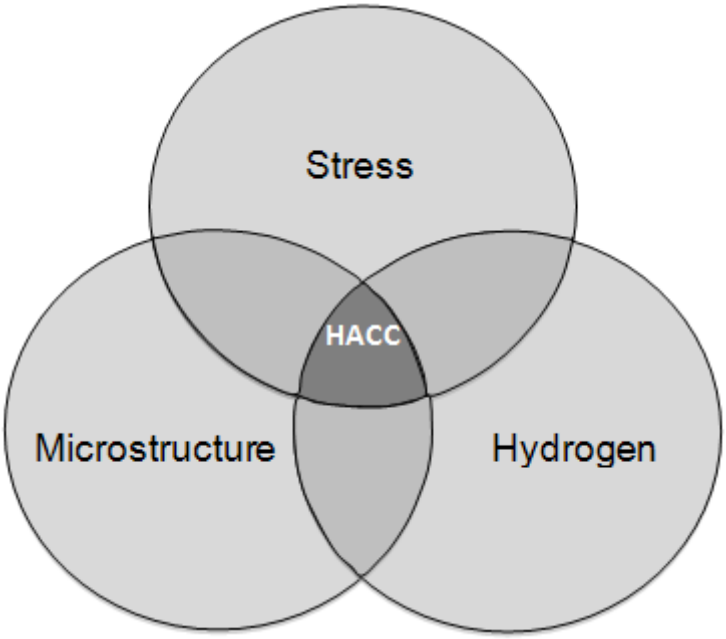

Figure 1 Basic factors responsible for hydrogen assisted cold cracking (HACC).

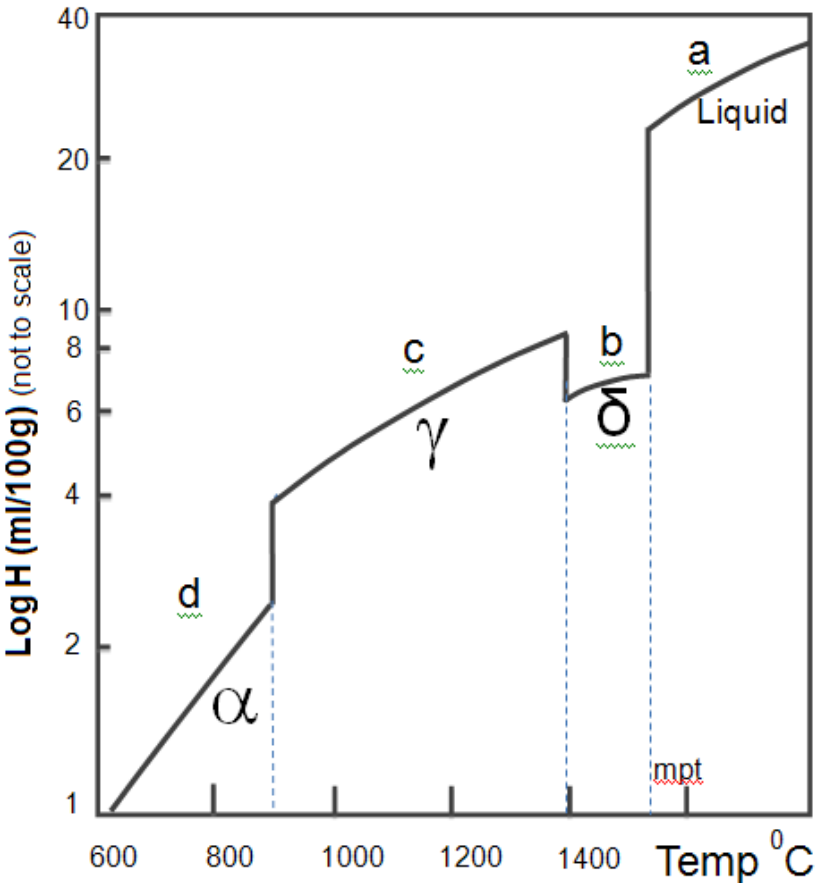

Figure 2 Relative solubility of hydrogen in steel during cooling from the liquid.

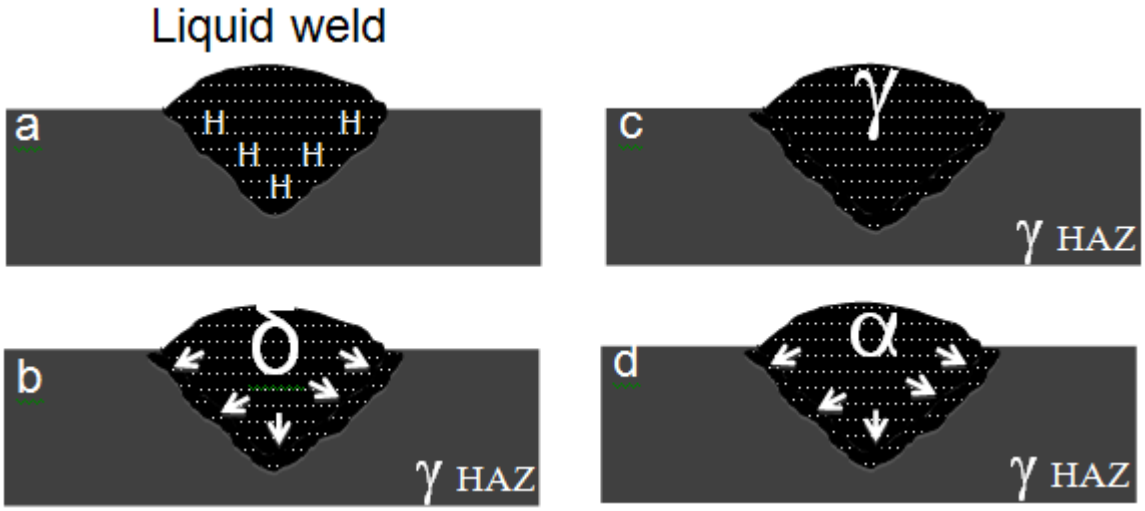

Figure 3 Schematic diagrams indicating distribution of hydrogen during cooling following welding (refer to Figure 2 for location wrt hydrogen solubility curve)
a) liquid weld containing H,
b) weld solidification to delta ferrite, H is rejected into the austenitic HAZ,
c) weld metal transforms to austenite – equilibrium conditions with HAZ,
d) weld metal transforms from austenite to ferrite before HAZ – driving force is for H to move into the HAZ.

2 EXPERIMENTAL APPROACH

Stress is unavoidable in welded joints and can be quantified in various ways along with the resultant microstructure in the weld zone. The action or distribution of hydrogen however is not very well understood.

The fundamental basis of this experimental program was to use different weld metals and evaluate both the diffusible hydrogen and the residual (retained) hydrogen in the weld zone. Measurement of diffusible hydrogen is achievable by collection over mercury or glycerol at a defined temperature (usually room temperature), while the total hydrogen can be determined by complete fusion methods. The use of different consumables, viz ferritic and/or austenitic weld metal, provides the opportunity to systematically evaluate the distribution of hydrogen within the regions of a completed weld.

The high strength steel used was typical of those used for high hardness wear plate, microalloyed with Nb, Ti, V and B to ensure adequate hardenability in quench and tempering (Q&T) processing. This is a steel grade with sufficiently low austenite to ferrite transformation temperature to evaluate the aims of the current work. The chemical composition is presented in **Table 1**. The typical microstructure of the plate following the Q&T process would consist of tempered martensite and the final hardness would be dependent on tempering temperature.

Table 1. Chemical composition of investigated steel in wt% max.

Element	C	P	Mn	Si	S	Ni	Cr	Mo
wt% max	0.32	0.02	0.40	0.35	0.005	0.35	1.15	0.3

Element	Cu	Al	Nb	Ti	V	B	CE_{IIW}
wt% max	0.20	0.06	0.005	0.030	0.050	0.0020	0.72

Transformation temperature

The continuous cooling transformation (CCT) behavior of the steel [1] revealed that peak hardenability was achieved at a cooling rate representative of real welding conditions (cooling at 20°C/s to 30°C/s) in the temperature range of 800-200°C. At these cooling rates the austenite transformation takes place over a range of 200°C with transformation start and finish temperatures approximately 410°C and 205°C respectively.

Hydrogen determination

The primary objective of this investigation was to determine hydrogen distribution in the weld zone with the following variables:

- ferritic and austenitic consumables,
- a range of preheat (PH) temperatures, and
- different weld consumable types.

Weld samples were produced using the following austenitic consumables:

- flux-cored wire - AWS A5.22 E308 MoT1 type,
- metal-cored wire - AWS A5.9 EC308 Mo type,
- solid wire - AWS A5.9 ER(307) and,

one ferritic consumable:

- flux-cored wire - AWS A5.20 E71T-1

A robotic GMAW system was utilised to deposit consistent single weld beads onto the test piece assembly clamped in a copper jig. The welding procedures, including assemblies complied with the Australian Standard AS/NZS 3752:2006 [2] for hydrogen determination in weld metals.

Preheating was carried out utilising an electric resistance heating blanket and undercooling of the test piece assembly to 7°C was achieved using dry ice (solid CO_2). After deposition of the weld beads, samples were quenched in stirred iced water and transferred into the bath of liquid nitrogen. The run-on and run-off pieces were detached and the weld sample (ie centre section) was thoroughly cleaned with a steel wire brush. The intervals spent outside the liquid nitrogen did not exceed 15seconds. Parameters that were kept constant for all trials are shown in **Table 2**. Variable welding parameters are displayed in **Table 3**.

Table 2 Welding parameters common to all welding trials.

Welding parameter	Value
Travel speed	400 mm/min
Wire feed speed	9.5 m/min
Stick out	16 mm
Voltage	26.3 V
Polarity	DC+
Shielding gas flow rate	16-20 l/min
Wire diameter	1.2 mm

Table 3 Variable welding parameters. Note: The values are the average of three welds completed

Weld #	Flux type	WM	Base Plate	Preheat [°C]	Quench Temp. [°C]	Shielding gas, BOC	Amp [A]	Heat input [kJ/mm]
1	FC	Austenitic	Ferritic	20	Direct	Argoshield 52	215	0.85
2	FC	Ferritic	Ferritic	24	Direct	Argoshield 52	253	0.998
3	FC	Austenitic	Austenitic	22	Direct	Argoshield 52	218	0.86
4	FC	Austenitic	Ferritic	22	150	Argoshield 52	220	0.87
5	MC	Austenitic	Ferritic	22	150	Stainshield	294	1.16
6	Solid	Austenitic	Ferritic	21	150	Stainshield	245	0.97
7	FC	Austenitic	Ferritic	6	150	Argoshield 52	215	0.85

8	FC	Austenitic	Ferritic	80	150	Argoshield 52	213	0.84

2.1 Diffusible hydrogen testing

The 'Reference test method' - collection of hydrogen over mercury was selected to measure the diffusible hydrogen content present in the weldments. Testing was performed in accordance with Australian Standard AS/NZS 3752:2006 [2] and every test was repeated three times to ensure accuracy of analysis.

Test samples were stored in liquid nitrogen prior to transferring to the Hg filled y-tubes, and were left for 7 days at room temperature (around 20°C) to allow the majority of diffusible hydrogen to evolve and collect in the capillary tube. The readings of atmospheric temperature and pressure were taken every day prior to measuring the volume of hydrogen. The volume of evolved hydrogen was corrected to standard temperature and barometric pressure.

2.2 Residual hydrogen testing

The inert gas melt extraction method, using the Eltra ONH 2000, was selected because it is a rapid process and has proven reliability. Testing was carried out according to the Australian Standard AS/NZS 1050 [3].

After completion of diffusible hydrogen testing, three slices transverse to the longitudinal axis of each centre weld sample were sectioned utilising a water-cooled precision cutting machine. The weld metal was separated from the rest of the sample using a grinding wheel. In between grinding steps, samples were cooled in water to prevent heating due to friction and possible loss of residual hydrogen. The resultant samples of weld metal of approximately 1g were washed in acetone, dried and subjected to residual hydrogen testing.

3 RESULTS

3.1 Effect of welding consumable type on hydrogen level

To directly compare the overall amount of hydrogen introduced into the weldment utilising ferritic and austenitic flux-cored wires, samples were quenched in stirred iced water immediately after completion of welding, in accordance with Australian standard AS/NZS 3752:2006 [2]. All samples were welded without preheat at ambient temperature.

Table 4 Levels of diffusible and residual hydrogen measured using different combinations of weld metal consumable and base plate.

Weld #	Consumable	Base Metal	Diffusible H content [ml/100g of WM]	Residual H content [ml/100g of WM]
1	Austenitic	Ferritic	1.3	5.8
2	Ferritic	Ferritic	23.4	0.9
3	Austenitic	Austenitic	0.0	8.0

The results presented in Table 4, reveal that very little diffusible hydrogen was detected where an austenitic consumable was employed. The relatively high residual levels of

hydrogen for Welds 1 & 3 confirm that the weld metal generated hydrogen is retained within the austenitic structure and is only liberated by complete fusion analysis. The recorded diffusible hydrogen in Weld 1 is assumed to be related to the hydrogen liberated from the small region of ferritic HAZ surrounding the weld metal.

The high level of diffusible hydrogen recorded in the ferritic weld metal, and the associated low residual level in Weld 2, confirms that ferritic structures liberate hydrogen over a time period at room temperature, as revealed by the over Hg method. The extremely high level of diffusible hydrogen recorded in this particular fully ferritic weld joint appears to be related to contamination of the weld consumable because such a consumable would normally be expected to yield only 6-10 ml/100gm of weld metal hydrogen. This has been observed previously [4] and despite this high hydrogen result, the data confirms the effectiveness of the two different hydrogen analysis techniques to detect the diffusible hydrogen in the ferritic structure and the residual hydrogen in the austenitic structure.
To unequivocally demonstrate that only the diffusible hydrogen originated from the ferritic structures using the over Hg method, a complete austenitic weld metal and base plate was subjected to diffusible hydrogen analysis. The result presented in **Table 4** (Weld 3) clearly demonstrates the effectiveness of hydrogen retention in an austenitic structure and that complete fusion analysis was required to liberate the hydrogen.

3.2 Comparison of hydrogen levels for three types of austenitic consumables

It is well known that the type or design of a weld consumable can generate different levels of hydrogen within the deposited weld metal. To assess the influence of flux type, 3 different austenitic consumables were deposited onto the ferritic base plate. The consumable types were a rutile flux cored, metal cored and a solid metal wire and the recorded levels of both diffusible and residual hydrogen contents are presented in **Table 5**.

Table 5 Values of diffusible and residual hydrogen levels measured for three different types of austenitic consumables deposited onto the ferritic base plate.

Weld #	Austenitic consumable type	Diffusible H content [ml/100g of WM]	Residual H content [ml/100g of WM]	Total H content [ml/100g of WM]
4	Flux-cored	0.8	7.9	8.7
5	Metal-cored	0.5	4.6	5.1
6	Solid	0.0	3.7	3.7

The rutile flux cored wire produced the highest level of residual hydrogen followed by the metal-cored wire and then the solid metal wire. These values are a consequence of the flux employed and it is well known [5] that the rutile flux is hygroscopic and can generate high levels of weld metal hydrogen (as shown in section 1). Conversely, the metal cored wire, because of the lack of a flux produced a low level of weld metal hydrogen.

A significant point to note here is the reduction in diffusible hydrogen (ie from the ferritic base plate), as the total level of hydrogen is reduced. From these results, it appears that the level of hydrogen diffusion into the adjacent HAZ is related to the total level of weld metal

hydrogen and that possibly a certain level of weld metal hydrogen is required before the hydrogen is able to diffuse into the adjacent HAZ.

For this reason, the flux-cored consumable was selected for further evaluation of hydrogen diffusion using different weld preheats, as described in section 3.

3.3 Effect of preheat temperature on hydrogen content

To determine the effect of weld preheat and the extent of hydrogen diffusion following welding, the flux cored austenitic consumable was deposited on the ferritic base plate at different preheat levels and quenched into ice brine when the weld had cooled to a temperature of 150°C. This weld procedure provided firstly sufficient hydrogen within the weld metal, and secondly a reasonable difference in time after welding and before quenching to evaluate hydrogen distribution in the weldment. Hydrogen analysis using both the over Hg method and complete fusion technique would therefore provide evaluation of the retained hydrogen in the austenitic weld metal and the level of hydrogen in the adjacent ferritic HAZ.

Table 6 Levels of diffusible and residual hydrogen measured for the flux cored austenitic WM deposited on the ferritic base plate under different preheat conditions.

Weld #	Preheat temperature [°C]	Cooling time to 150°C (seconds)	Diffusible H content [ml/100g of WM]	Ave	Residual H content [ml/100g of WM]	Ave
7	7	71	1.29		7.1	
7	6	65	1.00		6.3	
7	6	42	1.61	1.30	4.9	6.1
4	Amb (22)	ND	0.96		7.7	
4	Amb (22)	91	0.78		8.0	
4	Amb (22)	95	0.81	0.85	8.1	7.9
8	80	163	0.64		7.8	
8	80	150	0.50		8.6	
8	80	180	0.50	0.55	7.6	8.0

The results presented in Table 6 reveal that an increase in preheat temperature from 7°C to 80°C resulted in a decrease in diffusible hydrogen (average) 1.30 to 0.55 ml/100g and an increase in residual weld metal hydrogen content (average) 6.1 to 8.0 ml/100g). Although there were minor variations in total hydrogen content, it is clear that, with increased time before quenching, the driving force for hydrogen diffusion was to partition to the austenitic weld metal.

These results strongly suggest that hydrogen had diffused from the weld metal immediately after the weld was deposited, ie into the HAZ, but after transformation of the HAZ to the lower temperature ferritic phase, the hydrogen had sufficient time, before quenching, to allow back diffusion into the austenitic weld metal.

The austenitic weld structure, which in conventional ferritic weldments, would be equivalent to the weld metal transforming after the HAZ, therefore promotes hydrogen diffusion from the HAZ back into weld metal. In other words the austenitic weld metal microstructure having a high solubility provides the "sink" for hydrogen. Therefore reduced cooling times to 150°C (ie less time for diffusion of hydrogen from HAZ back into the weld metal) as a consequence of lowering the preheat temperature, resulted in lower levels of weld metal residual hydrogen content.

Therefore the condition of the weld metal, ie austenitic or ferritic, will have an influence on the distribution of hydrogen following completion of welding.

Further analysis of the level of hydrogen with respect to time of cooling after welding, as presented in Figure 4, provides the basis for additional weld metal testing and ultimately more accurate modelling of hydrogen diffusion. Such an appreciation of the distribution of hydrogen as a function of weld and HAZ transformation temperature may provide a basis for a better understanding of the mechanism of WMHACC in modern high strength steels.

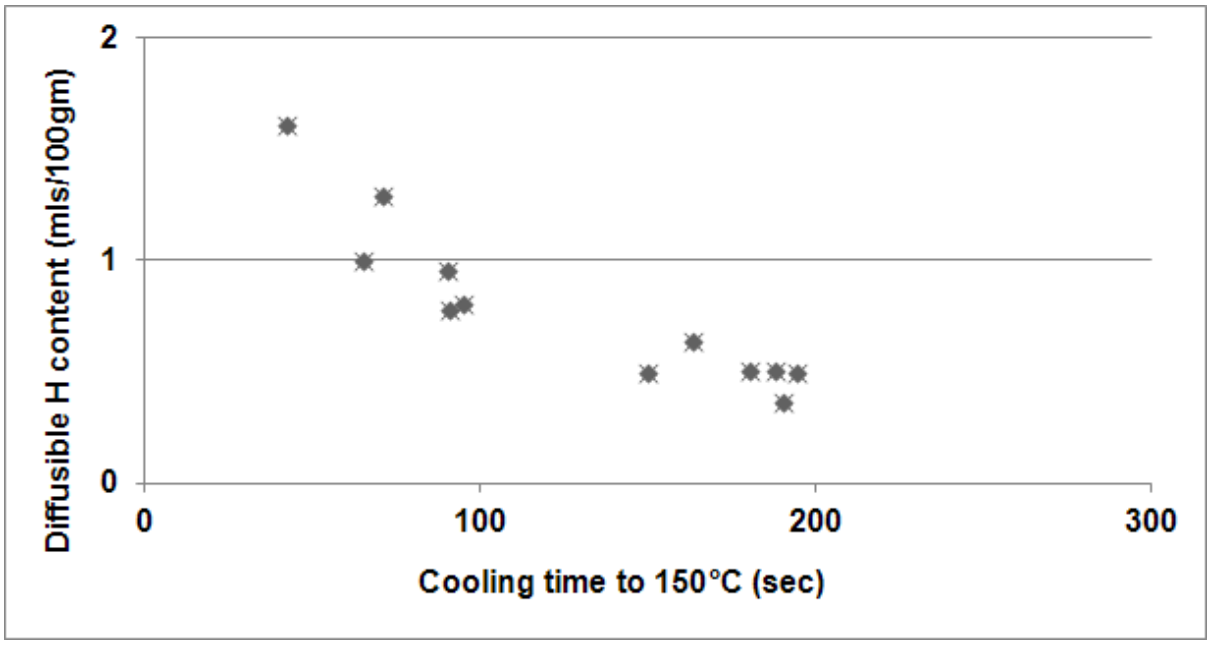

Figure 4 Diffusible hydrogen levels recorded in the ferritic base plate following different cooling times after welding.

4 CONCLUSIONS

The use of established methods of hydrogen analysis on welds containing different weld metals have provided new information on the diffusion of hydrogen following weld fabrication. From the results of this investigation the following conclusions are drawn:

1. The use of rutile flux type consumables can introduce high levels of hydrogen into the deposited weldment. In ferritic rutile flux cored consumables, the level of weld metal hydrogen can, depending on the condition of the consumable, be extremely high.
2. The level of hydrogen diffusion from the weld metal into the high temperature austenitic HAZ is dependent on the level of weld metal hydrogen content. In the present investigation, a weld metal hydrogen content of 4.6 ml/100gm was required to detect any diffusible hydrogen into the HAZ
3. The presence of an austenitic weld metal, and / or a weld metal that transforms after the HAZ will provide a sink for hydrogen and so reduce the level of hydrogen in the adjacent HAZ,
4. Where a ferritic weld metal transforms after the HAZ, the level of hydrogen diffusion from the weld metal is reduced and thus reduces susceptibility to HAZHACC but increases the risk of WMHACC.
5. This work has confirmed the long held view and widely known benefit that an austenitic weld metal will reduce the risk of HACC in both the HAZ and the weld metal.

Acknowledgements

This work was mainly supported by the Defence Materials Technology Centre (DMTC), which was established and is supported by the Australian Government's Defence Future Capability Technology Centre (DFCTC) initiative. The support of BlueScope Steel Ltd for provision of hydrogen analysis facilities is also gratefully acknowledged. Special thanks are extended to Rudy Drmota for assistance in diffusible hydrogen testing. Thales Group is acknowledged for providing the steel plate and welding consumables. NSW science leverage grant from the NSW Government is acknowledged, for resource contribution to the lean automation work cell in which the welding work was conducted.

References

1. L.Kuzmikova, M. Callaghan, N. Larkin, R. Scott, R. De Jong, H. Li, J. Norrish, "A Study of a Continuous Cooling Behaviour & Effect of Preheat & Interpass Temperature on the HAZ of High Strength Quenched and Tempered Steel" Doc IX-2352-10. Paper presented in commission IX the IIW Annual Assembly, Istanbul, July 2010.
2. Australian Standard AS/NZS 3752:2006
3. Australian Standard AS/NZS 1050
4. D. Nolan and M. Pitrun, "Diffusible Hydrogen Testing in Australia", *Welding Research Abroad*, Vol.51, No.2, pp.45-51, 2005.
5. D. Nolan, M. Pitrun and D. Dunne, "Diffusible Hydrogen Content in Rutile Flux-Cored Arc Welds as a Function of Welding Parameters", *Welding in the World*, Vol.48, No.1/2, p2, 2004.

DEVELOPMENT OF SAFE OPTIMISED WELDING PROCEDURES FOR HIGH STRENGTH Q&T STEEL WELDED WITH AUSTENITIC CONSUMABLES

Authors: L. Kuzmikova, H. Li and J. Norrish

This paper has been accepted to be published in Brazilian Welding Journal

ABSTRACT

High strength quenched and tempered (Q&T) steels offer obvious economic benefits originating from their advantageous strength to price and weight ratios. These steels are usually welded using ferritic consumables and for this combination the risk of hydrogen assisted cold cracking (HACC) is high. The use of austenitic stainless steel (ASS) consumables has great potential to significantly improve this issue. Yet, there are no guidelines for determination of safe level of preheat for welding ferritic steels with ASS consumables. For this reason manufacturers adopt this parameter from procedures developed for conventional ferritic consumables thus significantly limiting the benefits ASS consumables are capable to deliver. Productivity could be further enhanced by identifying the upper interpass temperature threshold, thus reducing the stand-off times. Aim of this work is to develop safe highly optimised procedures for welding of high strength Q&T steel with ASS consumable.

1 INTRODUCTION

In fabrication of steel structures productivity and cost-effectiveness of the welding process significantly affect the price of the final product. Therefore, ways of improving these factors are constantly being reviewed and advanced solutions are being implemented.

The main concern when welding Q&T steels is the risk HACC. Common practice to avoid this defect from occurring is to employ sufficient pre or post heating of the weldment. However, both these treatments represent an additional step in the welding process, significantly reduce productivity and increase fabrication costs. Further, post weld heat treatment is not recommended for Q&T steels due to stress relief cracking [1].

Industry partner initially welded high strength Q&T steel in high hardness condition with ferritic consumables and preheating was necessary even for thin sections to reduce the cooling rate and allow additional time for hydrogen to diffuse out of the joint. Despite this measure the risk of HACC was still very high as it was difficult to ensure that these restricted procedures were narrowly followed in every day manufacturing practice. The use of flux-cored ASS consumable offered optimum solution to this problem as it has got much higher solubility and considerably lower diffusivity of hydrogen compared to ferritic fillers. However the level of preheat remained unchanged due to the lack of guidance on welding ferritic steel with ASS consumable provided by welding standards.

Various methods of determination of minimum level of preheat ensuring freedom from HACC are summarised in ISO/TR 17844 [2]. For a given chemistry and heat treatment history this standard advises to use so called CET method. Following this method the

minimum preheat temperature was calculated to be 78°C. This value is in good agreement with the preheat temperature range used in the industry practice (80-120°C) originally developed for ferritic filler. This document further states that preheat can be reduced when ASS consumable is used as a result of better strain condition and hydrogen distribution across the weldment. Lower levels of preheat are also permissible for multi-pass welding if adequately high inter-pass temperature is maintained in between the deposition of the single passes assisting the diffusion of hydrogen out of the areas of previous passes. However, no indication of the lower safe threshold for welding ferritic steels with austenitic stainless steel consumable is provided.

Further to reduce the risk of HACC adequate inter-pass temperature in between deposition of the single passes has to be maintained. Inter-pass temperature range is typically identical with preheat. High strength Q&T steels are not only prone to HACC but also to excessive softening of heat-affected zone (HAZ) and over-tempered region that can compromise the properties of the welded structure. From productivity view point it is beneficial to employ highest inter-pass temperature that does not produce extensively wide areas with high degree of softening. However when designing welding procedures the selection of inter-pass temperature ensures only freedom from HACC and the upper threshold is not usually explored. This is not necessary for conventional manual and semi-automatic welding. The customers demand to increase the production outputs indicated necessity to explore fully automatic processes utilising welding robots that can achieve very high welding speeds, thus information about the higher inter-pass temperature thresholds became desirable.

Productivity could be further improved by employing metal-cored wire instead of currently used flux-cored. Flux-cored wire produces slag deposit on the surface of the weld. In case of multi-pass welding, the slag needs to be removed before deposition of the subsequent pass. This introduces additional difficulty for automation and is disadvantageous in terms of both productivity and cost. Additionally, the flux also has the potential to pick-up hydrogen from the surrounding atmosphere if the consumable is stored inappropriately or over a long period of time. This hydrogen can be absorbed by the weld pool, increasing the risk of HACC. Other advantages of the metal-cored wire include higher duty cycles, faster travel speeds, low fume formation and very good cost effectiveness. This makes this wire ideal candidate for automated processes.

The objective of this work was to develop safe highly optimised procedures for fully automated welding of high strength Q&T steel with metal-cored ASS consumable by identifying the lower preheat and upper inter-pass temperature threshold.

2 MATERIALS

The chemical composition of the investigated high strength Q&T steel is listed in Table 1. The microstructure of the plate in Q&T condition consists of tempered martensite with an average hardness of 519 HV and is shown in Figure 1.

The alloy design of this steel utilises the novel low manganese approach in order to reduce centreline segregation of MnS inclusions and thus improve mechanical properties and weldability. The steel is microalloyed with Nb, Ti, V, and B in order to increase hardenability and enhance the HAZ properties.

Table 1 Chemical composition of 8.5mm HHA steel in wt % max.

Element	**C**	**Mn**	**Si**	**Ni**	**Cr**	**Mo**	**S**	**P**
Wt% max	0.32	0.4	0.35	0.35	1.15	0.3	0.005	0.02

Element	**Cu**	**Al**	**Nb**	**Ti**	**V**	**B**	**CE_{IIW}**	**P_{cm}**
Wt% max	0.2	0.06	0.005	0.03	0.05	0.002	0.72	0.46

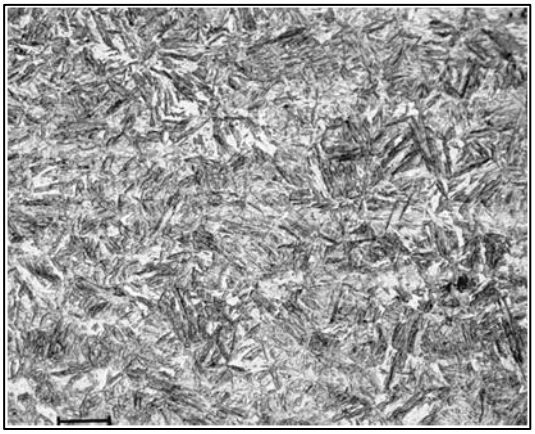

Figure 1 Representative microstructure of investigated steel in Q&T condition. Note the micron bar represents 20μm.

Metal-cored consumable AWS A5.9 EC308Mo type is ideal candidate for fully automated welding and was selected for this investigation. It is a versatile gas shielded, seamless wire capable of out of position welding and exhibits enhanced productivity and wetting action when compared to equivalent solid wire.

3 EXPERIMENTAL PROCEDURES

3.1 Welding set-up

To determine the lower preheat temperature threshold, single pass fillet weld configuration was selected and is shown in Figure 2 - a. This arrangement is the most susceptible to HACC as the HAZ is not tempered by the subsequent passes. Samples were welded with following levels of preheat 5°C (simulating ambient temperature during winter periods), 20°C and 80°C (current industry practice).

The deposition of multiple passes can result in formation of extensively wide softened zones especially when high heat inputs or inadequately high inter-pass temperatures are employed. Therefore to optimise the inter-pass temperature multi-pass corner joint configuration shown in Figure 2 – b was used for this investigation. Inter-pass temperatures of 120°C (current industry practice), 200°C and 250°C were selected for this study. Any higher inter-pass temperature would not have a practical benefit (especially for longer weld sections) as the

weld initially cools very rapidly and only during the later stages the cooling rate is significantly reduced.

After completion of welding samples were prepared according to standard procedures for metallographic investigation and Vickers hardness testing

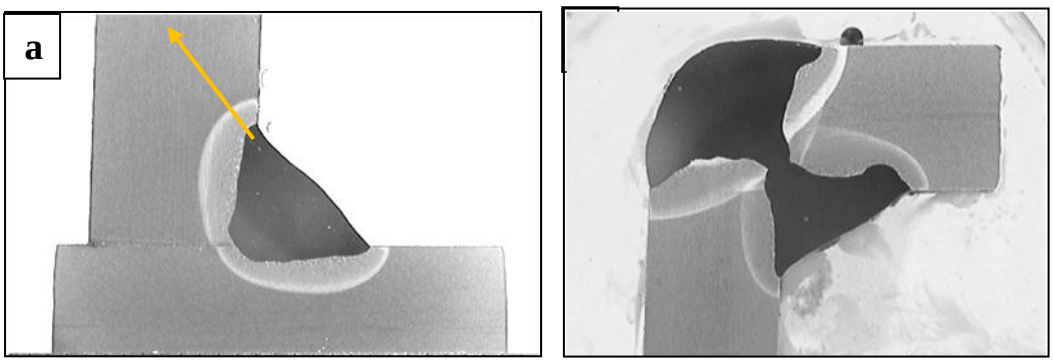

Figure 2 Macrophotograph showing the weld geometry and orientation of hardness traverses for: a – single and b - multi-pass weldments.

3.2 Weld thermal history

Resultant microstructure and hence mechanical properties of the HAZ are function of chemical composition of the steel, peak temperature and cooling cycle experienced during welding.

Coarse-grain (CG) HAZ is the most susceptible to HACC out of all HAZ subzones. To demonstrate the effect of various levels of preheat on CGHAZ microstructure thermal profiles were acquired using technique of embedding thermocouples.

Weld thermal history of multi-pass joints was acquired to provide information about effects of various inter-pass temperatures on cooling rate and cooling times of the over-tempered region of the welded joint. For this purpose the thermocouples were spot-welded 15 mm from the edge of the plate.

4 RESULTS

To confirm safety of the proposed welding procedures with reduced (ideally removed) preheat and increased inter-pass temperatures the information about the effect of various levels of these two temperatures on the HAZ microstructure and hardness is essential.

5. Optimisation of preheat temperature

Weld thermal history

From HACC view point the most important part of the thermal history is the cooling leg that will influence resultant microstructure, diffusible hydrogen level and also the residual stresses formed as a consequence of welding process. As mentioned previously CGHAZ is the most

susceptible subzone thus the aim was to acquire thermal profile of this area. Measured peak temperature listed in Table was in the range of 1349°C to 1411°C confirming that acquired thermal history was the measured in the CGHAZ.

Cooling time from 800°C to 500°C (t8/5) is usually selected to define the cooling cycle of a weldment. The susceptibility to HACC for various heat inputs and preheat conditions can be directly assessed based on this parameter. However the continuous cooling transformation investigation of the high strength steel used in this investigation revealed that transformation of HHA steel occurs in the temperature interval of 600°C to 200°C [3]. Therefore cooling time t6/2 more accurately represents cooling conditions crucial for evolution of microstructure. The hydrogen diffusion is the most active at high temperatures but continues to take place at lower temperatures at slower rate. The HACC typically occurs when temperature of the weldment drops below 200°C; therefore overall cooling time from the peak temperature to 100°C (tp/1) most precisely describes the conditions for hydrogen diffusion.

Table 2 Cooling cycle characteristics (cooling time t8/5, t6/2 average cooling rate through 800°C - 500°C, and tp/1) measured for coarse-grain HAZ of single pass filet weldments preheated to 5°C, 20°C and 80°C.

Preheat temperature [°C]	Tp [°C]	t8/5 [s]	t6/2 [s]	tp/1 [s]
5	1348	9.3	81	353
20	1411	9.7	97	410
80	1374	12.6	159	608

From data presented in Table 2 it is obvious that increasing the preheat temperature resulted in longer cooling times and slower cooling rates through the whole course of cooling. The value of conventional parameter describing the cooling conditions t8/5 increased from 9.3 s to 12.6 s with increasing the preheat temperature from 5°C to 80°C. The cooling time through the transformation region t6/2 doubled with increasing the level of preheat from 5°C to 80°C. The overall cooling time from peak temperature to 100 °C tp/1 increased by 72% with increasing the level of preheat from 5°C to 80°C.

Weld hardness profiles

Fundamental trend in hardness was gradual increase in across the entire weldment, with respect to decreasing the preheat temperature. This is due to the formation of harder microstructures as a result of increased cooling rate. From the graph presented in Figure 3 it can be observed that CGHAZ hardness increased by approximately 50 HV with decreasing preheat temperature from 80°C to 5°C. The hardness of over-tempered (OT) region gradually

increased by 30HV and the width decreased by 3 mm with decreasing preheat from 80°C to 5°C.

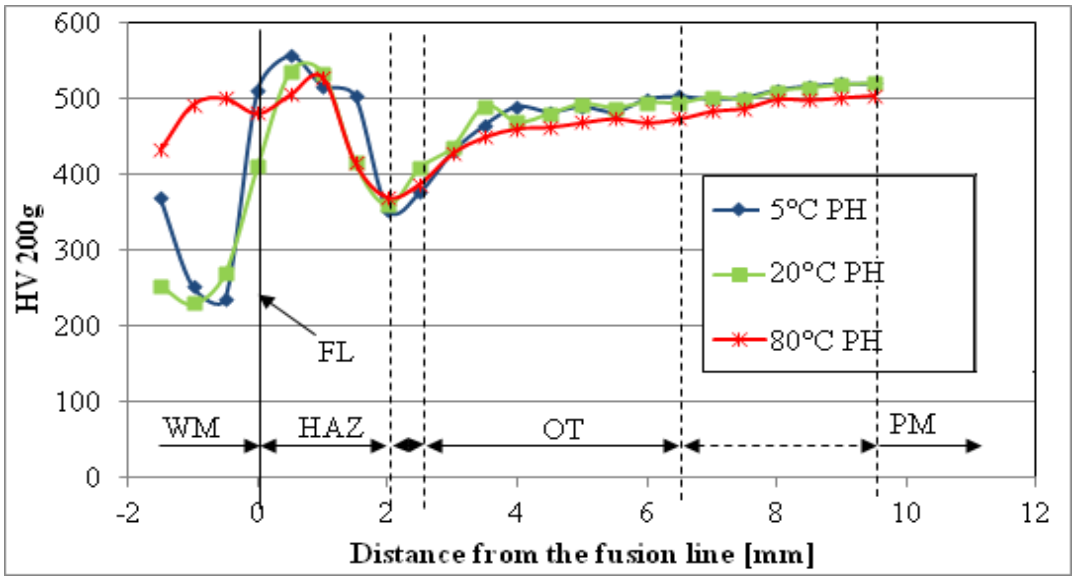

Figure 3 Weld hardness profiles of the 1 pass filet joints welded employing preheat temperatures of 5°C, 20°C, and 80°C.

CGHAZ microstructure

The microstructure of the CGHAZ of the 1 pass fillet weld is presented in Figure 4. Samples preheated to 80°C consisted of mixture of upper and lower bainite and lath martensite. Ferrite was also present in the form of very fine ferritic laths of upper bainite. When 20°C preheat temperature was employed ferritic laths were no longer present in the structure of coarse-grained region. Lowering the preheat temperature favoured the formation of higher volume fraction of harder phases and the microstructural features became finer. The amount of martensite increased at the expense of bainite with lowering the preheat temperature.

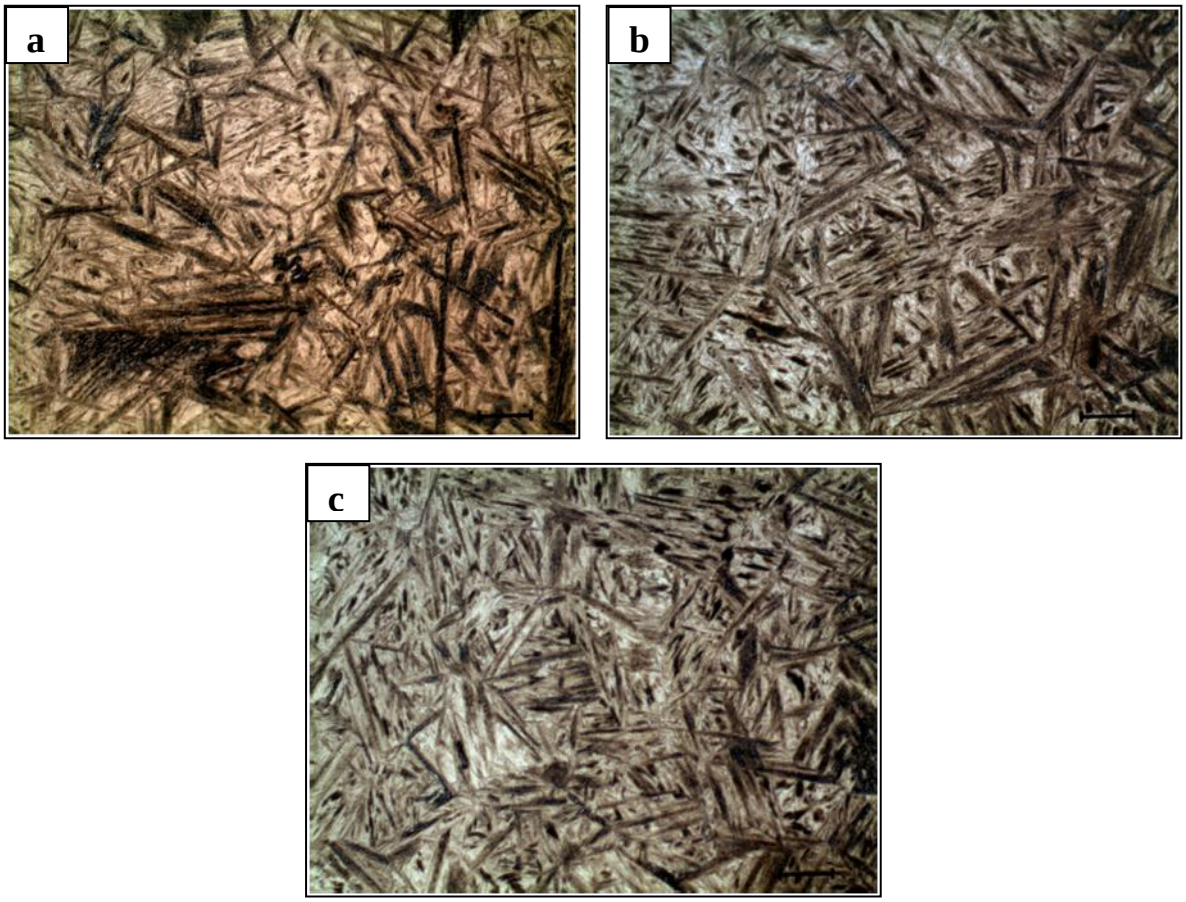

Figure 4 Microstructure of the coarse-grained HAZ subzone of the 1 pass fillet welds deposited using various levels of preheat: a - 80°C, b – 20°C, c - 5°C. Note: micron bar represents 20 micrometers.

6. Optimisation of inter-pass temperature

The cooling time data presented Table 3 show that increasing inter-pass temperature from 120°C to 250°C reduced the welding time (from the peak temperature of the first cap pass [tp(1st pass)] until the peak temperature of the final pass was reached [tp(final pass)]) from 923s to 203s. These data are particularly significant to industry and are a useful tool to gauge productivity gains during fabrication. Increasing the inter-pass temperature to 200° and 250°C resulted in reduction in cooling time of approximately 10 minutes (66%) and 12 minutes (78%). Overall cooling time (from the peak temperature of the first cap pass [tp(1st pass)] until 100°C was reached after completion of welding [t100˚C(final pass)]) was gradually reduced from 1904s to 1400s with the increase of inter-pass temperature from 120°C to 250°C. Overall cooling time data is important in assessing time taken for cooling with respect to diffusion of hydrogen out of the weldment during the welding process.

Table 3 Cooling times of the cap passes of the corner joint.

Interpass temperature [°C]	120	200	250
Cooling time {t_p(1st pass) to t_p(3rd pass)} [sec]	923	315	203
Cooling time {t_p(1st pass) to $t_{100°C}$(3rd pass)} [sec]	1904	1486	1400

Weld hardness profiles

It was observed that with an increase in inter-pass temperature, a gradual decrease in HAZ hardness was found to occur, as a result of slower cooling rates in transformation region promoting formation of softer microstructures. The maximum difference between HAZ hardness at 120°C and 250°C was approximately 150HV. In addition, the HAZ widths for all inter-pass temperatures were very similar, with only slight increases of maximum 0.5mm. Hardness profiles measured in the OT region were found to be almost identical with only very slight decrease in hardness with increasing the inter-pass temperature to 200°C. Further increase to 250°C resulted in somewhat higher degree of softening of maximum 50 HV. The width of the OT increased with increasing cooling rate from 120°C to 250°C by 3.5mm

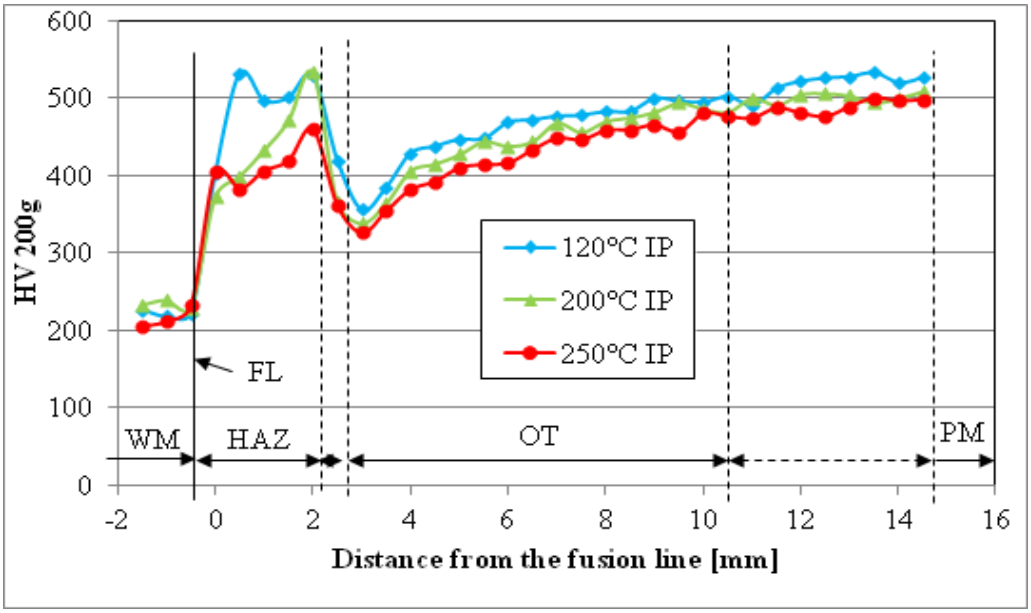

Figure 5 Weld hardness profiles measured in B orientation of the multi pass corner joints welded with interpass temperatures of 120°C, 200°C and 250°C.

Microstructure of OT region

When welding high strength steel in Q&T condition the deposition of multiple passes can result in formation of extensively wide softened regions especially when high inter-pass temperatures or high heat inputs are employed. Therefore the microstructure of OT region was subjected to close examination and micrographs are presented in Figure 6.

The microstructure of all investigated weldments consisted predominantly of tempered martensite. Increasing interpass temperature for 120°C to 250°C appears to have little to no effect on the microstructure of OT region. This observation is consistent with hardness data presented in previous section.

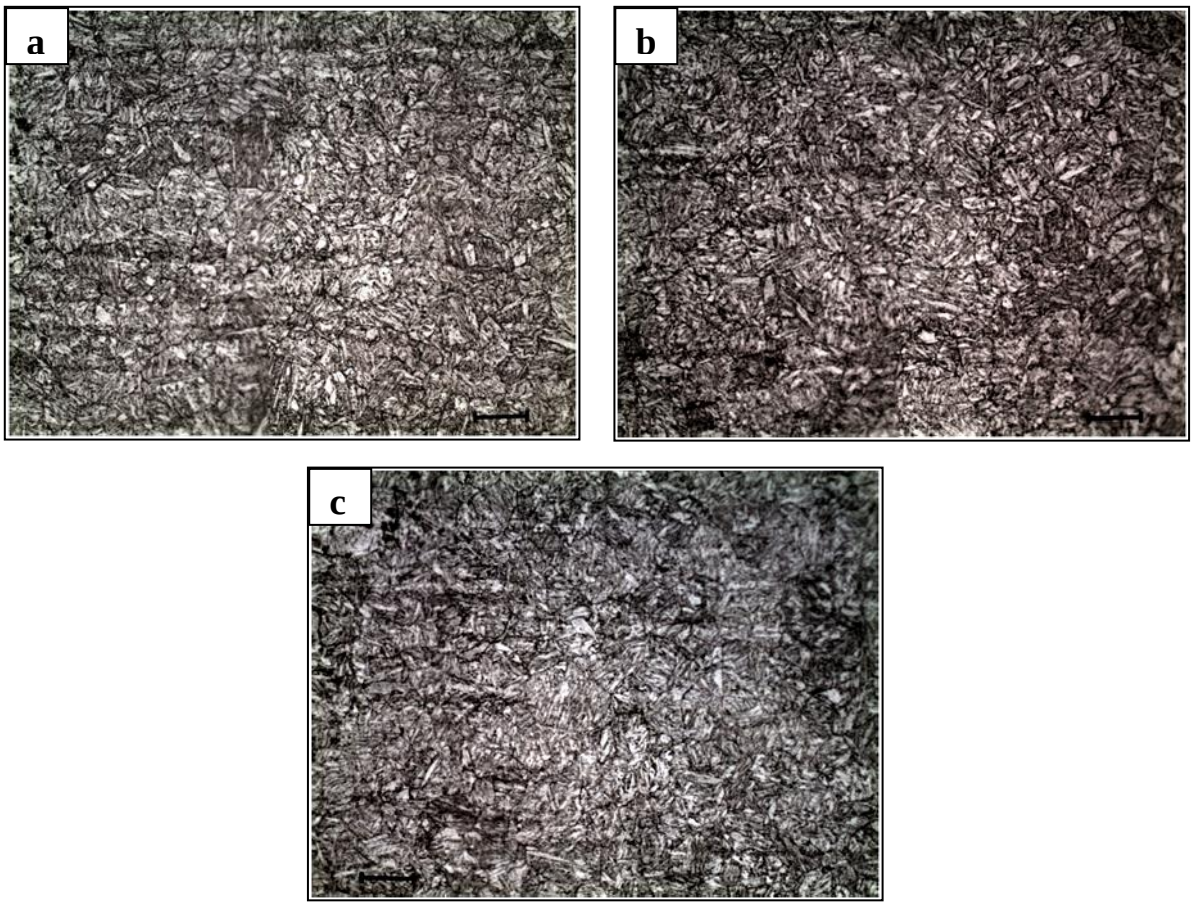

Figure 6 Microstructure of the over-tempered HAZ region of the multi-pass corner welds deposited employing interpass temperatures of: a - 120°C, b – 200°C, and c - 250°C. Note: micron bar represents 20 micrometers.

5 DISCUSSION

5.1 Optimisation of preheat

To be able to confirm the safety of proposed lower preheat temperature is necessary to assess the influence preheat reduction on all three factors contributing to HACC (microstructure, diffusible hydrogen and weld residual stresses).

Microstructure and hardness

From microstructural view point decreasing the preheat temperature from 80°C to 5°C produces slightly harder structures. However GGHAZ of the weldments produced employing both levels of preheat comprises of hard and brittle bainitic and martensitic constituents. The difference between the two levels of preheat is that joint simulating preheat temperature of

5°C contains higher martensite to bainite ratio compared to the one welded utilising 80°C preheat. Also HAZ hardness of the joints welded employing both preheats is very high, well about the level considered to be safe from HACC view point. The AS/NZS 1554.4 standard [4] states that even when welding Q&T steels employing low hydrogen consumable, maximum allowable HAZ hardness ensuring freedom from HACC is 450 HV. This critical hardness value is considered when welding utilising ferritic consumable. However, the industry procedures previously used for welding this high strength Q&T steel employed ferritic consumable in combination with 80°C that resulted in HAZ hardness levels above 500 HV. Slightly higher hardness obtained in the HAZ as a result of elimination of preheat is expected to be compensated by the ability of austenitic stainless steel weld metal to accommodate higher hydrogen and stress levels.

Diffusible hydrogen level

Results of previous work [5] revealed that weldments produced employing identical metal-cored austenitic stainless steel consumable as used in present study resulted in very low levels of diffusible hydrogen of 0.5 ml of hydrogen per 100g of weld metal. In fact previously used flux-cored ferritic consumable introduced 18 times more diffusible hydrogen into the weld pool compared to austenitic stainless steel filler. The study further revealed that preheat level in range of 5°C to 80°C had only minor effect on the value of the measured diffusible hydrogen measured for welds produced utilising ASS consumable.

Weld residual stresses

Austenite has considerably higher coefficient of thermal contraction than ferrite (typically 18 and 14 x 10^{-6} /°C in the range of 1°C – 100°C for austenitic and ferritic steel respectively) thus the overall contraction is higher than that of ferritic weld metal. However ASS weld metal possesses increased ability to yield and hence compensate thermal contraction resulting in limited evolution of residual stresses compared to ferritic weld metal [6]. Due to these phenomena residual stresses in joints welded with ASS consumable are likely to be lower compared to ferritic consumables, even though the lower preheat temperature is employed. In addition, on cooling HAZ of the parent material undergoes martensitic transformation that is accompanied by volume expansion which to certain extent compensates the thermal shrinkage.

5.2 Optimisation of inter-pass temperature

Microstructure and hardness

Increasing inter-pass temperature to 250°C had a beneficial influence on HAZ through slightly reducing the hardness levels. Formation of softer microstructures especially in coarse-grained region could have beneficial effects with respect to reducing the potential risk of HACC. Hardness of OT region exhibited only minor degree of softening with increasing inter-pass temperature from 120°C to 200°C. Slightly higher softening was observed with further increase of inter-pass temperature to 250°C. However this temperature was investigated as the worst case scenario to expand the temperature window when depositing short welds.

The main concern when employing higher inter-pass temperatures for welding high strength Q&T steel is formation of wide extensively softened areas in the over-tempered region that could compromise the mechanical properties of the welded structure. Conversely resulting prolonged cooling times after deposition of final pass favour the diffusion of the hydrogen and also temper rehardened HAZ areas thus reducing the risk of HACC. These effects are

likely to compensate implication resulting from employing proposed lower level of preheat for multi-pass joints.

6 CONCLUSOINS

Results of this and previous work suggest that for welding high strength Q&T steel with ASS consumable decreasing preheat temperature from 80°C to 5°C is safe in terms of HACC. Further in case of multi-pass welding the implications of increased cooling rate resulting from preheat reduction are likely to be compensated by employing proposed higher inter-pass temperature. The nature of an austenitic stainless steel filler has the potential to remove the preheat requirement, what would allow great benefits during welding fabrication in terms of time and costs for industry as the whole technological step of preheating could be avoided.
Findings of this investigation also revealed that increasing inter-pass temperature up to 250°C does not lead to formation of wide extensively softened areas when compare to weldments produced employing inter-pass temperature of 120°C. Employing higher inter-pass temperature would also have a great positive impact on productivity.

References

1. WTIA, *WTIA Technical Note No. 15 - Welding & fabrication of quenched and tempered steel* 1996, WTIA.
2. *ISO/TR 17844: Welding — Comparison of standardised methods for the avoidance of cold cracks*. 2004, International Organization for Standardization: Geneva.
3. Kuzmikova, L., et al., *A Study of the Continuous Cooling Behaviour of High Strength Quenched and Tempered Steel*
   in *63rd Annual Assembly & International Conference of the International Institute of Welding*. 2010: Istanbul, Turkey.
4. *AS/NZS 1554.4:2010: Structural steel welding - Welding of high strength quenched and tempered steels* 2010, Standards Australia.
5. Kuzmikova, L., et al., *Research to establish a systematic approach to safe welding procedure development using austenitic filler material for fabrication of high strength steel*, in *16th International Conference on the Joining of Materials*. 2011: Helsinki, Denmark.
6. Bhadeshia, H.K.D.H., *Developments in martensitic and bainitic steels: Role of the shape deformation.* Materials Science and Engineering A, 2004. **378**(1-2 SPEC. ISS.): p. 34-39.